

A European Union Initiative supported by the International Ocean-Colour Coordinating Group and FARO (Fisheries Applications of Remotely-Sensed Ocean Colour), a GEO Task supported by the Canadian Space Agency.

## Handbook of Satellite Remote Sensing Image Interpretation: Applications for Marine Living Resources Conservation and Management

Edited by:

Jesus Morales, Venetia Stuart, Trevor Platt and Shubha Sathyendranath

In conjunction with the EU PRESPO Project for sustainable development of the artisanal fisheries in the Atlantic area, within the INTERREG IVB Programme (a Community Initiative to stimulate inter-regional cooperation in the European Union)

This report is based on contributions from (in alphabetical order):

J. Acker, J.J. Agenbag, S. Alvain, R.J.W. Brewin, R. Cajal-Medrano, J. Cannizzaro, K.L. Carder, J. Dachs, D. Dagorne, H. Demarcq, L. Duforêt-Gaurier, L. Escudero, M-H. Forget, C. Fuentes-Yaco, A. González-Silvera, N.J. Hardman-Mountford, M-X. He, T. Hirata, N. Hoepffner, C. Hu, E. Jurado, T. Kuroyama, Z. Lee, D. Li, X. Li, J. Liu, Z. Liu, H. Loisel, F. Mélin, R. Millán-Núñez, R. Mugo, F.E. Muller-Karger, A. Nihira, C. Paulino, W.G. Pichel, T. Platt, A.I. Prados, S-I. Saitoh, E. Santamaría-del-Ángel, S. Sathyendranath, R. Simó, I. Soto, V. Stuart and F. Yu.

Published by the EU PRESPO Project and the International Ocean-Colour Coordinating Group

©PRESPO and IOCCG 2010

Correct citation for this publication:

*Morales, J., Stuart, V., Platt, T., Sathyendranath, S. (2010). Handbook of Satellite Remote Sensing Image Interpretation: Applications for Marine Living Resources Conservation and Management, PRESPO and IOCCG.*

# Contents

---

<b>Theme: Air/Water Quality</b>	<b>1</b>
<b>1 Remote-Sensing Case Study of the Chesapeake Bay Region</b>	<b>3</b>
1.1 Background Information . . . . .	3
1.2 Materials and Methods . . . . .	5
1.3 Demonstration Section . . . . .	6
1.4 Training and Questions . . . . .	9
1.5 Answers . . . . .	14
1.6 References . . . . .	20
<b>2 Red Tide Detection in the Eastern Gulf of Mexico Using MODIS Imagery</b>	<b>21</b>
2.1 Background . . . . .	21
2.2 Data and Methods . . . . .	24
2.3 Demonstration . . . . .	25
2.4 Training . . . . .	29
2.5 Questions . . . . .	31
2.6 Answers . . . . .	32
2.7 Discussion and Summary . . . . .	32
2.8 References . . . . .	34
<b>3 Monitoring Green Tides in Chinese Marginal Seas</b>	<b>37</b>
3.1 Background . . . . .	37
3.2 Data and Methods . . . . .	39
3.3 Demonstration . . . . .	41
3.4 Training . . . . .	45
3.5 Questions . . . . .	46
3.6 Answers . . . . .	47
3.7 Discussion and Summary . . . . .	48
3.8 References . . . . .	50
<b>4 Ocean-Atmosphere Exchanges of Persistent Organic Pollutants on the Atlantic Ocean</b>	<b>51</b>
4.1 Background Information . . . . .	51
4.2 Satellite Data Used . . . . .	54

4.3	Demonstration Section . . . . .	56
4.4	Trainings and Questions . . . . .	61
4.5	Answers . . . . .	64
4.6	References . . . . .	65
<b>5</b>	<b>Impacts of European Atmospheric Air Pollution on Water Nutrients</b>	<b>67</b>
5.1	Background Information . . . . .	67
5.2	Demonstration . . . . .	71
5.3	Questions . . . . .	73
5.4	Answers . . . . .	76
5.5	References . . . . .	77
<b>6</b>	<b>Detection of Oil Slicks using MODIS and SAR Imagery</b>	<b>79</b>
6.1	Background . . . . .	79
6.2	Demonstration . . . . .	83
6.3	Trainings and Questions . . . . .	88
6.4	Questions . . . . .	90
6.5	Answers . . . . .	90
6.6	Discussion and Summary . . . . .	91
6.7	References . . . . .	92
	<b>Theme: Phytoplankton and Macroalgae</b>	<b>93</b>
<b>7</b>	<b>Observation of Ocean Colour Beyond Chlorophyll-<i>a</i></b>	<b>95</b>
7.1	Background Information . . . . .	95
7.2	Materials and Methods . . . . .	96
7.3	Questions . . . . .	104
7.4	Answers . . . . .	104
7.5	References . . . . .	106
<b>8</b>	<b>Monitoring Phytoplankton Productivity from Satellite</b>	<b>109</b>
8.1	Introduction . . . . .	109
8.2	Materials and Methods . . . . .	109
8.3	Demonstration: Application to global primary production . . . . .	114
8.4	Questions . . . . .	118
8.5	Answers . . . . .	119
8.6	References and further reading . . . . .	122
<b>9</b>	<b>Detecting Phytoplankton Community Structure from Ocean Colour</b>	<b>125</b>
9.1	Background . . . . .	125
9.2	Data and Methods . . . . .	130
9.3	Demonstration Section . . . . .	133

9.4 Training . . . . .	133
9.5 Questions . . . . .	135
9.6 Answers . . . . .	135
9.7 Summary . . . . .	137
9.8 Acknowledgements . . . . .	138
9.9 References and further reading . . . . .	138
<b>Theme: Fisheries and Aquaculture</b>	<b>141</b>
<b>10 Use of Night Satellite Imagery to Monitor the Squid Fishery in Peru</b>	<b>143</b>
10.1 Introduction . . . . .	143
10.2 Study Area . . . . .	144
10.3 Materials and Methods . . . . .	144
10.4 Demonstration . . . . .	146
10.5 Training and Questions . . . . .	150
10.6 Answers . . . . .	151
10.7 References . . . . .	152
<b>11 Spring Algal Bloom and Haddock Larvae Survival</b>	<b>155</b>
11.1 Background Information . . . . .	155
11.2 Materials and Methods . . . . .	156
11.3 Demonstration . . . . .	159
11.4 Training . . . . .	161
11.5 Questions . . . . .	165
11.6 Answers . . . . .	166
11.7 References . . . . .	167
<b>12 Applications to Detect Habitat Preferences of Skipjack Tuna</b>	<b>169</b>
12.1 Introduction . . . . .	169
12.2 Background . . . . .	170
12.3 Data and Methods . . . . .	170
12.4 Demonstration Section . . . . .	177
12.5 Questions . . . . .	182
12.6 Answers . . . . .	182
12.7 References . . . . .	183
12.8 Glossary of Technical Terms . . . . .	185
<b>13 Monitoring Oysters Using Remote Sensing Data and Services</b>	<b>187</b>
13.1 Background . . . . .	187
13.2 Materials and Methods . . . . .	190
13.3 Demonstration . . . . .	191
13.4 Training and Questions . . . . .	197
13.5 Answers . . . . .	200

13.6 References . . . . .	201
13.7 Supplemental Information . . . . .	202
<b>Theme: Marine Ecosystem Characterization</b>	<b>207</b>
<b>14 Biological Response Associated With a Coastal Upwelling Event</b>	<b>209</b>
14.1 Introduction and Background . . . . .	209
14.2 Materials and Methods . . . . .	210
14.3 Training and Questions . . . . .	214
14.4 Answers . . . . .	216
14.5 References . . . . .	219
<b>15 Comparison of <i>In Situ</i> and Remotely-Sensed Chl-<i>a</i> concentrations</b>	<b>221</b>
15.1 Background . . . . .	221
15.2 Demonstration . . . . .	225
15.3 Training . . . . .	232
15.4 Questions . . . . .	236
15.5 Answers . . . . .	236
15.6 References . . . . .	238

## Theme: Water Quality

---



## Case Study 1

# Remote-Sensing Case Study of the Chesapeake Bay Region during Drought (2002) and Flood (2003) Years

James Acker\*<sup>1</sup> and Zhong Liu<sup>2</sup>

---

## 1.1 Background Information

The location of this study is the Chesapeake Bay estuary on the eastern Mid-Atlantic coast of the United States. The Chesapeake Bay system is the largest estuary in the United States and one of the largest in the world. Chesapeake Bay is approximately 320 kilometers long, with its mouth located in Virginia near Norfolk and Hampton Roads, to the upper part of the Bay at Havre de Grace, Maryland. The headwaters of the Susquehanna River (one of the major rivers entering the bay) are located near Cooperstown, New York. The Chesapeake Bay watershed is approximately 166,000 square kilometers, and the Bay itself has over 18,000 km of shoreline. The average depth of the Chesapeake Bay is about 6.5 meters, though it can be deeper than 45 meters in some locations.

Fresh water from five major rivers enters the Bay - these rivers are the Susquehanna, Potomac, James, York, and Rappahannock. Although there are many other rivers and streams feeding into the bay, about 90% of the fresh water input to the bay comes from these five rivers. Due to the large amount of fresh water delivered by the Susquehanna River, the upper portion of the Bay has much lower salinity than the lower portion of the Bay, where tidal flow from the Atlantic is significant. It is estimated that a roughly equal volume of salt water enters the Bay from the Atlantic compared to the volume of fresh water entering the Bay from river systems.

Due to the size of the estuary and the volume of fresh water that enters it, the physical characteristics of Chesapeake Bay water and the biological dynamics of the bay are strongly connected the flow of water and the quality of the water entering it from land. A large percentage of the bay's watershed land is used for agriculture, particularly in Pennsylvania and the Eastern Shore of Maryland. This land usage

---

<sup>1</sup>Goddard Earth Sciences Data and Information Services Center, Wyle IS LLC, NASA GES DISC Code 610.2, Greenbelt, MD 20771, USA. \*Email address: [james.g.acker@nasa.gov](mailto:james.g.acker@nasa.gov)

<sup>2</sup>Goddard Earth Sciences Data and Information Services Center, George Mason University, USA

results in large amounts of nutrients derived from agricultural fertilizer and animal wastes entering the bay in runoff from fields. A further influence on the bay waters is the increasing population and urban development in major cities, which include Washington D.C., Baltimore (Maryland), Richmond (Virginia) and Scranton/Wilkes-Barre (Pennsylvania), and many other smaller cities and towns in the watershed. Developmental sprawl means that an increasing area of the watershed is impervious to water penetration, resulting in increased runoff and additional input of nutrients and pollutants, as well as input from the growing human population. Therefore, the general quality of bay waters and the ability to host marine flora and fauna, which is subject to increasing environmental stress, is directly connected to the hydrological system of the Chesapeake Bay watershed.

During the year 2002, much of the United States experienced severe to extreme drought conditions. These conditions were acute in two locations: most states west of the Dakotas, Nebraska, Kansas, Oklahoma, and Texas; and the eastern seaboard from southern Georgia to New Jersey. On the eastern seaboard, the central portion of North and South Carolina, Virginia, and Maryland were subject to particularly acute conditions; the situation worsened in Virginia and Maryland during summer and autumn 2002, with some communities in these states imposing severe water use restrictions, and reservoirs dropping to very low capacities. One reservoir serving Baltimore dropped to 16% capacity and was estimated to have only a 30-day supply of water remaining.

Rain in late autumn began to alleviate the drought conditions, and the rain pattern persisted and became much stronger in the spring of 2003. Rainfall in March and April was particularly heavy in Virginia and Maryland. Over the course of the entire year of 2003, the Baltimore region set an annual precipitation record – a very distinct contrast from the dry conditions that had characterized much of 2002.

Due to these significantly different hydrological conditions, it was expected that the waters of the Chesapeake Bay would exhibit distinctly different bio-optical characteristics, related to the volumes of fresh water and associated nutrient transport during low- and high-flow conditions. The availability of ocean-colour radiometry data in the online data analysis system created by the NASA Goddard Earth Sciences Data and Information Services Center (GES DISC) provided the opportunity to investigate the effects of the "drought and flood" precipitation pattern on the waters of the Chesapeake Bay, which is the subject of this case study (Acker et al. 2005).

Three remotely-sensed variables, chlorophyll-*a* concentration (chl-*a*), the diffuse attenuation coefficient at 490 nm (K<sub>490</sub>), and remote-sensing reflectance at 555 nm (R<sub>rs555</sub>) will be used to examine the bio-optical characteristics of the Chesapeake Bay waters. Chl-*a* reflects the concentration of phytoplankton, the floating photosynthetic plants that form the base of the marine food chain. Phytoplankton are primary producers, creating carbon biomass through the process of photosynthesis. The photosynthetic pigment chlorophyll contained in their cells enables this process, and thus chl-*a* is an indicator of the prevalence of phytoplankton. Since, in

In addition to sunlight, phytoplankton require dissolved nutrients (primarily nitrate and phosphate) in seawater to grow, phytoplankton populations will grow more rapidly and abundantly in the presence of elevated nutrient concentrations. When this happens, an overabundance of phytoplankton can cause increased deposition of dead phytoplankton organic material on the estuarine bottom or seafloor. The digestion ("respiration") of this organic matter by bacteria uses dissolved oxygen in the water, which is important for most organisms living in the water. Increased bacterial respiration of organic matter can reduce dissolved oxygen so much that the water cannot support aquatic life.

Remote sensing estimates the concentration of chl-*a* by detecting the absorption of light by the chlorophyll in phytoplankton cells. It should also be noted that in turbid waters, remotely-sensed chl-*a* can be overestimated due to the absorption or reflection of light by other substances. This is an important point in many areas, but will be less important here.

K490 is simply a measure of how much the intensity of light entering the oceanic water column is attenuated (reduced) by interaction with substances either dissolved or suspended in the water, either through light absorption, light scattering, or light reflection. High values of K490 thus indicate more turbidity, and low values of K490 indicate less turbidity. Turbidity can be caused by increased concentrations of phytoplankton, suspended sediments, or dissolved substances, and usually is a combination of all three of these factors.

$R_{rs555}$  indicates light reflection, as there is very little absorption of light at this wavelength in marine waters. Thus,  $R_{rs555}$  is sensitive to the presence of suspended sediments, which reflect and scatter light without absorbing much light. Light at a wavelength of 555 nm will also be reflected off the seafloor when the water depth is sufficiently shallow for the light to penetrate to the bottom and reflect back toward the surface.

## 1.2 Materials and Methods

The primary data set for this investigation is ocean-colour radiometry (OCR) data acquired by the Sea-viewing Wide Field-of-view Sensor (SeaWiFS). SeaWiFS has been in nearly continuous operation since September 1997 and provides an exemplary calibrated remotely-sensed data set of ocean-colour variables, including chlorophyll-*a* concentration (chl-*a*) and the diffuse attenuation coefficient at 490 nm (K490).

The algorithm for the chl-*a* retrieval, OC4V4, is an empirical algorithm based on ratios of reflectances for the SeaWiFS bands at 443, 490, 510, and 555 nm (O'Reilly et al., 2000). The K490 algorithm uses data from the SeaWiFS band at 490 nm (Mueller and Trees, 1997).

SeaWiFS ocean-colour data will be analyzed utilizing the [GES DISC Interactive Online Visualization ANd aNalysis Infrastructure](#) (Giovanni) (Acker and Leptoukh,

2007). Giovanni will be used to generate maps of data products over the Chesapeake Bay during the spring months of 2002 and 2003, to contrast the low-flow conditions of 2002 with the high-flow conditions of 2003. The three data products that will be examined are chl-*a*, K490 and R<sub>rs</sub>555. To use Giovanni, a region of interest is selected either by clicking-and-dragging the display cursor on an interactive map, or by providing latitude-longitude corner points defining a specific region of interest. For this study, the corner points are provided to ensure uniformity of output visualizations. The time period of interest is specified for the spring months of 2002 and 2003.

Additional images are provided for context of the Chesapeake Bay region. URLs for these images are provided below. The MODIS images show the Chesapeake Bay, highlighting the major rivers and urban areas, and also demonstrating differences in land use patterns. The watershed image shows the regional extent of the Chesapeake Bay watershed. The impervious surface maps show that urbanization increases impervious surface area around the Chesapeake Bay (these are numbered Figures 1.6 to 1.8.)

Chesapeake Bay watershed:

[http://veimages.gsfc.nasa.gov/20832/image04162006\\_1km.jpg](http://veimages.gsfc.nasa.gov/20832/image04162006_1km.jpg)

Impervious surface, State of Maryland:

[http://www.dnr.state.md.us/watersheds/surf/indic/md/md\\_pctimp\\_indmap.html](http://www.dnr.state.md.us/watersheds/surf/indic/md/md_pctimp_indmap.html)

Impervious surface, urban areas in the Chesapeake Bay watershed:

[http://www.whrc.org/midatlantic/mapping\\_land\\_cover/products/impervious\\_surfaces.htm](http://www.whrc.org/midatlantic/mapping_land_cover/products/impervious_surfaces.htm)

### 1.3 Demonstration Section

The use of Giovanni provides the capability for users to generate their own images, rather than relying on previously-created images. Thus, the instructions in this demonstration section and the associated images will show how to create the images, and subsequently how to interpret them. There are no large image files that have to be opened; small images will be shown here to demonstrate what the end result should look like.

**Step 1:** Go to the Giovanni Ocean Color Radiometry Interface:

[http://gdata1.sci.gsfc.nasa.gov/daac-bin/G3/gui.cgi?instance\\_id=ocean\\_month](http://gdata1.sci.gsfc.nasa.gov/daac-bin/G3/gui.cgi?instance_id=ocean_month)

**Step 2:** Enter the geographical coordinates below the interactive map. West: -77.5 North: 40.0 South: 36.5 East: -75.0. Click the "Update Map" button. This will show the highlighted region, with the Chesapeake Bay inside the box defined by the coordinates.

**Step 3:** In the SeaWiFS.R2009 data set (the first data set listed), select the following parameters by clicking in the boxes on the left next to the parameter name:

Chlorophyll-*a* concentration, Diffuse attenuation coefficient at 490 nm, Remote sensing reflectance at 555 nm.

**Step 4:** In the calendar selection menu below the lists of parameters, select the following time period: Begin Date: Year = 2002, Month = April, End Date: Year = 2002, Month = Jun (June).

**Step 5:** Click the "Generate Visualization" button. The default option, "Lat-Lon Map, Time-Averaged", is the visualization option that will be utilized here. The Giovanni system will now generate the visualizations for the three selected parameters. When the maps have been generated, click on the "Download Data" tab at the top. Go to the "Output Files" section, and click on each filename listed. This will display the visualization. Download the images into a folder according to the method for image download appropriate to the Web browser that is being used. It may be necessary to add the suffix ".gif" to the filename in order to see the images in the folder. When the image has been downloaded, click the "Back" button on the browser and repeat the process until all the images have been downloaded.

**Step 6:** Click the "Visualization Results" tab. Now use the calendar menu to change the dates to the following. All that is changed is the year, from 2002 to 2003. Begin Date: Year = 2003, Month = April, End Date: Year = 2003, Month = Jun (June). Go to the bottom of the page and click the "Submit Refinements" button. The Giovanni system will now create the visualizations for the same data parameters for this second time period. **The bio-optical and optical parameter visualizations have now been generated.**

Steps 7-11 below will generate the TRMM precipitation maps for two consecutive nine-month periods in the years 2002 and 2003.

**Step 7:** Go to the Daily TRMM and Other Rainfall Estimate interface:

[http://gdata1.sci.gsfc.nasa.gov/daac-bin/G3/gui.cgi?instance\\_id=TRMM\\_3B42\\_Daily](http://gdata1.sci.gsfc.nasa.gov/daac-bin/G3/gui.cgi?instance_id=TRMM_3B42_Daily)

**Step 8:** Enter the following geographic coordinates: West: -81.0, North: 43.0, South: 36.0, East: -73.0. Click the "Update Map" button. This will show the highlighted region.

**Step 9:** The only parameter available, "precipitation", should already be selected. Click the box if it is not selected.

**Step 10:** Enter the following temporal information: Begin Date: Year = 2002, Month = Jan (January), Day = 01, End Date: Year = 2002, Month = Sep (September), Day = 30. Then click the "Generate Visualization" button. The default option, "Lat-Lon Map, Time-Averaged", is the visualization option that will be utilized here. Next to this option, click the "Edit Preferences" button. Scroll down to the "Color Bar" section, and change the "Mode" choice from Pre-Defined to Custom. In the "Min Value" box,

enter 0.0. In the "Max Value" box, enter 6.4. Now go to the bottom of the page and click the "Generate Visualization" button. The Giovanni system will now generate the visualization for the precipitation parameter. When the visualization is completed, save the image using the same procedure as in Step 5.

**Step 11:** Change the temporal information to the following: Begin Date: Year = 2002, Month = Oct (October), Day = 01, End Date: Year = 2003, Month = Jun (June), Day = 30. Go to the bottom of the page and click the "Submit Refinements" button. The Giovanni system will now create the map visualization of the precipitation parameter for this second time period. **The precipitation parameter visualizations have now been generated.**

### 1.3.1 Image Interpretation

Now that the visualizations have been generated, it is time to examine them for basic interpretation of these results. Each of these images depicts the data values utilizing a false-colour palette. The colour palette used in all cases here is the common "rainbow" palette, in which higher values of the data parameter are expressed in warmer colours (i.e. orange and red), low values are cooler colours (blue and purple), and intermediate values are greens and yellows. For chlorophyll-*a* data, the colour scale is logarithmic, so that the highest values are about 400-800 times greater than the lowest values. The scale for all of the other parameters is linear. Using the colour palette, interpretation of the images is straightforward. Each image shows a map of the values of the parameter averaged over the selected time period. These maps allow easy recognition of where the values were higher and lower in the region during the selected time period.

For the chl-*a* images, the highest values in the orange and red range show areas where phytoplankton chlorophyll concentration was elevated. This usually indicates where phytoplankton populations were thriving. Remotely-sensed chl-*a* can sometimes exhibit erroneously high values if there is a significant concentration of coloured dissolved organic matter (CDOM) also present in the water. Remember that the values of chl-*a*, and also K490 and  $R_{rs,555}$ , were averaged over a three-month period. The concentrations on any given day during the month could have been much higher or lower than the average calculated over three months.

For the K490 images, higher values indicate where the water was more turbid, i.e., where incoming light was attenuated more strongly due to the presence of interfering substances or particles in the water. For the  $R_{rs,555}$  images, higher values indicate where incoming light at this wavelength was reflected more strongly back toward the satellite sensor.

The TRMM precipitation data maps are also easy to interpret using the 'rainbow' palette. The warmer colours (higher values) indicate higher amounts of precipitation averaged over the nine-month time period. The average amount of precipitation

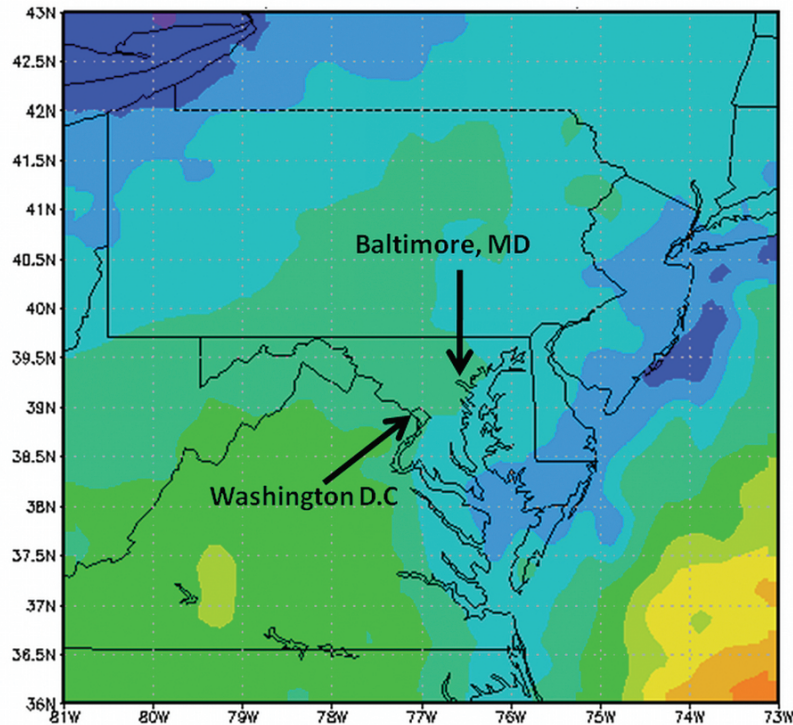


**Figure 1.1** Location map of the Chesapeake Bay with TRMM precipitation data, showing location of Washington DC, and Baltimore, MD.

indicates approximately the amount of rain that fell on a per-day basis in a given location over the entire time period. Of course, it is unlikely that there was rain on most of those days, so the average precipitation per day gives a general indication of the amount of rainfall the region received during the specified period of time. If the average value of mm/day is multiplied by the number of days in the period (about 270 for a nine-month period), this would give the approximate total amount of rainfall for that period. So an average precipitation amount of 3 mm/day means that about 800mm (or 30 inches) of rain fell during that period.

## 1.4 Training and Questions

Now we will examine each of the image pairs in turn to evaluate the environmental forcing in the Chesapeake Bay watershed and the effects that this forcing had on the bio-optical conditions in the Chesapeake Bay. The first set of images to examine is the pair of TRMM precipitation maps. Examine the labelled precipitation map (Figure 1.1 above) that shows the locations of Washington D.C. and Baltimore (note: this map used a different colour palette scale). Answer questions 1 and 2 below using Figure 1.2 depicting the average precipitation during the period 1 January to

30 September 2002.

**Q 1:** What was the average daily precipitation for the region including Washington D.C. and Baltimore?

**Q 2:** What was the approximate total precipitation for this region?

For the map depicting the average precipitation during the period of 1 October 2002 to 30 June 2003 (Figure 1.2b):

**Q 3:** What was the average daily precipitation for the region including Washington D.C. and Baltimore?

**Q 4:** What was the approximate total precipitation for this region? Now consider the potential implications of the different rainfall amounts for the region.

**Q 5:** What would be the effects of the markedly different rainfall amounts on the volume of water flowing in the streams and rivers in the Chesapeake Bay watershed?

**Q 6:** What differences would be expected on the amount of fresh water entering the Chesapeake Bay during the two periods that were depicted in the precipitation maps?

The next pair of images to examine is the pair of chl-*a* maps of the Chesapeake Bay. Examine the two maps side-by-side. Figure 1.3a depicts chl-*a* during April – June 2002, and Figure 1.3b depicts chl-*a* during April – June 2003.

**Q 7:** During which period are the chl-*a* values in the Bay significantly higher?

**Q 8:** Does this period of time correspond to the period when precipitation in the Chesapeake Bay watershed region was low (January – September 2002) or high (October 2002 – June 2003)?

**Q 9:** Given that higher chl-*a* values likely indicate higher values of phytoplankton productivity, what relationship may exist between precipitation, stream-flow, and phytoplankton productivity in the Chesapeake Bay? What could be the cause(s) of that relationship?

The next pair of images to examine is the pair of K490 maps of the Chesapeake Bay. Also examine the two maps side-by-side. Figure 1.4a depicts K490 during April – June 2002, and Figure 1.4b depicts K490 during April – June 2003.

**Q 10:** During which period are the K490 values in the Bay significantly higher?

**Q 11:** Does this period of time correspond to the period when precipitation in the Chesapeake Bay watershed region was low (January – September 2002) or high (October 2002 – June 2003)?

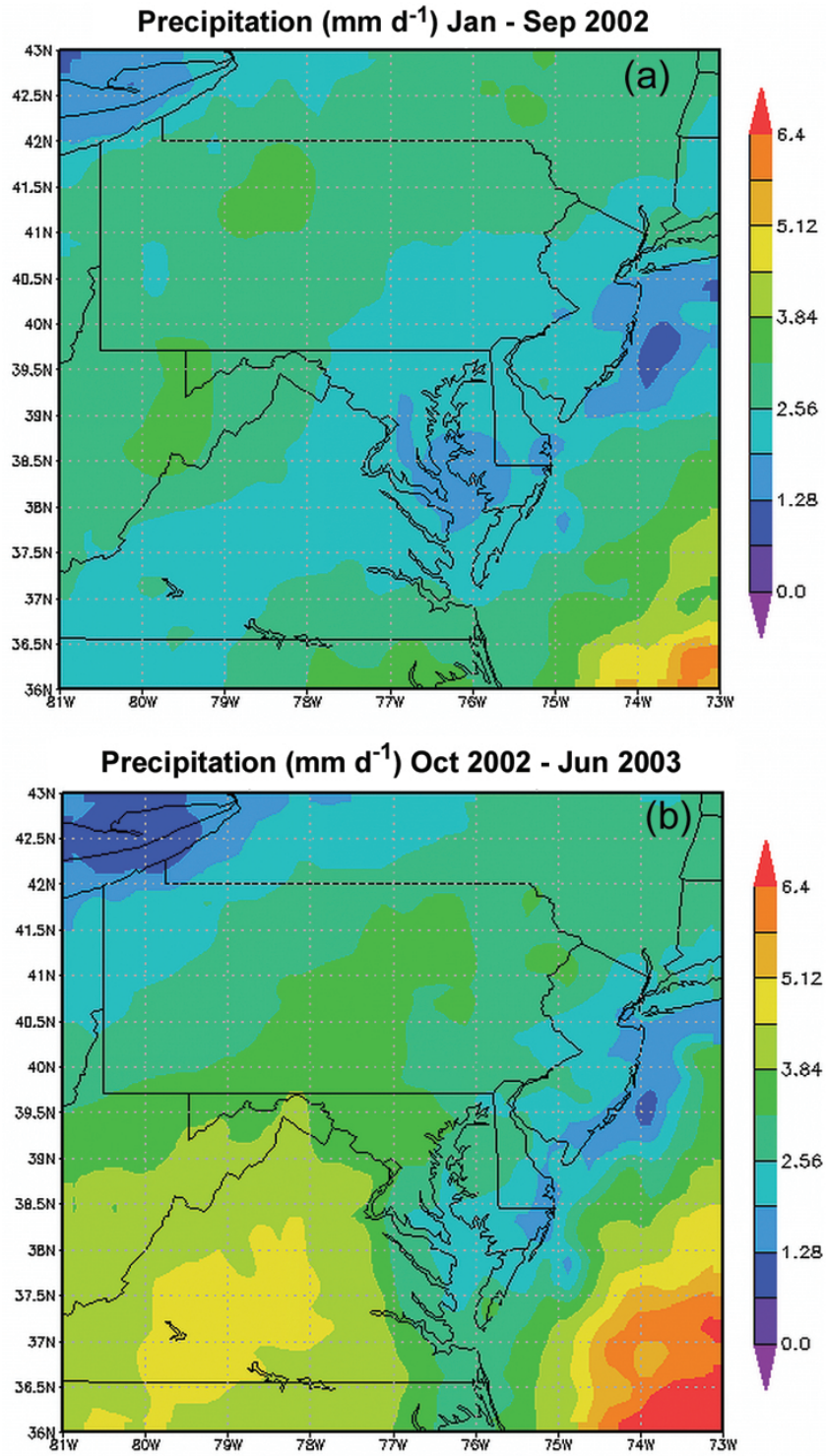


**Figure 1.2** (a) Average daily precipitation over the Chesapeake Bay watershed region, January - September 2002, (b) Average daily precipitation over the Chesapeake Bay watershed region, October 2002 - June 2003.

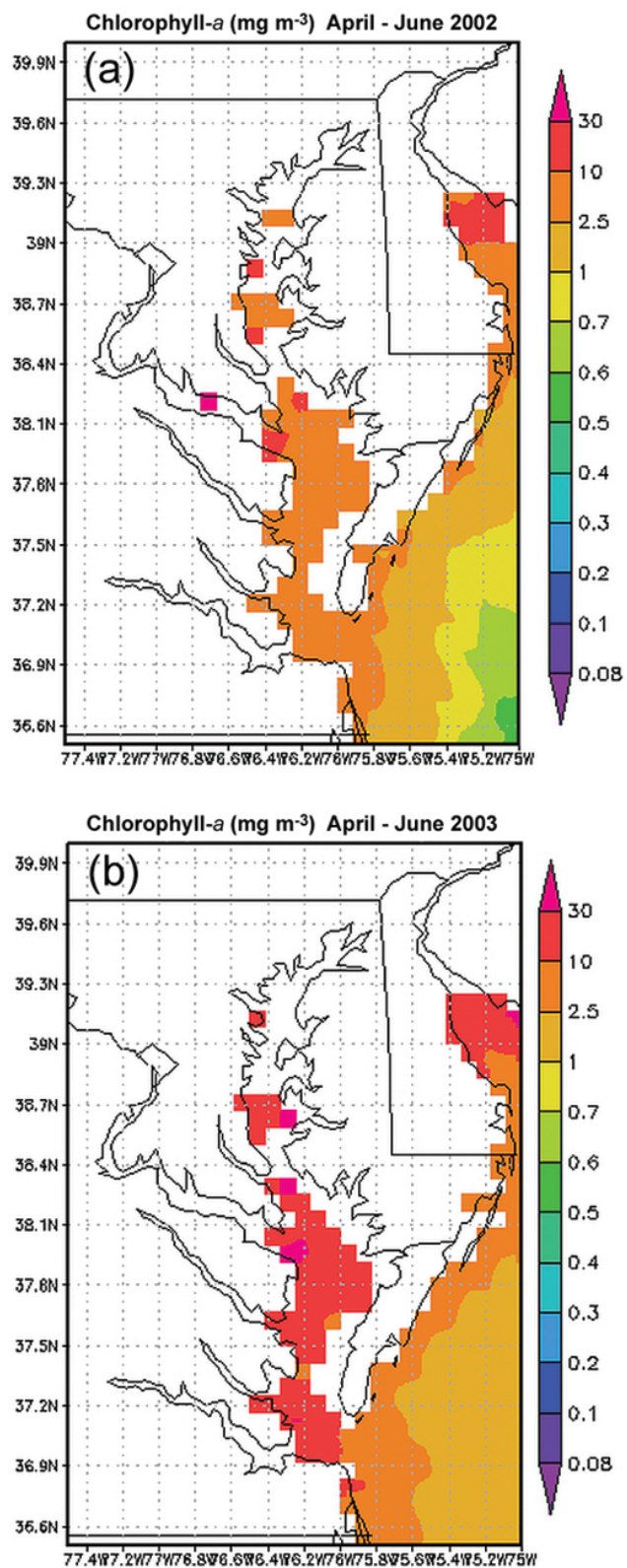


**Figure 1.3** (a) Average chl-*a* in the Chesapeake Bay, April - June 2002 (b) Average chl-*a* in the Chesapeake Bay, April - June 2003.

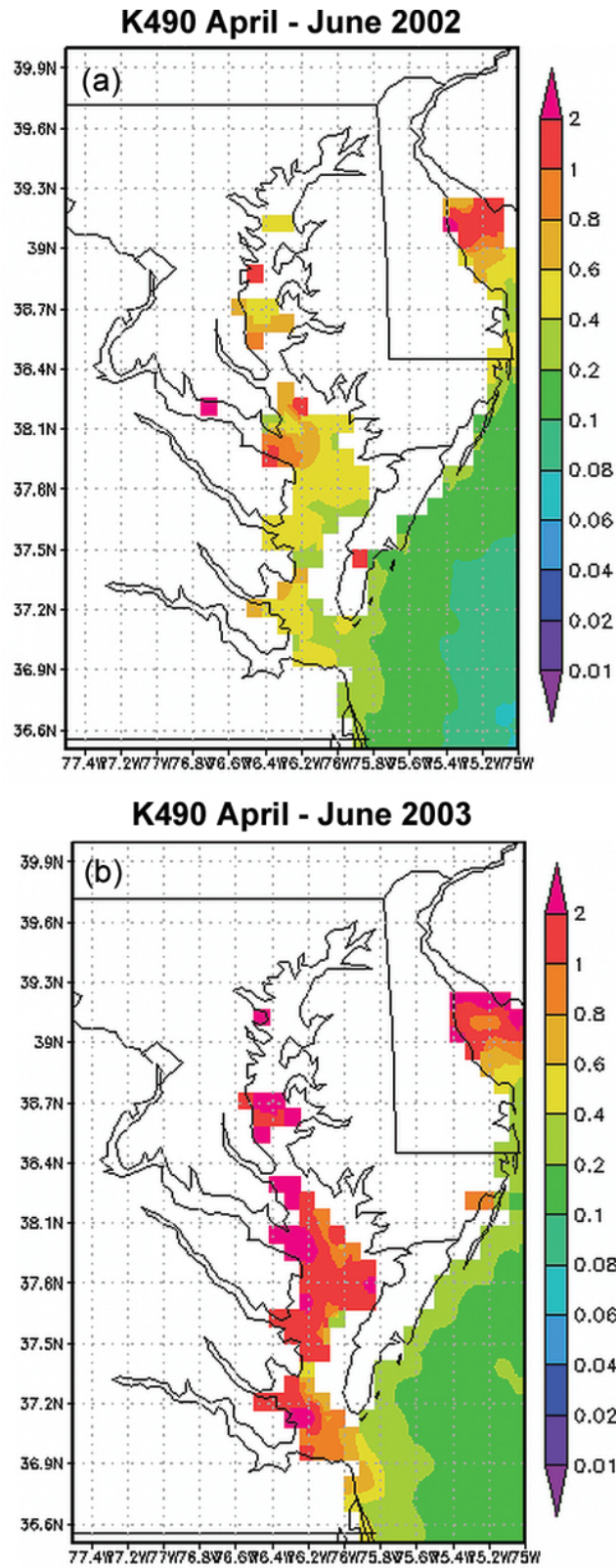


**Figure 1.4** (a) Average K490 in the Chesapeake Bay, April - June 2002 (b) Average K490 in the Chesapeake Bay, April - June 2003.

**Q 12:** What are the likeliest causes of the elevated values of K490 in the Chesapeake Bay, and what is the potential relationship to stream-flow and the transport of fresh water into the Bay?

The next pair of images to examine is the pair of  $R_{rs555}$  maps of the Chesapeake Bay. You will again examine the two maps side-by-side. Figure 1.5a depicts  $R_{rs555}$  during April – June 2002, and Figure 1.5b depicts  $R_{rs555}$  during April – June 2003.

**Q 13:** During which period are the  $R_{rs555}$  values in the Bay significantly higher?

**Q 14:** Does this period of time correspond to the period when precipitation in the Chesapeake Bay watershed region was low (January – September 2002) or high (October 2002 – June 2003)?

**Q 15:** The answer to the previous question may be surprising. Given what you have determined about the bio-optical conditions in the Chesapeake Bay from the previous two pairs of maps (for chl-*a* and K490), what is the likeliest explanation for the relationship between  $R_{rs555}$  and stream-flow during periods of high and low precipitation?

The final images that will be examined are the impervious surface maps of the Chesapeake Bay region and urban areas within this region (Figures 1.6 to 1.8) and supplemental material entitled "Breath of Life" (see [http://www.eco-check.org/pdfs/do\\_letter.pdf](http://www.eco-check.org/pdfs/do_letter.pdf)).

**Q 16:** What do you think would be the effects of increasing areas of impervious surface in the watershed of the Chesapeake Bay on the water conditions in the Bay? (Consider the effects on water clarity, water chemistry, bottom visibility, nutrient concentrations, and phytoplankton productivity.)

## 1.5 Answers

**A 1:** The average daily precipitation during this period was 1.9 – 2.6 mm day<sup>-1</sup>.

**A 2:** The approximate total precipitation during this period was 500 – 700 mm.

**A 3:** The average daily precipitation during this period was 3.2 – 3.8 mm day<sup>-1</sup>.

**A 4:** The approximate total precipitation during this period was 860 – 1030 mm.

**A 5:** The markedly different rainfall amounts would result in significant differences in the volume of water flowing in the streams and rivers. During the low precipitation period, stream-flow would be significantly reduced. During the high precipitation period, stream-flow would be considerably greater than during the low precipitation period.

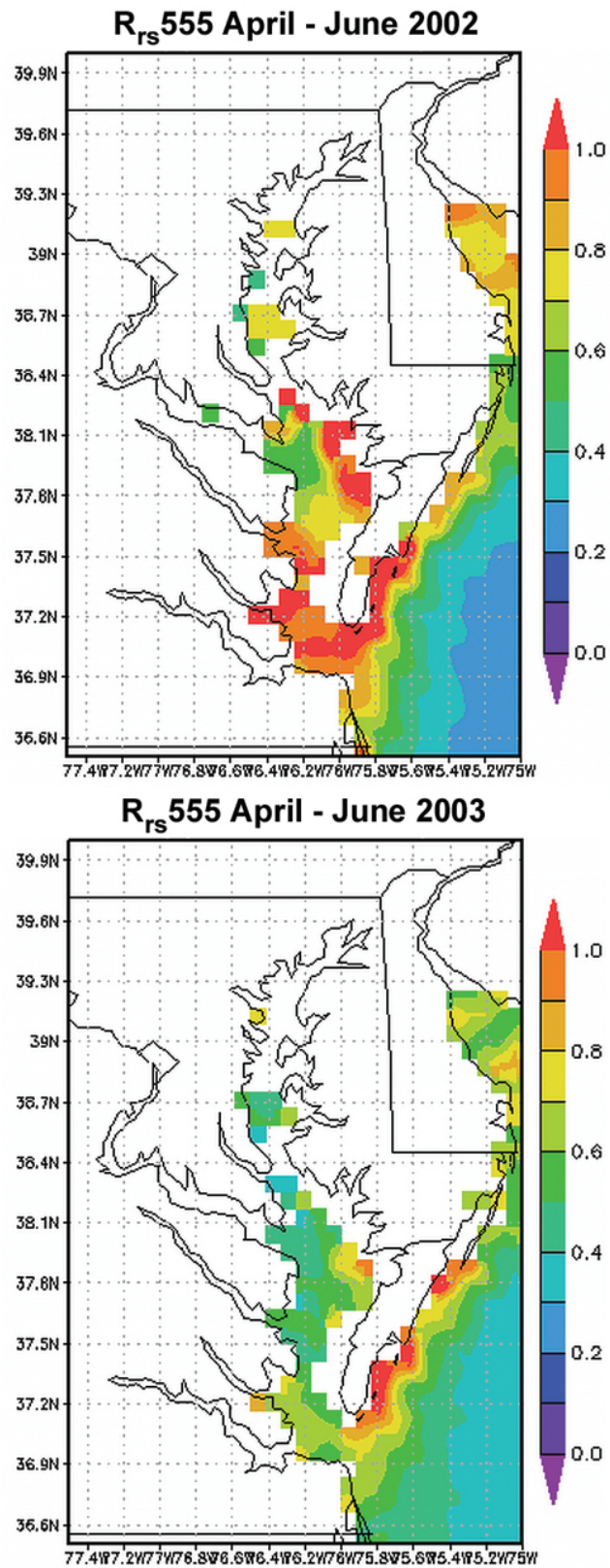


**Figure 1.5** (a) Average  $R_{rs555}$  in the Chesapeake Bay, April - June 2002 (b) Average  $R_{rs555}$  in the Chesapeake Bay, April - June 2003.

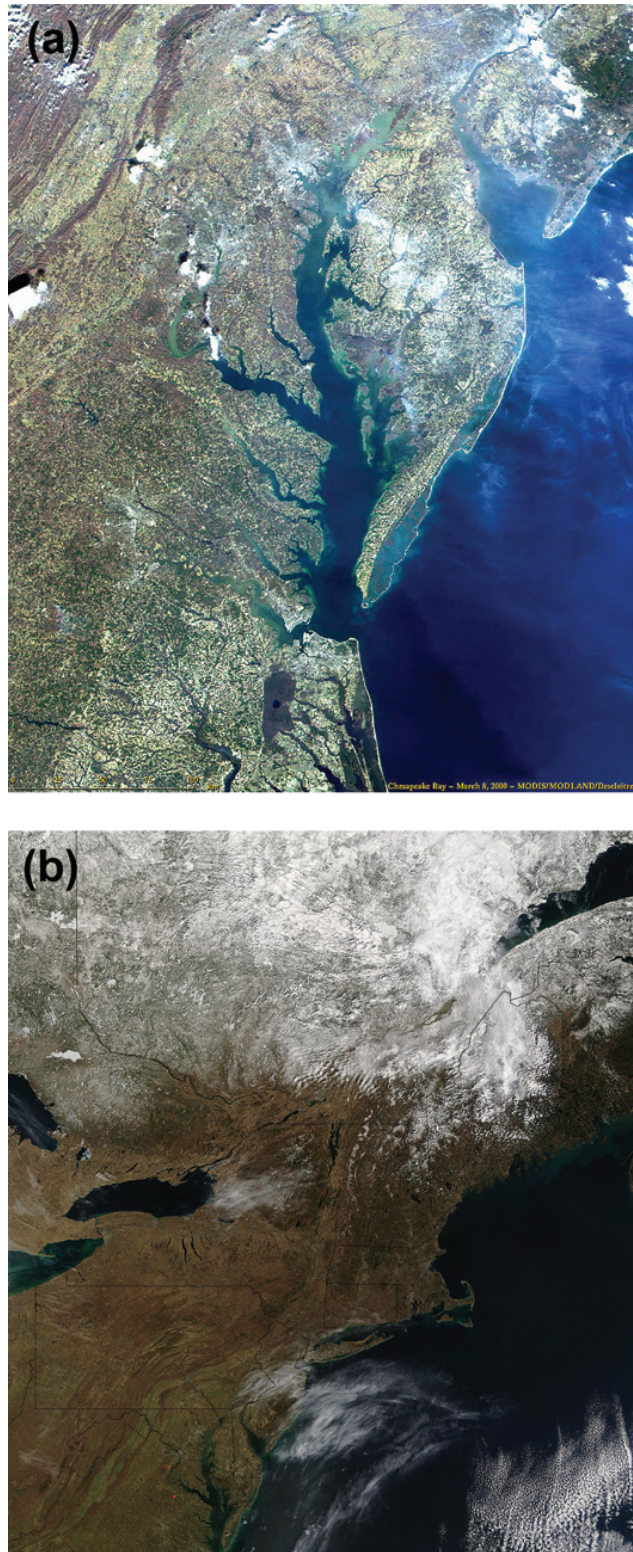


**Figure 1.6** (a) MODIS image of the Chesapeake Bay, acquired 20 April 2000 (b) MODIS image of the Chesapeake Bay watershed, acquired 16 April 2006.

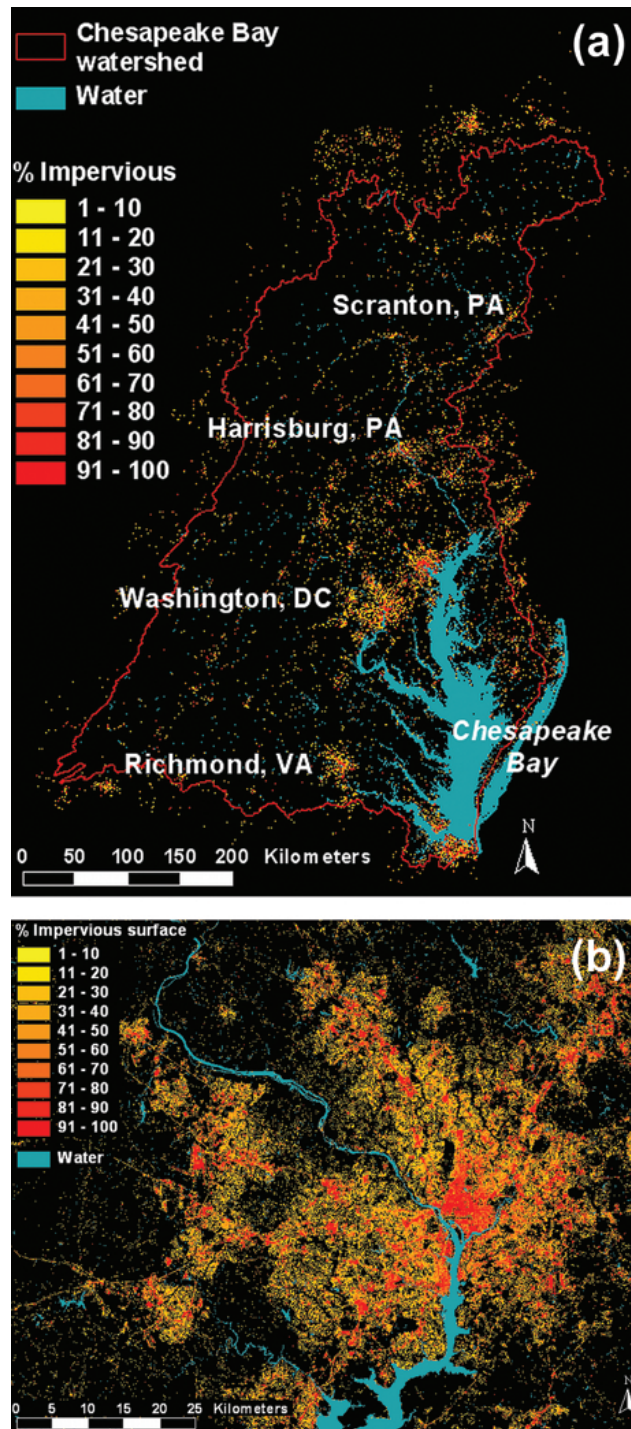


**Figure 1.7** (a) Percent impervious surface area in the Chesapeake Bay watershed (b) Percent impervious surface area in the Washington, DC metropolitan area.

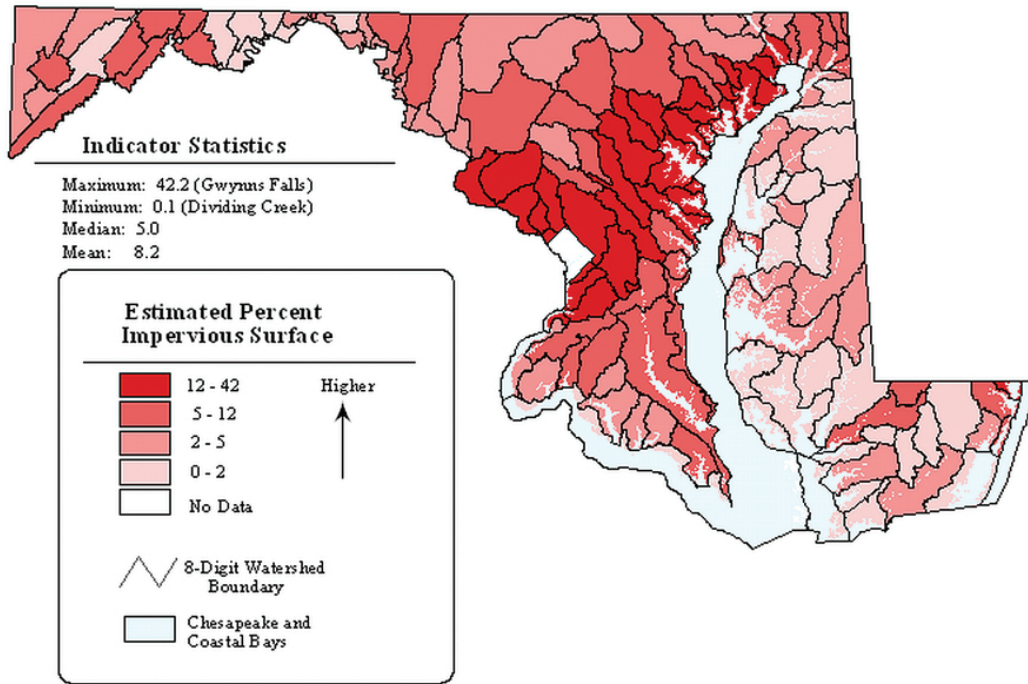


**Figure 1.8** Estimated percent impervious surface area in the state of Maryland.

**A 6:** Due to the increased stream-flow during the high precipitation period, a significantly larger volume of fresh water would enter the Chesapeake Bay, compared to the low precipitation period.

**A 7:** Chl-*a* values in the Chesapeake Bay are higher during the April 2003 - June 2003 period.

**A 8:** This period of time corresponds to the period when precipitation in the Chesapeake Bay watershed was high.

**A 9:** The higher values of chl-*a* corresponding to the period of high precipitation indicate that elevated stream-flow and increased transport of fresh water into the Chesapeake Bay may enhance phytoplankton productivity. This could also be due to increased turbidity (some of which could be more phytoplankton cells in the water). The possible causes are an increased delivery of nutrients in the elevated stream-flow entering the Bay, and also an increased concentration of suspended sediments carried by higher stream-flow volumes.

**A 10:** The K490 values in the Bay are significantly higher during the April - June 2003 period.

**A 11:** This period of time corresponds to the period when precipitation in the Chesapeake Bay watershed was high, October 2002 - June 2003.

**A 12:** The likeliest causes of the elevated values of K490 are directly related to the answer to Question 9. Increased concentrations of phytoplankton and higher concentrations of suspended sediments (and also coloured dissolved organic matter) will all contribute to enhanced light attenuation in the water column. This is the likeliest reason that higher stream-flow and transport of freshwater into the Bay are correlated with higher K490 values.

**A 13:** The  $R_{rs555}$  values in the Bay are significantly higher during the period April – June 2002.

**A 14:** This period of time corresponds to the period when precipitation in the Chesapeake Bay watershed was low, January – September 2002.

**A 15:** The surprising result should be related to the difference in the values of chl-*a* and K490 during the high precipitation (high stream-flow) and low precipitation (low stream-flow) periods. Light attenuation is caused by light absorption, light scattering, and light reflection. When the chl-*a* and K490 values are elevated, there are more substances and particles in the water column; thus, the scattering, absorption and reflection of light increases. Simply put, the water is less clear. During the low precipitation/low stream-flow period, the water in the Bay was clearer – and in the shallow depths of the Bay, this allowed more reflection from the bottom of the Bay, which is the likeliest explanation for the increased values of  $R_{rs555}$  during the low precipitation period.

**A 16:** Increased areas of impervious surface will increase both the volume of water entering the Bay at one time during high precipitation events, and will also deliver more undiluted water running off other types of surfaces, such as the lawns of homes or cleared fields. The increased areas of impervious surface can also contribute to erosion when flow volumes are elevated and cause flooding. All of these effects contribute to greater flow of nutrients into the Bay, and can enhance the concentrations of suspended sediments during certain times. These effects will enhance phytoplankton growth and cause decreased water clarity, which affects the survivability of benthic vegetation. Further, the increased growth of phytoplankton leads to increased organic matter deposition on the bottom, causing more bacterial respiration and the spread of areas of low oxygen or no oxygen (hypoxia/anoxia) in the bottom waters of the Bay. In the web document at [http://www.eco-check.org/pdfs/do\\_letter.pdf](http://www.eco-check.org/pdfs/do_letter.pdf) there is a chart (Figure 1.6) of dissolved oxygen levels in the Bay from 1985 – 2006. Note the difference between 2002 and 2003 in this chart. Due to the extremely low stream-flows in 2002, that year was the best overall, in terms of hypoxic and anoxic areal extent, for the entire 22-year period charted.

## 1.6 References

- Acker JG and Leptoukh G (2007) Online analysis enhances use of NASA earth science data. *Eos, Trans Am Geophys Union* 88(2): 14 and 17
- Acker J G, Harding L, Leptoukh G, Zhu T, and Shen S (2005) Remotely-sensed chl a at the Chesapeake Bay mouth is correlated with annual freshwater flow to Chesapeake Bay. *Geophys Res Lett* 32: L05601. doi:10.1029/2004GL021852 01
- O'Reilly JE, Maritorena S, Siegel D, O'Brien MC, Toole, D, Mitchell BG, Kahru, M, Chavez FP, Strutton P, Cota G, Hooker SB, McClain CR, Carder KL, Muller-Karger F, Harding L, Magnuson A, Phinney D, Moore GF, Aiken J, Arrigo KR, Letelier R, and Culver M (2000) Ocean color chlorophyll a algorithms for SeaWiFS, OC2 and OC4: Version 4. In: Hooker SB and Firestone ER (eds) *SeaWiFS Postlaunch Calibration and Validation Analyses (Part 3)*, NASA Technical Memorandum 2000-206892, Volume 10, NASA GSFC, 9-23
- Mueller JL and Trees, CC (1997) Revised SeaWiFS prelaunch algorithm for the diffuse attenuation coefficient K(490). In: Yeh, E-n, Barnes RA, Darzi M, Kumar L, Early EA, Johnson BC, Mueller JL and Trees, CC (eds) *Case Studies for SeaWiFS Calibration and Validation*, E-n. Yeh, R. A. Barnes, M. Darzi, L. Part 4, NASA Tech. Memo. 104566, NASA Goddard Space Flight Center, Greenbelt, Md., Volume 41

## Case Study 2

# Red Tide Detection in the Eastern Gulf of Mexico Using MODIS Imagery

Chuanmin Hu<sup>\*1</sup>, Jennifer Cannizzaro<sup>1</sup>, Kendall L. Carder<sup>1</sup>, Zhongping Lee<sup>2</sup>, Frank E. Muller-Karger<sup>1</sup> and Inia Soto<sup>1</sup>

---

## 2.1 Background

Many of the red tides (i.e., harmful algal blooms or HABs) in the eastern Gulf of Mexico (GOM) (24°–31°N, 90°–80°W) are caused by the toxic dinoflagellate, *Karenia brevis* (previously known as *Gymnodinium breve* or *G. breve*). Brevetoxins produced during *K. brevis* blooms can kill fish, mammals, and other marine organisms and cause respiratory irritation in humans (Hemmert, 1975; Asai et al., 1982; Landsberg and Steidinger, 1998; Kirkpatrick et al., 2004; Flewelling et al., 2005). *K. brevis* blooms can also adversely impact local tourism and commercial shellfish industries, leading to economic losses that have exceeded millions of US dollars during a single bloom event (Habas and Gilbert, 1974; Larkin and Adams, 2007).

Although *K. brevis* blooms can change the water to many different colours (e.g., brown, red, or even black) depending on the bloom's cell concentration and the concentration of other important optical constituents (Dierssen et al., 2006), they are commonly referred to as red tides. In the eastern GOM, red tides occur every year, mainly from late summer to early spring, yet their occurrence frequency, intensity, spatial extent, and duration all vary from year to year. Despite many years of community efforts, the mechanisms of initiation, maintenance and demise of red tides are still poorly understood and require further investigation. Data collected between the 1950's and the 1980's suggest that red tides are initiated offshore in nutrient-poor waters (Tester and Steidinger, 1997), and that they move toward shore by winds and currents, where they concentrate near fronts and utilize new nutrients from coastal runoff (Walsh et al., 2006). Several hypotheses that attempt to explain new nutrient supplies for these HABs have been proposed, including nitrogen fixation stimulated by atmospheric deposition of iron-rich Saharan dust particles

---

<sup>1</sup>College of Marine Science, University of South Florida, 140 7th Ave., S., St. Petersburg, FL 33701, USA. \*Email address: hu@marine.usf.edu

<sup>2</sup>Geosystems Research Institute, Mississippi State University, Stennis Space Center, MS 39529, USA

(Lenes et al., 2001; Walsh and Steidinger, 2001; Walsh et al., 2006), submarine groundwater discharge (Hu et al., 2006), and dead fish (Walsh et al., 2009). These hypotheses remain to be tested, and these possible sources need to be evaluated relative to sources such as upwelling of deeper GOM waters, riverine inputs, and benthic nutrient regeneration.

Timely information of *K. brevis* blooms is essential for all aspects of red tide studies, including testing hypotheses, assessing and managing the coastal environment, and forecasting and mitigation of red tides. In the past few decades, several long-term monitoring programs have invested significant resources in collecting red tide information. These include the Monitoring and Event Response for Harmful Algal Blooms (MERHAB) program supported by the U.S. NOAA (National Oceanic and Atmospheric Administration) and the Florida Fish and Wildlife Research Institute, several other programs supported by the state of Florida, local environmental groups, and volunteers. Most of these efforts rely on water sample analysis from field surveys because this is currently the only accurate means to differentiate *K. brevis* from other phytoplankton species. However, field surveys are often limited in spatial coverage and temporal frequency, especially during severe weather events. This lack of synoptic and frequent field observations makes it difficult to 1) provide near real-time information for rapid response, and 2) understand the long-term red tide occurrence statistics. For example, there has been substantial discussion and debate within the scientific community as to whether there is any historical trend in red tide occurrence along the west-central Florida coast. While Brand and Compton (2007) found that the frequency and duration of red tides appear to have increased in recent years, there was also argument (Christman and Young, 2006; Alcock, 2007) that this observation may simply be due to the unevenly distributed sampling scheme, the so-called observer effect (i.e. increased sampling during recent years because of increased public and scientific awareness - [http://research.myfwc.com/features/view\\_article.asp?id=27095](http://research.myfwc.com/features/view_article.asp?id=27095)).

In addition to the intensive field sampling efforts, satellite remote sensing can offer synoptic and more frequent measurements, with imagery available in near real-time (Babin et al., 2008). Therefore, detection of red tides via remote sensing is highly desirable, and thus has been an active research topic. Satellite imagery already has been used for operational monitoring of HABs in the GOM region. Some of the disadvantages are that satellite remote sensing using visible radiance is limited by cloud cover, spatial resolution, lack of information with depth below the surface, and algorithm uncertainty. While the first three are inherent with a given satellite-based instrument and cannot be fully "corrected", there has been continuous progress in algorithm development to improve the accuracy in red tide detection. Here, using several examples, we demonstrate how to use Moderate Resolution Imaging Spectroradiometer (MODIS) satellite imagery to differentiate the various waters, including *K. brevis* red tides in the eastern GOM. We will begin by reviewing briefly the underlying principles of red tide detection from space, and

follow with descriptions of the data and methods. We show several examples to illustrate the potential of this technology.

### 2.1.1 Principles

The use of ocean-colour satellites for rapid detection of red tides in the eastern GOM has been described previously (e.g., Stumpf et al., 2003a; Tomlinson et al., 2004; 2008; Hu et al., 2005; Cannizzaro et al., 2008; Amin et al., 2009). *K. brevis* cells contain chlorophyll-*a* and accessory pigments. These pigments have reflectance spectra that allow them to be differentiated from other water constituents, such as suspended non-living particles. The chlorophyll-*a* content of *K. brevis* cells ranges from ~8.5 pg/cell for natural populations to ~25 pg/cell for cultured populations (Evens et al., 2001). Assuming 10 pg/cell, a concentration of  $2 \times 10^4$  cells  $l^{-1}$  implies  $0.2 \text{ mg m}^{-3}$  of chlorophyll-*a*, close to the clear-water background chlorophyll-*a* concentration (Chl-*a*) in the eastern GOM. Satellite ocean-colour instruments typically have a measurement precision (not accuracy) of  $0.01 - 0.02 \text{ mg m}^{-3}$  for blue waters. In order for a *K. brevis* bloom to be detected and identified as such, however, Chl-*a* needs to exceed  $0.5 - 1 \text{ mg m}^{-3}$ , corresponding to *K. brevis* cell concentrations of  $5 \times 10^4$  to  $10^5$  cells  $l^{-1}$ . These concentrations are high enough to cause fish kills (Steidinger et al., 1998).

Satellite-derived Chl-*a* data products can be used to identify areas of possible red tides. For example, a Chl-anomaly technique was proposed by Stumpf et al. (2003a) to flag "new" blooms in an area relative to conditions two weeks earlier — under certain conditions these new blooms can be flagged as potential *K. brevis* blooms.

There are practical difficulties when applying the Chl-based approach to identify red tides in the eastern GOM using remote sensing data. The first is the difficulty with obtaining an accurate chlorophyll estimate in many coastal waters because of errors in the atmospheric correction algorithms (to remove atmospheric effects from the spectral satellite signal) and bio-optical inversion algorithms (to convert the surface spectral signal to Chl-*a* and other bio-optical parameters). In these waters, the optical signal may not be dominated by phytoplankton, but instead by coloured dissolved organic matter (CDOM) from *in situ* phytoplankton degradation or terrestrial runoff, resuspended sediments, and/or the bottom effects in clear, shallow water. The empirical band-ratio OC4 algorithm (O'Reilly et al., 2000; version 4) that is used to convert the surface spectral signal to Chl-*a* does not differentiate between optically important constituents, but rather regards all influences as originating from Chl-*a*. This causes large errors in the Chl-*a* estimates for the eastern GOM coastal waters (Hu et al., 2003; 2005). Although a semi-analytical algorithm designed for MODIS (Carder et al., 1999) can separate CDOM from Chl-*a* and thus improve Chl-*a* estimates in clear and moderately turbid waters (Hu et al., 2003), in highly turbid coastal waters the algorithm switches to an empirical blue/green band-ratio form.

The second difficulty is differentiating *K. brevis* blooms from other phytoplankton blooms. Chl-*a* cannot be used for this task because both types of blooms contain high Chl-*a*. Discrimination between *K. brevis* and other phytoplankton groups using *in situ* optical observations has been done with some success (Cullen et al., 1997; Millie et al., 1997; Lohrenz et al., 1999; Schofield et al., 1999; Kirkpatrick et al., 2000). However, these techniques require hyperspectral data (e.g., Craig et al., 2006), which are not available from satellites. Several HAB detection techniques have been proposed that can use multi-spectral satellite data. These include methods involving particulate backscattering (Cannizzaro et al., 2008), spectral curvature (Tomlinson et al., 2008), a combination of red-wavelength bands (Amin et al., 2009), and image segmentation (Zhang et al., 2002).

In this demonstration, we will combine the techniques proposed by Hu et al. (2005) and Cannizzaro et al. (2008). We used MODIS satellite data to show how to differentiate bloom waters from coastal waters in which other constituents dominate the optical signal, and to differentiate *K. brevis* blooms from other blooms. Specifically, we distinguished phytoplankton blooms from CDOM-rich waters by examining spectral water-leaving radiance and solar stimulated fluorescence (Hu et al., 2005), and *K. brevis* blooms were distinguished from non-*K. brevis* blooms by examining bloom backscattering efficiency (Cannizzaro et al., 2008).

## 2.2 Data and Methods

MODIS Level-1a data were obtained from the U.S. NASA Goddard Space Flight Center (GSFC) (<http://oceancolor.gsfc.nasa.gov>). These data are open to the public within a few hours (typically 3 – 6) of collection by the spacecraft. The following steps were used to generate georeferenced MODIS images at 1-km resolution:

1. MODIS/Aqua Level-1a data were processed to generate Level-1b (calibrated total radiance) data for the "ocean colour" spectral wavebands in the visible and near-infrared, and geolocation data using SeaWiFS Data Analysis System (SeaDAS) software. The 1-km bands were designed for the ocean with sufficient sensitivity to detect subtle changes in ocean colour. The Level-1b and geolocation data were stored in computer files in HDF (Hierarchical Data Format);
2. MODIS Level-1b data were atmospherically corrected to generate the spectral remote sensing reflectance ( $R_{rs}(\lambda)$ ,  $\text{sr}^{-1}$ ) and normalized water-leaving radiance ( $nLw(\lambda)$ ,  $\text{mW cm}^{-2} \mu\text{m}^{-1} \text{sr}^{-1}$ ) using SeaDAS. These two parameters can be derived from each other using the extraterrestrial solar irradiance (time-independent constants). During this step, ancillary data (surface wind, pressure, total ozone thickness, and atmospheric water vapor content) were downloaded from NASA/GSFC and used to estimate the atmospheric contribution to the satellite-received radiance. The atmospheric correction was based on the two near-infrared (NIR) bands at 748 nm and 869 nm, from which atmo-

spheric properties were derived and used to estimate the properties at other wavelengths on a per-pixel basis (Gordon and Wang, 1994). Over turbid coastal waters, a modification to the atmospheric correction scheme was used that involves using an iterative approach to account for the non-zero water-leaving radiance in the NIR (Stumpf et al., 2003b);

3. The spectral  $R_{rs}(\lambda)$  was used to derive two data products: Chl-*a* from an empirical band-ratio algorithm (OC4v4; O'Reilly et al., 2000); particulate backscattering coefficient at 551 nm ( $b_{bp,551}$ ) using a Quasi-Analytical Algorithm (QAA, Lee et al., 2002). Using  $nLw(\lambda)$  data from three MODIS wavebands at 667, 678, and 748 nm we derived the Fluorescence Line Height (FLH,  $mW\ cm^{-2}\ \mu m^{-1}\ sr^{-1}$ ) product using a linear baseline algorithm (Letelier et al., 1996). Further, the empirically-derived Chl-*a* was used to estimate the particulate backscattering coefficient at 551 nm using the Morel (1988) algorithm, designed for phytoplankton dominated (i.e., Case 1) waters:

$$b_{bp,Morel} = 0.3 \times Chl^{0.62} \times (0.002 + 0.02 \times (0.5 - 0.25 \times \log_{10} Chl)) \quad (2.1)$$

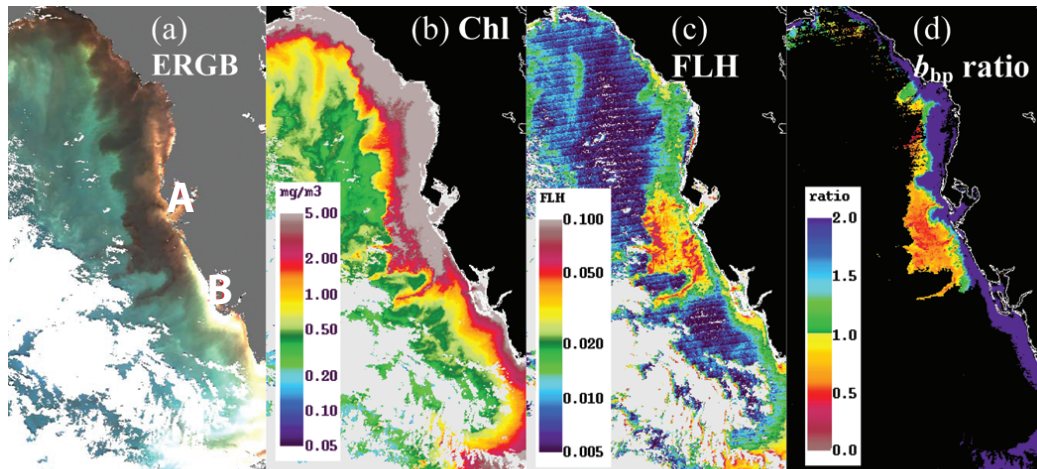
4. These products  $R_{rs}(\lambda)$ ,  $nLw(\lambda)$ , Chl-*a*,  $b_{bp,QAA}$ ,  $b_{bp,Morel}$  and FLH) were georeferenced to a cylindrical equidistant (rectangular, also called geographic lat/lon) projection for the area of interest. The final images had a spatial resolution equivalent to 1-km per image pixel. The map-projected products were stored in HDF files. Individual products were also converted to raster image formats with an embedded palette using pre-defined colour look-up tables;
5.  $nLw(\lambda)$  data at 551, 488, and 443 nm were used as the red, green and blue channels to compose an Enhanced RGB (ERGB) image. The red waveband (667 nm) was not used because water-leaving radiance at this wavelength ( $nLw(667)$ ) is very low except in sediment-rich waters, thus providing little information on red tides.

The Florida Fish and Wildlife Research Institute (FWRI) has compiled an *in situ* database for *K. brevis* cell concentration data. Water samples have been collected by various research and volunteer groups in the eastern GOM and analyzed using microscopic enumeration techniques. These data, although not continuous in either space or time, were used as ground-truth to help interpret the MODIS imagery. Below we demonstrate, step by step, how the various colour features are identified and interpreted from the MODIS imagery.

## 2.3 Demonstration

In 2005, a long-lasting, extensive red tide event occurred on the west Florida shelf (WFS, 24.5°–30.1°N and 85.1°–81.5°W), which may have been related to excessive rainfall in both 2004 and 2005 (Hu et al., 2006). The event started in January 2005

near Tampa Bay, Florida (Tampa Bay is marked as "A" in Figure 2.1a). Figure 2.1 shows several MODIS products from a scene collected on 21 January 2005, where the red tide patch can be seen.



*Karenia brevis* counts, 18-20 January 2005

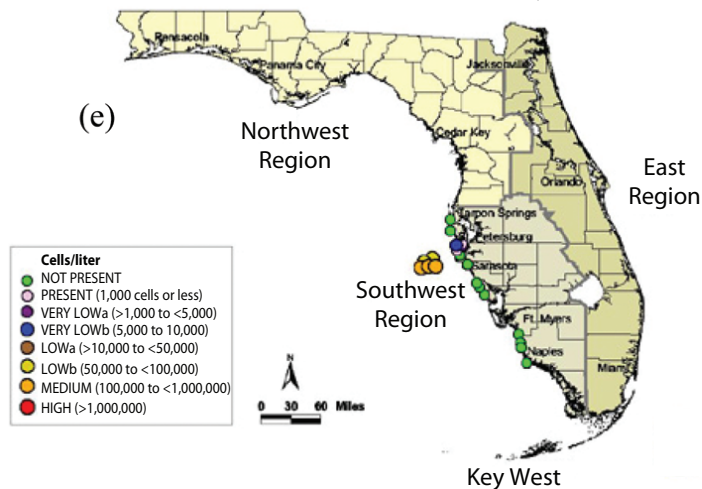


**Figure 2.1** (a - d) MODIS images on 21 January 2005 showing a *K. brevis* bloom in coastal waters between Tampa Bay (A, 27.75°N, 82.56°W) and Charlotte Harbor (B, 26.75°N, 82.1°W). The images cover the area between approximately 24.5°–30.1°N and 85.1°–81.5°W. The various image types were generated using Steps 1 - 5 described in the Data and Methods section. In (d), the  $b_{bp}$  ratio is defined as  $b_{bp,QAA} / b_{bp,Morel}$  (e) *K. brevis* concentration (in cells  $l^{-1}$ ) obtained from FWRI ([http://research.myfwc.com/gallery/image\\_details.asp?id=24764](http://research.myfwc.com/gallery/image_details.asp?id=24764)).

Figure 2.1a shows an ERGB image, where the dark colours result from increased light absorption in the blue wavelength (443 nm) due to high concentrations of CDOM and/or chlorophyll-*a*, and bright colours (light blue, yellow and white) result from suspended sediments and/or shallow bottom. The corresponding Chl-*a* image in Figure 2.1b, derived from the blue-green band ratio algorithm, shows erroneously

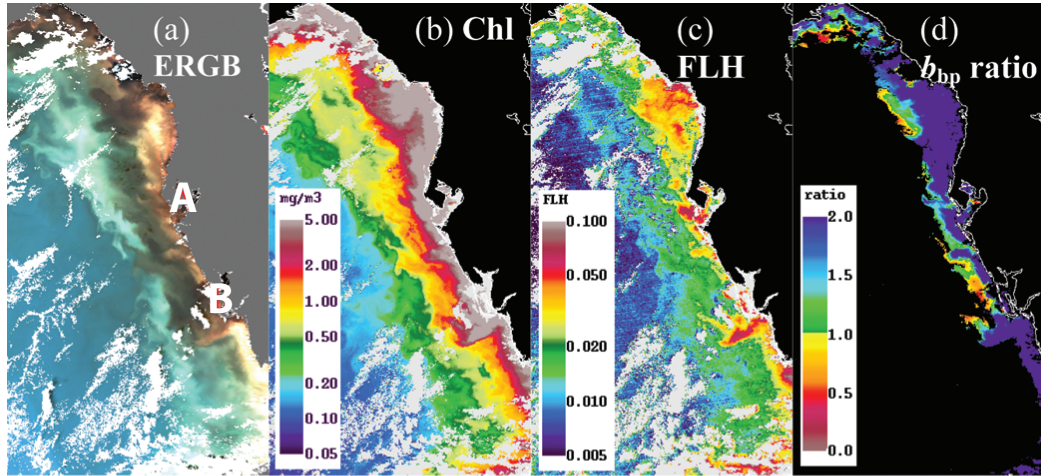
elevated Chl-*a* along the entire coast. In contrast, the FLH image in Figure 2.1c helps distinguish dark CDOM-rich waters (erroneously interpreted as high Chl-*a* in band ratio algorithms) from phytoplankton-rich waters. FLH is insensitive to CDOM (McKee et al., 2007). However, FLH is not a reliable parameter in sediment-rich waters (Gilerson et al., 2007). The high FLH values near Charlotte Harbor (Charlotte Harbor is marked as "B" in Figure 2.1a) for example, may in part be false interpretation of suspended sediments.

Figure 2.1 reveals: 1) Chl-rich waters (dark colour in ERGB with high FLH values); 2) CDOM-rich waters (dark colour in ERGB with low FLH values); 3) sediment-rich waters (bright colour in ERGB with high FLH values); and 4) shallow, clear waters (bright colour in ERGB with low FLH values). Of these, observations 3 and 4 are sometimes difficult to distinguish from each other, especially for very shallow waters (< 5 m water depth) because nLw in the fluorescence bands may also be influenced by benthic algae or sediments. This should not affect our interpretation because both cases are excluded as potential *K. brevis* blooms. Of the four, observation 1 represents waters with high biomass (Chl-*a*) and therefore can be *K. brevis* or other blooms. However, there are two drawbacks from this interpretation. The first is its qualitative nature. Indeed, the terms "high" and "low" only provide a relative sense. The second drawback is that it is impossible to tell if the high-FLH dark waters contain high concentrations of the toxic *K. brevis* or other phytoplankton species (such as diatoms).

To overcome these two difficulties, we first assume that  $FLH > 0.015 - 0.02 \text{ mW cm}^{-2} \mu\text{m}^{-1} \text{ sr}^{-1}$  can indicate bloom conditions and  $FLH < 0.01 - 0.015$  represent non-bloom conditions (note that the values between 0.01 and 0.02 represent transition conditions). Observations from South Florida coastal waters suggest that a FLH value of  $0.01 \text{ mW cm}^{-2} \mu\text{m}^{-1} \text{ sr}^{-1}$  is equivalent to about  $1 \text{ mg m}^{-3}$  Chl-*a* for the range of  $0.4 - 4 \text{ mg m}^{-3}$  ( $\text{Chl} = 1.255 \times (\text{FLH} \times 100)^{0.86}$ ,  $r=0.92$ ,  $n=77$ , Hu et al., 2005), although the relationship between FLH and Chl-*a* (a function of fluorescence efficiency) varies.

The technique proposed by Cannizzaro et al. (2008) was then used to examine the backscattering coefficient at 551 nm ( $b_{\text{bp},551}$ ) estimated with the QAA algorithm (Lee et al., 2002) in reference against  $b_{\text{bp},\text{Morel}}$  from a Case-1 empirical algorithm (Morel, 1988; Equation 2.1). Results are shown in Figure 2.1d. To exclude non-productive waters, pixels with Chl-*a* <  $1.5 \text{ mg m}^{-3}$  are masked as black. Because *K. brevis* blooms exhibit a lower backscattering efficiency compared to diatom blooms, the warm colours (yellow-red, with  $b_{\text{bp},551}/b_{\text{bp},\text{Morel}} < 1.0$ ) in Figure 2.1d represent potential *K. brevis* blooms. Indeed, near concurrent *in situ* water sample analysis from FWRI confirms this finding (Figure 2.1e), where waters offshore of Tampa Bay showed medium concentrations of *K. brevis* cells (100,000 to <1,000,000 cells  $\text{l}^{-1}$ ). Further, in nearshore waters there were no *K. brevis* found in these samples, consistent with the high  $b_{\text{bp}}$  ratios shown in Figure 2.1d. In other words, the high-FLH values near Charlotte Harbor (sediment-rich water as identified by the bright

colour in Figure 2.1a) is successfully discarded as potential *K. brevis* blooms in Figure 2.1d.



*Karenia brevis* counts, 4-7 October 2004

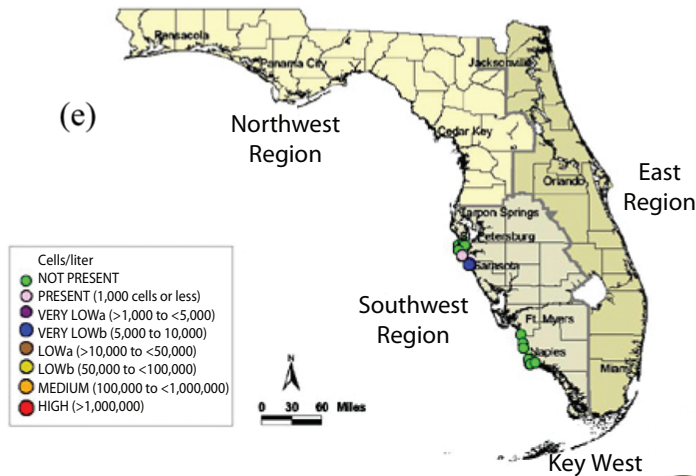


**Figure 2.2** (a - d) MODIS images on 1 October 2004 showing diatom blooms off Tampa Bay (A, 27.75°N, 82.56°W) and Charlotte Harbor (B, 26.75°N, 82.1°W). The images cover the area between approximately 24.5°–30.1°N and 85.1°–81.5°W. The various image types were generated using Steps 1 - 5 described above in the Data and Methods section. In (d), the  $b_{bp}$  ratio is defined as  $b_{bp,QA}/b_{bp,Morel}$  (e) *K. brevis* concentration (in cells  $l^{-1}$ ) obtained from FWRI ([http://research.myfwc.com/gallery/image\\_details.asp?id=20058](http://research.myfwc.com/gallery/image_details.asp?id=20058)).

While Figure 2.1 demonstrates the multiple steps used to delineate *K. brevis* blooms in optically complex waters on the WFS, Figure 2.2 shows another case where the same technique is used to identify non-*K. brevis* (in this case, diatom) blooms. Figure 2.2a shows that, in less than one week after Hurricane Jeanne’s passage on 26 September 2004, most of the WFS waters became enriched in CDOM/Chl-*a* and suspended sediments, all interpreted as high Chl-*a* (Figure 2.2b). While the FLH

image in Figure 2.2c shows potential blooms in nearshore waters, especially near the Tampa Bay and Charlotte Harbor mouths, the  $b_{bp}$  ratio image in Figure 2.2d indicates the possibility that these nearshore blooms are *K. brevis* blooms, is low. Although concurrent water sample data lack coverage of most shelf waters, the limited data in Figure 2.2e confirms that the high FLH patches near Tampa Bay and Charlotte Harbor mouths are non-*K. brevis* blooms. Indeed, the FWRI database showed 0 cells  $l^{-1}$  of *K. brevis* but very high levels (up to 230,000 cells  $l^{-1}$ ) of *Pseudonitzschia* (a toxic diatom) in water samples collected from piers/beaches off Tampa Bay (e.g. Mullet Key, Anna Maria Island, Skyway fishing pier, offshore Egmont Key) between 2–7 October 2004. In this case, the image set used here not only identifies blooms, but also recognizes non-*K. brevis* blooms. Combined with the results shown in Figure 2.1, we can conclude that this technique is efficient, at least for the two cases presented here, in delineating the following waters: Chl-rich, sediment-poor waters; CDOM-rich, Chl-poor waters; sediment-rich and/or shallow, clear waters; *K. brevis* and other bloom waters.

## 2.4 Training

To help prepare and interpret MODIS imagery, we now go through each step to generate the various types of MODIS images from a map-projected MODIS Level-3 HDF data file. The MODIS data (Figure 2.3) were collected on 7 October 2006, where ERGB, Chl-*a*, FLH, and  $b_{bp}$  ratio images are presented in Figures 2.3a-d, respectively. The following steps were used in SeaDAS for image generation, visualization, and interpretation, but any other software package that has basic image processing capabilities and HDF compatibility can also be used.

**Step 1:** Download the MODIS Level-3 HDF data file from the IOCCG website ([http://www.ioccg.org/handbook/Hu\\_red/](http://www.ioccg.org/handbook/Hu_red/)) and open in a SeaDAS Display window. Load the three bands nLw\_443, nLw\_488, and nLw\_551 in the "Band List Selection Window." Then, under Utilities => Data Visualization => Load True Color Image, choose "Band List" instead of "Input File." Choose band numbers 3, 2, 1, for the R, G, B channels, respectively. Enter 10 for slopes and 0 for intercepts. Load the RGB channels in the "Band List Selection" window, and display the true colour image. An image similar to Figure 2.3a should appear in a separate window. A high-resolution coastline can be overlaid on the image by selecting Setups => Coastline. The final image can be saved as an 8-bit png image (colour coded 2-dimensional image) or a 24-bit png image (3-dimensional image) under Functions => Output => Display.

**Step 2:** Use the same method in Step 1 above to load the "chlor\_a" data product from the HDF file into the "Band List Selection Window," and display the image in a separate window. The colour shades in this window appear strange because of the colour encoding in Step 1. The colour scheme can be changed to a "rainbow" colour

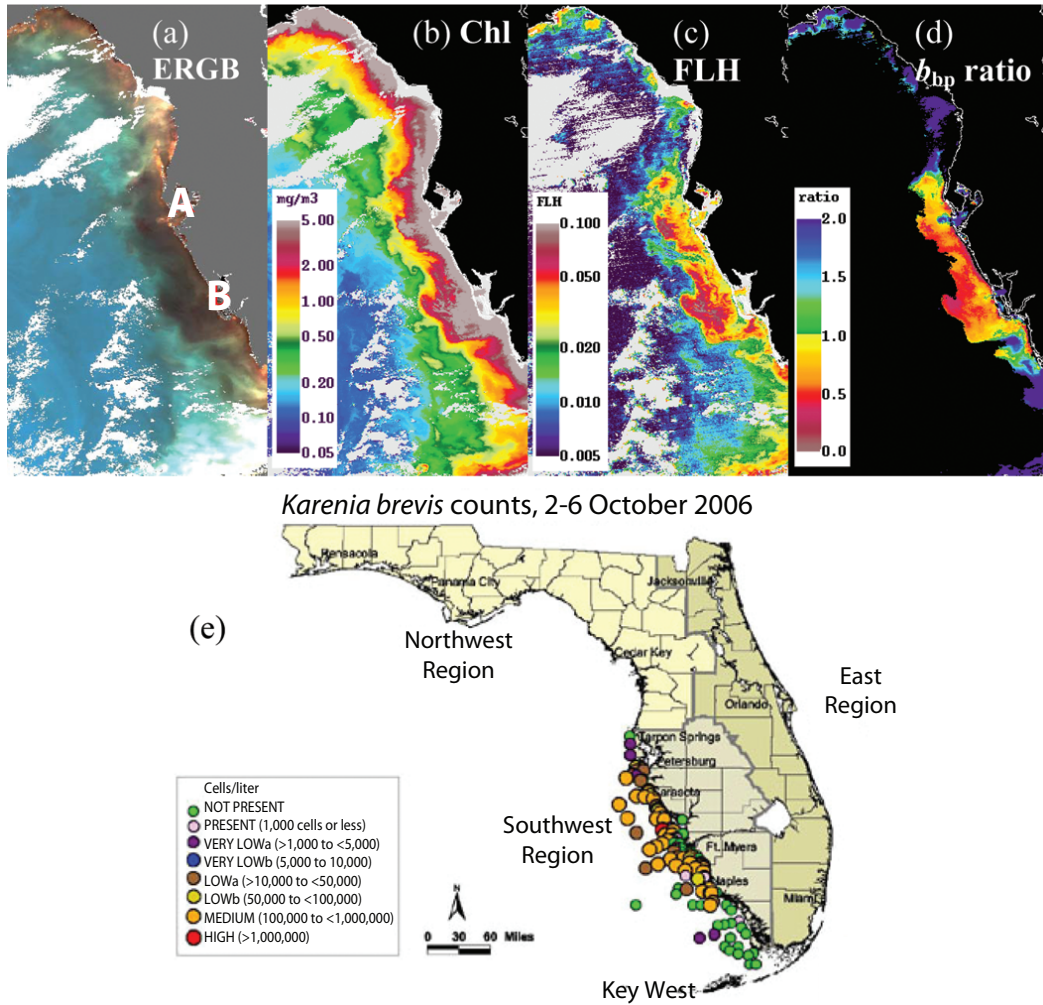


**Figure 2.3** (a – d) MODIS images on 7 October 2006 showing *K. brevis* blooms off the central west Florida between Tampa Bay (A, 27.75°N, 82.56°W) and Charlotte Harbor (B, 26.75°N, 82.1°W). The images cover the area between approximately 24.5°–30.1°N and 85.1°–81.5°W. The various image types were generated using Steps 1 – 5 described in the Data and Methods section. In (d), the  $b_{bp}$  ratio is defined as  $b_{bp,QAA}/b_{bp,Morel}$  (e) *K. brevis* concentration (in cells  $l^{-1}$ ) obtained from FWRI ([http://research.myfwc.com/gallery/image\\_details.asp?id=24504](http://research.myfwc.com/gallery/image_details.asp?id=24504)).

by selecting "Chlorophyll a" in the list of colours from Functions => Color Lut => Load Lut. The Chl-*a* image with this colour scheme may appear different to that in Figure 2.3b, but the colour stretch can be adjusted by selecting Functions => Rescale with a log stretch. A colour legend can be added by selecting Functions => Color Bar => On, and a high-resolution coastline can also be added using methods in Step 1. The final image can be saved as a colour-coded png image, similar to Step 1.

**Step 3:** The same steps as in Step 2 are used to load the "flh" data product from the

HDF file, display it in a separate window, adjust the colour stretch, and save it as a colour-coded png image. Note that to show details at low values, a logarithmic colour stretch is required under Functions => Rescale.

**Step 4:** The SeaDAS software allows a user to define a new parameter using existing parameters. Based on the "chlor\_a" data available in the "Band List Selection" window, Equation 2.1 is used to estimate  $b_{bp,Morel}$ . Assuming "chlor\_a" is the 5<sup>th</sup> band in the band list, type in the following commands under Utilities => Data Manipulation => User Defined Operations:

```
bad_idx=where(B5_l_t < 0.001)
B5[bad_idx]=0.001
result=0.3*B5^0.62*(0.002 + 0.02 * (0.5 - 0.25 * alog10(B5)))
```

Then, type in "bbp\_morel" in the "New band name" field, and click "Run." This will create a new parameter "bbp\_morel" in the "Band List Selection" window (assuming it is the 6<sup>th</sup> band in the window). Load bbp\_551\_qaa from the HDF file to this window (assuming it is the 7<sup>th</sup> band in the window). In the "User Defined Operations" window type in the following commands:

```
result=B7/B6
low_chl_idx = where(B5_l_t > 1.5)
result[low_chl_idx]=0.0
```

Then, type in "bbp\_ratio" in the "New band name" field, and click "Run." This will create a new parameter "bbp\_ratio" in the "Band List Selection" window. This band can be displayed, colour stretched, and saved as a colour-coded png image (together with a colour legend) using the same steps as above. The saved image should appear as the opposite of Figure 2.3d with the cold colours representing low values and the warm colours representing high values.

## 2.5 Questions

**Q1:** What do the various colour shades in Figure 2.3a mean? Do the dark shades between Tampa Bay and Charlotte Harbor indicate high Chl-*a*?

**Q2:** Do the high Chl-*a* values (yellowish and reddish colours indicated on the colour legend) in Figure 2.3b represent high chlorophyll-*a* concentrations or something else?

**Q3:** What do the high FLH values in Figure 2.3c mean?

**Q4:** Do the low "bbp\_ratio" values in Figure 2.3d indicate *K. brevis* blooms?

## 2.6 Answers

**A1:** Similar to Figure 2.1a, the various colour shades in the RGB image can be used to qualitatively distinguish various waters. Dark colours result from high concentrations of CDOM and/or chlorophyll-*a*, but it is impossible to tell which of the two is dominant because they both strongly absorb blue light. So the dark shades between Tampa Bay and Charlotte Harbor do not necessarily indicate high Chl-*a*. The bright colours in the ERGB image result from suspended sediments and/or shallow bottom because they both strongly scatter light.

**A2:** The warm colours in coastal waters do not necessarily indicate high Chl-*a* because the band-ratio empirical algorithm used to derive Chl-*a* could falsely interpret other water constituents (CDOM, suspended sediments, and shallow bottom) as chlorophyll-*a*.

**A3:** While FLH is a reliable measure of biomass (Chl-*a*) in sediment-poor waters, in sediment-rich waters high FLH values may be simply due to high turbidity and not due to high Chl-*a*. Thus, combining Figure 2.3c with Figure 2.3a where sediment-rich waters can be easily identified, we can infer that high FLH values associated with dark waters in Figure 2.3a (between Tampa Bay and Charlotte Harbor) are likely associated with high biomass, while high FLH values associated with bright waters in Figure 2.3a (in the northern and southern parts of the coastal waters) are likely associated with high concentrations of suspended sediments.

**A4:** The low "bbp\_ratio" values in Figure 2.3d very likely indicate *K. brevis* blooms. These blooms have a lower backscattering efficiency compared with non-*K. brevis* blooms. The waters with bbp\_ratio < 1 can be classified as dominated by *K. brevis* cells. Indeed, analysis of near-concurrent FWRI water sample data (Figure 2.3e) confirms this inference for coastal waters between Tampa Bay and Charlotte Harbor. However, it is unknown if waters in the northern part of Florida (associated also with low bbp\_ratio but high FLH) contain high concentrations of *K. brevis*, because CDOM interference to MODIS Chl may lead to erroneously overestimated Chl and lower-than-real bbp ratio. A related case can be found in Figure 2.1d, where offshore waters north of Tampa Bay show high CDOM (Figure 2.1a) and erroneously high MODIS Chl (Figure 2.1b and c), leading to low bbp\_ratio with high Chl. Cross-examination of all four types of imagery is necessary to rule out potential false positive detection.

## 2.7 Discussion and Summary

We demonstrated the principles of *K. brevis* bloom detection using a combination of MODIS imagery and techniques proposed by Hu et al. (2005) and Cannizzaro et al. (2008). Several other methods have been published (Stumpf et al., 2003a; Tomlinson

et al., 2004; 2008; Amin et al., 2009), but our purpose here is to show the principles as opposed to providing a comprehensive review on the various techniques.

The three cases shown here are successful examples. However, we must recognize that nature is more complex than shown here, and none of the published techniques is perfect. Indeed, our methods can result in both false-positives (i.e., identifies *K. brevis* blooms in non-bloom waters) and false negatives (i.e., identifies non-bloom in *K. brevis* bloom waters). Although the evaluation results of Tomlinson et al. (2008) show low possibilities (about 20 – 30%) for both error types if different image types are combined, such possibilities cannot be neglected.

The 70–80% success rate of the *K. brevis* bloom detection methods provides useful information in at least two aspects: 1) to document the *K. brevis* occurrence patterns in both space and time to help understand their initiation, maintenance, and control mechanisms and 2) to guide rapid response in field surveys. This capability, combined with the free availability of both MODIS data and processing software (SeaDAS), makes it particularly useful in implementing any regional satellite-based HABs monitoring system. The reader is cautioned, however, that not every HAB species contains high chlorophyll-*a* pigment or displays low backscattering efficiency. For a particular region, a regional algorithm based on the unique optical characteristics of HABs is often required.

At the time of writing, MODIS data from the Aqua satellite (afternoon pass, 2002 – present) are considered to be of science quality, but MODIS data from the Terra satellite (morning pass, 1999 – present) are provisional. The ocean colour community, especially the NASA Ocean Biology Processing Group (OBPG), is making progress by removing noise and improving calibration/retrieval algorithms for MODIS-Terra. The combined MODIS instruments will significantly increase the spatial/temporal coverage in many coastal regions, thus providing additional values in HABs monitoring. Likewise, when MERIS data (Medium Resolution Imaging Spectrometer, 2002 – present) at 300-m resolution are used, the capability to detect small-patch blooms should be enhanced. In the absence of fluorescence data (e.g., SeaWiFS is not equipped with the fluorescence bands), other techniques (e.g., Chl-anomaly or spectral curvature, see Tomlinson et al., 2008) can also be used.

In summary, ocean-colour satellite imagery is particularly useful in detecting and monitoring HAB events because of their synoptic and frequent coverage as well as the information carried in their spectral reflectance. Correct interpretation of the various image types requires sufficient knowledge in bio-optics and phytoplankton dynamics. In any case, the full potential of satellite remote sensing of HABs can only be realized through coordinated efforts between remote sensing specialists, environmental scientists, coastal managers, and other groups.

## 2.7.1 Acknowledgements

This work was supported by the U.S. NASA (NNX09AE17G and NNX09AV56G), EPA (MX964754070), and NOAA (NA06NES4400004). We thank the U.S. NASA/GSFC for providing MODIS data and thank FWRI for providing *in situ* *K. brevis* concentration data.

## 2.8 References

- Amin R, Zhou J, Gilerson A, Gross B, Moshary F, Ahmed S (2009) Novel optical techniques for detecting and classifying toxic dinoflagellate *Karenia brevis* blooms using satellite imagery. *Opt Express* 17:9126-9144
- Asai S Krzanowski JJ, Anderson WH, Martin DF, Polson JB, Lockey RF, Bukantz SC, Szentivanyi A (1982) Effects of the toxin of red tide, *Ptychodiscus brevis*, on canine tracheal smooth muscle: a possible new asthma-triggering mechanism. *J Allergy Clin Immunol* 69: 418- 428
- Babin M, Roesler CS, Cullen J J (eds) (2008) Real-time coastal observing systems for marine ecosystem dynamics and harmful algal blooms: Theory, instrumentation and modeling. UNESCO, Paris
- Brand L, Compton A (2007) Long-term increase in *Karenia brevis* abundance along the Southwest Florida Coast. *Harmful Algae* 6:232-252
- Cannizzaro JP, Carder KL, Chen FR, Heil CA, Vargo GA (2008) A novel technique for detection of the toxic dinoflagellate, *Karenia brevis*, in the Gulf of Mexico from remotely sensed ocean color data. *Cont Shelf Res* 28:137-158
- Carder KL, Chen FR, Lee ZP, Hawes SK, Kamykowski D (1999) Semianalytic Moderate-Resolution Imaging Spectrometer algorithms for chlorophyll *a* and absorption with bio-optical domains based on nitrate- depletion temperatures. *J Geophys Res* 104:5403-5421
- Christman, M , Young L (2006) Analysis of *Karenia brevis* Gulf Data. Final project report to Florida Wildlife Research Institute, from University of Florida, Gainesville, FL, June 2006
- Craig SE, Lohrenz SE, Lee ZP, Mahoney KL, Kirkpatrick GJ, Schofield OM, Steward RG (2006) Use of hyperspectral remote sensing reflectance for detection and assessment of the harmful alga, *Karenia brevis*. *Appl Optics* 45:5414-5425
- Cullen JJ, Ciotti AM, Davis RF, Lewis MR (1997) Optical detection and assessment of algal blooms. *Limnol Oceanogr* 42:1223-1239
- Dierssen HM, Kudela RM, Ryan JP, Zimmerman RC (2006) Red and black tides: Quantitative analysis of water-leaving radiance and perceived color for phytoplankton, colored dissolved organic matter, and suspended sediments. *Limnol Oceanogr* 51:2646-2659
- Evens TJ, Kirkpatrick GJ, Millie DF, Chapman DJ, Schofield OME (2001) Photophysiological responses of the toxic red-tide dinoflagellate *Gymnodinium breve* (Dinophyceae) under natural sunlight. *J Plank Res* 23:1177-1193
- Flewelling, LJ, Naar JP, Abbott JP, Baden DG, Barros NB, Bossart GD, et al. (2005) Brevetoxicosis: red tides and marine mammal mortalities. *Nature* 435: 755-756
- Gilerson A, Zhou J, Hlaing S, Ioannou I, Schalles J, Gross B, Moshary F, Ahmed S (2007) Fluorescence component in the reflectance spectra from coastal waters. Dependence on water composition. *Optics Express* 15:15702-15721
- Gordon HR, Wang M (1994) Retrieval of water-leaving radiance and aerosol optical thickness over the oceans with SeaWiFS: A preliminary algorithm. *Appl Optics* 33:443-452
- Habas EJ , Gilbert CK (1974) The economic effects of the 1971 Florida red tide and the damage it presages for future occurrences. *Environ Lett* 6: 139-147
- Hemmert WH (1975) The public health implications of *Gymnodinium breve* red tides, a review of the literature and recent events. In: LoCicero, VR (ed), Proceedings of the First International Conference on Toxic Dinoflagellate Blooms: 489-497
- Hu CM, Muller-Karger FE, Biggs DC, Carder KL, Nababan B, Nadeau D, Vanderbloemen J (2003) Comparison of ship and satellite bio-optical measurements on the continental margin of the NE Gulf of

- Mexico. *Int J Rem Sens* 24:2597-2612
- Hu CM, Muller-Karger FE, Taylor CJ, Carder KL, Kelble C, Johns E, Heil CA (2005) Red tide detection and tracing using MODIS fluorescence data: A regional example in SW Florida coastal waters. *Rem Sens Environ* 97:311-321
- Hu C, Swarzenski PW, Muller-Karger FE (2006) Hurricanes, submarine groundwater discharge, and Florida's red tides. *Geophys Res Lett* 33: L11601, doi:10.1029/2005GL025449
- Kirkpatrick B, Fleming LE, Squicciarini D, Backer LC, Clark R, Abraham W, Benson J, Cheng YS, Johnson D, Pierce R, Zaias J, Bossart GD, Baden DG (2004) Literature review of Florida red tide: implications for human health effects. *Harmful Algae* 3:99-115
- Kirkpatrick GJ, Millie DF, Moline MA, Schofield O (2000) Optical discrimination of a phytoplankton species in natural mixed populations. *Limnol Oceanogr* 45:467-471
- Landsberg JH, Steidinger KA (1998) A historical review of *Gymnodium breve* red tides implicated in mass mortalities of the manatee (*Trichechus manatus latirostris*) in Florida, USA. In: Reguera, B, Blanco J, Fernandez ML, Wyatt T (eds), Proceedings of the 8th International Conference on Harmful Algal Blooms, Vigo, Spain: 97-100
- Larkin, SL, Adams CM (2007) Harmful algal blooms and coastal business: economic consequences in Florida. *Soc Nat Resour* 20: 849-859
- Lee Z, Carder KL, Arnone RA (2002) Deriving inherent optical properties from water color: a multiband quasi-analytical algorithm for optically deep waters. *Appl Opt* 41: 5755-5772
- Lenes JM, Darrow BP, Cattrall C, Heil CA, Callahan M, Vargo GA, Byrne RH, Prospero JM, Bates DE, Fanning KA, Walsh JJ (2001) Iron fertilization and the *Trichodesmium* response on the West Florida shelf. *Limnol Oceanogr* 46:1261-1277
- Letelier RM, Abbott MR (1996) An analysis of chlorophyll fluorescence algorithms for the Moderate Resolution Imaging Spectrometer (MODIS). *Rem Sens Environ* 58:215-223
- Lohrenz SE, Fahnenstiel GL, Kirkpatrick GJ, Carroll CL, Kelly KA (1999) Microphotometric assessment of spectral absorption and its potential application for characterization of harmful algal species. *J Phycol* 35:1438-1446
- McKee D, Cunningham A, Wright D, Hay L (2007) Potential impacts of nonalgal materials on water-leaving Sun induced chlorophyll fluorescence signals in coastal waters. *Appl Opt* 46:7720-7729
- Millie DF, Schofield O, Kirkpatrick GJ, Johnsen G, Tester PA, Vinyard BT (1997) Phytoplankton pigments and absorption spectra as potential 'Biomarkers' for harmful algal blooms: a case study of the Florida red-tide dinoflagellate, *Gymnodinium breve*. *Limnol Oceanogr* 42:1240-1251
- Morel A (1988) Optical modeling of the upper ocean in relation to its biogenous matter content (Case I waters). *J Geophys Res* 93:10,749-10,768
- O'Reilly JE, Maritorena S, Siegel D, O'Brien MC, Toole, D, Mitchell BG, Kahru, M, Chavez FP, Strutton P, Cota G, Hooker SB, McClain CR, Carder KL, Muller-Karger F, Harding L, Magnuson A, Phinney D, Moore GF, Aiken J, Arrigo KR, Letelier R, Culver M (2000) Ocean color chlorophyll a algorithms for SeaWiFS, OC2 and OC4: Version 4. In: Hooker SB and Firestone ER (eds) SeaWiFS Postlaunch Calibration and Validation Analyses (Part 3), NASA Technical Memorandum 2000-206892, Volume 10, NASA GSFC, 9-23
- Schofield O, Grzymalski J, Bisset WP, Kirkpatrick GJ, Millie DF, Moline M, Roesler CS (1999) Optical monitoring and forecasting systems for harmful algal blooms: possibility or pipe dream? *J Phycol* 35:1477-1496
- Steidinger, KA, Vargo GA, Tester PA, Tomas CR (1998) Bloom dynamics and physiology of *Gymnodinium breve*, with emphasis on the Gulf of Mexico. In: Physiological Ecology of Harmful Algal Blooms (Anderson EM, Cembella AD, Hallegraff GM, eds) Springer-Verlag, New York: 135-153
- Stumpf RP, Culver ME, Tester PA, Tomlinson M, Kirkpatrick GJ, Pederson BA, Truby E, Ransibrahmanakul V, Soracco M (2003) Monitoring *Karenia brevis* blooms in the Gulf of Mexico using satellite ocean color imagery and other data. *Harmful Algae* 2:147-160
- Stumpf RP, Arnone RA, Gould RW, Martinolich PM, Ransibrahmanakul V (2003b) A partially coupled ocean-atmosphere model for retrieval of water-leaving radiance from SeaWiFS in coastal waters. In: S B Hooker and E R Firestone (eds) SeaWiFS postlaunch technical report series, Vol 22: Algorithm updates for the fourth SeaWiFS data processing, 51-59

- Tester PA, Steidinger KA (1997) *Gymnodinium breve* red tide blooms: Initiation, transport, and consequences of surface circulation. *Limnol Oceanogr* 42:1039-1051
- Tomlinson MC, Stumpf RP, Ransibrahmanakul V, Truby EW, Kirkpatrick GJ, Pederson BA, Vargo GA, Heil CA (2004) Evaluation of the use of SeaWiFS imagery for detecting *Karenia brevis* harmful algal blooms in the eastern Gulf of Mexico. *Rem Sens Environ* 91:293-303
- Tomlinson MC, Wynne TT, Stumpf RP (2008) An evaluation of remote sensing techniques for enhanced detection of the toxic dinoflagellate, *Karenia brevis*. *Remote Sens Environ* 113:598- 609
- Walsh JJ, Jolliff JK, Darrow BP, Lenes JM, Milroy SP, Remsen A, Dieterle DA, Carder KL, Chen FR, Vargo GA, Weisberg RH, Fanning KA, Muller-Karger FE, Shinn E, Steidinger KA, Heil CA, Tomas CR, Prospero JS, Lee TN, Kirkpatrick GJ, Whitedge TE, Stockwell DA, Villareal TA, Jochens AE, Bontempi PS (2006) Red tides in the Gulf of Mexico: Where, when, and why? *J Geophys Res* 111: 111: C11003, doi:10.1029/2004JC002813
- Walsh JJ, Steidinger KA (2001) Saharan dust and Florida red tides: The cyanophyte connection. *J Geophys Res* 106:11597-11612
- Walsh JJ, Weisberg RH, Lenes JM, Chen FR, Dieterle DA, Zheng L, Carder KL, Vargo GA, Havens JA, Peebles E, Hollander DJ, He R, Heil CA, Mahmoudi B, Landsberg JH (2009) Isotopic evidence for dead fish maintenance of Florida red tides, with implications for coastal fisheries over both source regions of the West Florida shelf and within downstream waters of the South Atlantic Bight. *Prog Oceanogr* 80:51-73
- Zhang H (2002) Detecting Red Tides on the West Florida Shelf by Classification of SeaWiFS Satellite Imagery. Master's thesis, Department of Computer Science and Engineering, University of South Florida, December 2002

## Case Study 3

# Monitoring Green Tides in Chinese Marginal Seas

Ming-Xia He<sup>1</sup>, Junpeng Liu<sup>1</sup>, Feng Yu<sup>1</sup>, Daqiu Li<sup>2</sup>, Chuanmin Hu<sup>\*3</sup>

---

## 3.1 Background

Coastal phytoplankton blooms have been reported world wide. These blooms sometimes cause environmental problems in both developed and developing countries where excessive nutrients and other pollutants from rapid-growing agriculture, aquaculture, and industries are delivered to the ocean. In Chinese coastal waters of the Yellow Sea, East China Sea, and Bohai Sea, the number and size of toxic algae blooms (often called red tides) as well as toxic species have increased significantly since 1998, a result of increased nutrient inputs from multiple sources (Zhou and Zhu, 2006).

Similar to red tides, green tides have also been reported in the world's oceans (e.g., Fletcher, 1996; Blomster et al, 2002; Nelson et al. 2003; Merceron et al., 2007). These green tides contain high concentrations of green macroalgae, but they are typically small in size and restricted to coastal areas. However, between May and July 2008, an extensive bloom of the green macroalgae *Ulva prolifera* (previously known as *Enteromorpha prolifera*, see Hayden et al., 2003) occurred in coastal and offshore waters in the Yellow Sea (YS) near Qingdao, China (Hu and He, 2008). The macroalgae bloom created an enormous burden on local government and management agencies because all the algae that washed up onto the beach and in the Olympic sailing area near Qingdao had to be physically removed (Figure 3.1). By the end of July 2008, >1,000,000 tons of algae had been removed. Other methods (e.g., using a 30-km boom) were employed to maintain an algae-free area of water near Qingdao for the Olympic sailing competition, with a total cost exceeding US\$100 million (Wang et al., 2009; Hu et al., 2010). The bloom was first speculated to be a result of local pollution, but analysis of MODIS (Moderate Resolution Imaging Spectroradiometer) satellite imagery revealed a remote origin (Hu and He, 2008). More recent studies suggested that the bloom was a result of rapid expansion of the coastal seaweed

---

<sup>1</sup>Ocean Remote Sensing Institute, Ocean University of China, 5 Yushan Road, Qingdao, China 266003

<sup>2</sup>Institute for Environmental Protection Science at Jinan, 183, Shanda Road, Jinan, China 250014

<sup>3</sup>College of Marine Science, University of South Florida, 140 7th Ave., S., St. Petersburg, FL 33701, USA. \*Email address: hu@marine.usf.edu

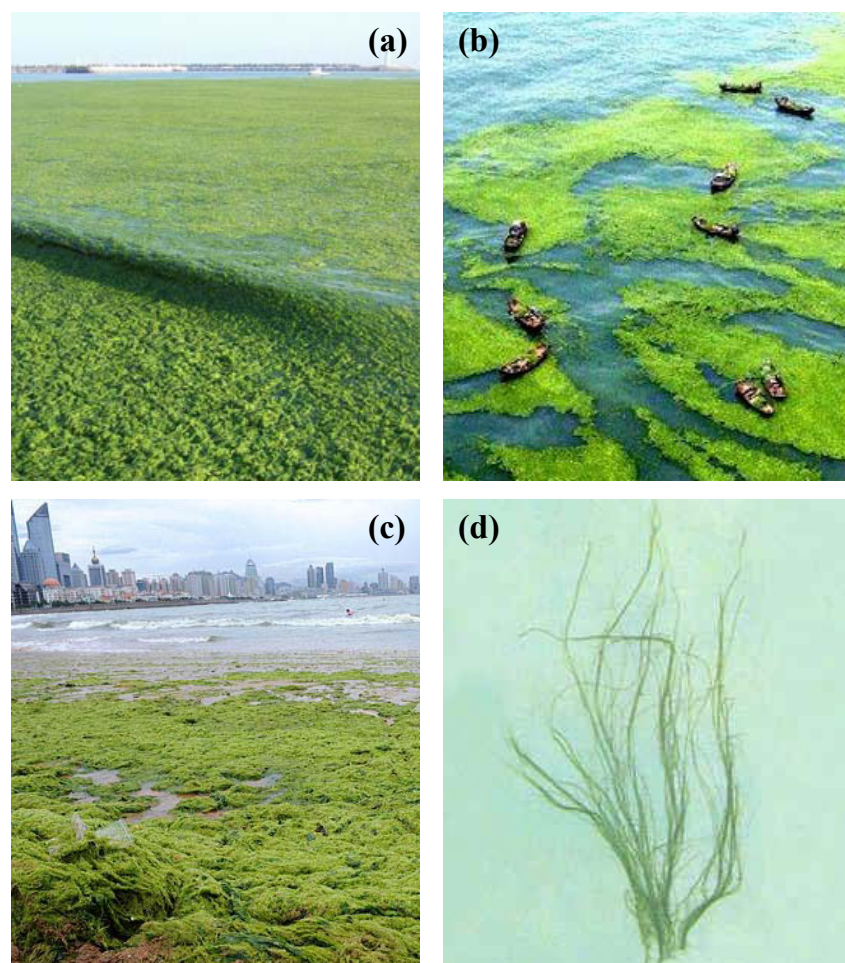


**Figure 3.1** Green tide of macroalgae *Ulva prolifera* in coastal waters of the Yellow Sea near Qingdao, China. (a) and (b) Macroalgae blooms in coastal waters; (c) algae washed onto the beach; (d) morphology of the algae, which can grow to >1 m in length. (Images from public news media [http://tupian.hudong.com/a2\\_70\\_76\\_01300000195282124057760319832\\_jpg.html](http://tupian.hudong.com/a2_70_76_01300000195282124057760319832_jpg.html)).

aquaculture of *P. yezoensis* where water circulation and favorable growth conditions brought remote *U. prolifera* to Qingdao (Li et al., 2008; Liang et al., 2008; Lu and Qiao, 2008; Qiao et al., 2008; Sun et al., 2008; Hu, 2009; Liu et al., 2009; Hu et al., 2010). Further, it was found that smaller green macroalgae blooms were recurrent in history not only in the YS but also in the East China Sea (ECS) (Hu et al., 2010). Because green tides of the same macroalgae may occur in the future in both YS and ECS, it is desirable to establish a remote-sensing based monitoring system to provide timely information on the occurrence and characteristics of green tides (location, size, and potential trajectory). Indeed, a rapid-response remote sensing system using multiple satellites has shown critical values to help implement management plans during the 2008 bloom event (Jiang et al., 2009). Here, using data from several

satellite instruments, we describe the methodology used to detect green tides, and a preliminary monitoring system that covers the entire YS and ECS (Figure 3.2). Our primary objective is to demonstrate the methods used to identify green tides from space, which may be applied in other coastal regions where similar green tides also occur.

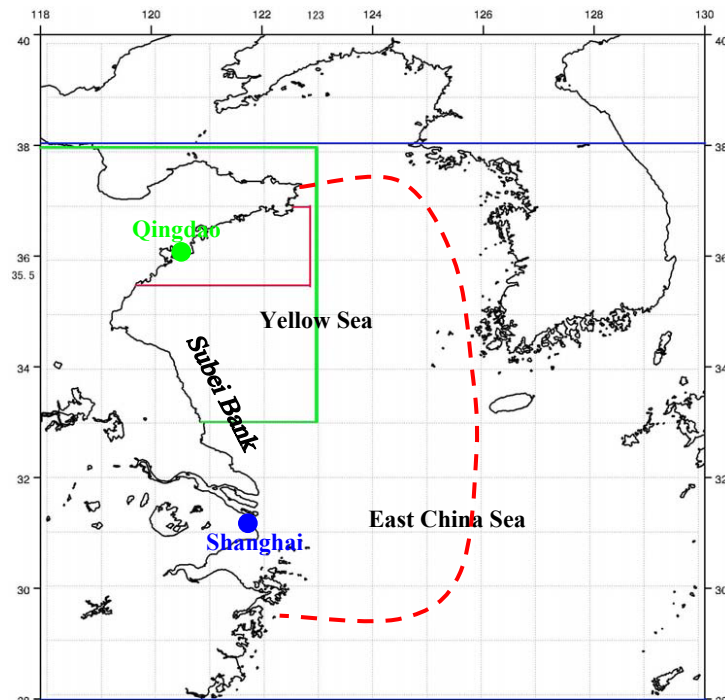


**Figure 3.2** Geographic areas (dashed red line) where green tides of the macroalga *Ulva prolifera* were found between 2000 and 2009. Our monitoring efforts are focused on the Yellow Sea and East China Sea. The various colour boxes represent several pre-defined regions to facilitate image display and interpretation. An experimental online monitoring system has been established and has been in operation since early 2009: <http://www.station.orsj.ouc.edu.cn:8080/algae/>.

## 3.2 Data and Methods

Three types of data were used. Type 1 is near real-time data obtained from the MODIS instruments onboard the U.S. NASA satellites Terra (1999 – present) and Aqua (2002 – present), and the MERSI (Medium Resolution Spectral Imager) instrument onboard the Chinese satellite FY-3A (2008 – present). These satellite instruments have a wide swath width (>2000 km) and frequent coverage, and provide medium-resolution (250-m) data suitable for identifying large-scale macroalgae blooms. Although the individual multi-cell algae are thin and small (Figure 3.1), their aggregation makes

them appear as surface vegetation and therefore detectable in satellite imagery. Type 2 is high-resolution data from satellite instruments designed for land and coastal waters, for example Landsat, SPOT, Synthetic Aperture Radar (SAR), and HJ-1. These data have limited spatial (hundreds of kilometers) and infrequent (one week to 16 days) coverage, but can be used to detect small-scale macroalgae blooms. Type 3 is near-real time data from MODIS, MERSI, COCTS (onboard the Chinese satellite HY-1B, 2007 – present), and QuikScat (1999 – present). These data can provide environmental conditions of the study regions, including sea surface temperature (SST), sea surface wind (SSW), and ocean chlorophyll-*a* concentrations.

For brevity, in this work we demonstrate primarily how to use MODIS (Type 1 data) and Landsat (Type 2 data) to detect macroalgae blooms in open oceans and coastal waters. The use of Type 3 data to assess environmental conditions is shown in other case studies. MODIS data source and most processing methods are described in detail in another case study (*Detection of Oil Slicks using MODIS and SAR Imagery*), but for completeness they are summarized here. All data were downloaded from the U.S. NASA Goddard Space Flight Center (GSFC) at no cost (<http://oceancolor.gsfc.nasa.gov>). The data are open to the public in near real-time and do not require data subscription. The following steps were used to generate geo-referenced MODIS products at 250-m resolution.

**Step 1:** MODIS Level-0, 5-minute granules (satellite data collected every 5 minutes were stored in a computer file to facilitate data management) were downloaded from NASA/GSFC;

**Step 2:** MODIS Level-0 data were processed to generate Level-1b (calibrated total radiance) data for the 36 spectral bands using the SeaWiFS Data Analysis System (SeaDAS) software. The software was originally designed to process SeaWiFS data only, but was updated to process data from other satellite instruments including MODIS. The free software is distributed by the U.S. NASA GSFC. The Level-1b data were stored in computer files in Hierarchical Data Format (HDF);

**Step 3:** MODIS Level-1b data were used to derive the spectral reflectance:

$$R_{rc,\lambda}(\theta_0, \theta, \Delta\phi) = \pi L_{t,\lambda}^*(\theta_0, \theta, \Delta\phi) / (F_{0,\lambda} \times \cos\theta_0) - R_{r,\lambda}(\theta_0, \theta, \Delta\phi), \quad (3.1)$$

where  $\lambda$  is the wavelength for the MODIS band,  $L_t^*$  is the calibrated sensor radiance after correction for gaseous absorption,  $F_0$  is the extraterrestrial solar irradiance,  $(\theta_0, \theta, \Delta\phi)$  represent the pixel-dependent solar-viewing geometry, and  $R_r$  is the reflectance due to Rayleigh (molecular) scattering. This step used the software CREFL from the NASA MODIS Rapid Response Team. The  $R_{rc}$  data of the 7 MODIS bands (469, 555, 645, 859, 1240, 1640, and 2130 nm) were stored in HDF computer files.

**Step 4:** The  $R_{rc}$  data were geo-referenced to a rectangular (also called geographic lat lon) projection for the area of interest, defined by the North-South and East-

West bounds. Because 1 degree is about 110 km at the equator, the map-projected data have 440 image pixels per degree, corresponding to 250 m per image pixel. Although only the MODIS 645- and 859-nm bands have a nadir resolution of 250 m, other bands at 500-m resolution were interpolated to 250-m resolution using a sharpening scheme similar to that for Landsat (i.e., the 250-m data at 645 nm were congregated to 500-m data, and the ratios between a congregated 500-m pixel and the 4 individual 250-m pixels were applied to "sharpen" the MODIS 500-m data from other bands). The mapping software was written in-house using C++ and PDL (Perl Data Language) with a mapping accuracy of about 0.5 image pixel;

**Step 5:** The map projected  $R_{rc}$  data at 645, 555, and 469 nm were converted to byte values using a logarithmic stretch, and then used as the Red, Green, and Blue channels, respectively, to compose a RGB image. The purpose was to visually identify land and clouds;

**Step 6:** A floating algae index (FAI) data product was derived as follows (Hu, 2009):

$$\begin{aligned} \text{FAI} &= R_{rc,\text{NIR}} - R_{rc,\text{NIR}'}, \\ R_{rc,\text{NIR}'} &= R_{rc,\text{RED}} + (R_{rc,\text{SWIR}} - R_{rc,\text{RED}}) \times (\lambda_{\text{NIR}} - \lambda_{\text{RED}}) / (\lambda_{\text{SWIR}} - \lambda_{\text{RED}}), \end{aligned} \quad (3.2)$$

where  $R_{rc,\text{NIR}'}$  is the baseline reflectance in the NIR band derived from a linear interpolation between the RED and shortwave IR (SWIR) bands. For MODIS,  $\lambda_{\text{RED}} = 645$  nm,  $\lambda_{\text{NIR}} = 859$  nm,  $\lambda_{\text{SWIR}} = 1240$  nm. FAI was designed to quantify the reflectance in the near-IR due to the vegetation "red-edge" effect, because green macroalgae floating on the water surface appear as surface vegetation.

**Step 7:** The RGB and FAI images were loaded in the software ENVI for display and analysis. The "Link Display" function connects the two image types, so a suspicious macroalgae slick/patch in the FAI image can be cross-examined with the RGB image to determine if it might be caused by small clouds instead of macroalgae.

Landsat-5 TM and Landsat-7 ETM+ Level-1b data were obtained from the U.S. Geological Survey at no cost (<http://glovis.usgs.gov>). These are radiometrically calibrated radiance data in seven spectral channels, geo-referenced to a UTM projection and stored in Geo-TIFF computer files. The same steps used for MODIS were used to generate Landsat RGB and FAI images using computer codes developed in-house, except that Landsat wavebands of  $\lambda_{\text{RED}} = 660$  nm,  $\lambda_{\text{NIR}} = 825$  nm, and  $\lambda_{\text{SWIR}} = 1650$  nm were used in Equation 3.2 to derive a Landsat FAI.

### 3.3 Demonstration

Figure 3.3 shows a MODIS 250-m resolution FAI image covering a portion of the YS, where land and clouds are masked by the RGB image, obtained on 29 June 2008. Two extensive bloom areas are outlined in the dashed circles. These are blooms of the

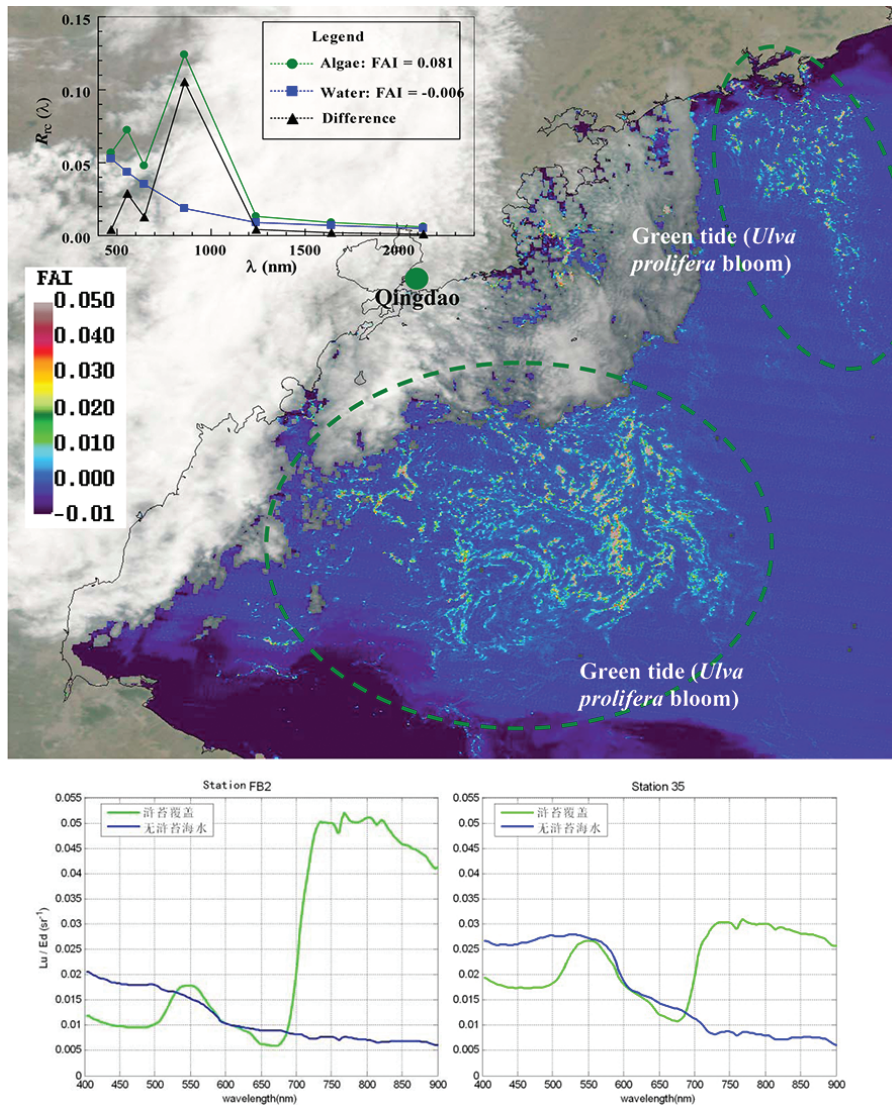


**Figure 3.3** Top: MODIS floating algae index (FAI) image on 29 June 2008 showing green tides (*Ulva prolifera* blooms) in the Yellow Sea near Qingdao, China. The image covers the area of 34.5°N - 37°N and 119°E - 122°E. Cloud and land masks are overlaid on the image. The reflectance spectra of an identified algae pixel and a water pixel are shown in the inset figure. Bottom: Reflectance spectra measured from macroalgae mats (green lines) and algae-free water (blue lines) in the same region, from two different stations.

green macroalgae, *U. prolifera*, as confirmed by concurrent management activities (>1000 vessels were utilized to clean the algae in this region between late June and early August 2008, with >1,000,000 tons of algae collected). Examination of the  $R_{rc,\lambda}$  spectral shapes of individual pixels from the slicks/patches show enhanced reflectance in the NIR, typical for surface vegetation. An example is shown in the

inset figure of Figure 3.3, where the spectral shape from the algae pixel is very similar to those obtained from *in situ* measurements from *U. prolifera* surface mats in the same region (Figure 3.3 bottom panels). Even though the *in situ* reflectance is defined differently (i.e., with units of  $\text{sr}^{-1}$ ) and MODIS  $R_{\text{rc},\lambda}$  is not corrected for aerosol scattering effects, they both show elevated reflectance in the NIR and in the green (555 nm).

Not every MODIS 250-m pixel is covered completely by the algae. Rather, the pixels may be mixed with algae and water. The linear design of FAI (Equation 3.2) makes the unmixing straightforward. Assuming  $\text{FAI} \leq 0.0$  for 0% algae coverage in a pixel and  $\text{FAI} \geq 0.02$  for 100% coverage in a pixel (these threshold values were determined by image gradient analysis and visual interpretation), algae coverage for FAI values between 0.0 and 0.02 can be determined using a linear interpolation. For the image shown in Figure 3.3, the total number of MODIS 250-m pixels containing the macroalgae was estimated to be 70,333, corresponding to an area of about 3600  $\text{km}^2$ . After linear unmixing, the coverage area of algae was estimated to be 1101  $\text{km}^2$ . The coverage area estimate, however, has some degree of uncertainty and requires field validation.

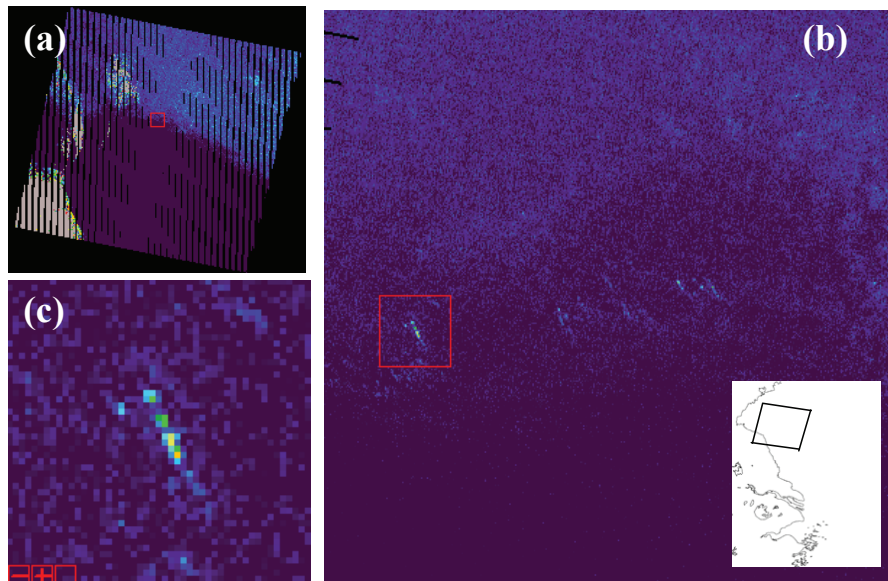


**Figure 3.4** (a) Landsat-7 ETM+ FAI image on 10 May 2008 covering the northern portion of Subei Bank, where the purple colour indicates high sediment concentrations. (b) A sub-scene of 512 x 512 pixels as outlined by the red box in (a). Inset figure shows the location of the Landsat image. (c) An enlarged portion of (b) showing the algae slick.

For the MODIS instrument sensitivity, we determined that the smallest size of the algae slick that MODIS FAI imagery could reveal was about 5 m, if the slick was at least 3 – 4 pixels in length (Hu et al., 2010). Smaller algae, especially during bloom initiation, could not be detected by MODIS, but could be detected by higher-

resolution instruments such as Landsat TM and ETM+. Figure 3.4 shows a sub-scene of a Landsat ETM+ FAI image collected on 10 May 2008 in the north of the Subei Bank. The small slicks of algae are impossible to find in the corresponding MODIS FAI image, but the spectral shapes show elevated reflectance in the NIR, indicating macroalgae blooms. Indeed, Landsat and MODIS were combined to reveal the temporal evolution of the 2008 bloom event, with the conclusion that the bloom started in near-shore waters of the shallow Subei Bank (Hu et al., 2010) where aquaculture of the seaweed *P. yezoensis* was practiced every year.

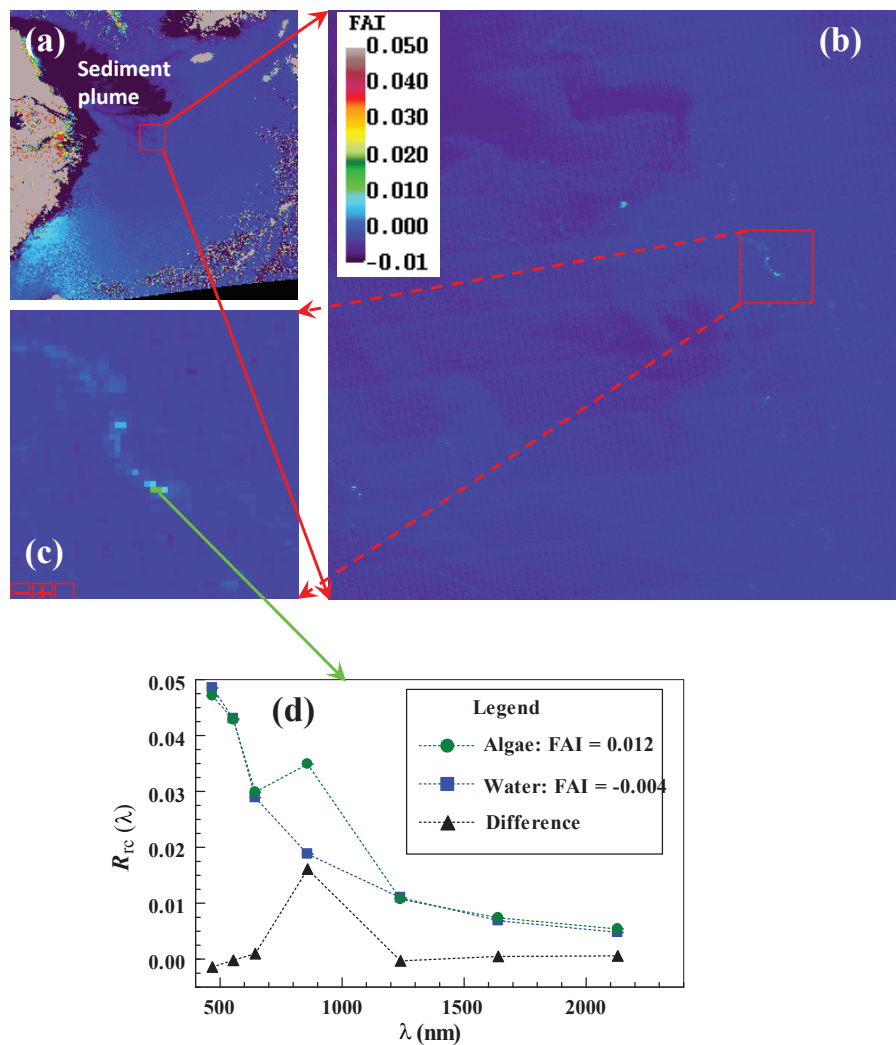


**Figure 3.5** (a) MODIS-Aqua 250-m resolution FAI image on 28 April 2009 covering the ECS. (b) A sub-scene of about 100 x 100 km east of the Changjiang River mouth. (c) An enlarged portion of (b) showing the algae slick. (d) The reflectance spectra of the identified algae pixel and nearby water pixel.

The retrospective analysis of satellite imagery showed the origin, size, distribu-

tion, and evolution of the 2008 bloom event as well as smaller blooms in previous years (Hu et al., 2010). For the purpose of monitoring, MODIS data were obtained and analyzed in near real-time since early 2009 to monitor the bloom conditions in both YS and ECS (Figure 3.2). The earliest MODIS FAI image where algae slicks can be identified, obtained on 28 April 2009 from the Aqua satellite, is shown in Figure 3.5. The MODIS image shows some slicks about 200 km east of the Changjiang River mouth in the downstream of a NW - SE sediment plume from the Subei Bank, indicating that the algae slicks originated from nearshore waters of the Subei Bank. This is the same place where the 2008 macroalgae bloom originated. Spectral shapes of the algae pixels show elevated reflectance in the NIR (Figure 3.5d), suggesting that this is some kind of floating vegetation. Considering the proximity to the coast and the same origin as for the 2008 bloom, it is very likely that the algae is the same type, i.e., *U. prolifera* from expanded seaweed aquaculture. Note that this analysis is based on MODIS data alone. Information derived from circulation models and environmental conditions (e.g., wind) provides additional evidence that these algae slicks can be *U. prolifera* (Hu et al., 2010).

### 3.4 Training

MODIS reflectance data collected on 19 May 2009 and 14 June 2000, and their corresponding RGB and FAI images for the ECS can be downloaded from the IOCCG website (<http://www.ioccg.org/handbook/He/>) for the demonstration on how to identify algae slicks and other features. Because of the synoptic coverage (often >10 degrees in both N-S and E-W directions) and medium resolution (250-m per pixel), the MODIS images are very large. Thus, commercial software packages (e.g., ENVI, ArcInfo, Erdas Imagine, or any other software that has basic image processing capabilities) are required to focus on a particular region. Here we use the software ENVI to demonstrate how to identify the algae slicks using the following visualization and analysis.

First, the RGB image is loaded into ENVI by using the "File -> Open Image File" function. Three display windows are shown (similar to Figures 3.6 a-c): scroll, image, and zoom. The scroll window shows the entire region at reduced resolution to serve as a browse image; the image window shows a portion of the image at full resolution (250-m); and the zoom image enlarges a smaller portion by 4 times. During the initial display in ENVI, the colours are stretched using histogram balancing over the entire image. The image window can be colour enhanced by a "Gaussian" or linear enhancement, using the menu of "Image -> Enhance".

Next, the FAI image is loaded into ENVI in the same way. The "Link Display" function is used to link the two images so that they can be cross examined. This way, any suspicious features identified on the FAI image can be easily determined if they are from clouds or land.

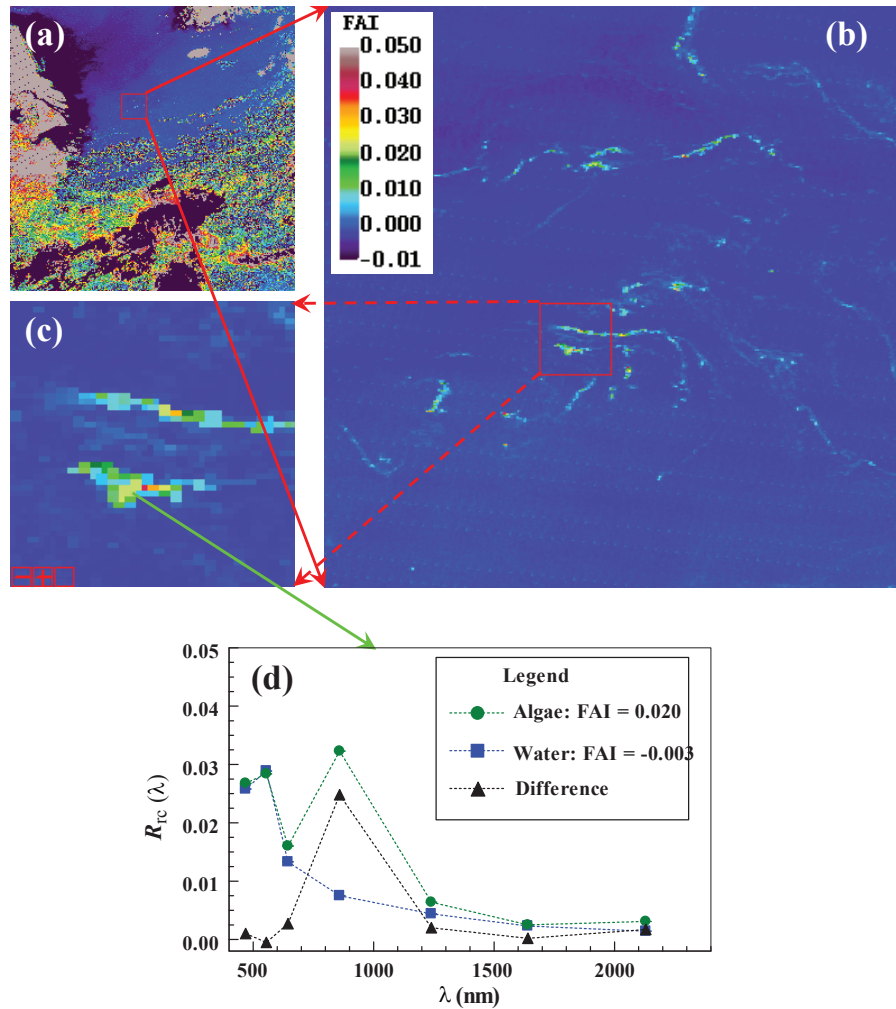


**Figure 3.6** (a) MODIS-Terra 250-m FAI image on 19 May 2009 covering the ECS. (b) A sub-scene of about 100 x 100 km east of the Changjiang River mouth is shown at 250-m resolution. (c) An enlarged portion of (b) showing the algae slick. (d) The reflectance spectra of the identified algae pixel and nearby water pixel.

Finally, the image window in the scroll image is moved to examine the entire image step by step. It is easy to find that clouds and land show high FAI values. In cloud-free waters, there are also some slicks associated with high FAI values, as shown in Figure 3.6b. The same steps are applied to display the MODIS FAI image from 14 June 2000 (Figure 3.7).

### 3.5 Questions

**Q1:** Are the high-FAI slicks in Figure 3.6b the green macroalgae *Ulva prolifera*?

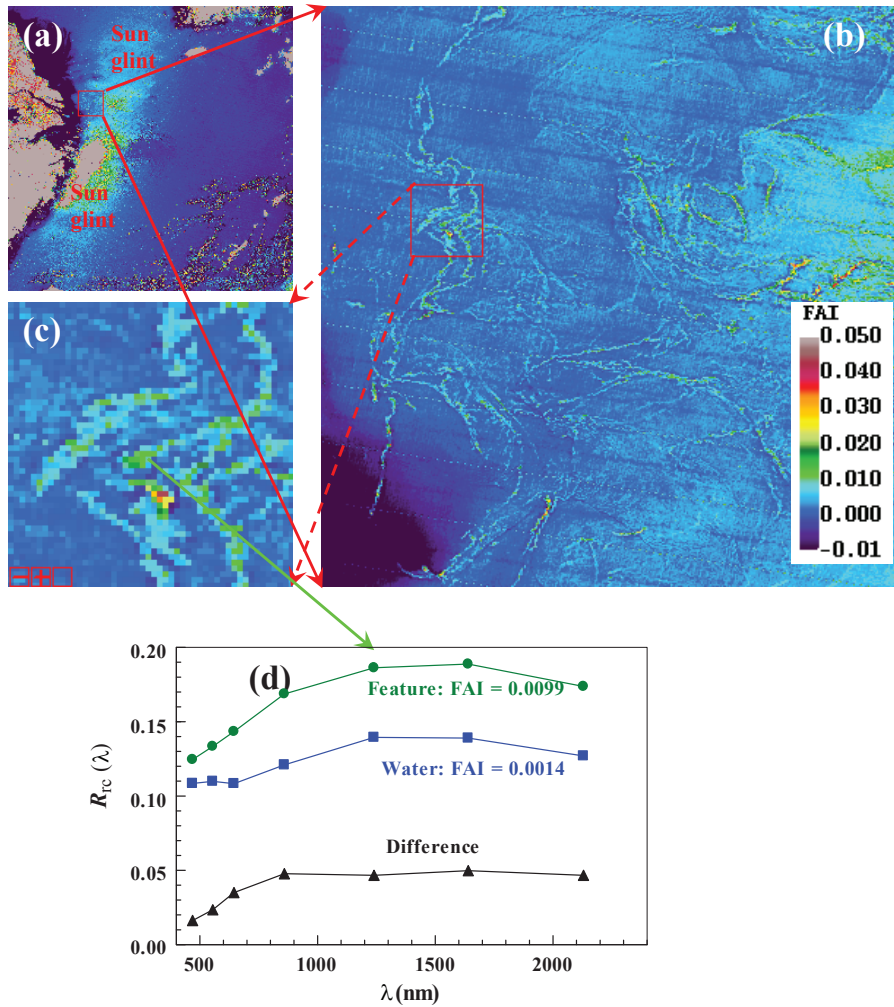


**Figure 3.7** (a) MODIS-Terra 250-m FAI image on 14 June 2000 covering the ECS. (b) A sub-scene of about 100 x 100 km east of the Changjiang River mouth is shown at 250-m resolution. (c) An enlarged portion of (b) showing some suspicious slicks. (d) The reflectance spectra of the suspicious feature and a nearby water pixel. Their difference spectrum is also shown.

**Q2:** Are the high-FAI slicks in Figure 3.7b the green macroalgae *Ulva prolifera*?

### 3.6 Answers

**A1:** Very likely. Once clouds and sun glint can be ruled out as the potential cause of the slicks, it is almost certain that they are some sort of surface vegetation. However, to add more confidence, reflectance spectra of the identified slicks and the nearby water can be examined. Similar to the case for Figure 3.5,  $R_{rc,\lambda}$  spectra extracted from pixels of the suspicious slicks show elevated reflectance in the NIR, where an

example is presented in Figure 3.6d. The data are extracted from the HDF data file for the locations (in image pixel line coordinates) of the slicks and nearby waters. The data extraction can be achieved through ENVI or simple computer programs. Although the high NIR reflectance is only an indication of surface vegetation and not necessarily the green macroalgae *Ulva prolifera*, the same arguments applied to Figure 3.5 can be used here to infer the algae type. In particular, the location is almost the same as three weeks ago (Figure 3.5) but the size is much larger, suggesting algae growth in this offshore region.

**A2:** Although the slicks appear to be floating algae, it is difficult to determine from the FAI image alone whether the suspicious features are freshwater slicks or whether they are due to water convergence, because the region is contaminated by significant sun glint (the extensive NE – SW high FAI band in Figure 3.7a).  $R_{rc,\lambda}$  spectra extracted from pixels of the suspicious features show elevated reflectance in all wavelengths (Figure 3.7d), and their difference from the nearby water spectra do not show distinctive peaks at 859 nm, but rather show flat spectra from 859 to 2130 nm. Therefore, it is unlikely that these high-FAI slicks are floating algae. Indeed, cloud-free and glint-free images from adjacent days do not show similar slicks in the same region, confirming this speculation. However, the origin of the slicks, whether from freshwater or from water convergence, is still unclear.

### 3.7 Discussion and Summary

Visualization of suspicious slicks in MODIS 250-m imagery and Landsat 30-m imagery is relatively easy. Indeed, an interactive colour stretch applied in ENVI to the single 859-nm band, as referenced against the corresponding RGB image (to detect clouds), can also reveal the same algae slicks. However, this is labour intensive due to the interactive colour stretch. First, it is difficult to establish a consistent time-series because the single band still contains variable aerosol contributions. Likewise, a simple Normalized Difference Vegetation Index (NDVI) based on the  $R_{rc,\lambda}$  data although partially removes the influence of aerosols and varying solar/viewing geometry, the residual uncertainties due to these spatially and temporarily varying properties can lead to highly variable NDVI values for the same targets. In contrast, the baseline subtraction method used in FAI serves as a simple but effective atmospheric correction, where FAI values from the same algae and water pixels remain relatively stable under varying conditions (Hu, 2009). The linear design also makes unmixing of mixed algae-water pixels straightforward. Thus, FAI is preferred to detect and quantify macroalgae blooms.

In this exercise, one must be cautious of the interpretation of suspicious slicks identified visually, especially in sun glint regions. Analysis of the spectral shape of the suspicious features and visual examination of images collected from adjacent days can add more confidence. The most difficult scenario is cloud masking. Clouds

are visually determined through examining RGB images. The reason for this is that although several cloud masking algorithms have been proposed and used to process MODIS data, in the YS and ECS where aerosols can sometimes lead to  $R_{rc,NIR}$  and  $R_{rc,SWIR}$  significantly higher than the pre-defined threshold reflectance for clouds, the cloud masks may reduce data coverage. Relaxing such threshold values, on the other hand, may lead to cloud pixels undetected. Developing a reliable cloud-detection algorithm specifically for this region should be the next step in this effort.

Synthetic Aperture Radar (SAR) can penetrate clouds. Limited SAR data suggest that green tide macroalgae blooms appear as bright slicks in C-band images but dark slicks in L-band images. SAR data therefore serve as an additional data source for green tide monitoring, although they have less spatial/temporal coverage and are not free. Likewise, data from other medium-resolution instruments (e.g., MERSI is equipped with similar 250-m bands as MODIS) and high-resolution instruments (e.g., HJ-1 is equipped with similar 30-m bands as Landsat TM and ETM+) can also provide complementary information to enhance our capability in green tide monitoring.

This work is focused on the green tide detection method. Understanding of the green tide characteristics (occurrence frequency, initiation, evolution, physiology, ecology, etc.), on the other hand, requires coordinated inter-disciplinary efforts in studying phytoplankton ecology, ocean circulation, and environmental forcing for algae growth (nutrient availability, temperature, etc.). These are beyond the scope of the current demonstration, but can be found in the refereed literature (e.g., Taylor et al., 2001; Merceron et al., 2007; Yuan et al., 2008). Our monitoring efforts, however, do include routine generation and analysis of ocean SST, wind, and chlorophyll-*a* concentrations. These properties provide ancillary information to understand the environmental conditions of the observed macroalgae blooms in the YS and ECS.

In summary, data from a suite of satellite instruments, from the medium-resolution MODIS and MERSI to the high-resolution Landsat and HJ as well as the cloud-free SAR, are effective in detecting blooms of the green macroalgae *Ulva prolifera* (green tides) in the YS and ECS under various conditions. Combined with other ancillary information, these data form the basis to establish a semi-operational monitoring system, currently being developed and operated jointly at the Ocean Remote Sensing Institute of the Ocean University of China (<http://www.station.orsi.ouc.edu.cn:8080/algae/>) and the Optical Oceanography Lab of the University of South Florida. This case study presents an example of how satellite imagery can be used to help understand and manage our coastal environments. Similar systems may be established for other coastal regions where green tides also occur.

### 3.7.1 Acknowledgements

This work was supported by the U.S. NASA (NNX09AE17G) and NOAA (NA06NES4400004), by a special project of the Qingdao government (NO.09-2-5-4-HY), and by the EU

FP6 DRAGONESS Project (No. SSA5.CT.2006- 030902) and the ESA-MOST Dragon Programme Ocean Project (ID2566). We thank the US NASA/GSFC and USGS for providing MODIS and Landsat data.

### 3.8 References

- Blomster J, Back S, Fewer DP, Kiirikki M, Lehvo A, Maggs CA, Stanhope MJ (2002) Novel morphology in *Enteromorpha* (Ulvophyceae) forming green tides. *Am J Bot* 89:1756-1763
- Fletcher, RL (1996) The occurrence of "green tides": a review In: Schramm W, Nienhuis PH ( eds) *Marine benthic Vegetation: recent changes and the effects of eutrophication*. Springer, Berlin, Germany, p 7-43
- Hayden HS, Blomster J, Maggs CA, Silva PC, Stanhope MJ, Waaland JR (2003) Linnaeus was right all along: *Ulva* and *Enteromorpha* are not distinct genera. *European J Phycol* 38:277-294
- Hu C, He M-X (2008) Origin and offshore extent of floating algae in Olympic sailing area. *EOS AGU Trans* 89(33): 302-303
- Hu C (2009) A novel ocean color index to detect floating algae in the global oceans. *Remote Sens Environ* 113: 2118-2129
- Hu C, Li D, Chen C, Ge J, Muller-Karger FE, Liu J, Yu F, He M-X (2010) On the recurrent *Ulva prolifera* blooms in the Yellow Sea and East China Sea. *J Geophys Res* 115: C04002, doi:10.1029/2009JC005511
- Jiang X, Liu J, Zou B, Wang Q, Zeng T, Guo M, Zhu H, Zou Y, Tang J (2009) The satellite remote sensing system used in emergency response monitoring for *Enteromorpha prolifera* disaster and its application. *Acta Oceanol Sin* 31: 52-64
- Li D, He S, Yang Q, Lin J, Yu F, He M-X, Hu C (2008) Origin and distribution characteristics of *Enteromorpha prolifera* in sea waters off Qingdao, China. *Environ Protection* 402(8B): 45-46 (in Chinese)
- Liang Z, Lin X, Ma M, Zhang J, Yan X, Liu T (2008) A preliminary study of the *Enteromorpha prolifera* drift gathering causing the green tide phenomenon. *Periodical of Ocean University of China* 38(4): 601-604 (in Chinese, with English abstract)
- Liu D, Keesing JK, Xing Q, Shi P (2009) World's largest macroalgal bloom caused by expansion of seaweed aquaculture in China. *Mar Sci Bulletin* doi:101016/j.marpolbul200901013
- Lü X, Qiao F (2008) Distribution of sunken macroalgae against the background of tidal circulation in the coastal waters of Qingdao, China, in summer 2008. *Geophys Res Lett* 35: L23614, doi:101029/2008GL036084
- Merceron M, Antoine V, Auby I, Morand P (2007) *In situ* growth potential of the subtidal part of green tide forming *Ulva* spp. stocks. *Sci Tot Environ* 384: 293-305
- Nelson TA, Nelson AV, Tjoelker M (2003) Seasonal and spatial patterns of "Green tides" (Ulvoid algal blooms) and related water quality parameters in the coastal waters of Washington state, USA. *Botanica Marina* 46: 263-275
- Qiao F, Ma D, Zhu M, Li MR, Zang J, Yu H (2008) Characteristics and scientific response of the 2008 *Enteromorpha prolifera* bloom in the Yellow Sea. *Adv Mar Sci* 26(3): 409-410 (in Chinese)
- Sun S, Wang F, Li C, Qin S, Zhou M, Ding L et al (2008) Emerging challenges: Massive green algae blooms in the Yellow Sea. *Nature Precedings*, hdl:10101/npre200822661
- Taylor R, Fletcher RL, Raven JA (2001) Preliminary studies on the growth of selected green-tide algae in laboratory culture: effects of irradiance, temperature, salinity and nutrients on growth rate. *Botanica Marina* 44: 327-336
- Wang J, Yan B, Lin A, Hu J, Shen S (2007) Ecological factor research on the growth and induction of spores release in *Enteromorpha Prolifera* (Chlorophyta). *Mar Sci Bull* 26 (2): 60-65
- Yuan D, Zhu J, Li C, Hu D (2008) Cross-shelf circulation in the Yellow and East China Seas indicated by MODIS satellite observations. *J Marine Sys* 70:134-149
- Zhou, MJ, Zhu MY (2006) Progress of the Project "Ecology and Oceanography of Harmful Algal Blooms in China". *Adv Earth Sci* 21: 673-679

## Case Study 4

# Ocean-Atmosphere Exchanges of Persistent Organic Pollutants on the Atlantic Ocean

Elena Jurado\*<sup>1</sup> Rafael Simó<sup>2</sup> and Jordi Dachs<sup>3</sup>

---

## 4.1 Background Information

Persistent Organic Pollutants (POPs), also termed by Persistent Bioaccumulable Toxic chemicals (PBTs), are bioaccumulable compounds of prolonged environmental persistence and are susceptible to long-range atmospheric transport. They have been detected in all the environmental compartments, even in remote areas such as the open ocean and the polar regions, where POPs have never been manufactured or used. Furthermore, once they appear in the environment they do not degrade. Instead, they recycle and partition between the major environmental media, and are an environmental concern since their toxic effects do not disappear, and their control is difficult. Their physicochemical properties, such as the high lipid/organic solubility, result in their bioaccumulation in lipid-rich tissues and 'bio-magnification' through the food chain. Even at low concentrations they are toxic to humans and wildlife, with suspected effects including carcinogenesis, immune dysfunction, neurobiological disorders and reproductive and endocrine disruption.

POPs comprise man-made organo-halogenated compounds (e.g. pesticide POPs such as DDT, industrially produced POPs such as polychlorinated biphenyls (PCBs) or POPs that are unintended byproducts such as polychlorinated dibenzo-p-dioxins and polychlorinated dibenzofurans (PCDD/Fs) and other chemicals that can, in part, be biogenic such as polycyclic aromatic hydrocarbons (PAHs). In particular, man-made POPs were initially produced and used in the 1940s. During the 1960s and 1970s, the use of certain POPs in industry or as pesticides increased dramatically. The first political regulations for the production and use of POPs dates from the late 1970s. Since then, a number of politically-binding regulations have entered into force to reduce or eliminate their emissions: the Convention on Long-Range Transboundary

---

<sup>1</sup>Institute for Marine and Atmospheric Research Utrecht (IMAU), Utrecht University, Princetonplein 5, 3584 CC Utrecht, The Netherlands. \*Email address: [e.juradocojo@uu.nl](mailto:e.juradocojo@uu.nl)

<sup>2</sup>Marine Sciences Institute, CMIMA-CSIC, Passeig Marítim de la Barceloneta 37-49, Barcelona 08003, Spain

<sup>3</sup>Department of Environmental Chemistry, IIQAB-CSIC, Jordi Girona 18-26, Barcelona 08034, Spain

Air Pollution on POPs, the Stockholm Convention on POPs, and, on a European Level, the Water Framework Directive.

Despite regulations, they still cycle between the different environmental compartments and there are non-controlled sources as well. For example, high concentrations of PCBs have been reported in arctic wildlife and breast milk. This is of special concern, not only because those contaminants were already banned in the late 1970s, but also because of the distance from the source where those pollutants were produced. There is thus a global occurrence of these contaminants and an urgent need to control their levels in the environment. Sampling of POPs, however, is time-consuming and expensive compared to many other contaminants. In this context, global models are a very valuable tool to predict and understand the distribution of POPs. Satellite data, with their global synoptic coverage, can provide environmental input data to global POPs models, as we will see later.

To understand how we can use remote sensing data to model the global distribution of POPs, we provide here a short explanation of the partitioning of POPs in the different environmental media. Because both atmosphere and oceans are critical compartments in the global distribution and cycling of POPs, the analysis will focus in the ocean-atmosphere exchanges of POPs. Atmospheric emissions and subsequent long-range transport have proven to provide a mechanism to distribute POPs widely through the global environment. In fact, atmospheric deposition of POPs may be the major process by which they impact remote oceans and other pristine environments. On the other hand, the oceans are also critical in the global cycling of those pollutants; their large volumes imply that they may represent an important inventory of POPs.

Figure 4.1 shows a diagram of the major processes affecting the transfer of POPs between the atmosphere and the ocean. In the atmosphere, POPs partition between the gas and aerosol phases and they may then be removed by three processes: dry deposition of aerosol-bound pollutants, diffusive gas exchange between the atmosphere and the ocean, and scavenging by rain (either from gas or particulate phases), the latter termed wet deposition. In the water column, POPs can be found either dissolved or sorbed to particulate organic matter. Dissolved POPs can revolatilize back to the atmosphere or they can stay in the water column and become bioavailable, i.e. they can be incorporated into the biota by passive diffusion. POPs sorbed to particulate organic matter cannot revolatilize back to the atmosphere, but can be deposited by gravity or sinking. In both particulate and dissolved phases, they are subject to turbulent mixing throughout the water column. Finally, in each medium, POPs are subject to degrade, but those fluxes are generally considered negligible. By means of simplification, no lateral advection of contaminants is considered, which is an assumption generally accepted in the open ocean, where contaminants enter primarily via atmospheric deposition.

The processes affecting the transfers of POPs between the atmosphere and the ocean are evaluated quantitatively by means of fluxes ( $F$  [ $\text{ng m}^{-2} \text{s}^{-1}$ ]), whose

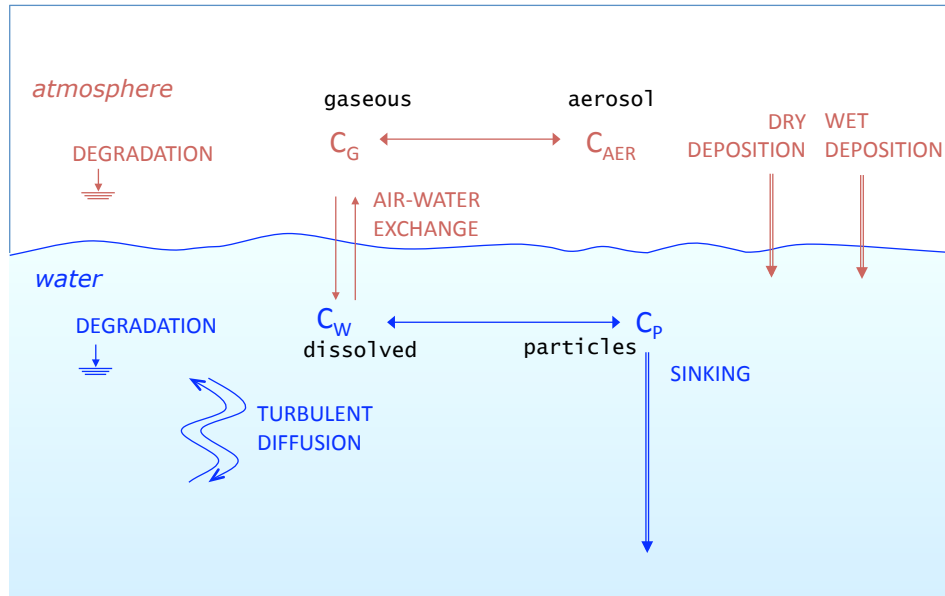


**Figure 4.1** Major processes affecting the transfer of POPs between the atmosphere and the ocean. The amount of contaminant in an environmental media is denoted by its concentration,  $C$ . Fluxes are marked in capital letters.

simplified mathematical formulation is presented next. Advective processes, where contaminants are transported by means of directed motion, such as dry deposition, wet deposition and sinking, are governed by:

$$F_{\text{advective}} = vC \quad (4.1)$$

where  $v$  [ $\text{m s}^{-1}$ ] is the advective velocity and  $C$  [ $\text{ng m}^{-3}$ ] is the concentration of the chemical.

Diffusive processes, such as air-water exchange or turbulent flux, where contaminants are transported by random motion, are governed by Fick's First Law:

$$F_{\text{diffusive}} = -D \frac{\partial C}{\partial x} \quad (4.2)$$

where  $D$  [ $\text{m}^2 \text{s}^{-1}$ ] is the molecular diffusivity and  $\partial C / \partial x$  is the gradient of concentrations in the  $x$  direction, along which the change of concentration of the contaminant occurs. The mathematical formulation of diffusion becomes more complex if the transport occurs between two media, as would be the case of the diffusive transport across the air-water interface. The resultant flux is then a combination of molecular and turbulent diffusion.

The last type of process, the degradation process, produces a loss in the system, and is characterized by a first order decay rate,  $k_{\text{degr}}$  [ $\text{s}^{-1}$ ].

$$F_{\text{transformation}} = h k_{\text{degr}} C \quad (4.3)$$

where  $h$  [m] is the height of the volume where degradation is acting.

It is important to note that the magnitude of the contaminant fluxes is a function of the measured concentration, physicochemical parameters, and environmental conditions. The environmental conditions do not only determine the parameters  $v$ ,  $D$  and  $k_{deg}$ , from Equations 4.1 to 4.3, they also influence the ratio of contaminant concentrations between two different phases of equilibrium. This ratio is termed the *equilibrium partition coefficient* and it is essential in the modelling of POPs. For example, the gas-particle partition coefficient  $K_p$  will allow us to calculate the concentration of a certain POP in its aerosol phase, knowing its concentration in the gaseous phase and assuming equilibrium conditions, which is a common assumption since these compounds are continuously seeking to equilibrate between the different reservoirs.

This case-study shows an example of the application of satellite data to estimate the spatial and temporal distribution of atmospheric-ocean fluxes of POPs in the Atlantic Ocean. It has been developed in detail in various publications (Dachs et al. 2002; Jurado et al. 2004; 2005; 2008) and it is based on the previous work of Dachs et al. (2002) and Simó and Dachs (2002). Essentially, satellite retrieved parameters and air measured concentrations (gaseous and aerosol phases) in two north-south campaigns across the Atlantic (Lohmann et al. 2001; Jaward et al. 2004) have been coupled in a 0D (i.e. zero- dimensional), spatially resolved, box model. A 0D model means, for example, that the vertical variation of the fluxes is not accounted for. A box model means that the system has been subdivided into well-mixed and interconnected compartments. The model was applied using monthly means of satellite data and assuming that measured atmospheric concentrations are constant in time.

Satellite-based environmental data correspond to monthly climatological means (average 2001 - 2003) of *Level 3* data with global coverage and resolutions of  $1^\circ \times 1^\circ$  or  $0.5^\circ \times 0.5^\circ$ , presented in greater detail below. Level 3 refers to data that is designed for the end user, which has been calibrated with *in situ* observations and data assimilation techniques.

## 4.2 Satellite Data Used

### 4.2.1 Wind speed distributions at 10m above the surface of the sea

The surface wind speed was used in this study ( $u_{10}$ ,  $m\ s^{-1}$ ). Values were obtained from the NOAA Special Sensor Microwave/Imager (SSM/I) at a resolution of  $1^\circ \times 1^\circ$  and an accuracy of  $\pm 2\ m\ s^{-1}$  (<http://1wf.ncdc.noaa.gov/oa/satellite/ssmi/ssmiwind.html>).

### 4.2.2 Aerosol parameters over the oceans

Aerosol values at a resolution of  $1^\circ \times 1^\circ$  were obtained from the Moderate-Resolution Imaging Spectrometer Instrument (MODIS, <http://modis.gsfc.nasa.gov/>) on board the Terra satellite, part of NASA's Earth Observing System (EOS). In particular, we used the effective radius ( $r_{\text{eff}}$ ,  $\mu\text{m}$ ) and its standard deviation (which provides information about the size distribution of aerosols), the aerosol optical depth (AOD) and its standard deviation (related to the aerosol density in the atmosphere), and the fraction of optical depth corresponding to submicron aerosols ( $\eta$ , [0 1]). The approximate accuracy is  $\pm 0.1\mu\text{m}$  for  $r_{\text{eff}}$ ,  $\pm 0.03 \cdot \text{AOD}$  (or  $\pm 0.05 \cdot \text{AOD}$  in dust regimes), and 25% for  $\eta$ . MODIS aerosol retrieved measurements refer to values integrated over the air column and they refer to the size range detected by the instrument (aerosol diameters from 0.1 to 20  $\mu\text{m}$ ). This information is important to derive aerosol dry deposition velocities from satellite data (Jurado et al. 2004).

It should be pointed that deriving aerosol sizes or concentrations from remote sensing measurements has a higher uncertainty than other variables such as wind speed, SST and  $p_0$  used in this study. Until recently, MODIS was the only sensor that gave information about aerosol sizes. This area of research is currently undergoing rapid development, and several satellite-based light imaging radars (lidars) are being launched (e.g. CALIPSO from NASA), providing information about the vertical structure of aerosol plumes, which is not available from MODIS data.

### 4.2.3 Precipitation data

Values of monthly rainfall rates ( $p_0$ , [ $\text{mm month}^{-1}$ ]) and the fractional occurrence of precipitation ( $f$ , [0-1]) were obtained from SSM/I NOAA at a resolution of  $1^\circ \times 1^\circ$  (<http://www.ncdc.noaa.gov/oa/satellite/ssmi/ssmiprecip.html>). Determination of rainfall by passive microwave sensors, such as SSM/I, may be underestimated during low rainfall periods and overestimated during wet periods, leading to some inaccuracies in the tropics. However, rainfall retrieval over the ocean from SSM/I represents the best compromise between estimation accuracy and spatial data coverage. Uncertainty is about 15 to 30% when compared to rain gauge data sets.

A novelty of the use of precipitation data in wet deposition modelling of POPs has been the consideration of the influence of the frequency of rain ( $f$ ). Hence, the instantaneous flux of contaminants scavenged by rain may be quite substantial in a month with a low frequency of rain. The methodology developed is further described in Jurado et al. (2005).

### 4.2.4 Sea Surface Temperature (SST, [K])

Values were obtained from the Along Track Scanning Radiometer (ATSR) on board the European Space Agency ERS-2 satellite (<http://www.atsr.rl.ac.uk/>). SST images

consist of monthly averaged data with a resolution of  $0.5^\circ \times 0.5^\circ$  and an accuracy of  $\pm 0.3K$ .

#### 4.2.5 Chlorophyll-*a* concentration (chl-*a*, $\text{mg m}^{-3}$ )

This was estimated from reflectance signals obtained from NASA's Sea-Viewing Wide Field-of-view Sensor (SeaWiFS) ([http://www.csc.noaa.gov/crs/rs\\_apps/sensors/seawifs.htm](http://www.csc.noaa.gov/crs/rs_apps/sensors/seawifs.htm)). The resolution is  $1^\circ \times 1^\circ$  and accuracies are around the 15%. This data allows the estimation of the phytoplankton biomass distribution in the surface mixed layer.

### 4.3 Demonstration Section

In this section we present the values of dry deposition flux, latitudinally-averaged for the Atlantic, together with satellite global maps of data that have a potential effect in the magnitude of the flux. Visually-based interrelations between this flux and that pertaining to the satellite data are explained, so that one can acquire the skills required to use the satellite images to understand better the latitudinally-averaged fluxes of POPs.

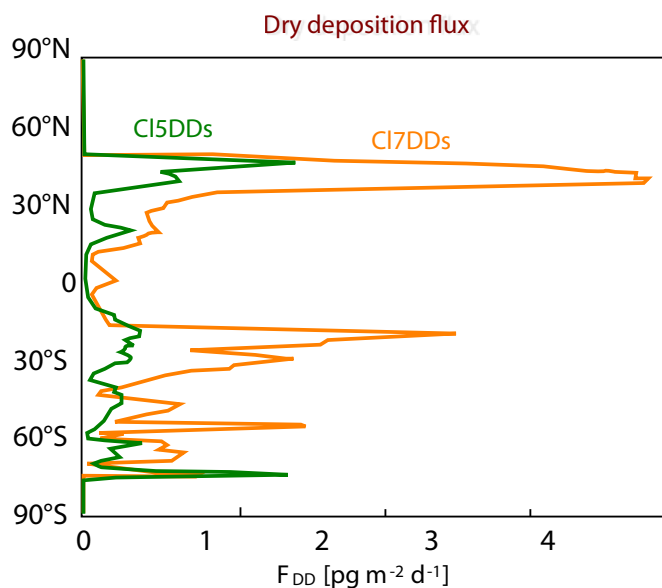


**Figure 4.2** Averaged latitudinal profile of the dry aerosol deposition fluxes for Cl5DDs and Cl7DDs over the Atlantic Ocean, for the period October-December 1998.

As a reminder, the dry aerosol deposition flux is the deposition of aerosol-bound contaminants in the absence of rain. Figure 4.2 depicts an example of a latitudinally-averaged profile of dry deposition flux over the Atlantic for two

reference compounds, the penta-dibenzo-p-dioxin (Cl5DDs) and the hepta-dibenzo-p-dioxin (Cl7DDs). The flux has been estimated using the methodology presented in the previous section, but developed in detail in Jurado et al. (2004). An example of measured air concentration data is depicted in Figure 4.3.

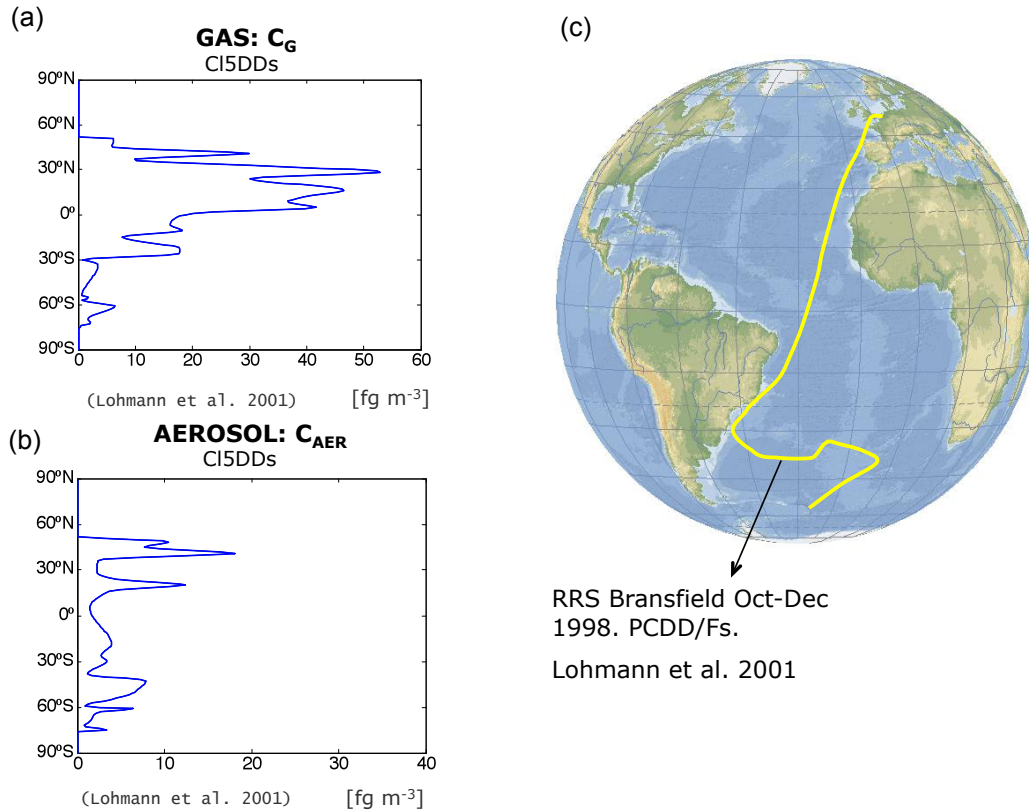


**Figure 4.3** Latitudinal profiles of Cl5DDs measured during a north-south Atlantic cruise: (a) gas and (b) aerosol sorbed profiles. Figure (c) depicts the cruise track.

For the interpretation of Figure 4.2 we provide the following satellite images: sea surface temperature (SST) (Figure 4.4), indicative of the temperature of the air close to the water surface, the effective radius ( $r_{\text{eff}}$ ) (Figure 4.5), defined as the weighted integral of the volume-surface ratio and indicative of the size of the aerosol, the aerosol mass concentration derived from the aerosol optical depth (Figure 4.6) (Gasso and Hegg 2003), and the wind speed at a height of 10 m ( $u_{10}$ ) (Figure 4.7).

As a first step to better understand the way that the dry aerosol deposition fluxes are connected to the environmental data provided in Figures 4.4 to 4.7, it is important to take into account the exact parameterization of this flux:

$$F_{\text{DD}} = V_{\text{D}}C_{\text{AER}} \quad (4.4)$$

where  $F_{\text{DD}}$  [ $\text{ng m}^{-2} \text{s}^{-1}$ ] is the dry aerosol deposition flux,  $v_{\text{D}}$  [ $\text{m s}^{-1}$ ] denotes the

aerosol overall dry deposition velocity and  $C_{AER}$  [ $\text{ng m}^{-3}$ ] is the POP aerosol-phase

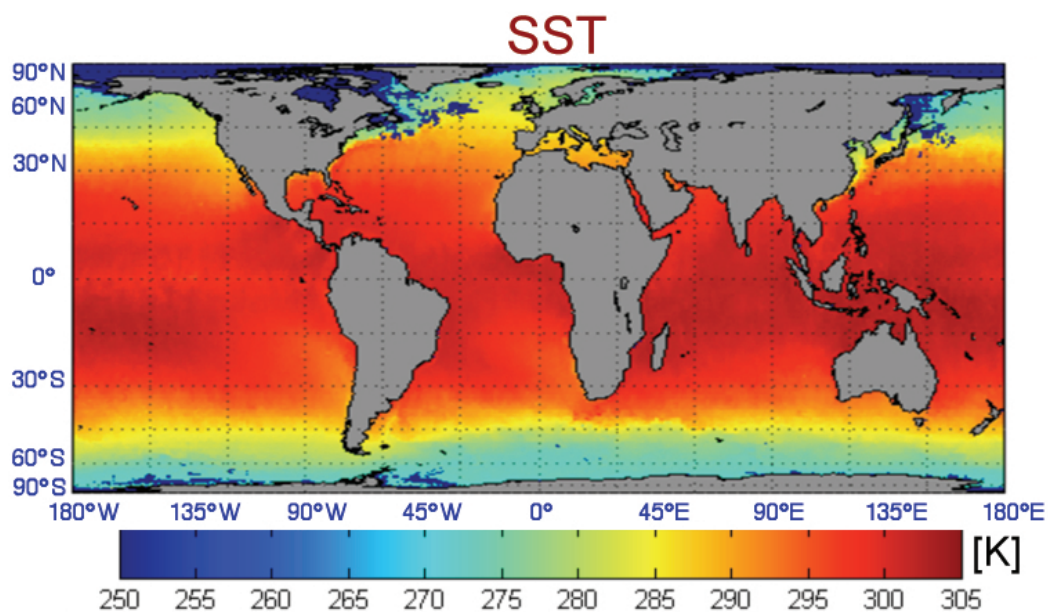


**Figure 4.4** Global distribution of Sea Surface Temperature (SST) in January (climatological monthly mean of 1998 - 2000).

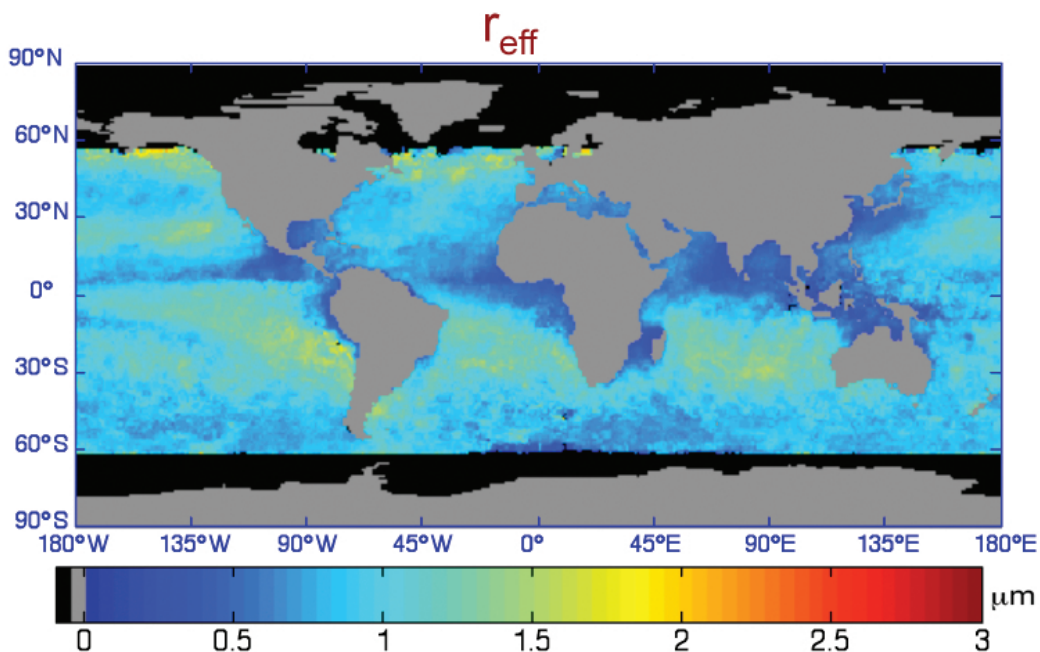


**Figure 4.5** Global distribution of effective radius ( $r_{eff}$ ) over the oceans in November (climatological monthly mean of 1998 - 2000).

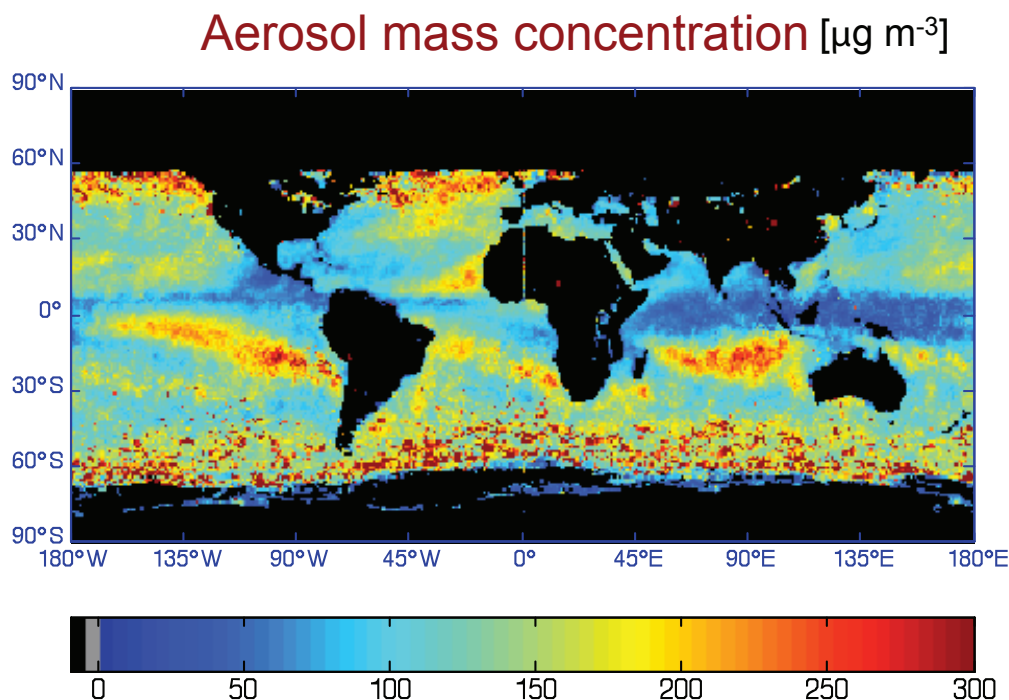


**Figure 4.6** Global distribution of the aerosol mass concentration over the oceans in November (climatological monthly mean of 1998 – 2000). Derived from MODIS Aerosol Optical depth parameter, and the algorithm developed in Gasso and Hegg (2003).

concentration.

From Equation 4.4 one should note that the dry aerosol deposition flux is directly proportional to the POP-aerosol-phase. Indeed, major dry deposition fluxes will be found in regions with major amounts of contaminants in the aerosol phase. The tendency to be in the aerosol-phase instead of the gas-phase is highly dependent on the air temperature, so that a lower air temperature will cause a higher partition to the aerosol phase. A map of SST, representative of the temperature of the air above the ocean surface, provides information of the regions over the oceans with a higher proportion of contaminants in the aerosol phase i.e. the temperate regions at higher latitudes.

The sea surface temperature (Figure 4.4) cannot be the only variable affecting the latitudinal trend in the fluxes from Figure 4.2, because it follows a smooth increase towards higher latitudes, while the fluxes depict an important variability. Other environmental variables, with a higher patchiness, should affect the magnitude of the fluxes. We envisage that the effective radius (Figure 4.5), aerosol mass concentration (Figure 4.6) or the wind speed (Figure 4.7) could contribute because their global distribution presents a higher variability than the SST.

How do Figures 4.5 to 4.7 combine to explain the fluxes in dry deposition of

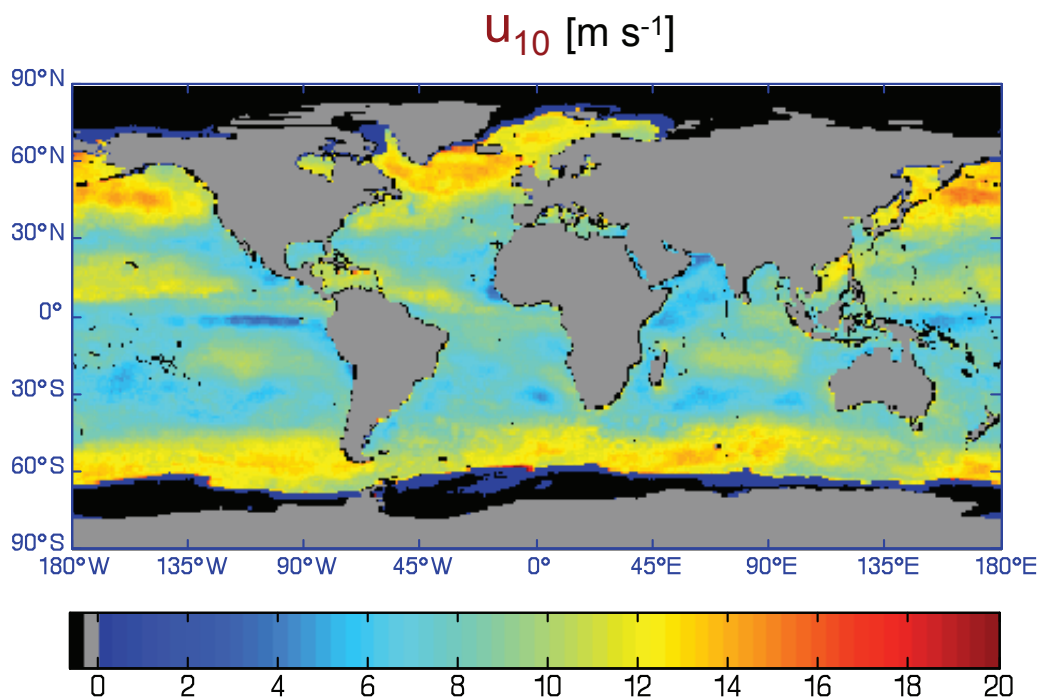


**Figure 4.7** Global distribution of the wind speed ( $u_{10}$ ) over the oceans in November (climatological monthly mean of 1998 - 2000).

POPs? The answer is found in the next variable, not yet assessed in equation 4.4, the overall dry deposition flux  $v_D$ . The  $v_D$  is greatly influenced by the aerosol size, by the atmospheric turbulent diffusion and by the atmospheric growth of particles at a high humidity. In particular,  $v_D$  will increase with the particle diameter and the wind speed for diameters  $>0.1 \mu\text{m}$ , governed by gravitational settling. Also, a high concentration of aerosol in the atmosphere will increase the dry deposition velocity. Knowing this information, it is possible to relate the large increase in the fluxes around  $15^\circ\text{S}$  to an increase of the effective radius, indicative of the size of aerosol particles, or the aerosol mass concentration in the Atlantic around this latitude. Furthermore, we can relate the peaks in the dry deposition fluxes around  $60^\circ\text{S}$  to strong winds in the Southern Ocean.

We end this section by explaining the differences in the fluxes of the two depicted contaminants: C15DDs and C17DDs. This is an example of how physico-chemical properties of the chemical compounds affect the fluxes. We see that the relative increase of dry deposition fluxes of the C17DFs in higher latitudes is greater than for C15DFs. This is because C17DFs sorb stronger to the organic matter of the aerosol, causing a major relative presence of those compounds in the aerosol phase. As a general rule, compounds with higher molecular weight will have less solubility in water, a higher affinity to organic matter and a lower vapour pressure.

## 4.4 Training and Questions

**Q 1:** Do you see any links between the flux of wet deposition (Figure 4.8), latitudinally-averaged for the Atlantic, and the satellite retrieved precipitation rate (Figure 4.9), referred to for the same climatological month of November? How are the data of sea surface temperature (Figure 4.4) useful to determine the wet deposition flux?

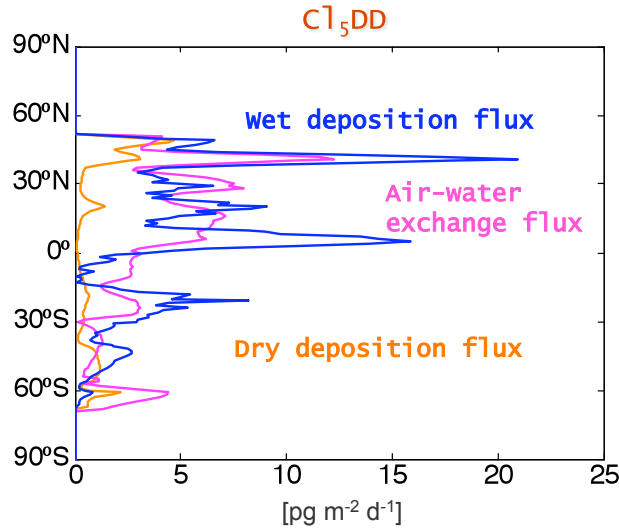


**Figure 4.8** Averaged latitudinal profiles of the atmospheric depositional fluxes for the Atlantic Ocean for Cl5DDs.

To answer this question it is important to take into account the parameterization of the wet deposition flux. The removal of semivolatile compounds by rain results from the scavenging both of gaseous dissolved compounds and particle-bound compounds. A common assumption is that the total wet deposition flux ( $F_{WD}$  [ $\text{ng m}^{-2} \text{s}^{-1}$ ]) is the product of the total (dissolved and particulate) concentration of contaminants in the rain ( $C_R$  [ $\text{ng m}^{-3}$ ]) and the precipitation rate ( $p_0$  [ $\text{m s}^{-1}$ ]). Furthermore, since  $C_R$  is generally unknown, it is commonly expressed in terms of the concentration of contaminant in the aerosol ( $C_{AER}$  [ $\text{ng m}^{-3}$ ]) and the gaseous phases ( $C_G$  [ $\text{ng m}^{-3}$ ]):

$$\begin{aligned}
 F_{WD} &= p_0 C_R = F_{WD\_Gaseous} + F_{WD\_Particulate} \\
 F_{WD\_Gaseous} &\cong \frac{C_G p_0 H}{RT} \\
 F_{WD\_Particulate} &\cong C_{AER} p_0 2.10^5
 \end{aligned}
 \tag{4.5}$$

where  $R$  is the ideal gas constant equal to  $8.13 \text{ Pa m}^3/\text{K mol}$ , and  $H$  is the Henry's law constant [ $\text{Pa m}^3/\text{mol}$ ], defined as the ratio between the compound's saturated liquid vapour pressure and its solubility in water, and dependent on physicochemical properties and environmental data.

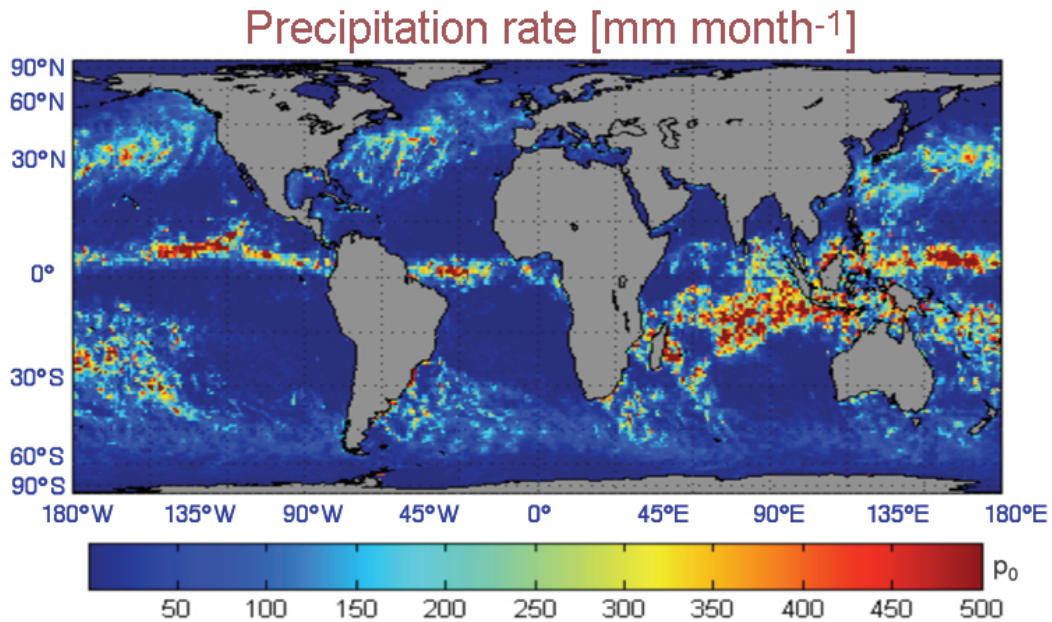


**Figure 4.9** Global distribution of the precipitation rate ( $p_0$ ) over the oceans in November (climatological monthly mean of 1998 - 2000).

**Q 2:** Which are the main satellite images, already displayed in this case-study, that potentially affect the flux of air-water exchange? Also consider the global distribution of chlorophyll-*a* depicted in Figure 4.10.

Again, to answer this question, it is important to first examine the parameterization of this flux. The flux of gaseous contaminants between the atmosphere and the oceans is driven by a concentration difference and by the transport due to molecular and turbulent motion. This flux combines turbulent and molecular diffusion since it occurs through an interface, thus the parameterization is not straightforward. It is based in the classical two-layer stagnant boundary layer model, where it is assumed that a well-mixed atmosphere and a well-mixed surface ocean are separated by a stagnant film through which gas transport is controlled by molecular diffusion. The resulting net air-water exchange flux ( $F_{AW}$  [ $\text{ng m}^{-2} \text{s}^{-1}$ ]) is a function of a term with velocity units (the air-water mass transfer coefficient  $k_{AW}$ , [ $\text{m s}^{-1}$ ]), the POP dissolved concentration in the water ( $C_W^{\text{dis}}$  [ $\text{ng m}^{-3}$ ]) and the corresponding concentration in the gaseous phase in equilibrium ( $C_G RT/H$ ). This flux is, in fact, the net difference of two processes acting in parallel: absorption of gaseous POPs from the atmosphere to the water ( $F_{AW\_abs}$ ) and the volatilization of POPs from the water to the atmosphere ( $F_{AW\_vol}$ ).

$$F_{AW} = F_{AW\_abs} - F_{AW\_vol} = k_{AW} \left( \frac{C_G RT}{H} - C_W^{\text{dis}} \right) \quad (4.6)$$

where  $H$  is, again, the Henry's law constant and  $k_{AW}$  the air-water mass transfer

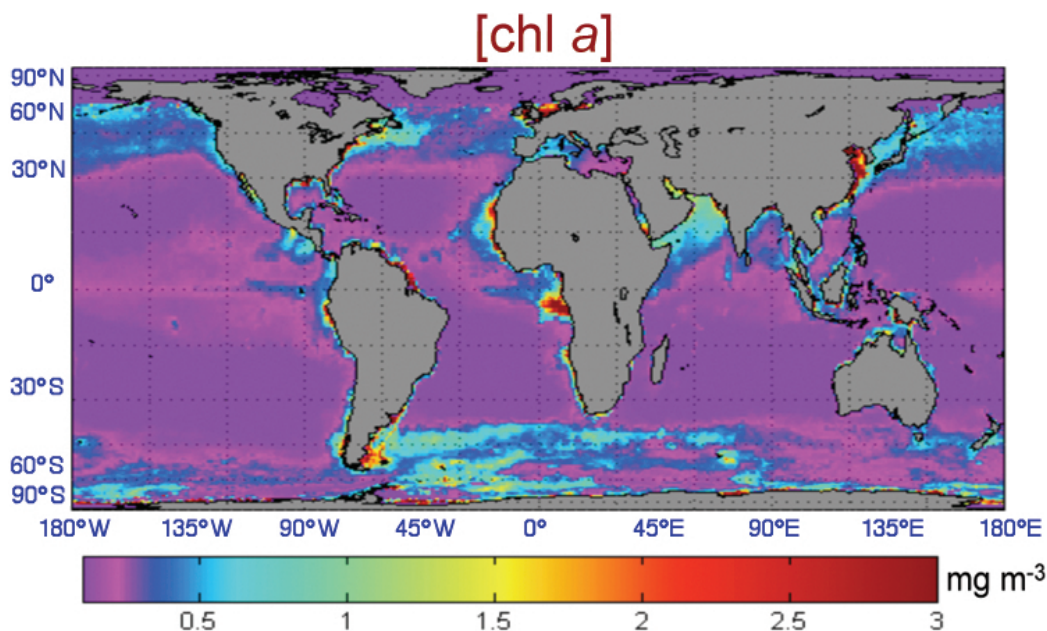


**Figure 4.10** Global distribution of the concentration of chlorophyll-*a* (chl-*a*) in the oceans in January (climatological monthly mean of 1998 - 2000).

coefficient.  $k_{AW}$  describes the rate at which chemicals partition between air and water surface and comprises resistance to mass transfer in both water ( $k_W$  [ $\text{m s}^{-1}$ ]) and air films ( $k_A$  [ $\text{m s}^{-1}$ ]):

$$\frac{1}{k_{AW}} = \frac{1}{k_W} + \frac{RT}{k_{AH}} \quad (4.7)$$

These mass transfer coefficients have been empirically defined based upon field studies using tracers such as  $\text{CO}_2$ ,  $\text{SF}_6$  and  $\text{O}_2$ .  $k_W$  is calculated from the mass transfer coefficient of  $\text{CO}_2$  in the water side ( $k_{W,\text{CO}_2}$  [ $\text{m d}^{-1}$ ]), itself generally correlated solely to wind speed ( $u_{10}$ , [ $\text{m s}^{-1}$ ]):

$$k_W = k_{W,\text{CO}_2} \left( \frac{S_{C\text{POP}}}{600} \right)^{-0.5} \quad (4.8)$$

$$k_{W,\text{CO}_2} = 0.24u_{10}^2 + 0.061u_{10}^2 \quad (4.9)$$

where  $S_{C\text{POP}}$  [dimensionless] is the Schmidt number of the POP and 600 is the Schmidt number of  $\text{CO}_2$  at 298K. Similarly  $k_A$  can be estimated from the mass transfer coefficient of  $\text{H}_2\text{O}$  in the air side ( $k_{A,\text{H}_2\text{O}}$  [ $\text{m d}^{-1}$ ]), also generally parameterized as a function of the wind speed:

$$k_A = k_{A,\text{H}_2\text{O}} \left( \frac{D_{\text{POP},a}}{D_{\text{H}_2\text{O},a}} \right)^{0.61} \quad (4.10)$$

$$k_{A,H_2O} = 0.2u_{10} + 0.3 \quad (4.11)$$

where  $D_{POP,a}$  and  $D_{H_2O,a}$  [ $\text{cm}^2 \text{s}^{-1}$ ] are the diffusivity coefficients of the POP and  $\text{H}_2\text{O}$  in air respectively.

**Q 3:** How can we determine the effect of short-term variations of the environmental data in the air-water POP fluxes if we use monthly means from satellite data?

## 4.5 Answers

**A 1:** Yes, we observe links between Figure 4.8 and Figure 4.9. In Figure 4.8 we observe an important variability in the Atlantic profiles of the fluxes, especially noteworthy for the wet deposition fluxes. Since the flux of wet deposition is directly proportional to the precipitation rate (see Equation 4.7), we can relate this variability to the spatial variability of the precipitation rates depicted in Figure 4.9. Therefore, it is clearly important to consider spatially-resolved data for the global assessment of POP cycling; in this context the use of remote sensing data is greatly justified. On the other hand, the wet deposition flux peaks in the high precipitation rates areas, such as in the Intertropical Convergence Zone (ITCZ). The positive gradient towards the northern hemisphere is related to the major emissions in the northern hemisphere.

As already pointed out in the Demonstration section, the SST data will be useful to assess which fraction of contaminants partition to the gaseous phase and which fraction of the contaminants partition to the aerosol phase. By looking in detail at Equation 4.7 we see that the fraction of contaminants that are in the gaseous phase versus the ones in the aerosol phase relates to the relative importance of the wet-gaseous flux versus the wet-particle flux. The temperature will affect also the gaseous wet deposition flux through its effect in  $H$  and also in the denominator of Equation 4.7. Putting it all together, the regions with lower SST, i.e. polar regions, will favor the particle-wet deposition.

**A 2:** The satellite-based remote sensing data that affect air-water exchange fluxes are sea surface temperature (Figure 4.4), wind speed (Figure 4.7) and chlorophyll- $a$  (Figure 4.10). From Equations 4.6, 4.9 and 4.11, it is clear that wind exerts an important effect on  $k_{AW}$ . On the other hand, temperature influences significantly the magnitude of  $k_{AW}$  through its influence on diffusivities, Schmidt numbers and  $H$ . Temperature may affect the partition between aerosol and gaseous phases in the atmosphere and between dissolved and particulate phases in the water. On the other hand, since it has been proven that the particulate phase to which pollutants sorb is mainly phytoplankton, it can be foreseen that the amount of phytoplankton in the water column will modify the air-water exchange flux. This amount of phytoplankton is estimated from the satellite-derived chlorophyll- $a$  concentration.

**A 3:** It is important to account for the short-term variability of wind speed and precipitation in the depositional fluxes of POPs because it can potentially affect the monthly averages. Averages have been corrected by the appropriate parameter. If an oceanic Weibull distribution of wind speed is considered, then a shape parameter of 2 seems appropriate. Conversely, precipitation amounts can be modelled by an exponential distribution that depends on the average non-zero precipitation amount. More information can be found in Dachs et al. (2002) and Jurado et al. (2005).

## 4.6 References

- Dachs J, Lohmann R, Ockenden WA, Méjanelle L, Eisenreich SJ, Jones KC (2002) Oceanic biogeochemical controls on global dynamics of Persistent Organic Pollutants. *Environ Sci Technol* 36 (20): 4229-4237
- Gassó S and Hegg DA (2003) On the retrieval of columnar aerosol mass and CCN concentration by MODIS. *J Geophys Res* 108(D1): 4010, doi:10.1029/2002JD002382.
- Jaward FM, Barber JL, Booij K, Dachs J, Lohmann R and Jones KC (2004) Evidence for dynamic air-water coupling and cycling of persistent organic pollutants over the open Atlantic Ocean. *Environ Sci Technol* 38 (9): 2617-2625.
- Jurado E, Jaward F, Lohmann R, Jones KC, Simó R, Dachs J (2004) Atmospheric dry deposition of persistent organic pollutants to the Atlantic ocean and inferences for the global oceans. *Environ Sci Technol* 38 (21): 5505-5513.
- Jurado E, Jaward F, Lohmann R, Jones KC, Simó R, Dachs J (2005) Wet deposition of Persistent Organic Pollutants to the global oceans. *Environ Sci Technol*. 39 (8): 2426-2435.
- Jurado, E., Dachs, J., Duarte, C. M., Simó, R (2008) Atmospheric deposition of Organic and Black Carbon to the global oceans. *Atmos Environ* 42: 7931-7939.
- Lohmann R, Ockenden WA, Shears J and Jones KC (2001) Atmospheric distribution of polychlorinated Dibenzo-p-dioxins, Dibenzofurans (PCDD/Fs), and Non-Ortho Biphenyls (PCBs) along a North-South transect. *Environ Sci Technol* 35 (20): 4046-4053.
- Simó R, Dachs J (2002) Global ocean emission of dimethylsulfide predicted from biogeophysical data. *Global Biogeochem Cy* 16 (4): 26-1 26-9

### 4.6.1 Further reading

- Jurado E (2006) Modelling the ocean-atmosphere exchanges of Persistent Organic Pollutants. PhD-thesis <http://www.tesisenxarxa.net/TDX-0330107-123245/index.html>
- Mackay D (2001) Multimedia Environmental Models. The fugacity approach. Lewis Publishers, Florida



## Case Study 5

# Impacts of European Atmospheric Air Pollution on Water Nutrients in the Atlantic Ocean, Baltic Sea, and Mediterranean Sea

Ana I. Prados\*<sup>1</sup> and James Acker<sup>2</sup>

---

## 5.1 Background Information

Combustion activities worldwide lead to atmospheric Nitrogen Oxides (NO<sub>x</sub>) emissions which can be transported over long distances and, via dry and wet deposition, contribute to excess nutrient loads in the world's rivers, estuaries and oceans, leading to water pollution and impacts such as the commonly observed coastal algal blooms. Satellite imagery can be used to track these anthropogenic NO<sub>x</sub> emissions and to study their potential impacts on water quality. This chapter provides a guide for obtaining and analyzing nitrogen dioxide imagery from the Ozone Monitoring Instrument (OMI).

The production of carbon, or primary productivity, by photosynthetic marine organisms provides the energy which ascends the marine trophic level ladder, from zooplankton to fish to whales, providing sustenance to the marine benthos when phytoplankton detritus descends to the seafloor. Phytoplankton productivity is controlled by the location and movement of these free-floating plants in oceanic currents, but their growth rate is determined primarily by the availability of sunlight and the necessary concentrations of vital nutrients. Enhanced phytoplankton productivity due to nutrient excess in waterways can lead to eutrophication, where organic detritus on the sea floor causes low dissolved oxygen, or zero dissolved oxygen concentrations in bottom waters due to bacterial decomposition. Increased nutrient levels may also cause species shifts from the common phytoplankton species to less desirable phytoplankton species, including species that are noxious or hazardous due to toxicity, otherwise known as harmful algal blooms.

The two primary marine macro-nutrients are familiar to many gardeners and

---

<sup>1</sup>University of Maryland Baltimore County, Joint Center for Earth Systems Technology, Greenbelt, Maryland, USA. \*Email address: [aprados@umbc.edu](mailto:aprados@umbc.edu)

<sup>2</sup>Goddard Earth Sciences Data and Information Services Center, Wyle IS LLC, Greenbelt, Maryland, USA

grounds keepers as the basic elements of fertilizer: nitrate and phosphate. Macro-nutrients can enter water ways either via terrestrial sources or via direct or indirect atmospheric deposition. Terrestrial sources of nutrients can be divided into two categories: point and non-point sources. The main terrestrial non-point sources of nutrients are fertilizers from the agricultural sector and runoff from impervious surfaces. In some regions of the world, the agricultural sector contributes the largest fraction of the entire nitrogen load. Nitrate and phosphate are also produced a result of various industrial processes and they are present in household chemicals such as dishwasher and laundry detergents. These pollutants are discharged into water ways via municipal water systems and they comprise the major point sources of nitrogen pollution. Although nitrogen and phosphate discharges from municipal waste water treatment plants today have been greatly reduced in some countries, nutrients continue to contribute to water pollution in rivers, estuaries and oceans worldwide.

In estuaries, nutrients are delivered by fresh water flow from rivers and streams into bays and sounds; where river flows enter the ocean directly, the nutrients from river waters can be transported hundreds of miles and foster enhanced productivity in their region of influence. Two fundamental processes, upwelling and mixing, bring deep-water nutrients to the surface, where they foster phytoplankton growth, such as the noteworthy Peru and Benguela upwelling zones. Because phytoplankton requires about 16 times as much nitrate as phosphate for optimum growth, nitrate is frequently the 'limiting nutrient', meaning that it controls the level of phytoplankton growth in ocean waters. Although nitrates are more commonly the limiting nutrient, there are times of the year and regions where it is possible for phosphate, iron, or silica to be the limiting nutrient.

Another important source of nitrogen to ocean waters is direct atmospheric deposition of nitrogen species. Atmospheric nitrogen species also contribute to nutrient loads in ocean waters through indirect deposition when nitrogen species deposit onto rivers that then feed into estuaries and open oceans. Combustion processes such as energy production from coal, vehicular emissions from gasoline and diesel fuel, other industrial activities, and fires lead to the emission of nitrogen oxide pollutants. Using the air shed for the Long Island Sound watershed as an example, the largest sources of nitrogen emissions are transportation  $\text{NO}_x$  (39%), electric utility  $\text{NO}_x$  (26%) and ammonia emitted from animal waste (16%). These nitrogen oxide species can undergo chemical modifications in the gas phase or liquid phase to species such as nitric acid and aerosol particles. When atmospheric nitrogen species are deposited on rivers, estuaries, or in the open ocean, they can also induce both surface water acidification and nitrification or excess nitrate. Sulfuric acid, which also has anthropogenic sources, is another contributor to water acidification. The deposited nitric acid is converted in surface seawater, which is basic (pH approximately 8.1 - 8.4), to nitrate, becoming biologically available.

Over certain water bodies around the world, atmospheric nitrogen deposition

constitutes a large fraction of the total nitrogen load, such as open ocean areas close to large sources of air pollution, regions with little water upwelling, and regions with little influence from terrestrial sources of nutrients. This atmospheric contribution of nitrogen augments primary productivity, particularly in oligotrophic waters. According to Pryor and Sørensen (2002), dry deposition of nitric acid, nitric oxides, particulate nitrate, and ammonia comprises about 20 - 40% of the total nitrogen flux in oceanic study regions. Prospero et al. (1996) reported that anthropogenic nitrogen emissions cause the deposition rate of nitrogen oxide species " $\text{NO}_y$ " to the North Atlantic Ocean to be about five times greater than pre-industrial levels; this increase is similar for reduced nitrogen species (" $\text{NH}_x$ "). Prados et al. (1999) found that much of the  $\text{NO}_y$  in the North Atlantic is transported over long distances. Jickells (1998) wrote that approximately one-third of anthropogenic nitrogen emissions in the North Sea are comprised of nitrogen dioxides; this percentage is similar for the Kattegat in the Baltic Sea, but in the form of reduced nitrogen. For estuaries such as the Chesapeake Bay in the United States, with substantial terrestrial inputs of nitrogen, the importance of atmospheric nitrogen deposition is reduced compared to riverine input, but is still substantial. He also notes that airborne sea salt from sea spray contributes to the formation of large aerosol particles laden with nitrate, which increases the efficiency of atmospheric nitrate deposition substantially. According to Duce et al. (2008) atmospheric nitrogen deposition could account for up to 3% of new annual oceanic primary productivity, an increase that is 10 times larger than pre-industrial times, and this represents about one-third of the primary productivity caused by all external (water and air) nitrogen input to the oceans.

Atmospheric nitrogen deposition can also influence the oceanic release of nitrous oxide ( $\text{N}_2\text{O}$ ), a greenhouse gas. According to Duce et al. (2008), "... the increase in AAN [anthropogenic atmospheric fixed nitrogen] has led to nearly an order of magnitude increase in anthropogenic  $\text{N}_2\text{O}$  emission from the oceans." Finally, atmospheric nitrogen deposition can shift the nitrogen/phosphate balance in surface waters. One of these areas is the North Atlantic Ocean, where Fanning (1989) documented, based on GEOSECS data, that while phosphate concentrations were depleted, nitrate and nitrite were detectable. He postulated that this was due to air pollution from the Eastern Seaboard, citing Levy and Moxim's (1989) map of global atmospheric combustion-produced nitrogen. In this area, phytoplankton productivity would have otherwise used up the available phosphate but atmospheric nitrogen provided an excess of nitrate, making phosphate the limiting nutrient.

This investigation uses atmospheric  $\text{NO}_2$  satellite observations from the Ozone Monitoring Instrument (OMI) to examine its potential effect on water quality in the Atlantic Ocean, Mediterranean Sea, and Baltic Sea. The OMI  $\text{NO}_2$  algorithm retrieval has been described by Bucsela et al. (2006). The product to be demonstrated is the total tropospheric column density in molecules/ $\text{cm}^2$ . This represents the integrated  $\text{NO}_2$  amount from the surface of the earth to the tropopause (the atmospheric boundary between the troposphere and the stratosphere). Because OMI  $\text{NO}_2$  is a

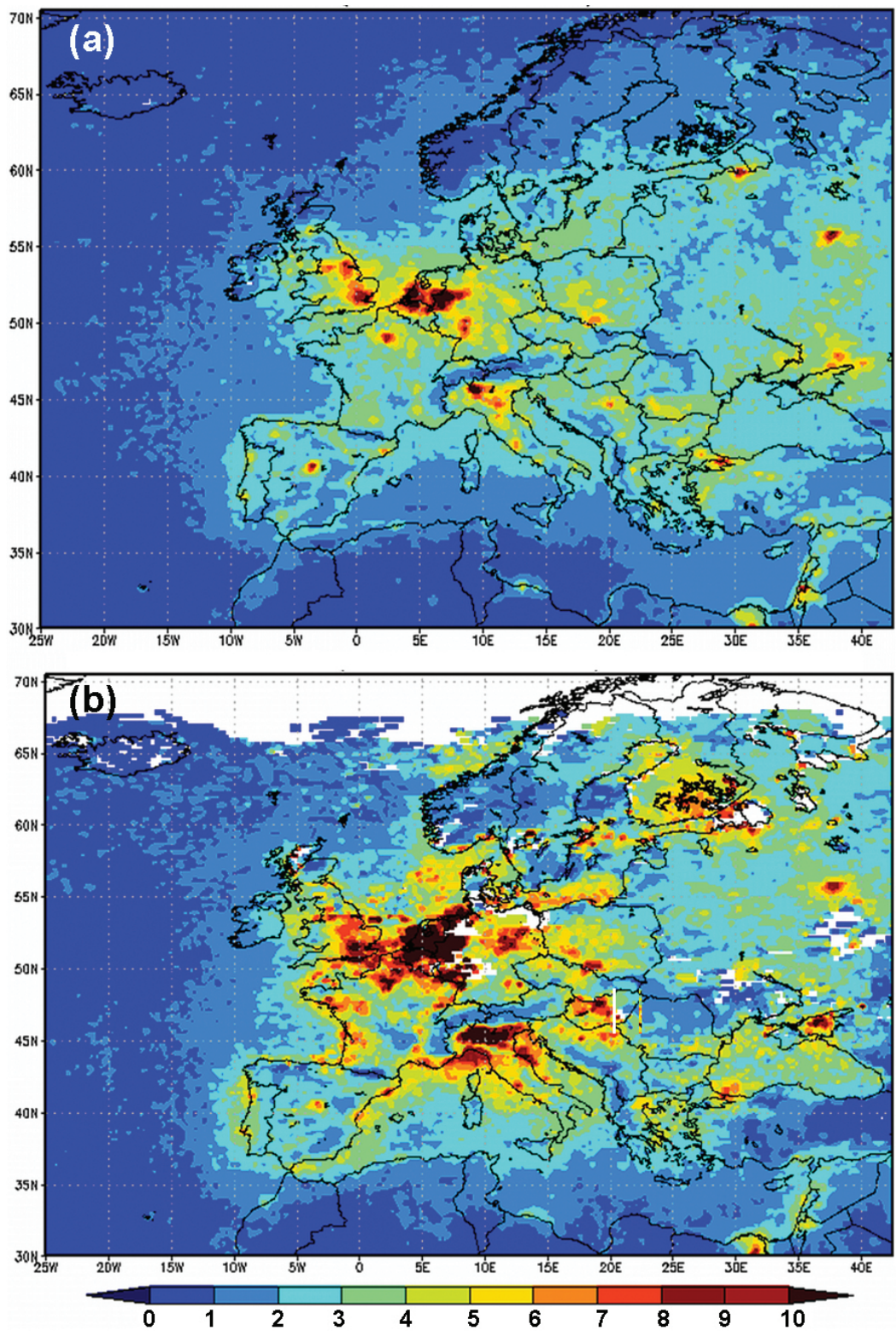


**Figure 5.1** Giovanni mean monthly OMI (Ozone Monitoring Instrument) tropospheric NO<sub>2</sub> column for (a) July 2008 and (b) January 2008.

column measurement, it does not give us information regarding its vertical distribution. NO<sub>2</sub> has a relatively short photochemical lifetime (from hour to days) and tends to concentrate near the surface of the earth. OMI NO<sub>2</sub> tropospheric column measurements have been shown to be sensitive to boundary layer, concentration based, comparisons with measurements from ground based networks (Celarier et al. 2008; Lamsal et al. 2008). However, atmospheric convective processes can also lead to high NO<sub>2</sub> concentrations in the mid to upper troposphere (Prados et al., 1999).

OMI NO<sub>2</sub> tropospheric columns from 2005 until present are available globally from several sources. The Royal Netherlands Meteorological Institute (KNMI) Tropospheric Emissions Monitoring Internet Service ([http://www.temis.nl/airpollution/no2col/no2regioomi\\_col3.php](http://www.temis.nl/airpollution/no2col/no2regioomi_col3.php)) has the advantage of providing near real-time imagery and maps for specific regions of the world. Another method for obtaining OMI NO<sub>2</sub> data is from the NASA GES DISC Interactive Online Visualization ANd aNalysis Infrastructure (Giovanni). Giovanni is a decision-support tool for air quality applications (Prados et al., 2010), among others, and it has the advantage of providing analysis tools, in addition to visualization capabilities.

This chapter will demonstrate how to access and interpret gridded 0.25 x 0.25 degree OMI NO<sub>2</sub> tropospheric columns through Giovanni. Visualizations are available both as jpg images and as a KMZ files which can be uploaded through Google Earth. Giovanni allows users to select areas of interest through an interactive map for the generation of latitude/longitude daily maps or temporally averaged maps. There are also a number of image analysis tools such as time series and correlation plots and maps.

## 5.2 Demonstration

**STEP 1: Go to the main Giovanni web page** <http://giovanni.gsfc.nasa.gov>

**STEP 2: Access Giovanni OMI NO<sub>2</sub>**

Go to the table in the main Giovanni page and click on 'Aura OMI L3' link.

**STEP 3: Generate Maps of OMI NO<sub>2</sub>**

In this section, you will generate several latitude/longitude plots to help with your image analysis.

1. Spatial Selection: Click on the map and with the mouse select a box that includes Europe, the North Atlantic Ocean, the Baltic Ocean, and the Mediterranean Ocean. Alternatively, enter these latitudes and longitudes in the boxes below the maps: North: 70.5; South: 30; East: 42.5; West: -25
2. Parameter Selection - select the box with the following parameter: NO<sub>2</sub> Tropospheric Column (Cloud-Screened at 30%).
3. Temporal Selection: Begin Date = 2008, July 1; End Date = 2008, July 31

4. Under "Select Visualization," select "Lat-Lon Map, Time-Averaged" and then click on "Generate Visualization". It will take a few moments for Giovanni to create the plot. Your plot should look similar to the one shown in Figure 5.1a.
5. Repeat the above for the following Time period: January 1 - January 31, 2008. Your plot should look similar to the one in Figure 5.1b.

#### STEP 4: Visualize images on Google Earth and download of GIF images

1. From the results page for the January 2008 visualization you just created, click on the "Download Data" tab at the top of the page.
2. To download a KMZ or other data files click on the items on the last column.
3. To view the image on Google Earth, click on the KMZ icon, then upload to Google Earth directly or you can choose to save the file, then open Google Earth, and then open the file after you start Google Earth.
4. Zoom in the country of Spain and make a note of where the OMI NO<sub>2</sub> is the highest. Your plot should look similar to Figure 5.2, which shows the OMI NO<sub>2</sub> over Spain overlaid on Google Earth.
5. To download a gif image click on the file name at the bottom of the first column.

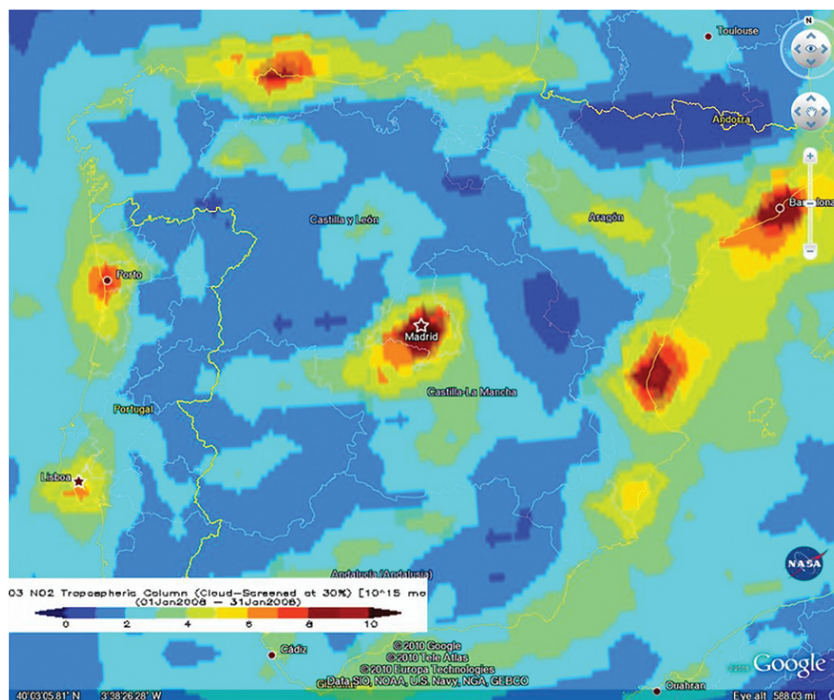


**Figure 5.2** Giovanni mean monthly OMI tropospheric NO<sub>2</sub> column for July 2008 over Spain using a KMZ output data file from Giovanni on Google Earth.

#### STEP 5: Generate Animation Plots of NO<sub>2</sub>

1. Now go back to the 'OMI AURA L3' page (click on Home in the tab above the

map).

2. Leave the same Spatial and Parameter Selections as in STEP 3
3. Temporal Selection: Begin Date = 2008, February 1 End Date = 2009, February 29
4. Under "Select Visualization," select "Animation" and then click on "Generate Visualization". You can use the tabs at the bottom of the plot to advance images one by one or to visualize all the images as an animation. We will be focusing on the images for February 12 - 14 (Figure 5.3).

#### **STEP 6: Generate an OMI NO<sub>2</sub> Time Series Plot**

1. Go back to the 'OMI AURA L3' Page (click on Home in the tab above the map).
2. Now we will want to narrow our frame to observe NO<sub>2</sub> over the North Sea between England and Norway. Select a region of the North Sea or alternatively, enter these latitudes and longitudes in the boxes below the maps: North: 59.6; South: 52.6; East: -84; West: -96 3.
3. Parameter Selection (select the box for the following parameter): NO<sub>2</sub> Tropospheric Column (Cloud-Screened at 30%).
4. Temporal Selection: Begin Date = 2008, Feb 1; End Date = 2008, Feb 29
5. Under "Select Visualization," select "Time Series" and then click on 'Generate Visualization'. It will take a moment for Giovanni to create the plot. If you chose the same latitudes and longitudes above, your plot should look similar to Figure 5.4. Write down the days in February in which OMI NO<sub>2</sub> is the highest over this region.

#### **STEP 7: Image Interpretation**

In order to interpret the images, look at the colour bar at the bottom of each map, which has a scale from 1 to  $10 \times 10^{15}$  molecules/cm<sup>2</sup>. Values over 7 indicate moderately polluted conditions. Keep in mind that these are column measurements. We do not know whether the pollution is closer to the surface, where it can have greater impacts on human health, or higher in the atmosphere. OMI data, however, are not always available. One of the main reasons for lack of data is cloudiness. The OMI data available through Giovanni have been automatically screened (the region appears white in the map because the data are not available) when the cloud cover is 30% or greater. The last figure you created (Figure 5.4) is called a time-series, and it shows the averaged NO<sub>2</sub> tropospheric column (y-axis) over the regions (square) you selected in Giovanni for each day. The day of the month is shown in the x-axis.

## **5.3 Questions**

**Q 1:** Look at the July 2008 map you generated (Figure 5.1a). Which countries have the highest NO<sub>2</sub> emissions and why? Think about what kinds of human activities in those countries may be contributing to the higher NO<sub>2</sub> levels compared to other

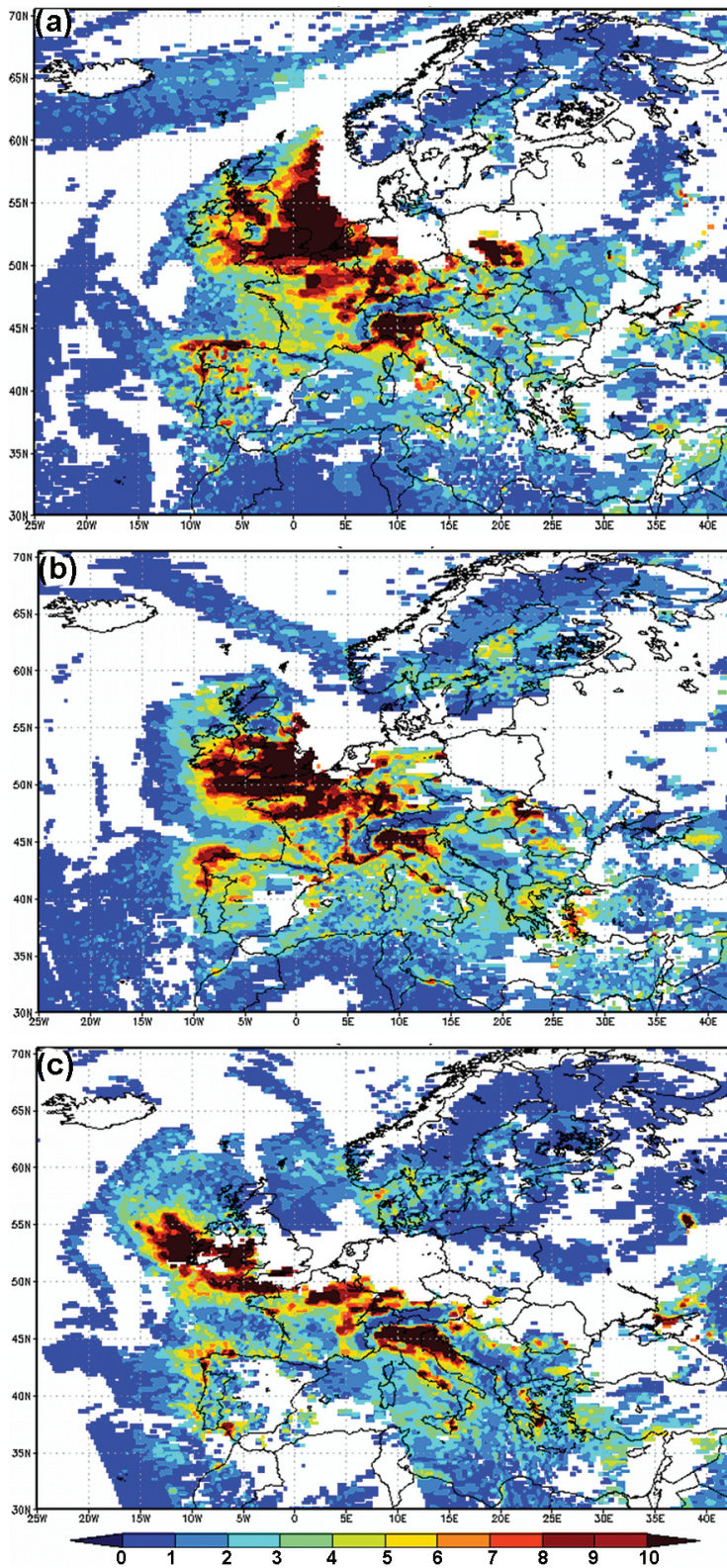


**Figure 5.3** Giovanni daily OMI tropospheric NO<sub>2</sub> column on (a) 12 February 2008, (b) 13 February 2008 and (c) 14 February 2008.

countries.

**Q 2:** Look at the January 2008 map you generated (Figure 5.1b). How do the mean values in January compare to those in July? Explain why the NO<sub>2</sub> tropospheric column is over land is higher in one month than in the other.

**Q 3:** During which month (January or July) would one expect a greater amount of NO<sub>2</sub> atmospheric deposition over the Baltic Sea, Mediterranean Sea, and the Atlantic Ocean?

**Q 4:** Look at the NO<sub>2</sub> values in Spain on January, 2008 (Figure 5.2). Which parts of Spain have the highest NO<sub>2</sub> concentrations and why? List several locations and activities in those locations which could be contributing to those high NO<sub>2</sub> concentrations. Why are some parts of Spain more polluted than others?

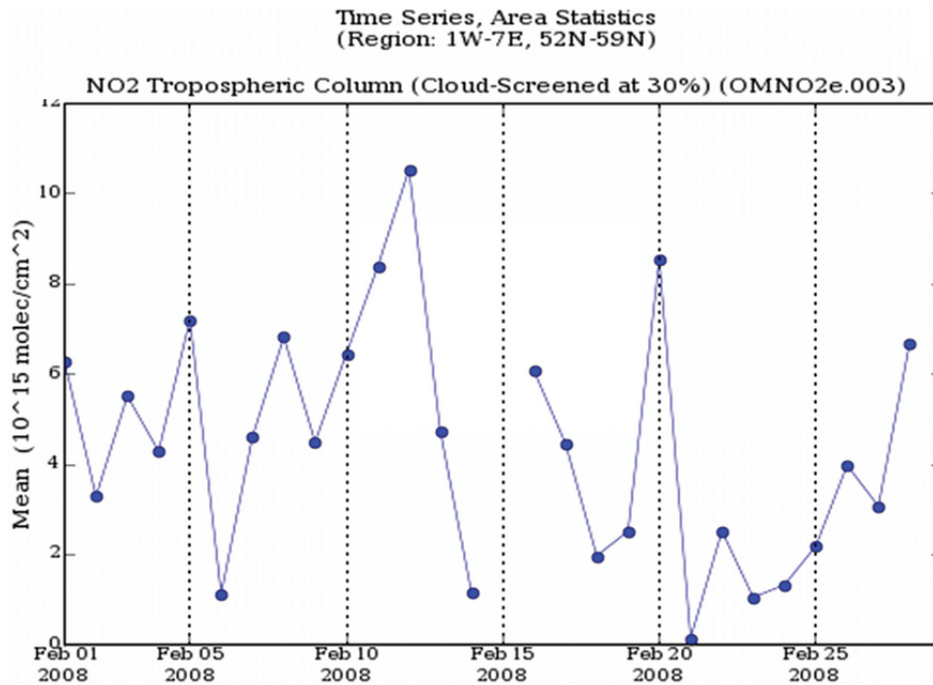


**Figure 5.4** Giovanni time series of OMI tropospheric NO<sub>2</sub> column over the North Sea for February 2008.

**Q 5:** What are the main differences between land and the surrounding oceans in Figures 5.1a and b? Which coastal areas in Europe and surrounding oceans would we expect to have the greatest problems with ocean productivity and water pollution impacts such as algal blooms?

**Q 6:** Pick a coastal region or ocean and list countries which are likely to contribute to excess nutrients and algal blooms in that particular coast or ocean?

**Q 7:** Now look at Figure 5.3. We will be focusing on the North Sea, which is the part of the Atlantic Ocean between England and Norway. We will also be looking at the North Atlantic west of Ireland. What do you observe in comparing the images for February 12, 13, and 14? You can also go back to the Giovanni session and use the controls to slow down the loop or view each image individually.

**Q 8:** Look at Figure 5.4. This figure shows the average NO<sub>2</sub> tropospheric column over the area you selected over the North Sea. Which days had the highest NO<sub>2</sub> pollution levels?

**Q 9:** Now compare the individual Giovanni NO<sub>2</sub> maps for each day in February and compare them to the time series (Figure 5.4). Is there a correspondence between the two? What is the source of the variability in the OMI tropospheric NO<sub>2</sub> over the North Sea in February 2008?

## 5.4 Answers

**A 1:** The Netherlands in northern Europe have some of the highest NO<sub>2</sub> concentrations. England has very high concentrations as well. These are the countries in Europe with the highest concentrations of industrial activity.

**A 2:** The July levels are generally lower. There is greater photochemical destruction on NO<sub>2</sub> in the summer due to higher ozone concentrations. Heating sources in the winter that depend on fossil fuel combustion, such as coal, are used in the winter but not in the summer. Coal is a fossil fuel and a large source of NO<sub>2</sub>.

**A 3:** We would expect greater atmospheric NO<sub>2</sub> deposition in the winter. This would be true for all the oceans surrounding Europe where the atmospheric deposition is dominated by the sources (countries) shown in Figures 5.1a and b, and where there is little contribution from sources further away that are not shown in the map.

**A 4:** Spanish cities are more polluted than rural areas because they have more cars and industrial activities. Cars and other equipment that burn gasoline or diesel lead to NO<sub>2</sub> emissions. Industrial activities also use up a lot of energy that leads to NO<sub>2</sub> emissions.

**A 5:** The land areas are generally more polluted than the oceans. However, some of the coastal areas can be just as polluted as the land. This is because of their close proximity to atmospheric pollution sources. For example, there are values of NO<sub>2</sub> along the Southern Coast of France and along the coast of Italy that approach 6 to 7 × 10<sup>15</sup> molecules/cm<sup>2</sup>. Some of the oceans (Figure 5.1b) have values of NO<sub>2</sub> that can be quite large. This is because under certain atmospheric conditions, atmospheric NO<sub>2</sub> can also travel long distances over oceans. The Baltic Sea north of Poland has high pollution levels in January 2008. The Atlantic Ocean also experienced levels of

NO<sub>2</sub> that were comparable to land, particularly in the North Sea. The oceans where we would expect the worst problems with algal blooms would be those affected by large terrestrial or atmospheric sources of nutrients, including NO<sub>2</sub> from both. Phosphorus and sediments, when in excess, also contribute to water pollution and impacts such as algal blooms. Based on these maps, we would expect the Baltic Ocean and the North Sea in particular to receive a strong influence from atmospheric sources, and therefore these bodies of water would be more vulnerable to water pollution. Some portions of the Mediterranean Ocean such as coastal areas of Northern Italy would also be more vulnerable to water pollution due to atmospheric NO<sub>2</sub> deposition.

**A 6:** Over the Baltic, we would expect several contributing sources. All land areas that surround the Baltic Sea would contribute terrestrial sources of nutrients, including NO<sub>2</sub> from the rivers that feed into the Baltic Sea. Atmospheric sources of nutrients would be dominated by the surrounding countries with the highest levels of OMI tropospheric NO<sub>2</sub>, primarily Germany, Poland, and Finland.

**A 7:** If you look at these figures in sequence you can see a plume of NO<sub>2</sub> over the North Sea on February 12th. On February 13th the plume moved west over the United Kingdom and Ireland, and by February 14th it has moved primarily offshore west of Ireland. The pollution over the North Sea on February 12th likely originated over northern Europe (the Netherlands, Belgium).

**A 8:** The highest NO<sub>2</sub> levels are on February 12th, 2008. However, there are other days later in the month, when the NO<sub>2</sub> tropospheric column increased again.

**A 9:** Go back and forth between the time series (Figure 5.4) and the maps for February 2008. There should be a correspondence between the two. If the map shows that the areas you selected had large NO<sub>2</sub> values, that should also be reflected as a peak in the time series. This variability is due to shifting meteorological patterns which cause varying degrees of transport of atmospheric NO<sub>2</sub> from land to the North Atlantic Ocean. You can select different regions (oceans) to create animation plots and time series and study the variability of atmospheric NO<sub>2</sub> and expected variability in water nutrient inputs.

## 5.5 References

- Bucsela, EJ, Celarier EA, Wenig MO, Gleason JF, Veefkind JP, Boersma KF, and Brinksma E (2006) Algorithm for NO<sub>2</sub> vertical column retrieval from the Ozone Monitoring Instrument. *IEEE Trans Geosci Rem Sens*, 44, 1245-1258
- Celarier EA, Brinksma EJ, Gleason JF, Veefkind JP, Cede A, Herman JR, Ionov D, Goutail F, Pommereau J-P, Lambert J-C et al. (2008) Validation of Ozone Monitoring Instrument nitrogen dioxide columns. *J Geophys Res* 113: D15S15, doi:10.1029/2007JD008908
- Duce, RA, LaRoche J, Altieri K, Arrigo KR, Baker AR, Capone DG, Cornell S, Dentener F, Galloway J, et al. , (2008) Impacts of Atmospheric Anthropogenic Nitrogen on the Open Ocean. *Science* 320 (5878) 893 [DOI: 10.1126/science.1150369]

- Fanning KA (1989) Influence of atmospheric pollution on oceanic nutrient limitation. *Nature* 339: 460-463
- Jickells, TD (1998) Nutrient biogeochemistry of the coastal zone. *Science* 281: 217-222 DOI: 10.1126/science.281.5374.217
- Lamsal, LM, Martin RV, van Donkelaar A, Steinbacher M, Celarier EA, Bucsela E, Dunlea EJ, Pinto JP (2008) Ground-level nitrogen dioxide concentrations inferred from the satellite-borne Ozone Monitoring Instrument. *J Geophys Res* 113: doi:10.1029/2007JD009235
- Levy H II, Moxim WJ (1989) Simulated global distribution and deposition of reactive nitrogen emitted by fossil fuel combustion. *Tellus* 41B: 256-271
- Prados, AI, Dickerson RR, Doddridge BG, Milne PA, Merrill JT, Moody JL (1999) Transport of ozone and pollutants from North America to the North Atlantic Ocean during the 1996 Atmosphere/Ocean Chemistry Experiment (AEROCE) Intensive. *J Geophys Res* 104: 26,219-26,233
- Prados, AI, Leptoukh G, Johnson J, Rui H, Lynnes C, Chen A, Husar RB (2010) Access, visualization, and interoperability of air quality remote sensing data sets via the Giovanni online tool. *IEEE J Selected Topics in Earth Observations and Remote Sensing*. In press
- Prospero JM, Barrett K, Church T, Dentener F, Duce RA, Galloway JN, Levy H II, Moody J, Quinn P (1996) Atmospheric deposition of nutrients to the North Atlantic Basin. *Biogeochem*, 35 (1): 27-73
- Pryor SC, and Sørensen LL (2002) Dry deposition of reactive nitrogen to marine environments: recent advances and remaining uncertainties, *Marine Pollut Bull*, 44 (12): 1336-1340, ISSN 0025-326X, DOI: 10.1016/S0025-326X(02)00234-5

## Case Study 6

# Detection of Oil Slicks using MODIS and SAR Imagery

Chuanmin Hu\*<sup>1</sup>, Xiaofeng Li<sup>2</sup>, William G. Pichel<sup>3</sup>

---

## 6.1 Background

Oil pollution can cause extensive damage to marine and terrestrial ecosystems. Every year, huge quantities of oil and petroleum products enter the sea, land, and groundwater (NAS, 2003). The pollution can come from a variety of sources, including leakage from oil transportation, accidents on oil platforms, atmospheric deposition, and seepage from natural seeps. Timely and accurate detection of oil pollution in the ocean can help management and research efforts, yet it is often a difficult task due to limited technical means in monitoring the vast ocean.

Remote sensing provides rapid, frequent, and synoptic measurement of the ocean's surface waters, and thus has been used widely to monitor oil pollution at sea, as well as in lakes. The remote sensing instruments include optical, microwave, and radar (e.g., synthetic aperture radar, SAR) sensors which can be equipped on both aircrafts and satellites. Each of the instruments and measurement platforms has its own advantages and disadvantages (Fingas and Brown, 1997; 2000; Brekke and Solberg, 2005). While airborne remote sensing offers the highest resolution (i.e., the sharpest image) and fastest response to a pollution event, it is often too expensive to be used for operational monitoring. In contrast, satellite remote sensing provides more frequent measurements of the ocean, hence more suitable for oil pollution monitoring.

Among the various satellite instruments, SAR is perhaps the most often used for oil detection at sea. The sea-surface backscattered radar signal is modulated by the wind-induced capillary waves, and thus carries information on the surface roughness. An ocean surface oil film has higher surface tension than water, and can dampen the surface capillary waves, resulting in a smoother sea surface. This in

---

<sup>1</sup>College of Marine Science, University of South Florida, 140 7th Ave., S., St. Petersburg, FL 33701, USA. \*Email address: [hu@marine.usf.edu](mailto:hu@marine.usf.edu)

<sup>2</sup>IMSG, NOAA NESDIS, USA

<sup>3</sup>NOAA NESDIS, USA

turn reduces the backscattered radar signal, making oil contaminated areas appear as dark patches in SAR images.

Because radar signals can "penetrate" clouds, SAR images are cloud free and efficient for detecting the various ocean surface features. However, routine application of SAR data is limited by its high-cost and narrow satellite swath (i.e., spatial and temporal coverage). Depending on the measurement mode, measurement of the same place can require days to weeks. These factors make it desirable to seek alternatives to complement SAR observations.

There are currently several Sun-synchronous, polar-orbiting satellite ocean-colour instruments that can measure the ocean's bio-optical properties every day. These include the Sea-viewing Wide Field-of-view Sensor (SeaWiFS, 1997 - present; McClain et al., 2004), the MODerate resolution Imaging Spectroradiometer (MODIS, 1999 - present for Terra, and 2002 - present for Aqua; Esaias et al., 1998), and the Medium Resolution Imaging Spectrometer (MERIS, 2002 - present). While MERIS was launched by the European Space Agency (ESA), SeaWiFS and MODIS are supported by the U.S. NASA. Global data are available for free downloading in near real-time. In particular, MODIS is equipped with several 250-m and 500-m resolution bands, representing a significant enhancement over the present coastal observation capability for the international community. The combined MODIS-Terra and MODIS-Aqua missions cover the global ocean in any single day, thus providing great potential to develop ocean applications.

Hu et al. (2003) used MODIS 250-m resolution data to detect and monitor oil spills in a turbid lake in Venezuela. After removing clouds, two images per week were obtained at no cost. The detection was possible because the high turbidity of the lake water provided a "bright" background where the highly light-absorbing oil films could be visualized. In the oligotrophic ocean, the water background is also dark, making oil detection difficult. However, Hu et al. (2009) showed that when MODIS imagery contained sun glint (i.e., specular reflection of the solar beam), high contrast was found between oil slicks and the background water. The contrast is not due to the difference in optical properties of the oil film and the water (as evidenced by the lack of contrast in other glint-free images), but due to the oil-modulation of the surface capillary waves - the same principle for SAR measurements. Indeed, the ability of visible imagery (including those from space shuttle photos) over sun glint regions to serve as effective radar signals was recognized decades ago and demonstrated recently using satellite imagery (Chust and Sagarminaga, 2007). However, its routine application has been difficult due to lack of near-daily data. The free availability of MODIS daily data for the global oceans makes it possible to implement a cost-effective means for oil spill monitoring.

Here, using MODIS 250-m resolution imagery and RADARSAT-1 SAR 25-m resolution imagery, we show several examples of how oil slicks are identified and interpreted. Three case studies are presented here. The first covers the western Gulf of Mexico (GOM, 18° - 31°N, 98° - 81°W) where numerous oil seeps exist. The

second covers the NE GOM where a tragic oil spill event began on 20 April 2010. The last example covers the East China Sea (ECS, 25° – 35°N, 120° – 130°E) where oil pollution from terrestrial and ship discharges is well known.

### 6.1.1 Data Source and Processing Methods

SAR data from RADARSAT-1 (C-band radar with horizontal polarization and 100-km swath width) were obtained during the Alaska SAR Demonstration (AKDEMO) project. These 25-m resolution images were standard beam mode scenes, processed at the Alaska Satellite Facility (ASF) at the University of Alaska, Fairbanks. The images provided relative intensity of the SAR signal (in digital numbers), and were navigated and analyzed using the software ENVI (Environment for Visualizing Images, version 4.2). The geo-referenced (or map-projected) digital images were stored in PNG graphical format.

All MODIS data were downloaded from the NASA Goddard Space Flight Center (GSFC) at no cost (<http://oceancolor.gsfc.nasa.gov>). These data are open to the public in near real-time and do not require data subscription. The following steps were used to generate geo-referenced MODIS images at 250-m resolution.

1. MODIS Level-0, 5-minute granules, were downloaded from NASA/GSFC;
2. MODIS Level-0 data were processed to generate Level-1b (calibrated total radiance) data for the 36 spectral bands using the SeaWiFS Data Analysis System (SeaDAS version 5.1). The Level-1b data were stored in computer files in HDF (Hierarchical Data Format);
3. MODIS Level-1b data were corrected for gaseous absorption (ozone and other gases) and Rayleigh scattering effects, resulting in the Rayleigh-corrected reflectance:

$$R_{rc,\lambda}(\theta_0, \theta, \Delta\phi) = \pi L_{t,\lambda}^*(\theta_0, \theta, \Delta\phi)/(F_0\lambda \times \cos\theta_0) - R_{r,\lambda}(\theta_0, \theta, \Delta\phi) \quad (6.1)$$

where  $\lambda$  is the wavelength for the MODIS band,  $L_t^*$  is the calibrated sensor radiance after correction for gaseous absorption,  $F_0$  is the extraterrestrial solar irradiance,  $\theta_0$  is the solar zenith angle,  $\theta$  is the sensor (viewing) zenith angle,  $\Delta\phi$  is the relative azimuth between the sun and the satellite, and  $R_r$  is the reflectance due to Rayleigh (molecular) scattering. The solar-viewing geometry is defined by  $(\theta_0, \theta, \Delta\phi)$ , which changes from pixel to pixel. This step used the software CREFL from the University of Wisconsin (Liam Gumley). The  $R_{rc}$  data of 7 MODIS bands (469, 555, 645, 859, 1240, 1640, and 2130 nm) were stored in HDF computer files. Figures 6.1a and b show examples of the  $R_{rc}$  Red-Green-Blue images using 645, 555, and 469-nm as R, G, and B, respectively. If two consecutive 5-minute granules were required to cover the study region, the Level-0 data were combined together before Step 2 was performed;

4. The  $R_{rc}$  data were geo-referenced to a cylindrical/equidistance (rectangular or geographic lat/lon) projection for the area of interest, defined by the

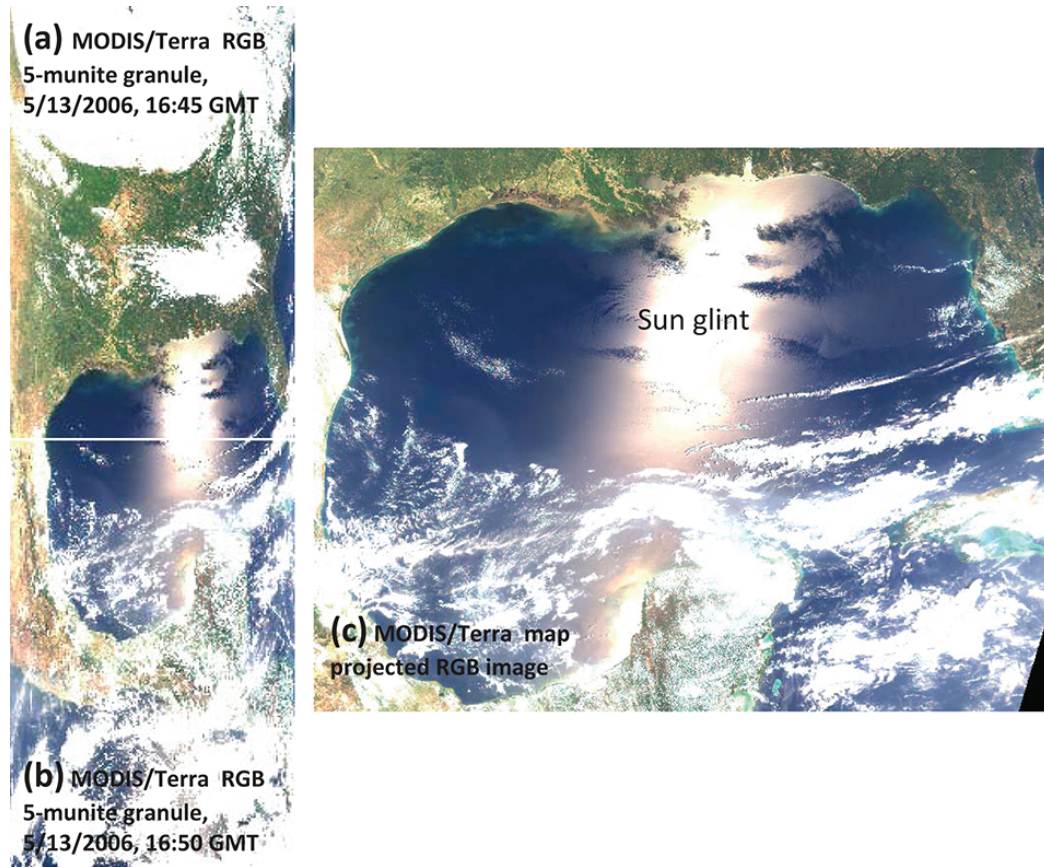


**Figure 6.1** Map projection of the MODIS Level-1b  $R_{rc}$  data. (a) and (b): two consecutive MODIS/Terra 5-minute granules on 13 May 2006. Each granule contains  $R_{rc}$  data at 645 and 859 nm with a dimension of 5416 x 8120, and  $R_{rc}$  data from other bands (469, 555, 1240, 1640, and 2130 nm) with a dimension of 2708 x 4060. The RGB images were composed of  $R_{rc}$  at 645 (R), 555 (G), and 469 nm (B). (c): rectangular projection of the two granules to cover the area of interest (Gulf of Mexico, from 18° to 31°N and 98° to 81°W). There are 440 image pixels per degree, corresponding to about 250-m per pixel.

North-South and East-West bounds. Because 1 degree is about 110 km, the map-projected data have 440 image pixels per degree, corresponding to 250 m per image pixel. Although only the MODIS 645- and 859-nm bands have a nadir resolution of 250 m, other bands at 500-m resolution were interpolated to 250-m resolution using a sharpening scheme similar to that for Landsat. The mapping software was written in-house using C++ and PDL (Perl Data Language) with an accuracy of about 0.5 image pixel;

5. The map projected  $R_{rc}$  data at 645, 555, and 469 nm were converted to byte values using a linear stretch (coefficients determined by trial-and-error), and then used as the red, green, and blue (RGB) channels, respectively, to compose a RGB image. Figures 6.1c shows the map projected RGB image at 250-m

- resolution from the combined 5-minute granules in Figures 6.1a and b;
6. The RGB image was loaded in the software ENVI for display and analysis.

## 6.2 Demonstration

Because of the synoptic coverage (often >10 degrees in both N-S and E-W directions) and medium resolution (250-m per pixel), the MODIS RGB image is very large (e.g., the dimension of Figure 6.1c is  $7480 \times 5720$  pixels). Further, the colour stretch is compromised to cover both sensitivity (the smallest difference between pixels) and dynamic range (the lowest and highest pixel values). Thus, interactive stretching and zooming functions are required to visualize the various image features. While several commercial software packages (e.g., ArcInfo or Erdas Imagine, or any other software that has basic image processing capabilities) can be used, we use the software ENVI to demonstrate how the oil-like features are identified.

First, the RGB image is loaded into ENVI by using the "File → Open Image File" function. Three display windows are shown (Figure 6.2 top panels): scroll, image, and zoom. The scroll window shows the entire region at reduced resolution to serve as a browse image; the image window shows a portion of the image at full resolution (250-m); and the zoom image enlarges a smaller portion by 4 times.

During the initial display in ENVI, the colours are stretched linearly from 0 to 255 to cover the entire image. This often makes the subtle surface features invisible. The image window is thus colour enhanced by a "Gaussian" enhancement, using the menu of "Image → Enhance → Gaussian". The result is that the image window is colour enhanced, at the price of either over-stretching or under-stretching for other regions. The various image panels in Figure 6.2 show the before-after comparison using the Gaussian enhancement.

What are the identified dark slicks in Figure 6.2? SAR data collected on the same day in an adjacent region showed identical features to those appearing in the corresponding MODIS image (Figure 6.3). Further, the MODIS image for the region in Figure 6.3 contains low to moderate sun glint (Hu et al., 2009), and another MODIS image collected 3 hours later over the same region, but without sun glint, shows no features at all. All this combined evidence suggests that these dark features are indeed due to dampened surface roughness and not due to changes in water's optical properties.

Several other processes, in addition to oil films, can lead to reduced surface roughness. These include phytoplankton or fish induced surface surfactant, shoals, and coastal freshwater jets (Alpers and Espedal, 2004). The region shown in Figure 6.3 is located in an oligotrophic ocean away from land, so these potential processes can be ruled out. The most striking evidence is that these features are recurrent in the same place, and they can also be observed in other images under optimal conditions (cloud free, with some degree of sun glint). Figure 6.4 shows two other

examples, both using ENVI's Gaussian enhancement, where the slicks from two different days appear to have a one-to-one relationship and originate from the same locations. They are oriented differently due to different surface currents and winds. The only explanation, then, is that these surface slicks are oil films from oil seeps on the ocean floor. Indeed, the NW GOM is well known to have numerous oil seeps and previous studies using a variety of methods (including remote sensing) confirmed the existence of oil seeps (McDonald et al., 1993; 1996). Thus, even without *in situ* validation, we can conclude that these surface features are indeed oil slicks floating on the surface.

This application is further demonstrated using MODIS imagery to examine a recent tragic oil spill event. On 20 April 2010, an explosion occurred on the oil drilling rig, the Deepwater Horizon, in the northern GOM (28.74°N, 88.37°W). After burning for a day, the rig sank to the 1500-m ocean floor, resulting in the largest oil spill event in the U.S. history. The main cause of the spill was a continuously leaking oil well, with estimates of at least 5,000 barrels per day (indeed, later estimates by several independent groups showed up to 50,000 barrels per day). Various methods have been used to assess the volume, fate, and trajectory of the spilled oil to help mitigate the potential adverse impacts on ocean and terrestrial ecosystems. Using the principles shown above, we processed and provided MODIS imagery in near real-time to the management agencies and researchers, and made them available online in Google-Earth compatible format to facilitate visualization and tracking of the spill ([http://optics.marine.usf.edu/events/GOM\\_rigfire](http://optics.marine.usf.edu/events/GOM_rigfire), Figure 6.5). In Figure 6.5b it can be seen that among the scattered clouds there is a suspicious feature. The feature appears like clouds, but its spectral shape is noticeably different from clouds, with relatively lower reflectance in the blue wavelengths due to enhanced Rayleigh scattering along the sun glint beam (the same principle behind why sunset is reddish). The sun glint reflectance and viewing angle (relative to the mirror direction of the sun) were estimated as  $0.048 \text{ sr}^{-1}$  and  $12.6^\circ$ , respectively. Further, the spatial shape and lack of shadow also indicate that the suspicious feature is oil. Figures 6.5c and d show two other examples from the same day from MODIS-Terra and MODIS-Aqua observations, respectively. Due to changes in the solar/viewing geometry, the same oil slicks show positive contrast in the morning but negative contrast in the afternoon, agreeing with what has been observed from natural oil slicks in the GOM (e.g., Figure 6.4).

Note that the reason for using RGB images instead of individual MODIS bands (e.g., 859 nm) is that clouds and cloud shadows can be easily visualized and ruled out as potential oil slicks.

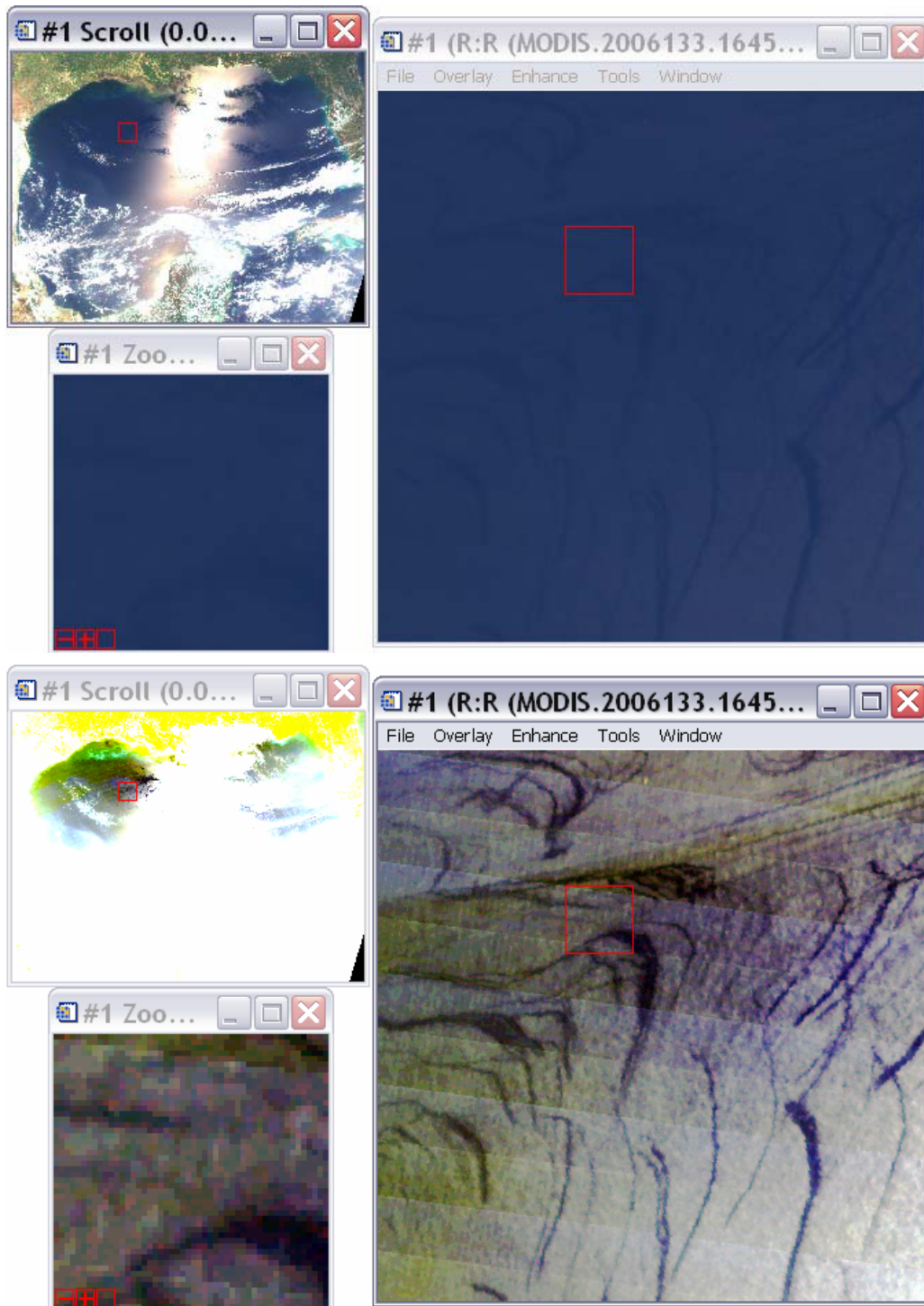


**Figure 6.2** Interactive colour stretching within the software ENVI is used to enhance the contrast between the oil-like features and the background water. Top: original RGB image in scroll (upper left), image (upper right), and zoom (bottom left) display windows. Bottom: the same image after Gaussian enhancement. Similar enhancement can be performed in other software packages.

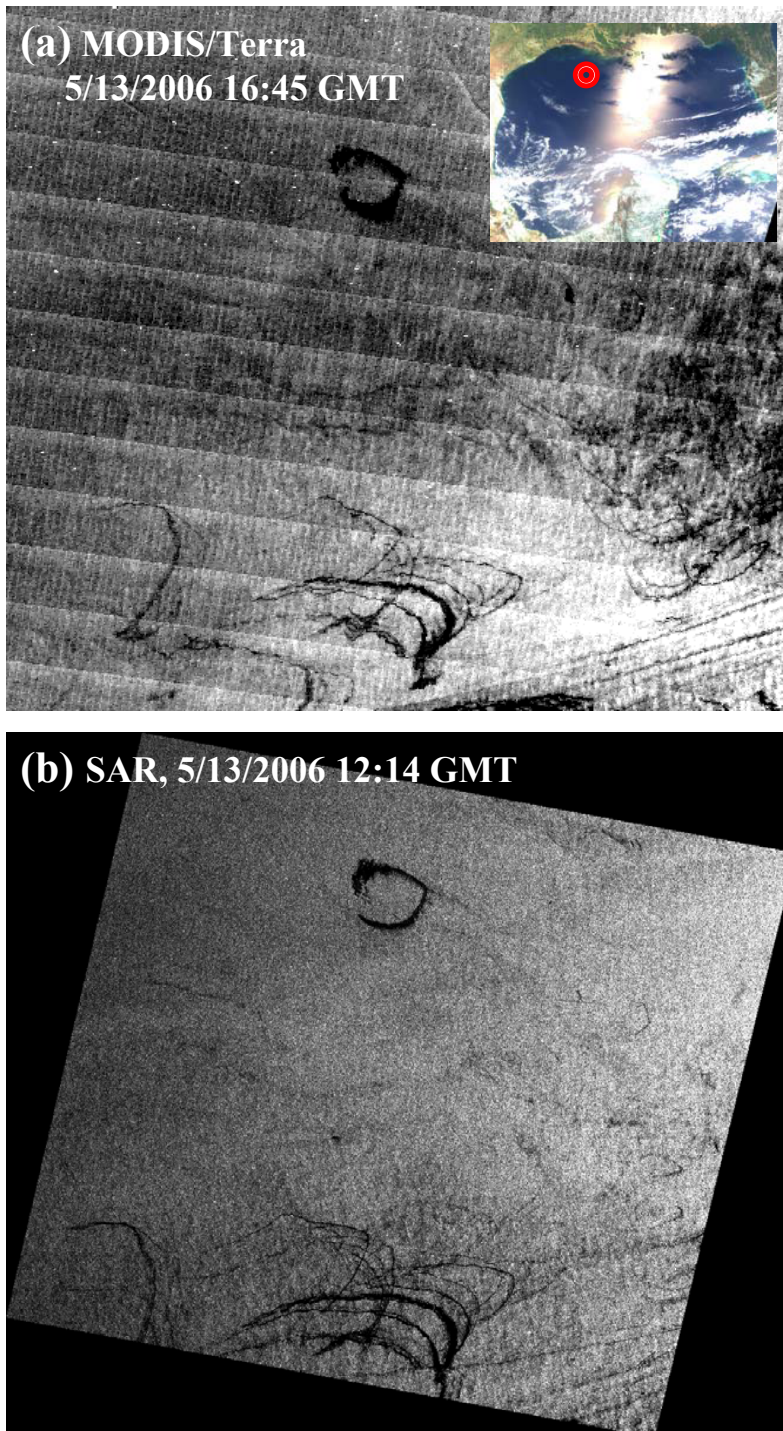


**Figure 6.3** MODIS/Terra image (a) and SAR image (b) showing oil slicks in the NW Gulf of Mexico (inset MODIS Red-Green-Blue figure) between 27.38° to 28.48°N and 93.25° to 92.01°W. The data were collected 4.5 hours apart, yet the slick patterns appear identical. The MODIS image was coloured stretched in ENVI using Gaussian enhancement.

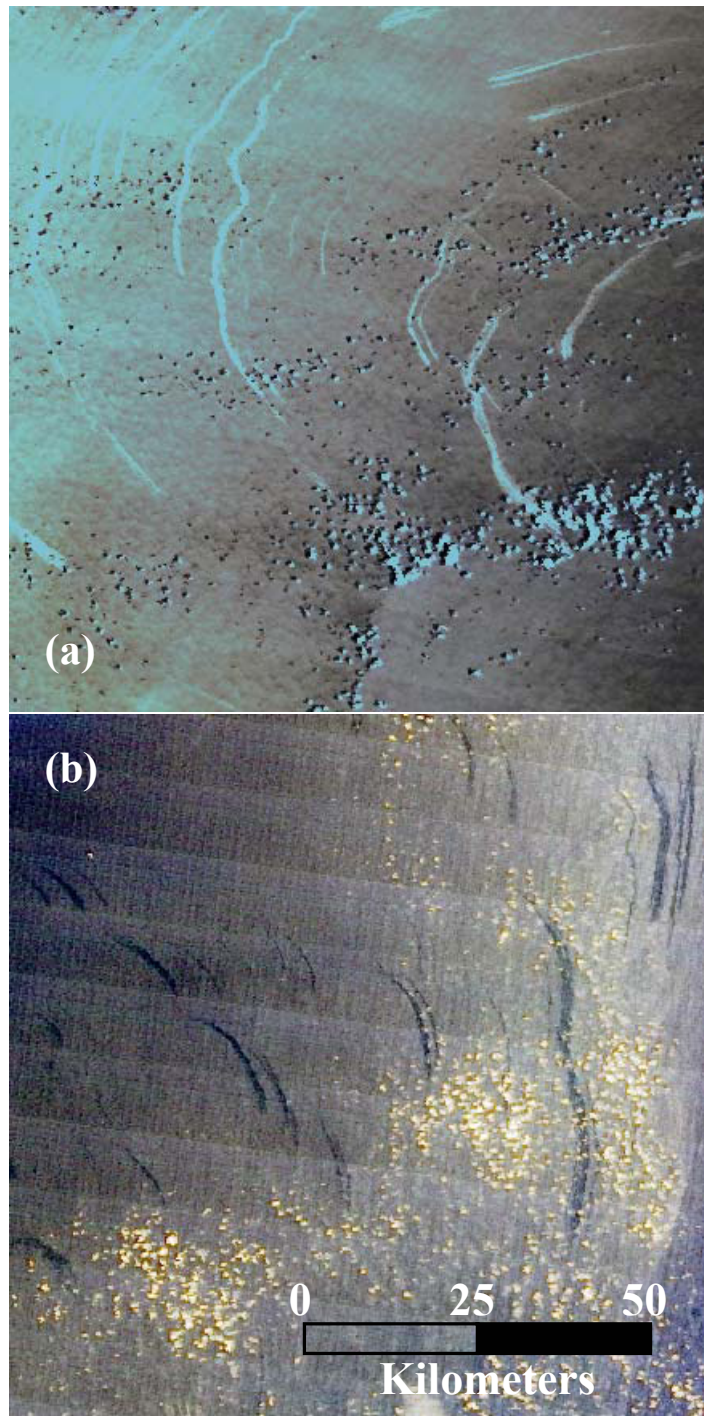


**Figure 6.4** MODIS/Terra images collected on 5/13/2001 (a) and 5/24/2001 (b) showing oil slicks in the NW Gulf of Mexico as positive and negative contrasts, respectively, against the background. The contrast change is due to different solar/viewing geometry in the sun glint patterns (Hu et al., 2009).

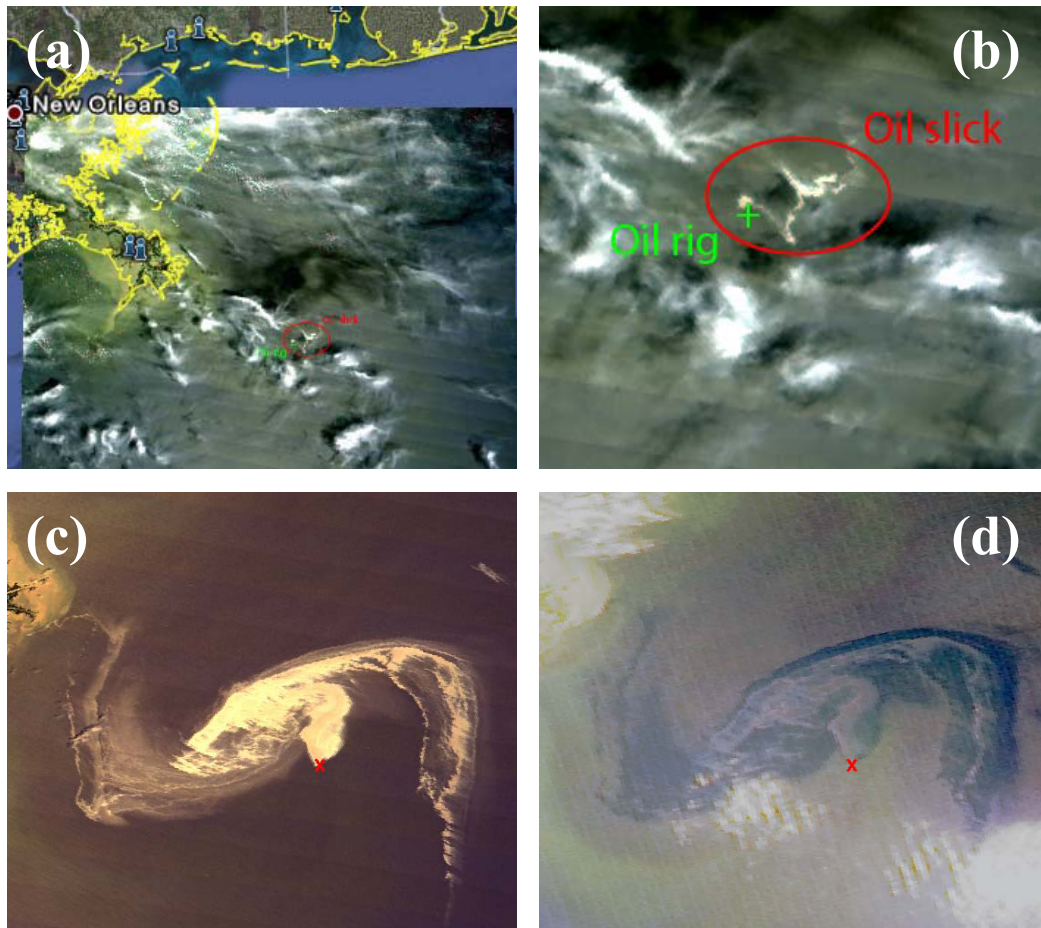


**Figure 6.5** MODIS images showing oil slicks in the northern Gulf of Mexico due to oil spills from a sunken oil rig (the Deepwater Horizon) on 20 April 2010. The location of the oil rig is marked with a cross. (a) MODIS image on 22 April 2010 overlaid on a Google-Earth map shows that the oil rig is approximately 40 km southwest of the Mississippi River mouth near New Orleans, Louisiana, U.S.A. (b) An enlarged image shows the oil slick and the surrounding clouds. (c) MODIS image on 29 April 2010 (16:55 GMT) shows the oil slicks in positive contrast. (d) MODIS image on the same day but at 18:30 GMT shows the same oil slicks in negative contrast. The horizontal scale of (b)-(d) is about 120 km. More images are available at [http://optics.marine.usf.edu/events/GOM\\_rigfire](http://optics.marine.usf.edu/events/GOM_rigfire).

### 6.3 Training and Questions

Three MODIS RGB images are provided on the IOCCG website ([http://www.ioccg.org/handbook/Hu\\_oil/](http://www.ioccg.org/handbook/Hu_oil/)) to help identify oil slicks and oil-like features. The first two cover the GOM, collected on 13 and 24 May 2001 by MODIS-Terra. The third image covers the ECS (25 to 35°N, 120 to 130°E), collected by MODIS-Aqua on 18 July 2008. The visualization and analysis can be performed in the following steps. We use ENVI to

describe the steps, but any other software package that has basic image processing capabilities can also be used.

1. Open the two MODIS images in ENVI. Use the "Tools → Link → Link Displays" to link the two images, so that they both show the identical region at the same time. By clicking on one image and toggling "on-off", the other image is co-registered and shown on top of the current image. This way, it is easy to identify whether certain features on the two images originate from the same locations;
2. Move the image window to the NW GOM, and use the Gaussian enhancement to enhance the colour contrast. Repeat this until a satisfactory enhanced image is obtained. This step should result in two images similar to those shown in Figure 6.4.

The second exercise is to explore the MODIS image covering the ECS. Using the interactive Gaussian stretch in ENVI, a colour-enhanced image should be obtained to show dark slicks and patches near the Yangtze River estuary in the sun glint region (Figure 6.6).

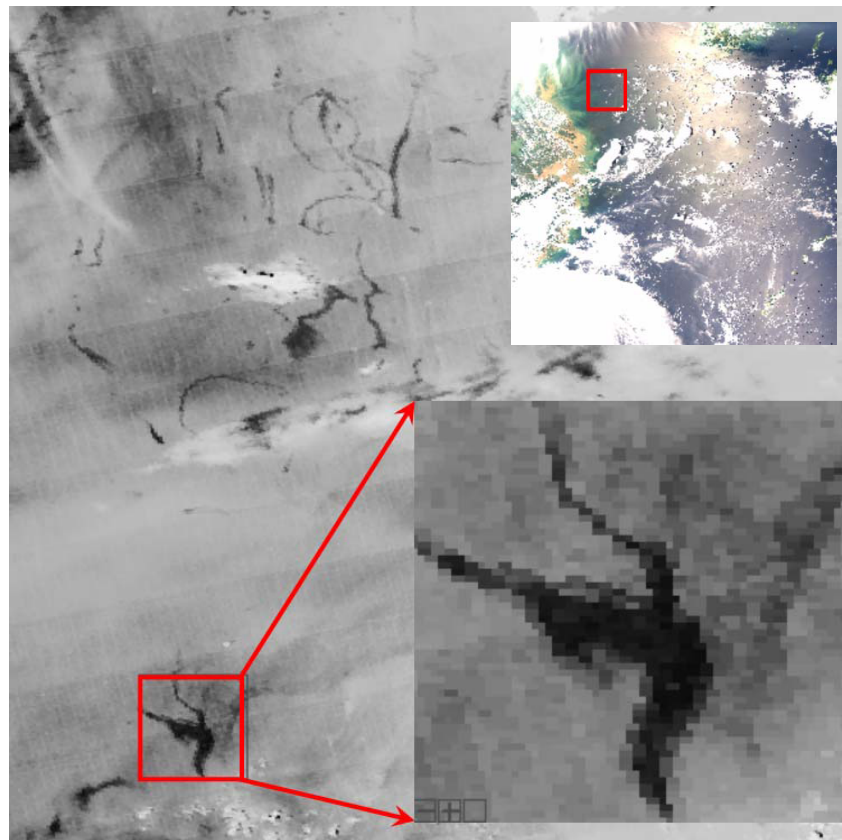


**Figure 6.6** MODIS image showing surface features that appear to be oil slicks in the East China Sea (ECS). Inset: MODIS Red-Green-Blue figure covering 25 to 35°N and 120 to 130°E on 7/18/2008 04:40 GMT.

## 6.4 Questions

**Q1:** Why are the slicks brighter than the surrounding water (i.e., positive contrast) in Figure 6.4a?

**Q2:** Is there a one-to-one relationship between the bright slicks (Figure 6.4a) and dark slicks (Figure 6.4b), and do they have the same origins?

**Q3:** Are these dark features in Figure 6.6 oil films? If so, where do they come from?

## 6.5 Answers

**A1:** Crude oil from oil seeps strongly absorbs light and therefore should appear darker than the adjacent waters. Then, why are the slicks in Figure 6.4a brighter? Using MODIS data and sun-glint estimates based on solar/viewing geometry and surface wind, Hu et al. (2009) demonstrated that if the satellite views the region close to the "mirror direction" of the sun ( $< 12\text{-}14^\circ$ ), positive (i.e., brighter) contrast can result from enhanced specular reflection by the oil film. Thus, depending on how the region is viewed by the satellite (relative to the sun), the oil slicks can show no contrast (in glint-free imagery), negative contrast (low to moderate sun glint) or positive contrast (strong sun glint) in MODIS imagery. The same positive contrast is also observed in Figure 6.5a.

**A2:** The ENVI "Link Displays" function provides an excellent tool for tracing features on two different images. By clicking on one image with the other toggled on or off, one can easily visualize that the bright and dark slicks have a one-to-one relationship and that they indeed have the same origins. The slight difference in the traced origins between the two different days should be due to the horizontal movement during the upwelling of the bottom oil (from 1 - 2 km deep). Nevertheless, the rough locations can significantly narrow down the search range when *in situ* operations are used to locate the exact locations of the oil seeps.

**A3:** It is well known that the ECS, particularly the western part, is subject to oil pollution from a variety of sources, including land-based sewage discharge, illegal ship discharge, and oil transportation accidents (Li and Daler, 2004; Shi et al., 2008). Using over 600 SAR images collected over the western ECS between 2002 and 2005, Shi et al. (2008) concluded that most of the oil-like slicks were from ship discharges. The dark features shown in Figure 6.6 are from MODIS sun-glint regions, and they have spatial texture (shape, size, spatial contrast) similar to oil slicks found in MODIS sun-glint imagery in the western GOM. Therefore, in the absence of an *in situ* validation effort, and considering their proximity to the shipping routes, we can conclude that these dark features are very likely oil slicks from ship discharge. Note

that without background information or *a priori* knowledge of the study region, the difficulty in recognizing oil slicks from suspicious features also holds true for SAR imagery (Alpers and Espedal, 2004). In this regard, the performance of the MODIS sun-glint imagery in detecting oil slicks is comparable to that of SAR, except that MODIS has a lower resolution (250-m versus 25 or 10-m for SAR) and is restricted by clouds.

## 6.6 Discussion and Summary

The three case studies demonstrated here (one for natural oil seeps in the western GOM, one for a tragic oil spill event in the eastern GOM, and one for ship or river discharges in the western ECS) clearly show the potential of MODIS imagery in detecting oil slicks in both oligotrophic and turbid ocean waters. In turbid coastal waters where water reflectance is high, observation of oil slicks does not require sun glint, as shown by Hu et al. (2003) for Lake Maracaibo, Venezuela. Likewise, when surface oil slicks are thick, sun glint is not required either (Figure 5d). However, such potential of MODIS should not be over-emphasized compared with other means (e.g., SAR detection) because 1) the MODIS visible and near-IR bands cannot penetrate clouds, and the method is useless for cloud contaminated image pixels; and 2) for oligotrophic oceans and thin slicks, some degree of sun glint is required to detect the changes in surface roughness, and this requirement limits its use in high latitude regions. Finally, when sun glint is required for the observations, all limitations that apply to SAR applications for oil detection (e.g., optimal wind speed, difficulty in differentiating the various dark features) may also apply to MODIS imagery because they are based on the same principles (i.e., changes in surface roughness).

However, MODIS has the advantage of greater coverage and no data cost, thus enabling a potentially quasi-operational system to be implemented for routine applications, and fast response in case of oil spill events. MODIS has a swath width of about 2300 km, and the two MODIS instruments onboard the Terra (morning pass) and Aqua (afternoon pass) satellites make the spatial/temporal coverage at moderate resolution (250-m) unprecedented by any in-orbit satellite instruments. In this regard, for regions with a potential for heavy oil spills, a MODIS-based system could be implemented. Indeed, the most recent oil spill event in the Gulf of Mexico (Figure 5) provides an excellent example as to how a MODIS-based, quasi-operational system can contribute to monitoring and mitigation of oil spills. MODIS provided near daily oil spill coverage for most of the NE GOM during the first month of the spill event (21 April to late May 2010). When cloud cover increased from late May towards the summer, SAR data from several sources were combined with MODIS observations to improve the coverage. The advantage of combining more synoptic and frequent MODIS data with cloud-free SAR data in oil spill monitoring has been clearly demonstrated in this case.

In summary, oil films on the sea surface modulate the surface roughness (capillary/gravity waves), and thus can be differentiated from their surrounding waters in MODIS sun glint imagery. This ability is demonstrated by three case studies where oil slicks from natural seeps, an oil spill accident, and possible ship discharges are identified. When oil films are thick, their optical properties (light absorption and surface Fresnel reflection) can make them well distinguished from the surrounding waters, as shown in the recent GOM oil spill case study. Because of the free availability of the MODIS 250-m data since 2000, a monitoring system at low cost can be established, in principle, for any part of the global oceans where sun glint is frequently observed. Combined with SAR observations, such a system may significantly enhance our capability to monitor oil spills in most of the global oceans. Automated delineation and quantification of oil slicks (e.g., thickness) using texture analysis as well as image segmentation, however, still requires further research.

## 6.7 References

- Alpers W, Espedal HA (2004) Oils and surfactants. In: Jackson CR and Apel JR (eds) Synthetic Aperture Radar Marine User's Manual. U.S. Department of Commerce, Washington, DC, September 2004. pp 263-275
- Brekke C, Solberg AHS (2005) Oil spill detection by satellite remote sensing. *Remote Sens Environ* 95:1-13
- Chust G, Sagarminaga Y (2007) The multi-angle view of MISR detects oil slicks under sun glitter conditions. *Remote Sens Environ* 107:232-239
- Esaias WE, Abbott MR, Barton I, Brown OB, Campbell JW, Carder KL, et al. (1998) An overview of MODIS capabilities for ocean science observations *IEEE Trans. Geosci Remote Sens* 36:1250-1265
- Fingas M, Brown C (1997) Remote sensing of oil spills. *Sea Technology* 38:37-46
- Fingas M, Brown C (2000) Oil-spill remote sensing - An update. *Sea Technol* 41:21-26
- Hu C, Muller-Karger FE, Taylor CJ, Myhre D, Murch B, Odriozola AL, Godoy G (2003) MODIS detects oil spills in Lake Maracaibo, Venezuela. *EOS, Transactions, AGU*, 84(33):313,319
- Li D, Daler D (2004) Ocean pollution from land-based sources: East China Sea, China. *ABBIO*, 33:107-113
- MacDonald IR, Guinasso NL, Ackleson SG, Amos JF, Duckworth R, Sassen R, Brooks JM (1993) Natural oil slicks in the Gulf of Mexico visible from space. *J Geophys Res* 98(C9):16,351-16364
- MacDonald IR, Reilly JF, Best SE, Venkataramaiah R, Sassen R, Guinasso N, Amos J (1996) Remote sensing inventory of active oil seeps and chemosynthetic communities in the northern Gulf of Mexico. In: Schumacher D, and Abrams MA (eds) *Hydrocarbon migration and its near-surface expression*. *Am Assoc Petrol Geol Mem.* 66:27-37
- McClain CR, Feldman GC, Hooker SB (2004) An overview of the SeaWiFS project and strategies for producing a climate research quality global ocean bio-optical time series. *Deep-Sea Res II* 51:5-42
- NAS (2003) *Oil in the sea III. Committee on Oil in the Sea: Inputs, Fates, and Effects*, Ocean Studies Board and Marine Board, Divisions of Earth and Life Studies and Transportation Research Board, National Research Council. The National Academies Press.
- Shi LA, Ivanov YU, He M, Zhao C (2008) Oil spill mapping in the western part of the East China Sea using synthetic aperture radar imagery. *Int J Remote Sens* 29:6315-6329

## Theme: Phytoplankton and Macroalgae

---



## Case Study 7

# Observation of Ocean Colour Beyond Chlorophyll-*a*: From Particulate Organic Carbon Content and Size Distribution to Phytoplankton Functional Groups

S everine Alvain\*<sup>1</sup>, Lucile Dufor t-Gaurier<sup>1</sup> and Hubert Loisel<sup>1</sup>

---

## 7.1 Background Information

The term phytoplankton encompasses all microscopic plant-like organisms living in the illuminated surface layers of the ocean. The existence of phytoplankton is of fundamental interest as they form the base of the aquatic food web, providing an essential ecological function for all aquatic life.

Phytoplankton also play an important role in the biological pump of carbon and CO<sub>2</sub> sequestration. During the process of photosynthesis, phytoplankton take up dissolved CO<sub>2</sub> and convert it into organic compounds, using energy from the sun. This transformation is of biogeochemical importance for two reasons: firstly the resulting organic carbon no longer participates in the equilibrium of the carbonate system, thus increasing the ocean's ability to dissolve carbon dioxide. Secondly, the particulate organic carbon sinks from surface waters to deeper layers, removing carbon from the surface layer. The biological pump thus plays a very important role in the Earth's carbon cycle, and the evolution of the biological pump will play a key role in understanding climate change scenarios.

Like terrestrial plants, phytoplankton use pigment antennae to capture the energy of photons. Among these phytoplankton pigments is chlorophyll-*a*, which is used as an index of the phytoplankton biomass. Chlorophyll-*a* selectively modifies the flux of photons that penetrate the ocean's surface layer. It absorbs the red and blue wavelengths and scatters the green ones. For this reason, the colour of the ocean will range from blue-green to green depending on the type and density of phytoplankton populations. Thus, by studying the colour of light reflected from the oceans, in other words ocean colour, optical sensors can quantify the amount of chlorophyll and other constituents.

---

<sup>1</sup>Universit  Lille Nord de France, LOG CNRS, ULCO, USTL, UMR8187, F-62930 Wimereux, France.  
\*Email address: [severine.alvain@univ-littoral.fr](mailto:severine.alvain@univ-littoral.fr)

Visible and near-infrared passive radiometers onboard spacecraft provide useful data at spatial and temporal scales unattainable by shipboard sampling. This was fully demonstrated by the first satellite, CZCS, dedicated to the observation of ocean colour. Since then, a number of advanced ocean-colour satellites have been launched. In the past few years, inversion of ocean-colour satellite data has moved beyond the estimation of chlorophyll-*a* concentration to include new parameters which make it possible, for example, to determine the dominant phytoplankton species in the surface waters, to get information about particle size distribution (Loisel et al., 2006) and to retrieve information about other biogeochemical components such as particulate organic carbon (POC), and coloured detrital matter (Stramski et al., 1999; Loisel et al., 2002; Siegel et al., 2002). Consequently, information on dominant phytoplankton groups can be superimposed on POC and size distribution maps, allowing for a large range of new applications. Information obtained from satellite observation is restricted to the near-surface layer. Indeed, the surface oceanic layer that is remotely sensed in the visible part of the spectrum is the first attenuation layer, generating 90% of the photons that form the upward flux just beneath the surface (Gordon and McCluney, 1975). The thickness of this layer typically varies from a few meters to about 60 meters, depending on the presence of optically-significant constituents in the water and the wavelength considered (Smith and Baker, 1978). Products derived from satellite data such as chlorophyll or POC concentration are integrated over the first penetration depth.

## 7.2 Materials and Methods

### 7.2.1 POC Estimates from Space

In this section, we will present the Loisel et al. (2002) method used to estimate the near-surface concentration of POC from satellite data ( $POC_{surf}$ ). This method consists of deriving  $POC_{surf}$  from the inherent optical properties, as presented in Loisel et al. (2002). The natural variations of optically-significant substances in seawater can be observed through the measurements of inherent optical properties (IOPs). Among these IOPs, the total backscattering coefficient of seawater,  $b_b$ , is not sensitive to the dissolved material. The  $b_b$  coefficient can therefore be partitioned into two components  $b_b = b_{bp} + b_{bw}$  where  $b_{bw}$  is the backscattering coefficient of seawater (Morel and Prieur, 1977) and  $b_{bp}$  is the backscattering coefficient of particles. The  $b_{bp}$  variability is governed (to the first order) by changes in the abundance and (to the second order) composition of the particle assemblage.

Previous studies at regional (Stramski et al., 1999; Loisel et al., 2001) and global scales (Loisel et al., 2002) have demonstrated the feasibility of estimating POC from  $b_{bp}$ . The robust relationship found between POC and  $b_{bp}$  can be explained by the fact that under non-bloom conditions,  $b_{bp}$  is governed mainly by small-sized, non-living particles (Stramski and Kiefer, 1991; Morel and Ahn, 1991), which represent the

dominant contribution of POC in the open ocean (Koike et al., 1990). Note that previous studies have shown a good correlation between *in situ*  $b_{bp}$  and POC values in different oceanic areas (Reynolds et al., 2001; Stramski et al., 2008).

In a remote-sensing context, the backscattering coefficient of seawater is not measured directly, but is derived by the inversion of the natural light field reflected back out of the ocean and detected by the satellite ocean-colour sensor. In this study,  $b_b(490)$  is retrieved from the remote-sensing reflectance at 443nm, 490nm and 555nm, using the method developed by Loisel and Stramski (2000), and slightly modified by Loisel and Poteau (2006).

Because coincident measurements of the particle backscattering coefficient and POC are still very scarce, the parameterization of  $POC_{surf}$  is established as a function of the particle scattering coefficient,  $b_p$ , which is derived from  $b_{bp}$  using the following empirical relationship (Twardowski et al., 2001):

$$b_{bp}(490)/b_b(490) = 0.0096 \times [chl-a]^{-0.253} \quad (7.1)$$

A simple linear relationship is used between  $POC_{surf}$  and  $b_p$  (Claustre et al., 1999; Loisel et al., 2001). Based on results of previous studies carried out in different regions of the global ocean, a mean slope value of  $400 \text{ mg m}^{-2}$  is adopted (Claustre et al., 1999; Loisel et al., 2002) with a null intercept as a first approximation.

Figure 7.1 displays the global maps of the  $POC_{surf}$  near-surface concentration for the SeaWiFS period 1997-2008 during June and January. The global distribution of  $POC_{surf}$  follows the major gyre systems and other large scale circulation features of the ocean. Low surface POC concentrations are encountered in subtropical gyres, where large scale downwelling is expected. For example in the South Pacific gyre,  $POC_{surf}$  is less than  $50 \text{ mg m}^{-3}$ . Elevated near-surface POC concentrations in the range  $100\text{-}200 \text{ mg m}^{-3}$  are encountered at high and temperate latitudes (e.g. Antarctic Circumpolar Current, sub-arctic gyres, temperate North Atlantic). Compared to subtropical gyres, these areas are characterized by a high chlorophyll concentration (by a factor of about ten, Figure 7.2) supported by inputs of nutrients injected from below the euphotic layer by advection or vertical mixing, or from terrestrial sources.

### 7.2.2 Spectral Dependency of Optical Backscattering by Marine Particles: A Proxy of the Particle Size Distribution

Knowledge of the relative proportions of small- and large-sized particles in the surface ocean is essential for understanding the ocean ecology and biogeochemistry, including particle dynamics and carbon cycling. This information may be assessed qualitatively from satellite observations of ocean colour (see Figure 7.3). Such capability is based on the estimation of spectral dependence of the particulate backscattering coefficient,  $b_{bp}$ , denoted  $\gamma$ , which is sensitive to particle size distribu-

tion. The greater the value of  $\gamma$  (the steeper the slope), the more small particles are present in the water column, relative to large particles (and vice versa).

The retrieval of  $\gamma$  from ocean-colour remote sensing observations is performed in two steps. First,  $b_{bp}(\lambda)$  is assessed at different visible wavelengths,  $\lambda$ , by an inverse algorithm which uses the light field estimated from the total signal measured at the top of the atmosphere and corrected for atmospheric effects (Loisel and Stramski, 2000). Then,  $\gamma$  is calculated by linear regression between  $\text{Log}(b_{bp})$  and  $\text{Log}(\lambda)$ . In general, the  $\gamma$  values are much greater in summer than in winter, which holds true for both the northern and southern hemisphere (Figure 7.3). Seasonal variations of  $\gamma$  indicate that the proportion of small-sized particles compared to larger particles increases from winter to summer in the surface waters of the global oceans. These spatio-temporal patterns are interpreted in terms of processes that modify the composition of particulate assemblages and physiology of phytoplankton in response to environmental forcing.

### 7.2.3 Detection of Dominant Phytoplankton Groups: The PHYSAT Method

Phytoplankton play an important role in many global biogeochemical cycles. However, the efficiency and impact of phytoplankton depends strongly on the nature of phytoplankton itself. Thus monitoring the spatial and temporal distribution of dominant phytoplankton groups is of critical importance. From a pigment point of view, the main phytoplankton groups have specific pigments, called biomarkers. The PHYSAT algorithm (Alvain et al., 2005; Alvain et al., 2008) has been developed based on an empirical relationship between coincident *in situ* biomarker pigment measurements and remote sensing reflectance anomalies. The PHYSAT method has been applied to the SeaWiFS satellite archive, from September 1997 to December 2008. Monthly PHYSAT data have been used to retrieve the monthly climatology maps for January and June, shown in Figure 7.4.

The main difficulty in ocean-colour measurements (in the visible spectrum) is caused by the atmosphere and aerosols which act to diffuse and absorb light. The atmosphere is responsible for about 95% of the signal detected by a satellite sensor. However, the portion of the signal that carries information from the ocean and the atmosphere respectively can be deconvoluted. This is currently done using atmospheric correction algorithms. The measurements we used here are obtained after atmospheric correction. However, since we used second order variability for the PHYSAT method, some additional criteria have to be applied. Thus, we will consider, for the PHYSAT part, only pixels associated with an aerosol optical thickness less than 0.15. Another validity criteria concerns the concentration of chlorophyll-*a*, [chl-*a*], which has to be lower than  $3 \text{ mg m}^{-3}$  to exclude waters possibly contaminated by coastal material, and higher than  $0.04 \text{ mg m}^{-3}$  to discard ultra-oligotrophic waters where it is unlikely that a dominant group can be found using ocean-colour data.

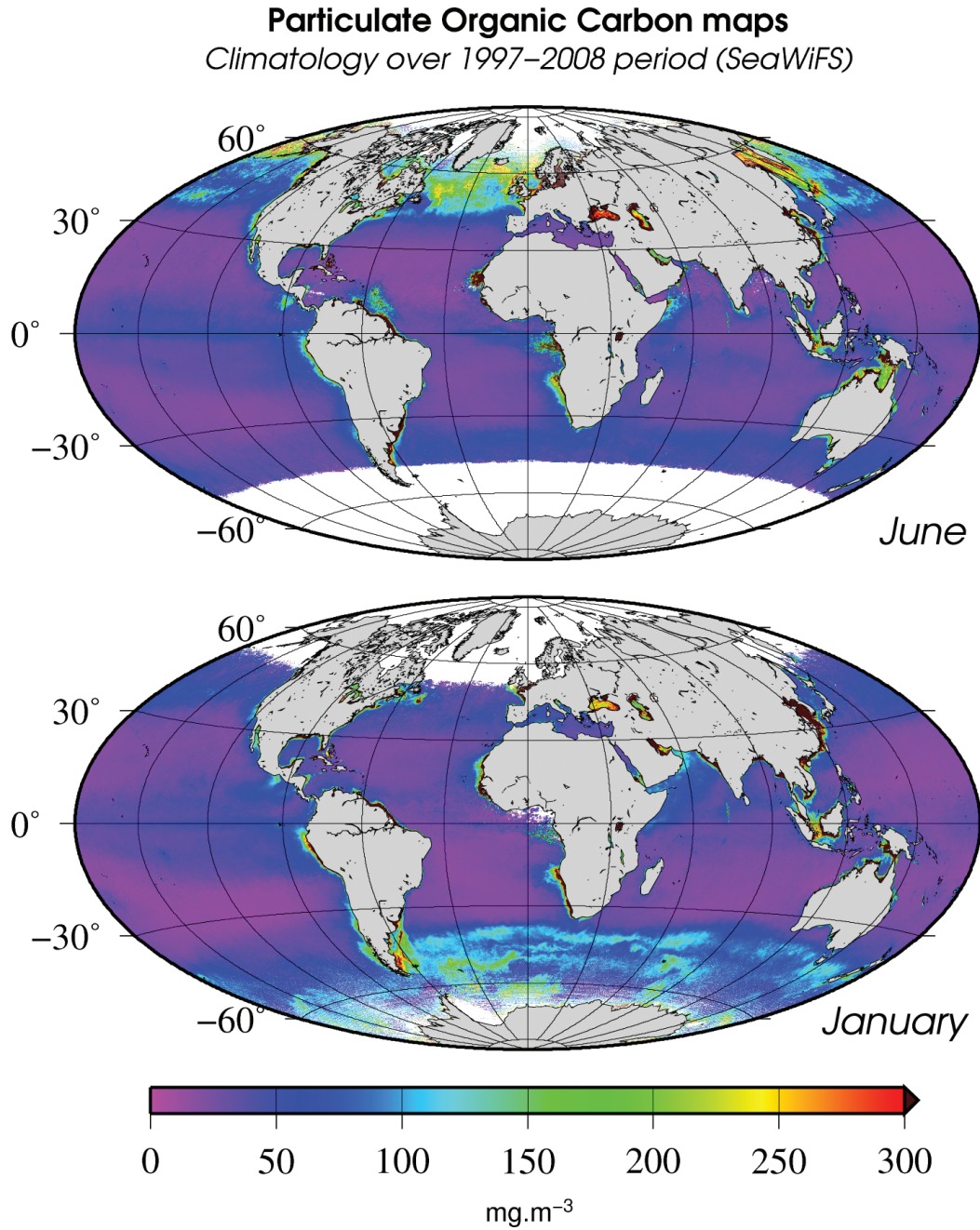


**Figure 7.1** Particulate organic carbon (POC) climatology maps (1997 - 2008, SeaWiFS) for the months of June and January.

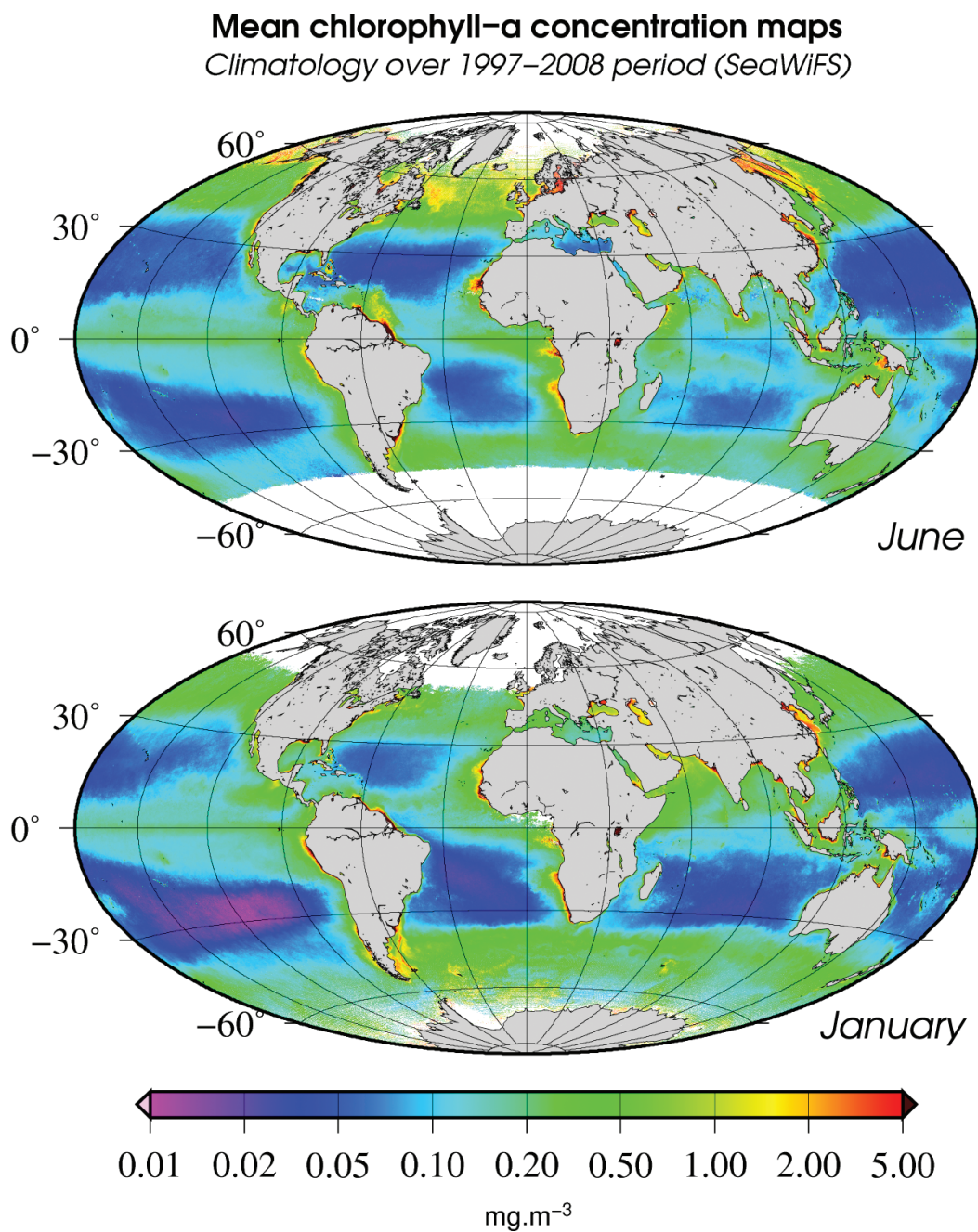


**Figure 7.2** Mean chlorophyll-*a* concentration climatology maps (1997 - 2008, SeaWiFS) for the months of June and January.

**Proxy of particle size distribution ( $\gamma$ ) maps**  
*Climatology over 1997–2008 period (SeaWiFS)*

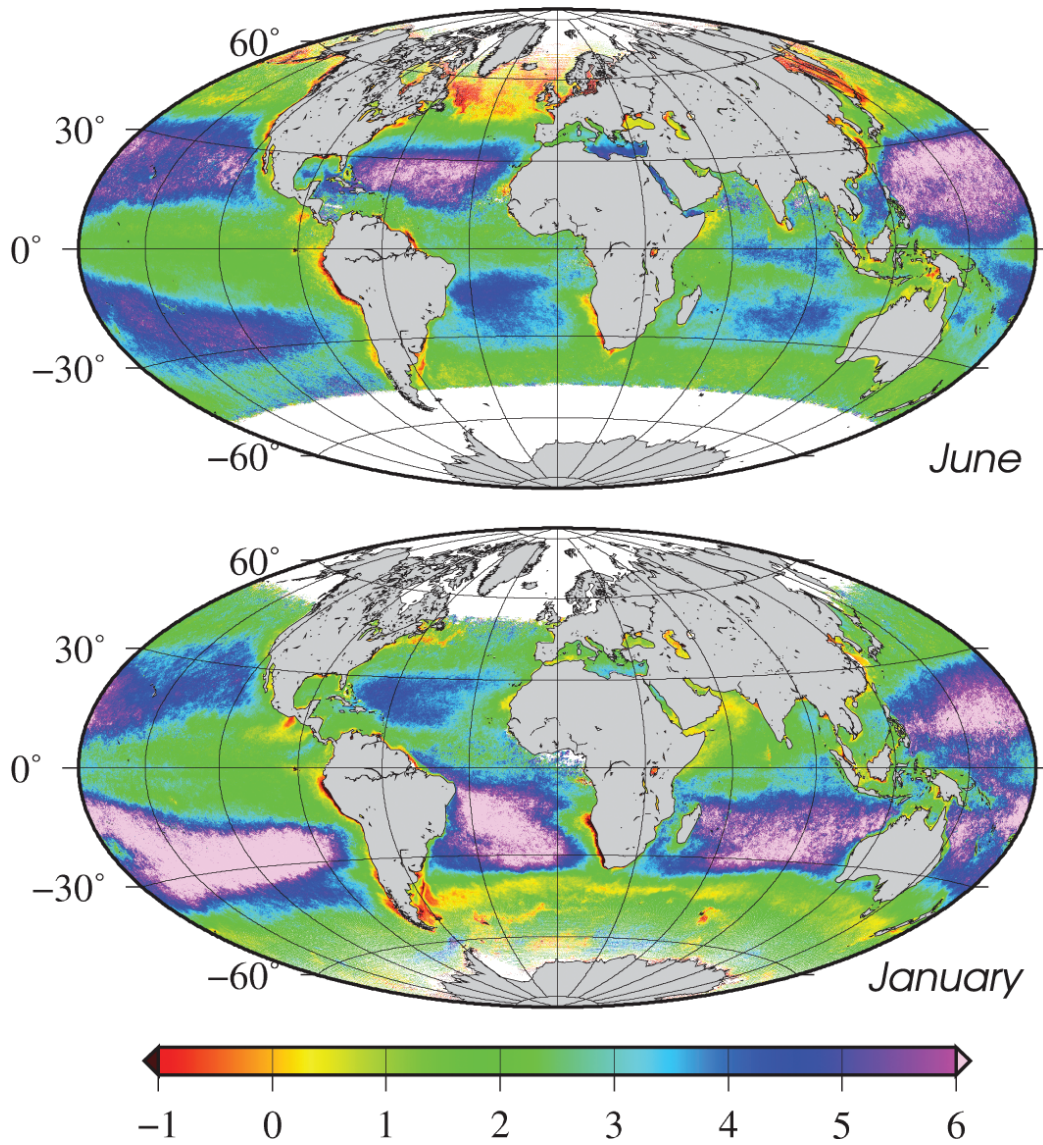


**Figure 7.3** Particle size distribution proxy ( $\gamma$ ) climatology maps (1997–2008, SeaWiFS) for the months of June and January.

**Dominant phytoplankton groups maps from PHYSAT**  
Climatology over 1997–2008 period (SeaWiFS)

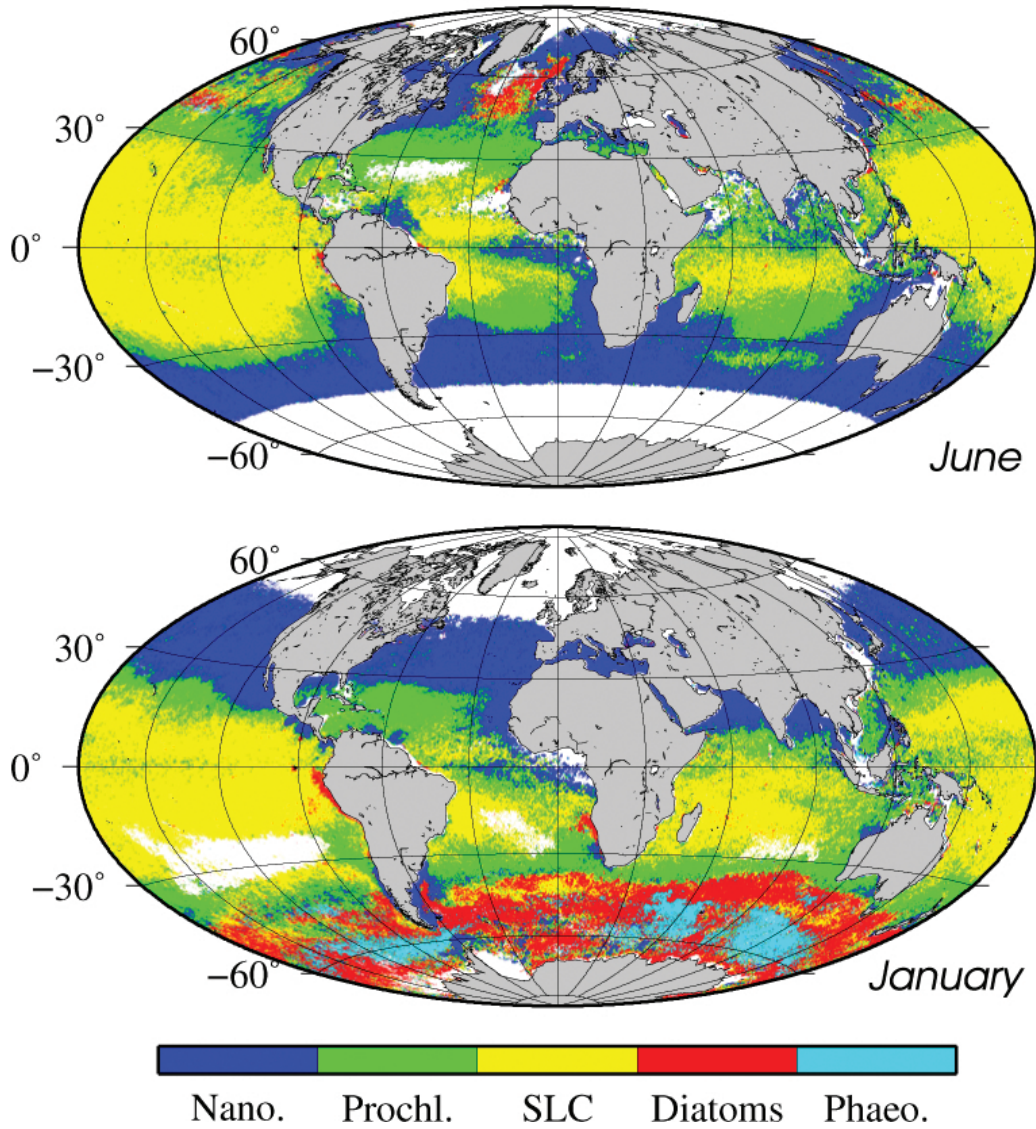


**Figure 7.4** Climatology maps (1997 - 2008, SeaWiFS) of dominant phytoplankton groups for the months of June and January, estimated using PHYSAT. Nano. = nanophytoplankton, Prochl. = *Prochlorococcus*, SLC = *Synechococcus*-like cyanobacteria (SLC), and Phaeo. = *Phaeocystis*.

The PHYSAT approach is based on the identification of specific signatures in the nLw spectra classically measured by ocean-colour sensors, after the previous criteria concerning atmospheric correction and [chl-*a*] has been applied. PHYSAT is an empirical method, established by comparing two kinds of simultaneous and coincident measurements: SeaWiFS nLw measurements and *in situ* measurements of biomarker phytoplankton pigments performed in the framework of the Gep&Co program (Dandonneau et al., 2004). In a first study, four dominant phytoplankton groups were identified within the GeP&CO dataset: diatoms, nanoeukaryotes, *Synechococcus* and *Prochlorococcus*. Recently, the PHYSAT method has been improved to detect an additional group, namely the *Phaeocystis*-like group, by analyzing specific signal anomalies in the Southern Ocean during winter months (Alvain et al., 2008). Note that the PHYSAT method allows detection of these groups only when they are dominant, that is, in situations where a given phytoplankton group is a major contributor (>60%) of the total pigment concentration. It is important to point out that, even if there is a general agreement on the taxonomic message of each biomarker pigment, for example, divinyl chlorophyll-*a* (d-chl-*a*), is associated with *Prochlorococcus*, a large range of relative concentrations (pigments ratios) can be found in the literature. Pigment ratios are defined as:

$$P_{\text{rel}} = P / ([\text{chl-}a] + [\text{d-chl-}a]), \quad (7.2)$$

where P is the measured biomarker pigment concentration. A thorough analysis of pigment ratios from the literature has allowed us to define a mean, relative concentration for each group, thus allowing thresholds to be fixed. A group is considered dominant when  $P_{\text{rel}}$  is at least equal to 60% of the total. Detailed information of the method including the use of thresholds is available in Alvain et al. (2005).

The key step in the success of methods such as PHYSAT is to associate *in situ* measurements with remote sensing measurements after having removed the first order variations due to the chlorophyll-*a* concentration (and classically used in previous ocean-colour products). Thus, a second step to establish PHYSAT has been to transform the nLw SeaWiFS spectra into specific normalized water leaving radiance, noted nLw\*, to determine the second order variability of the satellite signal. This was done by dividing the actual nLw by a mean nLw model (nLw<sub>ref</sub>), established from a large remote sensing dataset of nLw( $\lambda$ ) and [chl-*a*], cf. equation 7.3.

$$\text{nLw}^*(\lambda) = \text{nLw}(\lambda) / \text{nLw}_{\text{ref}}(\lambda, [\text{chl-}a]) \quad (7.3)$$

The nLw<sub>ref</sub> depends only on the standard SeaWiFS chlorophyll-*a*. By dividing nLw by this reference, we obtain a new product, denoted nLw\*, which is used in PHYSAT. Indeed, it has been shown that every dominant phytoplankton group sampled during the GeP&Co dataset is associated with a specific nLw\* spectrum. It is thus possible

to define a set of criteria to characterize each group as a function of its nLw\* spectrum. These criteria can thus be applied to the global daily SeaWiFS archive to obtain global monthly maps of the most frequently detected dominant groups, as shown in Figure 7.4. Note that when no group prevails over the period of one month, the pixels are associated with an 'unidentified' group. Alvain et al. (2008) studied the geographical distribution and seasonal succession of major dominant phytoplankton groups which are in good agreement with previous studies (Zubkov et al., 2000; DuRand et al., 2001; Marty and Chivérini, 2002; Dandonneau et al., 2004; Longhurst 2007). However, as for all empirical ocean-colour methodology, validation based on *in situ* measurements has to be pursued each time a suitable dataset is available.

### 7.3 Questions

**Q 1:** What can you say about the spatial distribution of POC, chl-*a* and dominant phytoplankton groups (from Figures 7.1, 7.2, and 7.4)? Look specifically at the following areas: (i) 45 - 52°N, 30 - 15°W and (ii) 47 - 40°S, 65 - 80°E for the month of January.

**Q 2:** In the future, what sort of potential applications could be considered from synergy of data of POC, [chl-*a*] and dominant phytoplankton groups?

**Q 3:** How would you explain the high POC concentration ( $\sim 250 - 300 \text{ mg m}^{-3}$ ) encountered around Alaska, British Isles and the Yellow East China Sea seen in Figure 7.1?

**Q 4:** What can you say about diatom distribution in Figure 7.4?

**Q 5:** What will PHYSAT detect (ideally) if the relative contribution to the total pigment concentration is: 20% for group 1, 40% for group 2 and 40% for group 3?

**Q 6:** Is it possible to apply PHYSAT, as described above, to coastal waters, and why?

**Q 7:** What should I do if I want to apply the PHYSAT method to a different satellite?

**Q 8:** What is essential to establish a method like PHYSAT ?

**Q 9:** What is essential to apply a method like PHYSAT, in addition to water leaving radiances?

**Q 10:** How could we validate PHYSAT or improve PHYSAT?

## 7.4 Answers

**A 1:** These two areas are almost identical in terms of chlorophyll-*a* concentration but are distinct in term of POC concentration. Furthermore, these two areas are also distinct in terms of phytoplankton groups. The region in the Southern ocean is dominated by diatoms whereas the region in the northern Atlantic is dominated by nanoeukaryotes. The actual results for these two areas for the period 1998 – 2006 are summarised below in Table. 1.

**Table 7.1** Mean near-surface POC and chlorophyll-*a* concentration over the areas in question for the SeaWiFS monthly climatology of January (1998 – 2006), as well as the percentage of pixels dominated by various phytoplankton groups (nano= nanophytoplankton; Prochl = *Prochlorococcus*; SLC = *Synechococcus*-like cyanobacteria; and Phaeo = *Phaeocystis*-like).

	(45–52°N, 30–15°W)	(47–40°S, 65–80°E)
Chl- <i>a</i> (mg m <sup>-3</sup> )	0.20 ± 0.07	0.33 ± 0.10
POC (mg m <sup>-3</sup> )	40.07 ± 10.8	172.8 ± 23.5
% Nano	98	8
% Prochl	2	4
% SLC	0	15
% Diatoms	0	69
% Phaeo	0	4

**A 2:** Coincident information of [chl-*a*], POC and dominant phytoplankton groups could be interpreted from an ecological point of view. We could carry out studies to investigate:

- ❖ links between dominant phytoplankton groups and the food web
- ❖ links between phytoplankton species and POC and chlorophyll-*a* concentration
- ❖ relationship between phytoplankton and POC and nutrients, irradiance and stratification.

In the future, new ocean colour parameters will help to assess the relationship between the total biomass and/or phytoplankton composition and productivity (for resource management).

**A 3:** In these areas, some of the high POC<sub>surf</sub> values may result from the presence of coastal waters, which carry particles of terrigenous origin which affect the remote sensing reflectance, resulting in an overestimate of the near-surface POC concentration. The algorithm described above is not appropriate for estimating POC content in these coastal waters. Consequently, these high POC concentrations should not be considered.

**A 4:** Diatom blooms are observed mainly in the North Atlantic and North Pacific Ocean during spring. During the austral summer, large blooms of diatoms are also observed at latitudes less than 30°S as well as in upwelling areas off the west coast

of southern Africa and South America.

**A 5:** In this case, PHYSAT will not detect a dominant group, since a dominant group should contribute at least 60% of the total pigment concentration.

**A 6:** No, because coastal waters are influenced by other organic and inorganic material (e.g. sediments, mineral particles, coloured dissolved organic matter) that can change the nLw but are not related to phytoplankton, and are not taken into account in PHYSAT.

**A 7:** In this case, it is necessary to calculate a new look up table containing the nLw<sub>ref</sub> spectra for the new satellite. It is also necessary to check and adapt thresholds used to classify nLw\* spectra.

**A 8:** As PHYSAT is an empirical method, it is essential to have *in situ* information about dominant phytoplankton groups (e.g. using pigments or others methods) and coincident and simultaneous water leaving radiance measurements, during very clear sky atmosphere conditions.

**A 9:** It is essential to have information about atmospheric conditions (such as aerosol optical thickness) and the concentration of chlorophyll-*a*.

**A 10:** Since PHYSAT is an empirical method, it is rather difficult to evaluate errors precisely. However, each time an *in situ* dataset with enough information about dominant phytoplankton groups is available, it is essential to use it to validate the method. Some optical studies are currently in progress to better understand the relationship between specific nLw\* spectra and specific dominant groups.

## 7.5 References

- Alvain S, Moulin C, Dandonneau Y, Bréon FM (2005) Remote sensing of phytoplankton groups in case 1 waters from global SeaWiFS imagery. *Deep-Sea Res I* 52: 1989-2004
- Alvain S, Moulin C, Dandonneau Y, Loisel H (2008) Seasonal distribution and succession of dominant phytoplankton groups in the global ocean: A satellite view. *Global Biogeochem Cycles* 22: GB3001, doi:10.1029/2007GB003154
- Claustre H, Morel A, Babin M, Cailliau C, Marie D, Marty JC, Talliez D, Vaulot D, (1999) Variability in particle attenuation and chlorophyll fluorescence in the tropical Pacific: Scales, patterns and biogeochemical implications. *J Geophys Res* 104(C2): 3401-3422
- Dandonneau Y, PY Deschamps, JM Nicolas, H Loisel, J Blanchot, Y Montel, F Thieuleux and G Bécu (2004) Seasonal and interannual variability of ocean color and composition of phytoplankton communities in the North Atlantic, Equatorial Pacific and South Pacific. *Deep Sea Res II* 51: 303-318
- DuRand MD, Olson RJ, Chisholm SW (2001) Phytoplankton population dynamics at the Bermuda Atlantic time-series station in the Sargasso Sea. *Deep Sea Res II* 48: 1983-2003
- Gordon HR, McCluney MR (1975) Estimation of the depth of the sunlight penetration in the sea for remote sensing. *Appl Opt* 14(2): 413-416
- Koike I, Hara S, Terauchi K, Kogure K (1990) Role of submicrometer particles in the ocean. *Nature* 345: 242-244

- Loisel H, Stramski D (2000) Estimation of the inherent optical properties of natural waters from the irradiance attenuation coefficient and reflectance in the presence of Raman scattering. *Appl Opt* 39(18): 3001-3011
- Loisel H, Bosc E, Stramski D, Oubelkheir K, Deschamps PY (2001) Seasonal variability of the backscattering coefficient in the Mediterranean Sea based on Satellite SeaWiFS imagery. *J Geophys Res Lett* 28(22): 4203-4206
- Loisel H, Nicolas J M, Deschamps P Y, Frouin R (2002) Seasonal and inter-annual variability of particulate organic matter in the global ocean. *Geophys Res Lett* 29(49): 2196, doi:10.1029/2002GL015948
- Loisel H, Poteau A (2006) Inversion of IOP based on Rrs and remotely retrieved Kd. In: IOCCG (2006). *Remote Sensing of Inherent Optical Properties: fundamental tests of algorithms and applications*. Reports of the International Ocean-Colour Coordinating Groups, No 5, Lee, ZP (ed), IOCCG, Dartmouth, Canada, p 35-42
- Longhurst A (2007) *Ecological Geography of the Sea*, 2nd Edition, Academic Press, San Diego, USA
- Marty JC, Chiavérini J, Pizay MD, Avril B (2002) Seasonal and interannual dynamics of nutrients and phytoplankton pigments in the western Mediterranean Sea at the DYFAMED time series station (1991-1999) *Deep Sea Res II*, 49: 2017-2030
- Morel A, Ahn YH (1991) Optics of heterotrophic nanoflagellates and ciliates: A tentative assessment of their scattering role in oceanic waters compared to those of bacterial and algal cells. *J Marine Res* 48: 1-26
- Morel A, Prieur L (1977) Analysis of variations in ocean color. *Limnol Oceanogr* 22(4): 709-722
- Reynolds RA, Stramski D, Mitchell BG (2001) A chlorophyll-dependent semi-analytical model derived from field measurements of absorption and backscattering coefficients within the Southern Ocean. *J Geophys Res* 106: 7125-7138
- Siegel DA, Maritorena S, Nelson NB (2002). Global distribution and dynamics of colored dissolved and detrital organic materials. *J Geophys Res* 107(C2): 3228, doi:10.1029/2001JC000965
- Smith RC, and Baker KS (1978) The bio-optical state of ocean waters and remote sensing. *Limnol Oceanogr* 23: 247-259.
- Stramski D, Kiefer DA (1991) Light scattering by microorganisms in the open ocean, *Prog Oceanogr* 28: 343-383
- Stramski D, Reynolds RA, Kahru M, Mitchell, BG (1999) Estimation of particulate organic carbon in the ocean from satellite remote sensing. *Science* 285: 239-241
- Stramski, D Reynolds RA, Babin M, Kaczmarek S, Lewis MR, Rottgers R, Sciandra A, Stramska M, Twardowski MS, Franz BA, Claustre H (2008) Relationships between the surface concentration of particulate organic carbon and optical properties in the eastern South Pacific and eastern Atlantic Oceans *Biogeosciences* 5: 171-201
- Twardowski MS, Boss E, Macdonald JB, Pegau WS, Barnard AH, Zaneveld JR (2001) A model for bulk refractive index from the optical backscattering ratio and the implications for understanding particle composition in case I and case II waters. *J Geophys Res* 106(C7): 14,129-14,142
- Zubkov MV, Sleigh MA, Burkill PH, Leakey RJG (2000) Picoplankton community structure on the Atlantic Meridional transect : A comparison between seasons. *Prog Oceanogr* 45: 369-386



## Case Study 8

# Monitoring Phytoplankton Productivity from Satellite: An Aid to Marine Resources Management

Frédéric Mélin<sup>\*1</sup> and Nicolas Hoepffner<sup>\*1</sup>

---

## 8.1 Introduction

An important biogeochemical quantity monitored by satellites is the concentration of chlorophyll-*a*, an omnipresent pigment in all phytoplankton species and, for this reason, commonly used as an index of phytoplankton biomass. In marine waters, phytoplankton biomass is a key component of the ecosystem. Phytoplankton are responsible for the conversion of carbon dioxide to organic carbon through the process of photosynthesis, i.e. primary production. Marine photosynthesis represents approximately half of the total carbon fixation in the global biosphere, making it a critical element of the Earth's carbon budget and biogeochemical cycles. In addition, phytoplankton biomass and primary production are descriptors of the first trophic level in the marine food chain. Quantitative estimates of these variables from satellite could therefore provide important information on the structure and functioning of the rest of the food web, up to commercially exploited fish populations.

## 8.2 Materials and Methods

### 8.2.1 Modelling phytoplankton photosynthesis

The process of photosynthesis requires the energy from sunlight, and takes place essentially in the euphotic layer of the oceans. For ecosystem analysis, the meaningful quantity to retrieve is the daily water column primary production, in mg of carbon fixed per m<sup>2</sup> per day. Several numerical methods have been described to estimate primary production in marine waters (see Behrenfeld and Falkowski 1997), all differing to some extent according to their resolution in depth and irradiance. Friedrichs et al. (2008) distinguished four categories of models: depth-integrated,

---

<sup>1</sup>European Commission - Joint Research Centre, Institute for Environment and Sustainability, Via E. Fermi 2749, I-21027 Ispra, Italy. \*Email addresses: [frederic.melin@jrc.it](mailto:frederic.melin@jrc.it) and [nicolas.hoepffner@jrc.ec.europa.eu](mailto:nicolas.hoepffner@jrc.ec.europa.eu)

wavelength-integrated models; depth-resolved but wavelength integrated models; depth-integrated but wavelength-resolved models; and models resolving both the depth and the irradiance wavelength. For the purpose of this exercise, the model used fits within the fully resolved category, following the developments by Platt and Sathyendranath (1988) as implemented at global scale by Longhurst et al. (1995). A commonality in many of these models is the requirement for a suitable knowledge of the light field and phytoplankton biomass at any given location, depth and time. The instantaneous rate of photosynthesis or primary production is commonly formulated as:

$$PP(z, \lambda, t) = f[B(z), \phi(\lambda, z), E_{PAR}(\lambda, t)] \quad (8.1)$$

where  $B$  is the phytoplankton biomass commonly indexed by the concentration of chlorophyll- $a$ ,  $\phi$  measures the physiological capacity of phytoplankton organisms to perform photosynthesis considering the surrounding conditions, and  $E_{PAR}$  is the total irradiance available for photosynthesis between 400 and 750 nm.

### 8.2.2 Estimation of surface irradiance

The estimation of surface irradiance and the modelling of its propagation through the water column are key aspects of oceanography. This is particularly true in the spectral range 350–700 nm that defines the photosynthetically available radiation, PAR. Assuming that this spectral interval represents roughly half of the total solar flux at the ocean surface, total PAR could be derived simply from a global database of solar fluxes, such as the International Satellite Cloud Climatology Project (ISCCP, Schiffer and Rossow 1983). Another method is to obtain PAR directly from ocean-colour satellites (Frouin et al. 2003). However, the selected model of primary production for this exercise requires a complete description of the spectral and angular characteristics of the incident light. Ignoring these properties could result in a significant bias in the light absorption by phytoplankton and subsequent errors in the final results (Kyewalyanga et al. 1992).

The formalism used here to calculate the incident light at the sea surface was originally described by Bird and Riordan (1986) and adapted by Platt and Sathyendranath (1988) for its implementation in marine primary production modelling. Gregg and Carder (1990) have completed this model for purely oceanographic applications with a spectral resolution for direct and diffuse irradiance of 1 nm over the interval 350–700 nm. In the case of clear sky, the direct [ $E_{dd}(\lambda)$ ] and diffuse [ $E_{ds}(\lambda)$ ] components of the irradiance are formulated separately as:

$$E_{dd}(\lambda) = \mu_0 E_0(\lambda) T_r(\lambda) T_a(\lambda) T_{03}(\lambda) T_{02}(\lambda) T_w(\lambda) \quad (8.2)$$

$$E_{ds}(\lambda) = E_{dsr}(\lambda) + E_{dsa}(\lambda) \quad (8.3)$$

where  $\mu_0$  is the cosine of the sun zenith angle, and  $E_0$  the extra-terrestrial solar irradiance. The direct light path through the atmosphere is modified according to the transmittance properties of various compounds, including Rayleigh scattering ( $T_r$ ), aerosol extinction ( $T_a$ ), as well as ozone ( $T_{O_3}$ ), water vapor ( $T_w$ ), and oxygen ( $T_{O_2}$ ) absorption. The diffuse component is the sum of the contributions from the molecules (Rayleigh scattering)  $E_{dsr}$  and the aerosols  $E_{dsa}$ .

All transmittance functions are calculated using meteorological variables either directly available from satellite data or from climatological databases. Under clear sky conditions, an accurate description of the aerosol optical properties and their distribution in time and space is a necessary requirement to estimate the irradiance at the surface. Satellite-based ocean colour radiometry has the capacity to provide aerosol characteristics (optical thickness and Ångström exponent), with an appropriate resolution in time and space to monitor their variability over the oceans.

The effect of clouds on the surface light field is three fold. They i) lower the irradiance intensity at the sea surface; ii) change the shape of the irradiance spectrum; and iii) reinforce the diffuse part of the irradiance with respect to the direct component. These effects can be modelled if appropriate information on clouds is available, such as the cloud optical thickness and structure derived by remote sensing, or the value of the albedo of the ocean-cloud system, for instance known with the distribution of reflectivity in the UV as provided by TOMS (McPeters 1998).

### 8.2.3 Underwater light field

Estimating primary production in the entire illuminated layer of the ocean requires some knowledge of the light field at any depth within the water column up to a level of minimum sunlight (i.e. euphotic depth). This is done through a bio-optical model which accounts for both the optical properties inherent to the water itself and material in suspension (absorption and scattering), and the distribution /geometry of the light field.

#### 8.2.3.1 Water optical properties

As the sunlight penetrates in the water column, its magnitude and spectral quality is altered by water molecules ( $w$ ) and optically significant constituents like phytoplankton ( $ph$ ), non-algal particles ( $np$ ) (detritus, minerals) and a coloured fraction of the total dissolved organic matter ( $cdom$ ). The total absorption [ $a(\lambda)$ ] and scattering [ $b(\lambda)$ ] coefficients of the water are then:

$$a(\lambda) = a_w(\lambda) + a_{ph}(\lambda) + a_{np}(\lambda) + a_{cdom}(\lambda) \quad (8.4)$$

represented by the sum of the optical properties inherent to each of these constituents.

$$b(\lambda) = b_w(\lambda) + b_{ph}(\lambda) + b_{np}(\lambda) \quad (8.5)$$

In practice, the bio-optical model assumes Case 1 waters where the inherent optical properties of the constituents co-vary with phytoplankton concentration.

The absorption spectrum of phytoplankton,  $a_{ph}(\lambda)$ , between 400 and 750 nm is characterized by a continuous envelope reflecting a strong coupling in the energy transfer between photosynthetic pigments to the photosystems. The spectral shape and magnitude of the absorption coefficient is parameterized as a function of the chlorophyll concentration according to Bricaud et al. (1995), statistically representative of various marine conditions. The formulation accounts for differences in the composition of pigments within the phytoplankton cells, as well as in cell size (package effect) which translates to a flattening effect of  $a_{ph}(\lambda)$  for large-cell phytoplankton communities.

For non-algal particles and dissolved organic substances, the spectral absorption obeys a similar exponential curve defined by the absorption coefficient at a reference wavelength and its slope in the lower part of the spectrum (400–440 nm). The curve parameters for  $a_{np}(\lambda)$  are parameterized as a function of the chlorophyll-*a* concentration according to Bricaud et al. (1998). In the case of  $a_{cdom}(\lambda)$ , the bio-optical model assumes a constant slope and an amplitude of the absorption coefficient at 440 nm equivalent to a fixed ratio of the total absorption by particles and pure sea water.

The absorption due to pure sea water,  $a_w(\lambda)$ , plays a large role in the photon budget calculation, particularly in the red part of the visible spectrum where it reaches maximal values. In the blue part of the spectrum, the absorption coefficient of water molecules is used to determine the level of the euphotic depth, hence the productive layer.

With respect to scattering properties, a clear identification of the particles responsible for the optical signal remains difficult. In the estimation of primary production, scattering properties are calculated for total particulate matter, i.e. phytoplankton and non-algal particles, based on a statistical regression between chlorophyll-*a* concentration and the scattering coefficient at 550 nm (Loisel and Morel 1998). Scattering by dissolved substances is assumed to be negligible.

### 8.2.3.2 Propagation of the light in the water column

The vertical propagation of the light field is modelled according to Sathyendranath and Platt (1988; 1989), taking into account the attenuation coefficients for direct and diffuse light. The geometry of the light field is expressed through the mean cosine of light propagation weighted by the direct and diffuse component of the

downwelling irradiance. The objective of this exercise is to estimate the light flux received by a unit volume of water from all directions, the so-called scalar irradiance, which is the quantity useful for photosynthesis.

### 8.2.4 Model implementation

Measuring the water column primary production from space also requires some knowledge of parameters that are not accessible from satellite, such as the vertical profile of phytoplankton biomass, as well as other optically-significant constituents, and the photosynthetic parameters reflecting the capacity of phytoplankton communities to assimilate dissolved inorganic carbon through photosynthesis. These parameters have to be retrieved from field observations and their interpolation to meet the spatial and temporal resolution of satellite data are a key step of the work.

#### 8.2.4.1 Biomass depth profile

The absorption and scattering coefficients, as well as the attenuation of light through the water column, are functions of the chlorophyll concentration. Two options can be considered for the vertical distribution of phytoplankton biomass: i) the vertical distribution of the phytoplankton biomass is uniform in a well-mixed surface layer, therefore the chlorophyll concentration at any depth is equivalent to that at the surface (possibly retrieved by satellite), and ii) in stratified conditions, a subsurface maximum usually occurs at depths ranging from close to the surface down to the bottom of the euphotic layer (i.e., 1% or 0.1% light level). The vertical distribution of the phytoplankton biomass in this case is represented by assuming a Gaussian distribution superimposed on a background chlorophyll concentration (Sathyendranath and Platt 1989). Its application in our primary production model requires *a priori* knowledge of three additional parameters defining the Gaussian curve.

#### 8.2.4.2 Photosynthetic parameters

The relationship between the rate of carbon assimilation by phytoplankton and the submarine irradiance is described by a well-known photosynthesis-light model. More specifically, the primary production normalized to chlorophyll concentration is a function of scalar irradiance, described through a curve (P-E curve) defined by two parameters: the photosynthetic rate at light saturation (or assimilation number,  $P_m^B$ ) and the initial slope of the curve (light-limited photosynthetic rate,  $\alpha^B$ ). A number of mathematical formalisms have been proposed to describe the P-E curve, starting with a 2-step linear function (Blackman 1906), to hyperbolic tangent (Jassby and Platt 1976), and exponential formulations with or without photo-inhibition (Platt et al. 1980). The photosynthetic parameters issued from statistical

regression on field measurements using one or another of these formalisms reflects the physiological characteristics of the phytoplankton community under specific environmental factors.

#### **8.2.4.3 Biogeographical provinces**

Applying satellite data to retrieve the water column daily primary production requires specification of the five parameters described above (three describing the vertical structure of the biomass profile and two for the photosynthetic efficiency) on a pixel-by-pixel basis. Different options can be considered when assigning the parameters: i) constant values of the parameters at all locations and time; ii) the parameters are continuously variable, responding in the same way to changes in the forcing factors or; iii) some regional differences in the relationship between the parameters and the forcing factors constrict the assignment of the parameters to some ecological provinces, well defined in time and space. Substantial variability has been observed in the parameters of the biomass profile (Morel and Berthon 1989; Uitz et al. 2006), as well as the photosynthetic parameters (Kyewalyenga et al. 1998; Forget et al. 2007). In light of these *in situ* measurements, assigning a constant value to the parameters is therefore not appropriate. The application of a global smooth function relating each, or a combination of these parameters, to physical variables would be ideal, especially if the physical variables can be retrieved from satellite. Morel and Berthon (1989) provided solutions to retrieve the Gaussian parameters of the biomass profile from surface chlorophyll, which was used as an indicator of the trophic state. These relationships were then confirmed by Uitz et al. (2006) using a different data set.

On the other hand, the relationships between phytoplankton physiology and physical variables are more complex. Spatial discontinuities in the photosynthetic parameters are perceptible, reflecting regional diversity in the phytoplankton community response to physical forcing (Bouman et al. 2005). One technique suggested by Platt and Sathyendranath (1988), consists of partitioning the studied area into several provinces, each having its own set of the required parameters. Within each province, the parameters are either assumed constant for a given time period, e.g. seasons (Longhurst et al. 1995; Sathyendranath et al. 1995) or vary continuously with the physical conditions (Platt et al. 2008).

### **8.3 Demonstration: Application to global primary production**

The primary production budget is calculated for three different months in 2006 and given for the global ocean, as well as selected basins. The processing starts with the global estimation of the sun irradiance at the surface and satellite-derived

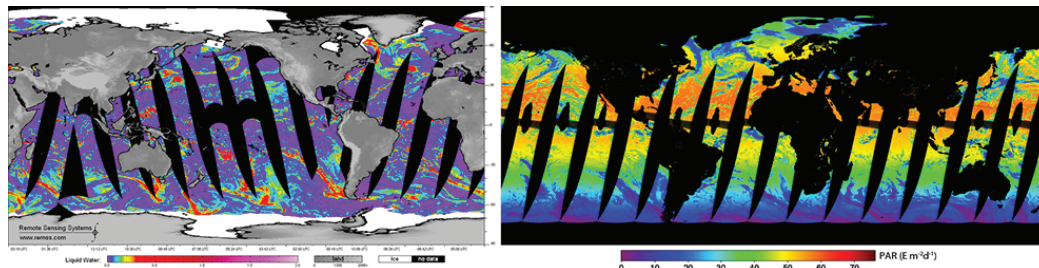


**Figure 8.1** Daily maps of cloud liquid water content (left panel) and photosynthetically available radiation, PAR (right panel) for May 8, 2006.

chlorophyll concentration. These are inputs to the local model of primary production which, after selection of the parameters, will then be integrated over time (first over a day), depth and wavelength to yield a monthly map of daily water-column primary production.

The geophysical products necessary for the calculation of irradiance in the case of a clear sky can be identified as: i) atmospheric pressure, relative humidity, precipitable water vapor, and wind at the water surface; ii) ozone concentration; iii) aerosol characteristics. The values for the first group are provided as meteorological products by NCEP (National Center for Environmental Prediction, <http://www.ncep.noaa.gov/>), with a spatial resolution of  $1^\circ \times 1^\circ$  (only the NCEP map given at noon is used). The ozone concentration is available through TOMS (Total Ozone Mapping Spectrometer, <http://toms.gsfc.nasa.gov/>) with a spatial resolution of  $1.25^\circ$  in longitude and  $1^\circ$  in latitude, which is extrapolated onto a grid of  $1^\circ \times 1^\circ$ . The aerosol characteristics are provided on a monthly basis by the SeaWiFS products ( $\sim 9$  km resolution, as provided by the GSFC- DAAC, Goddard Space Flight Center, Distributed Active Archive Center, <http://daac.gsfc.nasa.gov/>). Since this temporal frequency does not guarantee a complete coverage, the SeaWiFS aerosol maps are re-gridded onto maps of reduced spatial resolution ( $1^\circ$ ).

For cloudy sky, it is assumed that the value of the albedo of the ocean-cloud system is known with the distribution of reflectivity (at 360 nm) provided by TOMS (McPeters 1998). The value of reflectivity provided by TOMS is then compared to the content of a look-up table of solutions of the radiative transfer problem for the cloud layer, pre-computed for various values of cloud liquid water path (LWP, Figure 8.1). The associated value of LWP immediately provides the value of transmittance for direct light from the same look-up table of pre-computed solutions of the radiative transfer problem with the cloud layer. Total direct irradiance is finally calculated as the direct irradiance for clear sky weighted by the direct transmittance under cloud conditions (Figure 8.2).

The surface chlorophyll concentration or phytoplankton biomass can be obtained directly from various ocean colour sensors and data archives, at the appropriate space agencies (e.g., <http://oceancolor.gsfc.nasa.gov/>). In the case of SeaWiFS and

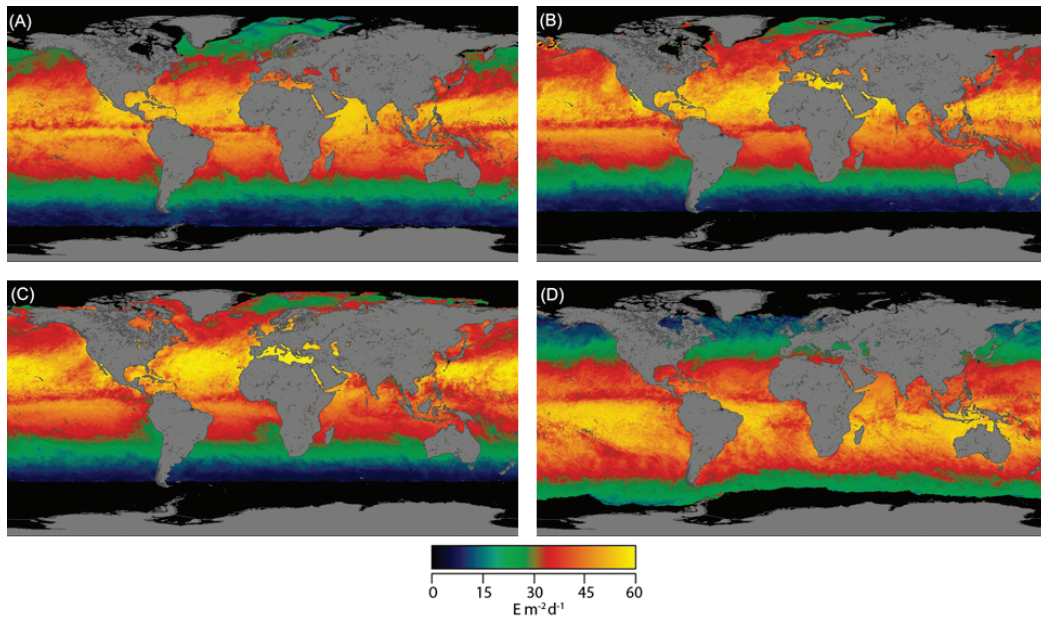


**Figure 8.2** Monthly composites of daily photosynthetic active radiation (PAR) as computed directly from SeaWiFS data for April (A), May (B), July (C) and October (D), using top-of-atmosphere radiance to infer the attenuation of solar irradiance through the atmosphere (Frouin et al. 2003). Units are Einstein  $\text{m}^{-2} \text{day}^{-1}$  with a scale typically ranging from 0 to 60. One "Einstein" is equivalent to one mole of photons.

MODIS chlorophyll products, daily standard mapped image (SMI) Level 3 (Figure 8.3) are distributed in a global equidistant cylindrical projection (or sinusoidal equal area grid for MERIS data) with a spatial resolution of 4320 pixels in longitude and 2160 pixels in latitude. The resolution is ca. 0.0833, equivalent to 9.28 km at the equator. For global and regional analysis, higher resolution data can be obtained by processing Level 1-A data with dedicated software packages freely available from space agencies (e.g., SeaDAS, <http://oceancolor.gsfc.nasa.gov/seadas/>; and BEAM, <http://www.brockmann-consult.de/cms/web/beam/software>).

Having defined the surface photosynthetically active radiation and phytoplankton biomass, we now need to specify the five parameters required to obtain the water-column integrated daily primary production i.e. three parameters to describe the vertical structure of the phytoplankton biomass, and two parameters to describe the photosynthetic efficiency of the organisms.

In this exercise, the primary production model uses a partition of the global ocean into biomes and provinces (Longhurst 1998; Figure 8.4), based on factors such as light conditions, circulation patterns, nutrient inputs, the bathymetry and other elements linking our current knowledge on regional oceanography to the response of phytoplankton to physical forcing. Statistical analyses are performed on the available *in situ* databases to retrieve the most representative set of parameters for

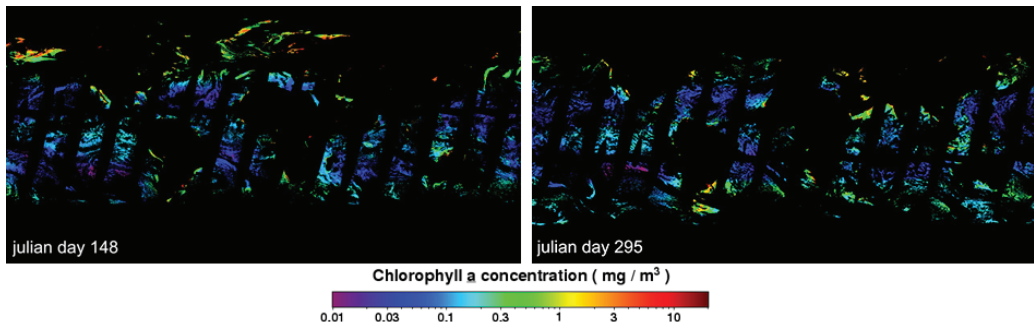


**Figure 8.3** Daily scenes of Level 3 chlorophyll product as processed from SeaWiFS for day 148 (May 28, 2006) and day 295 (Oct. 22, 2006).

each of the provinces and/or biomes that will be assumed to remain constant for an appropriate time period (e.g. seasons).

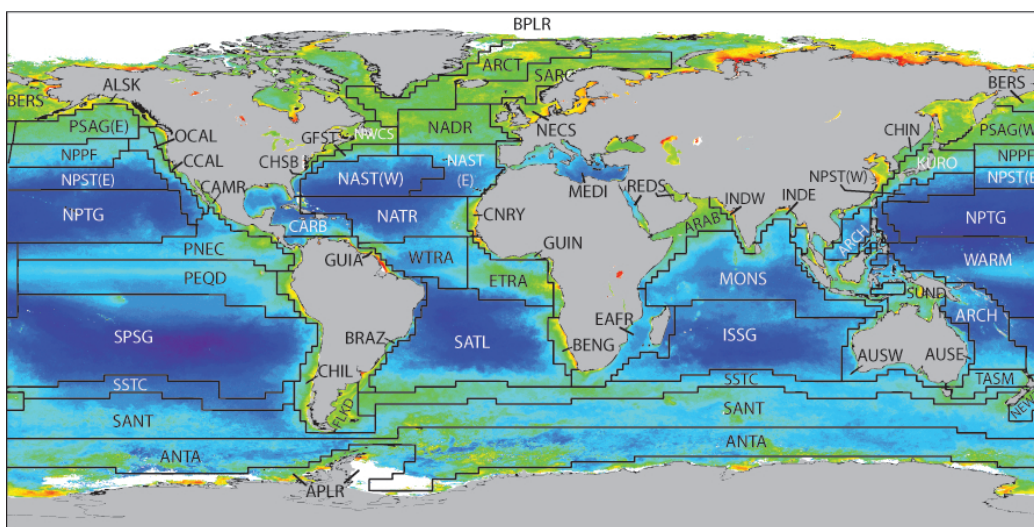


**Figure 8.4** Distribution of the Longhurst oceanographic provinces adopted for the global ocean. Definition and acronyms of the provinces are detailed in Longhurst (1998; 2006).

Equation 15.1 can now be used to calculate primary production from daily scenes of surface chlorophyll concentrations, applying a spectral model to estimate the underwater light field at a given time and depth interval within the euphotic zone. The final output is the water-column integrated daily rate of primary production given in  $\text{g C m}^{-2} \text{d}^{-1}$ .

## 8.4 Questions

**Q1:** Based on Figure 8.2 and the section on estimation of surface irradiance (Section 8.2.2), what would be the primary and secondary drivers of PAR (photosynthetically active radiation) on a global scale?

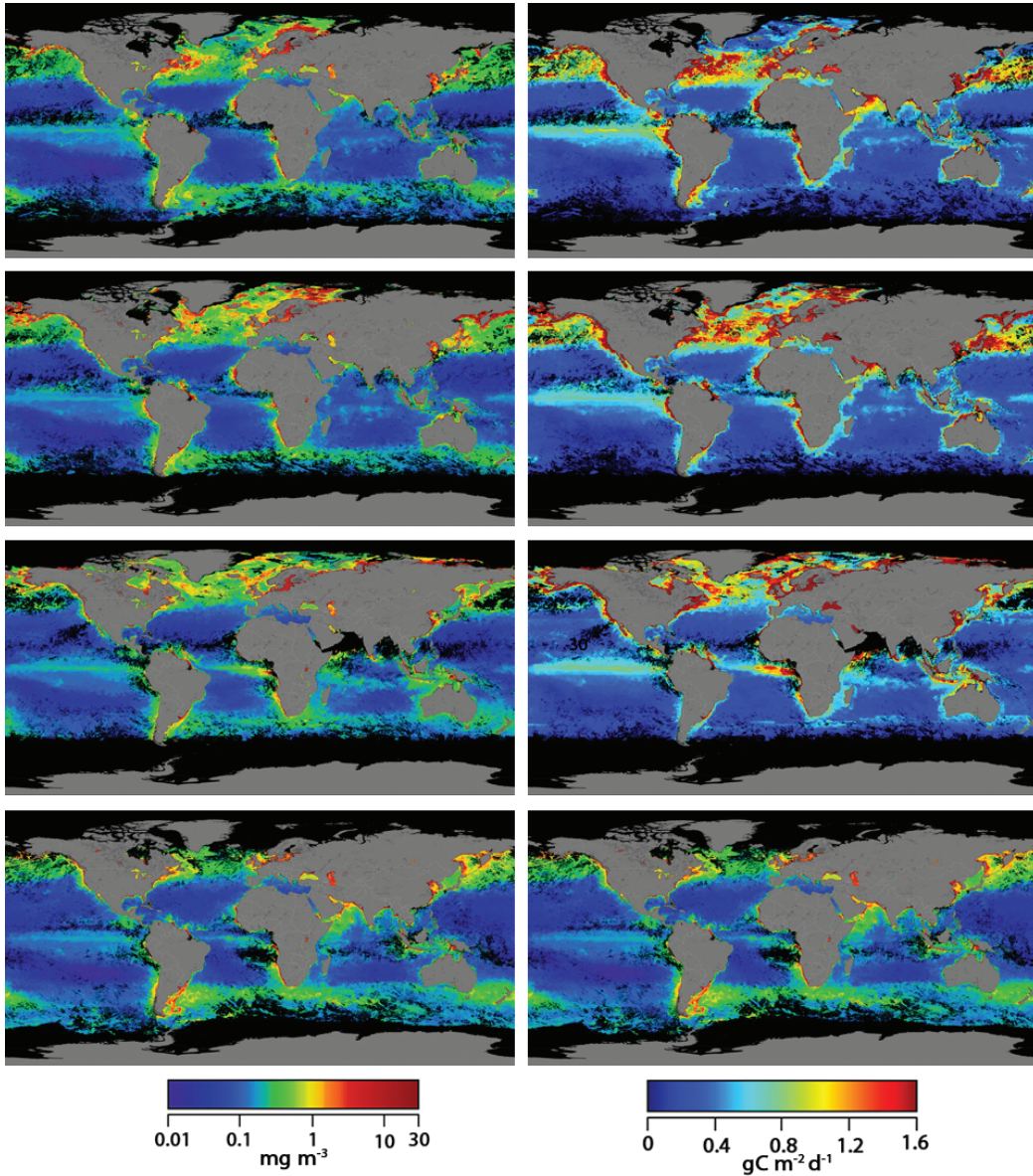


**Figure 8.5** Global monthly composites of surface chlorophyll concentration (left panel) and primary production (right panel) as derived from SeaWiFS data for April, May, July and October 2006. Areas in black have no data.

**Q2:** What are the main drivers of primary production on a global scale? Discuss this by comparing the maps for primary production (Figure 8.5 right panel) with those of PAR (Figure 8.2) and chlorophyll concentrations (Figure 8.5 left panel).

**Q3:** What are the reasons for lack of data for Chla and primary production on Figure 8.5?

**Q4:** Looking at the maps in Figure 8.5, what are the main features you can observe in terms of temporal and spatial variability?

**Q5:** High primary production can be seen in coastal zones and marginal seas. Why is it consistent with expectations? Given the models presented above, why is the uncertainty on the derived primary production likely to be higher?

**Q6:** Looking at the global maps of primary production and zooming in on some regions, e.g. southeastern Africa and the Agulhas Current (Figure 8.6), what can you say about some of the surface features?

**Q7:** At what level of accuracy can primary production be retrieved using satellite data?

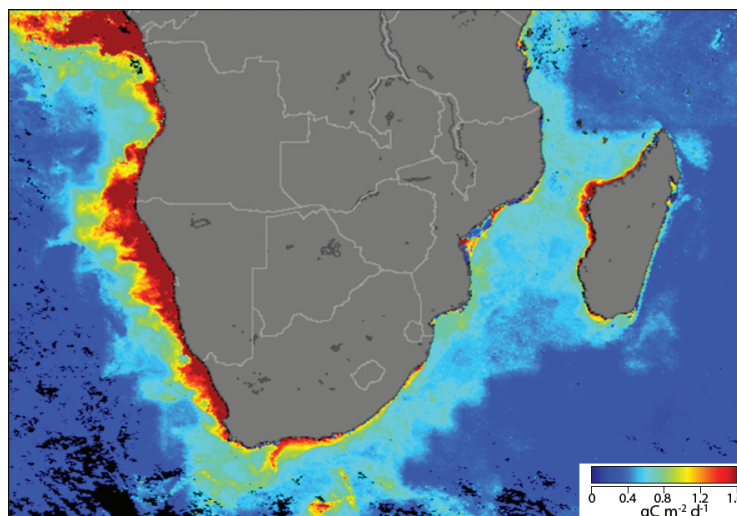


**Figure 8.6** Primary production along South Africa-Madagascar region (extracted from the global map in Figure 8.5)

## 8.5 Answers

**A1:** On a theoretical basis, the solar irradiance at the top-of-atmosphere is proportional to the cosine of the solar zenith angle. The irradiance value at the sea surface is therefore directly affected by the solar angle. In turn, the solar zenith angle is a

function of latitude and day of the year (or season). PAR intensity and day length thus vary with location and season, which can be seen when comparing Figures 8.2c and d: the zone of maximum PAR shifts in latitude with season.

The other main driver of PAR is cloud cover. It changes the PAR amplitude, spectral shape at the surface, and geometry (diffuse-to-direct ratio). Aerosols have a similar effect, even though it is less pronounced, except in cases of strong aerosol events linked with desert dust or biomass burning. In general, these secondary effects are seen in the figures by zonal variations of PAR at a given latitude (Figure 8.2). A persistent feature is the relative minimum in PAR found slightly north of the Equator. This should be a region of maximum PAR, but it is characterized by a recurrent cloud cover associated with the Inter-Tropical Convergence Zone, where convection generates clouds.

**A2:** Phytoplankton biomass or chlorophyll concentration is the main driver of primary production. This is further modulated by PAR. If PAR was the dominant controlling factor, areas at subtropical latitudes with high PAR would show high productivity, which is generally not the case. At these latitudes, heat energy from the more intense sunlight is absorbed in the upper layers of the ocean, leading to a quasi-persistent stratification of the water column. This structure would prevent any supply of new nutrients from the deep oceans to the productive illuminated surface layer, thus keeping the productivity at low levels based on locally regenerated nutrients.

At higher latitudes, stratification of the water column occurs in spring as temperature increases, subsequently trapping large amount of nutrients from winter mixing in the euphotic layer. Favorable conditions of nutrients and light trigger phytoplankton blooms and productivity as seen in Figure 8.5 in the April and May composites.

**A3:** Lack of data in monthly composites of phytoplankton biomass and primary production could result from:

1. Very low sun zenith angle in local winter: for example, the northern seas between Scandinavia and Greenland have significantly more coverage in April and May than in October (Figure 8.5). Processing of chlorophyll images, and hence the estimation of primary production, is restricted to sun zenith angles lower than  $70^\circ$ . The sun zenith angle is a function of time, day number and latitude.
2. Persistent cloud cover: ocean colour sensors only perform in clear sky conditions. Time-composite mapping enables a better coverage of the area of interest, to some extent, increasing the probability of obtaining cloud free scenes over each pixel. Nevertheless, areas with no data are still visible in monthly maps (Figure 8.5), especially along the equator. This area corresponds to a zone of persistent cloud cover previously described (see Answer 1) as the

Inter-Tropical Convergence Zone.

3. Persistent thick aerosol plumes: as for clouds, important aerosol emission events such as desert dust plumes or biomass burning can prevent any signal from the water surface from reaching the satellite sensor. These events are recurrent along the west coast of Africa as wind blows over the Sahara and Sahel regions.

**A4:** On a global scale, the variability in primary production is driven by the seasonal cycle. Comparing productivity values in the North Atlantic in April-May with that in October clearly shows an intensification of phytoplankton production in spring. On the contrary, in the southern hemisphere, productivity at higher latitudes tends to be higher in the October map than in April-May. The mechanism associated with that seasonal cycle is partly explain in Answer 2. Another noticeable feature in Figure 8.5 is a narrow band of higher productivity along the equator. The prevailing currents, combined with the Earth's rotation generates an upwelling process, and nutrient-rich deep waters are lifted to the surface layers.

**A5:** Relative to open ocean waters, coastal and shelf areas receive large fluxes of nutrients from rivers, and from upwelling processes at the coast. Higher productivity in these waters is thus expected. The four major eastern boundary upwelling systems along the coast of north- and southwest Africa, California, and Peru are well identified in the primary production maps (Figure 8.5) as permanent features, although the strength of the upwelling process varies seasonally. Note that these upwelling systems account for only 5% of the global ocean, but support major world fisheries.

Caution should be taken in the interpretation of primary production values in coastal areas: the bio-optical model presented above follows the Case-1 water assumption, where optical properties co-vary with Chlorophyll-*a*. At the coast, the water can be optically more complex than the open ocean waters because of the large influence by the land system and catchment basins delivering significant amounts of dissolved and particulate material to the coast. These additional substances, evolving independently from phytoplankton, impact on the derivation of chlorophyll concentration from satellite using standard "case 1 water" algorithms, but also on the propagation of light through the water column, as they compete with phytoplankton for light absorption.

**A6:** Caution should be taken in the interpretation of some surface features observed in the primary production maps (e.g. staircase-like features, straight and squared angle fronts). These are methodological artifacts associated with the partition of the global ocean into specific biogeographical provinces, each of them having their own set of model parameters reflecting their ecological characteristics (Longhurst, 1998). To tackle regional issues, it may be necessary to re-examine in more detail, the interactions between physics and biology in the region and the annual variability

of the forcing fields, such that more realistic provinces can be established for the studied area. The number of provinces will depend on the knowledge of the regional oceanography and the availability of the data required for primary production calculation.

In Longhurst's original work, the provinces have geometrical shapes (Figure 8.4) with fixed boundaries in space and time, although some adjustment could be applied from year to year according to the variability of inter-annual forcings. As a result, sharp squared-like discontinuities occur between provinces. This artifact does not alter in any way the estimated value of the primary production for each province, which relies on careful selection of parameters. Various protocols have been developed for a more dynamic partitioning of the oceans, using remotely-sensed data to locate the province boundaries and enable their adjustment in real-time. Readers are referred to Report # 9 of the International Ocean Colour Coordinating Group (IOCCG, 2009) for the various approaches in addressing oceanic ecosystem classification.

**A7:** As mentioned in the introduction, several models to retrieve primary production from remotely-sensed data have been developed during the last two decades. The performance of these models, including the one described in this exercise, were analysed in a series of round-robin experiments aiming at an extensive comparative assessment of the models (Carr et al., 2006), and their validation against *in situ* measurements (Friedrichs et al., 2009; Saba et al., in press). The mean RMSD (root mean square deviation) of 21 ocean colour models was 0.29 relative to *in situ* primary production values collected in the tropical Pacific, with the model described here being amongst the best performing (Friedrichs et al., 2009). However, the model's success varies substantially from region to region (Saba et al., in press), and in general the performance is still limited by the accuracy of the input variables, particularly uncertainties in satellite-derived chlorophyll values.

## 8.6 References and further reading

- Behrenfeld M, Falkowski P (1997) A consumer's guide to phytoplankton primary production models. *Limnol Oceanogr* 42: 1479-1491
- Bird R, Riordan C (1986) Simple solar spectral model for direct-normal and diffuse horizontal irradiance. *Sol Energy* 32: 461-471
- Bouman H, Platt T, Sathyendranath S, Stuart V (2005) Dependence of light-saturated photosynthesis on temperature and community structure. *Deep-Sea Res I* 52: 1284-1299
- Bricaud A, Morel A, Babin M, Allali K, Claustre H (1998) Variations of light absorption by suspended particles with chlorophyll a concentration in oceanic (case 1) waters: analysis and implications for bio-optical models. *J Geophys Res* 103: 31033-31044
- Bricaud A, Babin M, Morel A, Claustre H (1995) Variability in the chlorophyll-specific absorption coefficients of natural phytoplankton: analysis and parameterization. *J Geophys Res* 100: 13321-13332
- Carr M-E, et al. (2006) A comparison of global estimates of marine primary production from ocean color. *Deep-Sea Res II* 53: 741-770

- Dowell M, Platt T (eds) *Partition of the Ocean into Ecological Provinces: Role of Ocean-Colour Radiometry*. Reports of the International Ocean Colour Coordinating Group, No 9, IOCCG, Dartmouth, Canada
- Forget M-H, Sathyendranath S, Platt T, Pommier J, Vis C, Kyewalyanga MS, Hudon C (2007) Extraction of photosynthesis-irradiance parameters from phytoplankton production data: demonstration in various aquatic systems. *J Plank Res* 29: 249-262
- Friedrichs MAM et al. (2009) Assessing the uncertainties of model estimates of primary productivity in the tropical Pacific Ocean. *J Mar Syst* 76: 113-133
- Frouin R, Franz B, Werdell P (2003) The SeaWiFS PAR product. In SB Hooker and ER Firestone (eds ), NASA TM, 2003-206892, Vol 22, chap 8, pp 46-50 NASA-GSFC
- Gregg W, Carder K (1990) A simple spectral irradiance model for cloudless maritime atmospheres. *Limnol Oceanogr* 35: 1657-1675
- Jassby A, Platt T (1976) The relationship between photosynthesis and light for natural assemblages of marine phytoplankton. *J Mar Res* 12: 421-430
- Kyewalyanga M, Platt T, Sathyendranath S (1992) Ocean primary production calculated by spectral and broad-band models. *Mar Ecol Prog Ser* 85: 171-185
- Kyewalyanga M, Platt T, Sathyendranath S, Lutz VA, Stuart V (1998) Seasonal variations in physiological parameters of phytoplankton across the North Atlantic. *J Plank Res* 20: 17-42
- Loisel H, Morel A (1998) Light scattering and chlorophyll concentration in case 1 waters: a reexamination *Limnol Oceanogr* 43: 847-858
- Longhurst A, Sathyendranath S, Platt T, Caverhill C (1995) An estimate of global primary production in the ocean from satellite radiometer data. *J Plank Res* 17: 1245-1271
- Longhurst A (1998) *Ecological geography of the sea*, pp 398. San Diego: Academic Press.
- IOCCG (2009) *Partition of the Ocean into ecological provinces: role of ocean colour radiometry*. Dowell M, Platt T (eds) Reports of the International Ocean Colour Coordinating Group, No 9, IOCCG, Dartmouth, Canada
- McPeters R, et al. (1998) Earth Probe Total Ozone Mapping Spectrometer (TOMS) data user's guide. In NASA TM, 1998-206895, pp 1-64 NASA-GSFC
- Morel A, and J-F Berthon (1989) Surface pigments, algal biomass profiles and potential production of the euphotic layer: relationships reinvestigated in view of remote sensing applications. *Limnol Oceanogr* 34: 1545-1562
- Platt T, Sathyendranath S (1988) Oceanic primary production: estimation by remote sensing at local and regional scales. *Science*, 241: 1613-1620
- Platt T, Gallegos C, Harrison W (1980) Photoinhibition of photosynthesis in natural assemblages of marine phytoplankton. *J Mar Res* 38: 687-701
- Platt T, Sathyendranath S, Forget M-H, White III GN, Caverhill C, Bouman H, Devred E, and Son S (2008) Operational estimation of primary production at large geographical scales. *Rem Sens Environ* 112: 3437-3448
- Saba VS et al. (in press) Estimating marine primary productivity in coastal and pelagic regions across the globe: an evaluation of satellite-based ocean color models. *Biogeosciences*
- Sathyendranath S, Platt T (1988) The spectral irradiance field at the surface and in the interior of the ocean: a model for applications in oceanography and remote sensing. *J Geophys Res* 93: 9270-9280
- Sathyendranath S, Platt T (1989) Computation of aquatic primary production: extended formalism to include effect of angular and spectral distribution of light. *Limnol Oceanogr* 34: 188-198
- Sathyendranath S, Longhurst A, Caverhill C, Platt T (1995) Regionally and seasonally differentiated primary production in the North Atlantic. *Deep-Sea Res* 42: 1773-1802
- Schiffer R, Rossow W (1983) The international cloud climatology project (ISCCP): The first project of the Worlds Climate Research Program. *Bull Amer Meteor Soc* 64: 779-784
- Uitz J, Claustre H, Morel A, Hooker SB (2006) Vertical distribution of phytoplankton communities in open ocean: an assessment based on surface chlorophyll. *J Geophys Res* 111: C08005, doi:10.1029/2005JC003207



## Case Study 9

# Detecting Phytoplankton Community Structure from Ocean Colour

R.J.W. Brewin<sup>\*1</sup>, N.J. Hardman-Mountford<sup>2</sup>, T. Hirata<sup>3</sup>

---

## 9.1 Background

Phytoplankton play a fundamental role in the biogeochemical cycling of the planet, with different phytoplankton communities having specific biogeochemical roles (Le Quéré et al. 2005; Nair et al. 2008). Phytoplankton support marine ecosystems as the primary carbon source for zooplankton, fish and ultimately higher predators. Furthermore, zooplankton and fish can have selective feeding preferences for phytoplankton of different sizes and types (Hansen et al. 1994; Scharf et al. 2000; Jennings et al. 2002). By improving our understanding of the spatial structure of the different phytoplankton communities, advances in biogeochemical and food-web models can be made, which may enhance our comprehension of the Earth system needed to predict future change.

Methods that can identify and quantify different elements of the phytoplankton community can provide useful information to help understand biogeochemical and ecological processes. Observing the *in situ* size structure and taxonomic grouping of phytoplankton at a global scale is, however, a challenging task. Satellite observation is currently the only practical method of observing the global ocean synoptically. With increasing concern as to how climate variation is affecting marine ecosystems, there is a large expectation of satellite remote sensing to provide global observations of the taxonomic or functional groups of phytoplankton, moving beyond conventional pigment biomass (i.e. chlorophyll).

Recently, a variety of bio-optical and ecological methods have been established that use satellite data to identify and differentiate between phytoplankton functional types (PFTs) or phytoplankton size classes (PSCs) in the surface ocean. These can be summarised into four main types: spectral-response methods which are based on

---

<sup>1</sup>School of Marine Science and Engineering, University of Plymouth, UK. \*Email address: [robert.brewin@plymouth.ac.uk](mailto:robert.brewin@plymouth.ac.uk)

<sup>2</sup>National Centre for Earth Observation, Plymouth Marine Laboratory, UK

<sup>3</sup>Graduate School of Environmental Earth Science, Hokkaido University, Japan

differences in the shape of the light reflectance/absorption spectrum for different PFTs/PSCs (Sathyendranath et al. 2004; Alvain et al. 2005; Ciotti and Bricaud 2006; Alvain et al. 2008; Brewin et al. 2010a), abundance-based methods which use information on the magnitude of chlorophyll biomass or light absorption to distinguish between phytoplankton communities (Devred et al. 2006; Uitz et al. 2006; Hirata et al. 2008a; Brewin et al. 2010b), methods that retrieve the particle size distribution from satellite-derived backscattering signal and then relate the particle size to the phytoplankton community (Hirata et al. 2008b; Kostadinov et al. 2009), and ecological-based approaches which use information on environmental factors, such as temperature and wind stress to supplement the bio-optical data for investigating specific taxa (Raitsos et al. 2008). Recent intercomparison studies suggest that abundance-based approaches appear robust at detecting dominant phytoplankton size classes (Brewin et al. 2008).

### 9.1.1 Phytoplankton size class model

Here we present a method for determining the fractional contribution of a phytoplankton size class (pico-  $<2\mu\text{m}$ , nano-  $2\text{--}20\mu\text{m}$  and micro-phytoplankton  $>20\mu\text{m}$ ) to the overall chlorophyll concentration (Brewin et al. 2010b). The model is an extension of the Sathyendranath et al. (2001) approach, based on the assumption that small cells dominate at low chlorophyll concentrations and large cells at high concentrations. The model can be expressed through two simple exponential equations. In this example the subscripts 1, 2 and 3 refer to pico-, nano- and microphytoplankton, and the total chlorophyll-*a* concentration is referred to as  $C$  ( $\text{mg m}^{-3}$ ). Firstly, the chlorophyll concentration of the combined pico-nanophytoplankton population ( $C_{1,2}$ ) can be expressed as:

$$C_{1,2} = C_{1,2}^m [1 - \exp(-S_{1,2}C)], \quad (9.1)$$

where,  $C_{1,2}^m$  is the asymptotic maximum value for  $C_{1,2}$  and  $S_{1,2}$  determines the increase in  $C_{1,2}$  with increasing total chlorophyll ( $C$ ). Secondly, the chlorophyll concentration of the picophytoplankton population ( $C_1$ ) can be expressed as:

$$C_1 = C_1^m [1 - \exp(-S_1C)], \quad (9.2)$$

where  $C_1^m$  is the asymptotic maximum value for  $C_1$  and  $S_1$  determines the increase in  $C_1$  with increasing total chlorophyll-*a* ( $C$ ). The chlorophyll-*a* concentration of nanophytoplankton ( $C_2$ ) and microphytoplankton ( $C_3$ ) can then be calculated according to:

$$C_2 = C_{1,2} - C_1, \quad (9.3)$$

$$C_3 = C - C_{1,2}. \quad (9.4)$$

The percentage of each phytoplankton size class to the total chlorophyll concentration ( $C$ ) can then be calculated by dividing the size-specific chlorophyll concentrations ( $C_1$ ,  $C_2$  and  $C_3$ ) by the total chlorophyll concentration ( $C$ ) and multiplying by 100, such that

$$P_1 = (C_1/C) \times 100, \quad (9.5)$$

$$P_2 = (C_2/C) \times 100, \quad (9.6)$$

$$P_3 = (C_3/C) \times 100, \quad (9.7)$$

where  $P_1$ ,  $P_2$  and  $P_3$  represent the percentages of pico-, nano- and microphytoplankton to the total chlorophyll concentration ( $C$ ). Parameter values for  $C_{1,2}^m$ ,  $C_1^m$ ,  $S_{1,2}$  and  $S_1$  were taken from Table 1 in Brewin et al. (2010b), and set to 1.06, 0.11, 0.85 and 6.80, respectively. When using these parameters, the model performed well when applied to satellite chlorophyll data and compared with *in situ* measurements (see section 4.3 in Brewin et al. 2010b).

Figure 9.1 shows the results from applying the model of Brewin et al. (2010b) to SeaWiFS satellite data for January and July 2006. The model was applied to daily total chlorophyll ( $C$ ) images from each month and then averaged to produce the two monthly composite images. The results show clearly that very small phytoplankton cells (picophytoplankton,  $<2\mu\text{m}$ ) dominate in the low-production, subtropical gyres, medium-sized cells (nanophytoplankton,  $2\text{-}20\mu\text{m}$ ) predominate in the equatorial upwelling area and in higher latitude regions depending on the boreal or austral summer. Relatively large cells (microphytoplankton,  $>20\mu\text{m}$ ) dominate in coastal areas and during highly productive events, such as high-latitude spring/summer blooms. Furthermore, the size fractionation shows that nanophytoplankton tend to maintain a background population of between 20-50% of the standing stock in most regions, whereas pico- and microphytoplankton have larger spatial variability.

### 9.1.2 Equatorial Pacific

The equatorial Pacific is a unique region of our oceans. It can act as a large source of  $\text{CO}_2$  to the atmosphere through the upwelling of  $\text{CO}_2$ -rich waters along the equator and advection of  $\text{CO}_2$ -rich waters from the South-American coast (Etcheto et al. 1999; Feely et al. 1999), and also a sink through primary production and export (Takahashi et al. 2002). It is one of only three open-ocean areas that, despite having high nitrate and phosphate concentrations, display moderately-low phytoplankton biomass (Martin 1991; Behrenfeld et al. 1996) and are referred to as exhibiting High Nutrient, Low Chlorophyll characteristics (HNLC, Thomas 1979). This enigma has been linked to either the lack of iron that limits the growth of the phytoplankton (Martin and Fitzwater 1988; Behrenfeld et al. 1996; Coale et al. 1996) or to a large amount

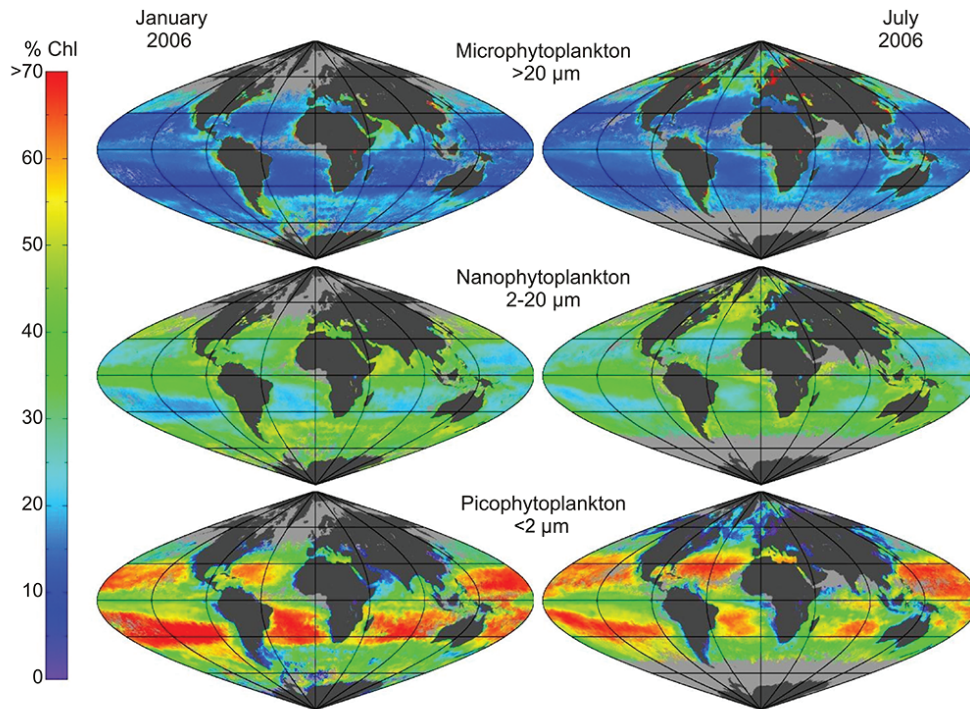


**Figure 9.1** The percentage of total chlorophyll-*a* attributed to each of three phytoplankton size classes calculated according to the model of Brewin et al. (2010b), for the months of January and July 2006. The model was applied to daily Level 3 SeaWiFS composite images from each month and then averaged to produce monthly composites. Light grey pixels represent unidentified pixels due to cloud coverage or high sun zenith angles and dark grey pixels represent land.

of grazing from higher trophic levels that limits phytoplankton growth (Walsh 1976; Cullen 1991). Despite exhibiting moderately-low phytoplankton biomass, changes in the phytoplankton composition and sporadic large-scale accumulations of phytoplankton biomass have been found to occur (Chavez et al. 1990; Ryan et al. 2002), making the equatorial Pacific an ideal site to monitor variations in phytoplankton composition from satellite.

The model of Brewin et al. (2010b) was developed using an extensive dataset from the Atlantic Ocean, and validated using data with wider geographical coverage. However, the model of Brewin et al. (2010b) has not been validated in the equatorial Pacific. In light of this, 32 High Performance Liquid Chromatography (HPLC) pigment measurements (depth <10m) were downloaded from the NASA SeaBASS dataset (Werdell and Bailey 2002). Using diagnostic pigment analysis (Vidussi et al. 2001; Uitz et al. 2006; Brewin et al. 2010b) the *in situ* size-specific chlorophyll concentrations ( $C_1$ ,  $C_2$  and  $C_3$ ) and size-specific percentage contributions to the total chlorophyll concentration ( $P_1$ ,  $P_2$  and  $P_3$ ) were calculated for each sample. Then the

model of Brewin et al. (2010b) was applied to the *in situ* chlorophyll concentration to estimate  $C_1$ ,  $C_2$ ,  $C_3$ ,  $P_1$ ,  $P_2$  and  $P_3$  (Equations 9.1 – 9.7). Figure 9.2 shows the location of the 32 pigment measurements and a comparison between the diagnostic pigment-derived values and the values derived using the model. The two agreed well with an absolute root mean square error (RMSE) of 0.006 to 0.010  $\text{mg m}^{-3}$  for the size-specific chlorophyll concentrations, and between 4.4 to 9.4 % for the percentage contributions to the total chlorophyll concentration, supporting the application of the Brewin et al. (2010b) model to the equatorial Pacific.

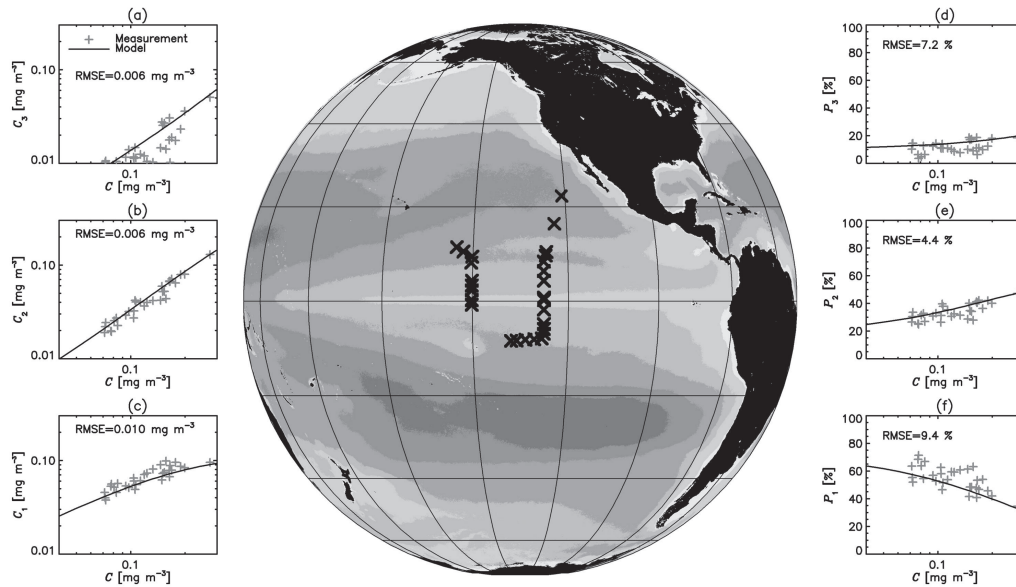


**Figure 9.2** Location of the 32 HPLC pigment measurements used to validate the model of Brewin et al. (2010b) for use in the equatorial Pacific. The biome-based system of Hardman-Mountford et al. (2008) is superimposed on the globe with dark grey to light grey areas representing a transition from biomes with very low chlorophyll-*a* to biomes with very high chlorophyll-*a*. Results of the validation are shown to the left ( $C_1$ ,  $C_2$  and  $C_3$ ) and right ( $P_1$ ,  $P_2$  and  $P_3$ ) of the globe.

In this case study we apply the model of Brewin et al. (2010b) to daily, Level 3, SeaWiFS chlorophyll composites to produce two 8-day composites of the percentage contribution of the three size classes to total chlorophyll ( $P_1$ ,  $P_2$  and  $P_3$ ), for 28 July – 4 August 1998 and 2003. We also produce two images of SST derived from the Advanced Very High Resolution Radiometer (AVHRR) sensor, for the same time periods. Differences in SST and the community composition of the three size classes, for the same seasonal week in the two contrasting years, are mapped in the equatorial Pacific.

## 9.2 Data and Methods

Sixteen daily Level 3 mapped SeaWiFS chlorophyll composites were downloaded from the NASA ocean colour website (<http://oceancolor.gsfc.nasa.gov/>), encompassing two eight-day periods.

- Week 1 (28 July – 4 August 1998)
- Week 2 (28 July – 4 August 2003)

All SeaWiFS data were extracted from the zipped format. Two SST AVHRR global composites for the same 8-day periods (week 1 and 2) were downloaded from the NASA Jet Propulsion Laboratory Physical Oceanography Distributed Active Archive Centre (<ftp://podaac.jpl.nasa.gov/>). Night time AVHRR Pathfinder (Version 5) 8-day means of sea surface temperature (SST) at 4 x 4 km<sup>2</sup> resolution were used. Night time SST products were used so that the solar radiation bias (the diurnal fluctuation in SST) that can occur from surface heating during daytime could be avoided. We used global, equal-angle, best SST. Information on the data used in this study is outlined in Table 9.1.

The software used in this study was IDL Version 6.3, Microsoft Windows (Win32 x86 m32). All IDL code developed for this study is available at <http://www.ioccg.org/handbook/Brewin/>. The procedure below has been developed into an IDL program (Handbook\_RS\_PSC\_code.pro) to allow the reader to reproduce this example (see section 1.4 Training below).

The first step involves loading the sixteen daily Level 3 mapped SeaWiFS chl-*a* composites into the IDL program. All sixteen daily SeaWiFS composites are loaded into IDL using code developed by the Ocean Color Discipline Processing Group (readl3smi.pro). This code is designed to simplify the reading of SeaWiFS standard L3 mapped images, and converts the digital numbers (DN) of the image to chlorophyll-*a* values (mg m<sup>-3</sup>). Once these images are loaded, the Brewin et al. (2010b) algorithm (Equations 9.1 – 9.7) is applied to each daily image on a pixel-by-pixel basis to derive  $P_1$ ,  $P_2$  and  $P_3$  (the percentages of pico-, nano- and microphytoplankton to the total chlorophyll-*a* concentration ( $C$ )).

The daily composites from week 1 are then averaged to create 8-day composites of  $P_1$ ,  $P_2$  and  $P_3$ , and the same averaging is applied to the eight daily composites from week 2. Note that we applied the Brewin et al. (2010b) algorithm to daily images then averaged to produce an 8-day composite, as opposed to applying the algorithm directly to 8-day SeaWiFS chlorophyll-*a* composites, as the nonlinearity of equations 1 and 2 could introduce errors when applying the model directly to 8-day SeaWiFS chlorophyll-*a* composites.

The two SST images are then loaded into IDL using IDL code developed by the National Oceanographic Data Centre (pathfinder\_v5\_hdf\_read.pro). Once these images are loaded, the data is converted to SST values (°C) from digital numbers (DN) according to:

$$\text{SST} = 0.075 \times \text{DN} - 3.0, \quad (9.8)$$

where the value 0.075 represents the slope and -3.0 the y-intercept. This results in six, 8-day,  $9 \times 9 \text{ km}^2$  resolution composites (arrays of [4320, 2160]) of  $P_1$ ,  $P_2$ ,  $P_3$  for both week 1 and 2, and two 8-day  $4 \times 4 \text{ km}^2$  resolution composites (arrays of [8192, 4096]) of SST for both week 1 and 2. The differences between the two contrasting weeks are then calculated according to:

$$P_{1,D} = P_1(\text{week1}) - P_1(\text{week2}), \quad (9.9)$$

$$P_{2,D} = P_2(\text{week1}) - P_2(\text{week2}), \quad (9.10)$$

$$P_{3,D} = P_3(\text{week1}) - P_3(\text{week2}), \quad (9.11)$$

$$\text{SST}_D = \text{SST}(\text{week1}) - \text{SST}(\text{week2}), \quad (9.12)$$

where,  $P_{1,D}$ ,  $P_{2,D}$ ,  $P_{3,D}$  and  $\text{SST}_D$  refer to the difference between the three size classes and SST of the two contrasting weeks. This results in 12 images to be used for analysis:  $P_1(\text{week1})$ ,  $P_2(\text{week1})$ ,  $P_3(\text{week1})$ ,  $\text{SST}(\text{week1})$ ,  $P_1(\text{week2})$ ,  $P_2(\text{week2})$ ,  $P_3(\text{week2})$ ,  $\text{SST}(\text{week2})$ ,  $P_{1,D}$ ,  $P_{2,D}$ ,  $P_{3,D}$  and  $\text{SST}_D$ . All 12 images are then rescaled to  $36 \times 36 \text{ km}^2$  resolution, to reduce computational requirements when plotting the images.

A plotting procedure is then set up to plot each of these 12 images and re-project them using an orthographic projection. The corresponding latitude and longitude values were calculated for each pixel. Values of each pixel in the image are binned into 256 ranges, and each range is assigned a colour depending on the colour scheme chosen. These 256 bins are then plotted onto an image of 1080 by 540 pixels, with each pixel representing  $36 \times 36 \text{ km}^2$  resolution. All pixels with no values (either due to cloud coverage or high sun zenith angles) are binned and assigned a light grey colour before being plotted. Using the SeaWiFS entire mission chlorophyll-*a* composite, a land mask has been developed (see "Land\_mask", <http://www.iocccg.org/handbook/Brewin/Data/>) and the land is assigned a dark grey colour before being plotted onto the image.

Each image is then re-projected to an orthographic projection using the IDL functions "map\_set.pro" and "map\_proj\_image.pro". Here we took the latitude of the point on the Earth's surface to be mapped to the centre of the projection plane to be  $0^\circ$ , and the longitude of the point on the Earth's surface to be mapped to the centre of the map projection to be  $-130^\circ$ , to focus our attention to the equatorial Pacific. All 12 images are then projected onto the same image montage for analysis, and the respective colour bars for each image are also plotted (Figure 9.3).

**Table 9.1** Satellite data used in the study (also available at <http://www.ioccg.org/handbook/Brewin/Data/>), including a land mask.

Date	Data	Filename	Location	Use
28/07/98	chl-a	S1998209.L3m_DAY _CHL_chlor_a_9km.bz2	<a href="http://oceancolor.gsfc.nasa.gov/cgi/13">http://oceancolor.gsfc.nasa.gov/cgi/13</a>	8-day PSC
29/07/98	chl-a	S1998210.L3m_DAY _CHL_chlor_a_9km.bz2	<a href="http://oceancolor.gsfc.nasa.gov/cgi/13">http://oceancolor.gsfc.nasa.gov/cgi/13</a>	8-day PSC
30/07/98	chl-a	S1998211.L3m_DAY _CHL_chlor_a_9km.bz2	<a href="http://oceancolor.gsfc.nasa.gov/cgi/13">http://oceancolor.gsfc.nasa.gov/cgi/13</a>	8-day PSC
31/07/98	chl-a	S1998212.L3m_DAY _CHL_chlor_a_9km.bz2	<a href="http://oceancolor.gsfc.nasa.gov/cgi/13">http://oceancolor.gsfc.nasa.gov/cgi/13</a>	8-day PSC
01/08/98	chl-a	S1998213.L3m_DAY _CHL_chlor_a_9km.bz2	<a href="http://oceancolor.gsfc.nasa.gov/cgi/13">http://oceancolor.gsfc.nasa.gov/cgi/13</a>	8-day PSC
02/08/98	chl-a	S1998214.L3m_DAY _CHL_chlor_a_9km.bz2	<a href="http://oceancolor.gsfc.nasa.gov/cgi/13">http://oceancolor.gsfc.nasa.gov/cgi/13</a>	8-day PSC
03/08/98	chl-a	S1998215.L3m_DAY _CHL_chlor_a_9km.bz2	<a href="http://oceancolor.gsfc.nasa.gov/cgi/13">http://oceancolor.gsfc.nasa.gov/cgi/13</a>	8-day PSC
04/08/98	chl-a	S1998216.L3m_DAY _CHL_chlor_a_9km.bz2	<a href="http://oceancolor.gsfc.nasa.gov/cgi/13">http://oceancolor.gsfc.nasa.gov/cgi/13</a>	8-day PSC
28/07/03	chl-a	S2003209.L3m_DAY _CHL_chlor_a_9km.bz2	<a href="http://oceancolor.gsfc.nasa.gov/cgi/13">http://oceancolor.gsfc.nasa.gov/cgi/13</a>	8-day PSC
29/07/03	chl-a	S2003210.L3m_DAY _CHL_chlor_a_9km.bz2	<a href="http://oceancolor.gsfc.nasa.gov/cgi/13">http://oceancolor.gsfc.nasa.gov/cgi/13</a>	8-day PSC
30/07/03	chl-a	S2003211.L3m_DAY _CHL_chlor_a_9km.bz2	<a href="http://oceancolor.gsfc.nasa.gov/cgi/13">http://oceancolor.gsfc.nasa.gov/cgi/13</a>	8-day PSC
31/07/03	chl-a	S2003212.L3m_DAY _CHL_chlor_a_9km.bz2	<a href="http://oceancolor.gsfc.nasa.gov/cgi/13">http://oceancolor.gsfc.nasa.gov/cgi/13</a>	8-day PSC
01/08/03	chl-a	S2003213.L3m_DAY _CHL_chlor_a_9km.bz2	<a href="http://oceancolor.gsfc.nasa.gov/cgi/13">http://oceancolor.gsfc.nasa.gov/cgi/13</a>	8-day PSC
02/08/03	chl-a	S2003214.L3m_DAY _CHL_chlor_a_9km.bz2	<a href="http://oceancolor.gsfc.nasa.gov/cgi/13">http://oceancolor.gsfc.nasa.gov/cgi/13</a>	8-day PSC
03/08/03	chl-a	S2003215.L3m_DAY _CHL_chlor_a_9km.bz2	<a href="http://oceancolor.gsfc.nasa.gov/cgi/13">http://oceancolor.gsfc.nasa.gov/cgi/13</a>	8-day PSC
04/08/03	chl-a	S2003216.L3m_DAY _CHL_chlor_a_9km.bz2	<a href="http://oceancolor.gsfc.nasa.gov/cgi/13">http://oceancolor.gsfc.nasa.gov/cgi/13</a>	8-day PSC
28/07/98 - 04/08/98	SST	1998209-1998216. s0481pfv50-bsst-16b	<a href="ftp://podaac.jpl.nasa.gov/pub/">ftp://podaac.jpl.nasa.gov/pub/</a>	8-day SST
28/07/03 - 04/08/03	SST	2003209-2003216. s0484pfv50-bsst	<a href="ftp://podaac.jpl.nasa.gov/pub/">ftp://podaac.jpl.nasa.gov/pub/</a>	8-day SST

### 9.3 Demonstration Section

Figure 9.3 shows a plot of the 12 images developed in the previous section where (a), (d), (g) and (j) are from week 1, (b), (e), (h) and (k) are from week 2, and (c), (f), (i), and (l) show the differences between the two weeks. The percentage of chlorophyll-*a* attributed to microphytoplankton is shown in the top three images (a-c), that attributed to nanophytoplankton in the next three (d-f), then picophytoplankton (g-i). The bottom three images represent SST ( $^{\circ}\text{C}$ , j-l).

When analysing the microphytoplankton images (Figure 9.3a-c), one notices a higher proportion of microphytoplankton in the equatorial region during week 1 compared with week 2. This is highlighted in Figure 9.3c which shows the differences between the two microphytoplankton images and indicates 20% higher microphytoplankton % chlorophyll-*a* in the equatorial Pacific during week 1, with differences as high as 50% in the centre of this bloom, when compared with week 2.

When analysing the nanophytoplankton images (Figure 9.3d-f), one also notes slightly higher nanophytoplankton % chlorophyll-*a* in the equatorial region and slightly lower % chlorophyll-*a* just south-east of the equator during week 1 when compared with week 2 (Figure 9.3f). In contrast to the microphytoplankton, there is a significantly lower picophytoplankton % chlorophyll-*a* in the equatorial region during week 1 when compared with week 2 (Figure 9.3i). Furthermore, in contrast to nanophytoplankton, higher picophytoplankton % chlorophyll-*a* can be observed just south-east of the equator during week 1, compared with week 2 (Figure 9.3i).

Turning our attention to the SST images (Figure 9.3j-l), significant differences are noted between the two weeks. During week 1, lower SST values are seen in the central equatorial Pacific and slightly higher SST values in the south-east equatorial Pacific when compared with week 2.

### 9.4 Training

To help interpret the case study, we will now go through each of the steps to generate Figure 9.3. An IDL program (Handbook\_RS\_PSC\_code.pro) was developed to allow the reader to reproduce this example.

1. Step 1: Download all the files needed for the case study (Table 1) from <http://www.ioccg.org/handbook/Brewin/Data/> and save them to an appropriate folder on your desktop. Extract all the SeaWiFS files with the extension ".bz2" from their zipped format.
2. Step 2: Download all the IDL code needed for the case study from <http://www.ioccg.org/handbook/Brewin/IDL%20Code/> and save it to your IDL path directory.
3. Step 3: Open IDL and type "handbook\_RS\_PSC\_code" into the command prompt. A dialog box will appear titled "Browse for folder". Locate the folder where

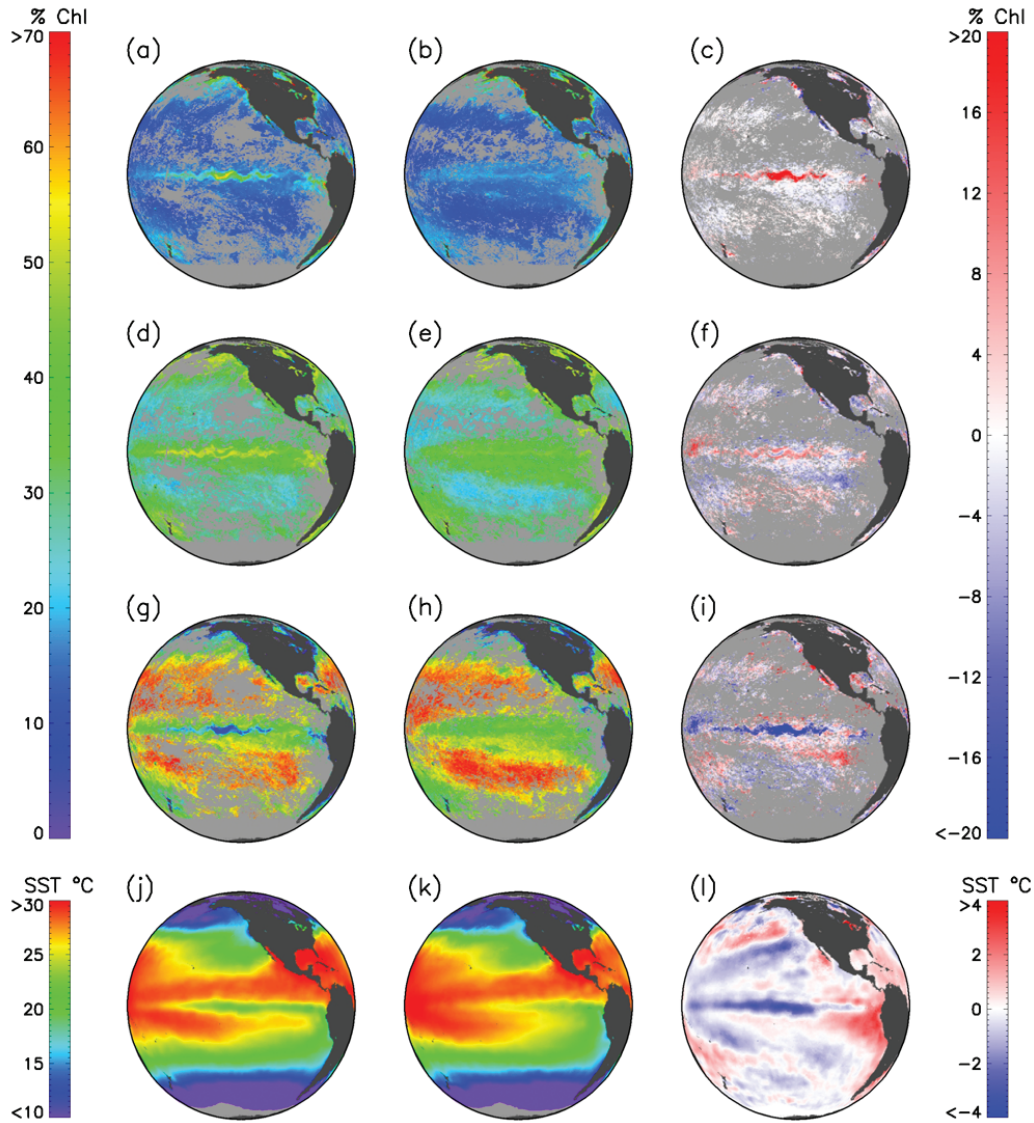


**Figure 9.3** Plot of the 12 images developed in the case study. Figures (a), (d), (g) and (j) are from week 1, (b), (e), (h) and (k) from week 2, and (c), (f), (i), and (l) show the differences between the two weeks. Microphytoplankton % chlorophyll-*a* is shown in the top three images (a-c), followed by nanophytoplankton (d-f), then picophytoplankton (g-i), and at the bottom are the three SST images (j-l) in °C.

you saved the input data in step 1 and press "OK".

4. Step 4: The code will then run through the methodology described in section

9.2 (Data and Methods) and save Figure 9.3 to the directory where the files were downloaded in step 1.

5. NOTE: This program was run on Windows, using an Intel(R) Core(TM) 2 CPU 6320 @ 1.86GHz with 1.97GB of RAM. Using this computer, the code takes about 8 minutes to run. The code may take longer/shorter to run on other machines, may need to be manipulated for a UNIX/LINUX environment, and may need to be manipulated for other version of IDL (currently developed for IDL Version 6.3).

## 9.5 Questions

**Q1:** What phenomena may be causing the high microplankton % chlorophyll-*a* (Figure 9.3a) and the low SST values (Figure 9.3j) in the central equatorial Pacific during week 1?

**Q2:** Considering that the two 8-day composites are taken at the same seasonal time period, why are there such large differences in both SST and the phytoplankton community composition in Figure 9.3c, f, i and l?

**Q3:** How do the higher SST values south-east of the equatorial Pacific in week 1 (Figure 9.3j and l) appear to be influencing the phytoplankton community composition?

## 9.6 Answers

**A1:** The phenomena causing the high microplankton % chlorophyll-*a* (Figure 9.3a) and the low SST values (Figure 9.3j) in week 1, in the central equatorial Pacific, is the 1997-1999 El Niño/La Niña event. The periodic occurrence of El Niño and La Niña episodes has a strong effect on the physical forcing in the equatorial Pacific. Under non-El Niño conditions, easterly trade winds create a channel of cold surface water along the equator, referred to as the Eastern Equatorial Undercurrent (EUC). The EUC flows eastward across the equator at a depth of 20 to 200 m (Toggweiler and Carson 1995). During an El Niño event, a weakening or reversal of the trade winds occurs, which weakens the EUC and hence subdues the upwelling of cold nutrient rich waters and deepens the thermocline. Surface waters become warmer and nutrient poor. During a La Niña event, there is a strengthening of the trade winds, which strengthens the EUC, enhancing the upwelling of cold nutrient rich waters and raising the thermocline.

The 1997-1999 El Niño/La Niña event was the strongest of the 20th century (Kerr 1998; McPhaden 1999). During July/August 1998 (week 1) a large La Niña event occurred which strengthened the trade winds resulting in upwelling of cold

nutrient rich waters close to the surface (McPhaden 1999). This is clearly seen in Figure 9.3l by the lower SST values during week 1 when compared with week 2 in the central equatorial Pacific (note that week 2 was during a non- El Niño/La Niña year). This injection of cold nutrient rich waters during July/August 1998 ignited a huge surface phytoplankton bloom, with a 40-fold increase in chlorophyll-*a* (Chavez et al. 1999). This phytoplankton bloom is the largest phytoplankton bloom observed in the equatorial Pacific to date. This bloom, driven by the EUC, migrated from east to west at a speed of 105 km day<sup>-1</sup> and its shape was distorted by Tropical Instability Waves (TIWs) (Chavez et al. 1999; Ryan et al. 2002) due to the meridional transport linked to the propagation of TIWs (notice the wave like shape of the bloom in Figure 9.3c).

**A2:** Despite the two 8-day composites being at the same seasonal time period, large differences in both SST and the phytoplankton community composition in Figure 9.3c, f, i and l are related to the fact that week 1 was during a large La Niña event (July/August 1998) and week 2 during non- El Niño/La Niña conditions. The inter-decadal occurrence of the El Niño/La Niña phenomena appears to be related to these differences.

Studies in the equatorial Pacific have suggested that diatoms do not contribute more than 20% of phytoplankton biomass (Blanchot et al. 2001; Kobayashi and Takahashi 2002; Dandonneau et al. 2004). Assuming diatoms comprise the majority of the microphytoplankton in the Equatorial Pacific, this value compliments our estimates of microphytoplankton % chlorophyll-*a* in non- El Niño/La Niña conditions (week 2, Figure 9.3b). However, blooms of diatoms have been reported in this area (Bender and McPhaden 1990; Chavez et al. 1990; Archer et al. 1997), particularly under La Niña events (Chavez et al. 1999; Strutton and Chavez 2000; Ryan et al. 2002; Alvain et al. 2008). Under such conditions, and using the algorithm of Brewin et al. (2010b), microphytoplankton appear to contribute as much as 70% of the phytoplankton biomass (Figure 9.3a).

Iron limitation is especially important for diatoms (Boyd, 2002) and when nutrients and iron are abundant in the photic layer, diatoms grow rapidly and dominate the phytoplankton population. Using *in situ* measurements, Chavez et al. (1999) linked the elevated levels of macronutrients and enhanced supply of iron associated with the La Niña event, to an increase in the concentration of diatoms (Table 1, Chavez et al. 1999), supporting the results shown in Figure 9.3a-c.

Differences in nanophytoplankton between the two weeks are less pronounced with slight increases in nanophytoplankton % chlorophyll-*a* at the periphery of the microphytoplankton bloom in week 1 (Figure 9.3f). In contrast to microphytoplankton, picophytoplankton are seen to have much lower % chlorophyll-*a* across the equatorial Pacific in week 1 when compared with week 2 (Figure 9.3i).

**A3:** The higher SST values seen in the south-east equatorial Pacific during week 1

(Figure 9.3j and l) appear to correspond to changes in the composition of nano- and picophytoplankton. While much of this area is masked by cloud coverage in Figure 9.3c, f and i, there is a slightly higher % chlorophyll-*a* of picophytoplankton in week 1 when compared with week 2 (Figure 9.3i) in the south-east equatorial Pacific. The inverse is seen for nanophytoplankton (Figure 9.3f).

Since picophytoplankton are smaller in size, they have a higher surface-to-volume ratio than nanophytoplankton, and hence can absorb nutrients with high efficiency under nutrient limited conditions (Raven 1998). Therefore, in stratified, nutrient depleted areas, such as the southern Pacific subtropical gyre, picophytoplankton are expected to dominate (Chisholm 1992; Dandonneau et al. 2004; Ras et al. 2008).

When comparing Figure 9.3g with Figure 9.3h, the southern subtropical gyre (indexed by the high levels of picophytoplankton >60 % chlorophyll-*a* south of the equator) appears further north and east in Figure 9.3g when compared with Figure 9.3h, possibly causing these discrepancies. This may be linked to changes in physical forcing during a La Niña event.

## 9.7 Summary

In this example we have highlighted the strong link between the community composition of the phytoplankton in the equatorial Pacific and the inter-decadal physical forcing (in this case the El Niño/La Niña phenomena). Changes in the community structure of phytoplankton appear to reflect changes in temperature in the equatorial Pacific. Larger phytoplankton cell sizes are associated with dynamic systems where fresh nutrients are available, and smaller size classes are associated with stratified, nutrient depleted regions. This tight coupling between the biology and physics in the equatorial Pacific supports the idea that all the components of a system, physical, biological and chemical, are intertwined, and that each component of the system is intrinsically linked with another (Lovelock 1992).

Remote sensing makes it possible to collect data in dangerous or inaccessible areas. It can also compliment costly and slow data collection *in situ*, ensuring that areas or particles are not disturbed, and it offers repeat viewing and can be used to monitor wide areas synoptically, not possible by conventional ground sampling methods. However, the true capabilities of remote sensing can only come to fruition when it is used in conjunction with *in situ* based measurements, for calibration and validation purposes. With more optical and biological *in situ* measurements, quantitative development and validation of the satellite PFT algorithms can continue. Furthermore, the synergistic benefits of using these observational techniques in conjunction allow for well-constrained, accurate biological and geophysical parameters that can then be assimilated into mathematical models to improve their parameterisation and our understanding needed to predict future change.

## 9.8 Acknowledgements

The NASA SeaWiFS project team and the NASA Jet Propulsion Laboratory Physical Oceanography Distributed Active Archive Centre is acknowledged for satellite data and all contributors to the SeaBASS data set for *in situ* pigment data. This work is funded by the National Environmental Research Council, UK, the National Centre for Earth Observation and NERC Oceans 2025 programme (Themes 6 and 10).

## 9.9 References and further reading

- Alvain S, Moulin C, Dandonneau Y, Breon FM (2005) Remote sensing of phytoplankton groups in case 1 waters from global SeaWiFS imagery. *Deep-Sea Res I* 52:1989-2004
- Alvain S, Moulin C, Dandonneau Y, Loisel H (2008) Seasonal distribution and succession of dominant phytoplankton groups in the global ocean: A satellite view. *Global Biogeochem Cycles* 22:GB3001, doi:3010.1029/2007GB003154
- Archer D, Aiken J, Balch W, Barber D, Dunne J, Flament P, Gardner W, Garside C, Goyet C, Johnson E, Kirchman D, McPhaden M, Newton J, Peltzer E, Welling L, White J, Yoder J (1997) A meeting place of great ocean currents: shipboard observations of a convergent front at 2 degrees N in the Pacific. *Deep-Sea Res II* 44:1827-1849
- Behrenfeld MJ, Bale AJ, Kolber DD, Aiken J, Falkowski PG (1996) Confirmation of iron limitation of phytoplankton photosynthesis in the equatorial Pacific Ocean. *Nature* 383:508-511
- Bender ML, McPhaden MJ (1990) Anomalous nutrient distribution in the equatorial Pacific in April 1988: Evidence for rapid biological uptake. *Deep-Sea Res I* 37:1075-1084
- Blanchot J, Andre JM, Navarette C, Neveux J, Radenac MH (2001) Picophytoplankton in the equatorial Pacific: vertical distributions in the warm pool and in the high nutrient low chlorophyll conditions. *Deep-Sea Res I* 48:297-314
- Boyd PW (2002) Environmental factors controlling phytoplankton processes in the Southern Ocean. *J Phycol* 38:844-861
- Brewin RJW, Lavender SJ, Hardman-Mountford NJ, Hirata T, Raitsos DE, Barciela R (2008) An inter-comparison of bio-optical techniques for detecting phytoplankton functional types from space Ocean Optics XIX. SPIE proceedings, PDF No. oo080577 (CDROM), Castelvechio Pascoli, Italy, 6-10 Oct. 2008
- Brewin RJW, Lavender SJ, Hardman-Mountford NJ, Hirata T (2010a) A spectral response approach for detecting dominant phytoplankton size class from satellite remote sensing. *Acta Oceanol Sin* 29:14-32
- Brewin RJW, Sathyendranath S, Hirata T, Lavender SJ, Barciela R, Hardman-Mountford NJ (2010b) A three-component model of phytoplankton size class for the Atlantic Ocean. *Ecol Model* 221:1472-1483
- Chavez FP, Buck KR, Barber RT (1990) Phytoplankton taxa in relation to primary production in the equatorial Pacific. *Deep-Sea Res I* 37:1733-1752
- Chavez FP, Strutton PG, Friederich GE, Feely RA, Feldman GC, Foley DG, McPhaden MJ (1999) Biological and Chemical Response of the Equatorial Pacific Ocean to the 1997-98 El Niño. *Science* 286: 2126 - 2131
- Chisholm SW (1992) Phytoplankton Size. In: *Primary Productivity and Biogeochemical Cycles in the Sea* edited by Falkowski PG, Woodhead AD pp 213-237, Springer, New York
- Ciotti AM, Bricaud A (2006) Retrievals of a size parameter for phytoplankton and spectral light absorption by coloured detrital matter from water-leaving radiances at SeaWiFS channels in a continental shelf off Brazil. *Limnol Oceanogr Methods* 4:237-253
- Coale KH, Fitzwater SE, Gordon RM, Johnson KS, Barber RT (1996) Control of community growth and export production by upwelled iron in the equatorial Pacific Ocean. *Nature* 379:621-624
- Cullen JJ (1991) Hypotheses to explain high-nutrient conditions in the open sea. *Limnol Oceanogr* 36:1578-1599

- Dandonneau Y, Deschamps PY, Nicolas JM, Loisel H, Blanchot J, Montel Y, Thieuleux F, Becu G (2004) Seasonal and interannual variability of ocean color and composition of phytoplankton communities in the North Atlantic, equatorial Pacific and South Pacific. *Deep-Sea Res II* 51:303-318
- Devred E, Sathyendranath S, Stuart V, Maas H, Ulloa O, Platt T (2006) A two-component model of phytoplankton absorption in the open ocean: Theory and applications. *J Geophys Res* 111:C03011, doi:03010.01029/02005JC002880
- Etcheto J, Boutin J, Dandonneau Y, Bakker DCE, Feely RA, Ling RD, Nightingale PD, Wanninkhof R (1999) Air-sea CO<sub>2</sub> flux variability in the equatorial Pacific Ocean near 110°W. *Tellus* 51B:734-747
- Feely RA, Wanninkhof R, Takahashi T, Tans P (1999) Influence of El Niño on the Equatorial Pacific contribution to atmospheric CO<sub>2</sub> accounts. *Nature* 398:597-601
- Hansen B, Bjørnsen PK, Hansen PJ (1994) The size ratio between planktonic predators and their prey. *Limnol Oceanogr* 39:395-403
- Hardman-Mountford NJ, Hirata T, Richardson KA, Aiken J (2008) An objective methodology for the classification of ecological pattern into biomes and provinces for the pelagic ocean. *Remote Sens Environ* 112:3341-3352
- Hirata T, Aiken J, Hardman-Mountford NJ, Smyth TJ, Barlow RG (2008a) An absorption model to derive phytoplankton size classes from satellite ocean colour. *Remote Sens Environ* 112:3153-3159
- Hirata T, Hardman-Mountford NJ, Aiken J, Smyth T, Barlow R, Martines-Vicente V, Fishwick J, Bernard S (2008b) Optical approach to derive phytoplankton size classes using ocean color remote sensing. *Ocean Optics XIX*, Castelvechio Pascoli, Italy, 6-10 Oct. 2008
- Jennings S, Warr KJ, Mackinson S (2002) Use of size-based production and stable isotope analyses to predict trophic transfer efficiencies and predator-prey body mass ratios in food webs. *Mar Ecol Prog Ser* 240:11-20
- Kerr RA (1998) Models win big in forecasting El Niño. *Science* 280:522-523
- Kobayashi F, Takahashi K (2002) Distribution of diatoms along the equatorial transect in the western and central Pacific during the 1999 La Niña conditions. *Deep-Sea Res II* 49:2801-2821
- Kostadinov TS, Siegel DA, Maritorena S (2009) Retrieval of the particle size distribution from satellite ocean colour observations. *J Geophys Res* 114:C09015, doi:09010.01029/02009JC005303
- Le Quéré C, Harrison SP, Prentice CI, Buitenhuis ET, Aumont O, Bopp L, Claustre H, Cotrim Da Cunha L, Geider R, Giraud X, Klaas C, Kohfeld KE, Legendre L, Manizza M, Platt T, Rivkin R, Sathyendranath S, Uitz J, Watson AJ, Wolf-Gladrow D (2005) Ecosystem dynamics based on plankton functional types for global ocean biogeochemistry models. *Glob Change Biol* 11:2016-2040
- Lovelock JE (1992) A numerical model for biodiversity. *Philos Trans R Soc B Bio Sci* 338:383-391, doi: 310.1098/rstb.1992.0156
- Martin JH, Fitzwater SE (1988) Iron deficiency limits phytoplankton growth in the north-east Pacific subarctic. *Nature* 331:341-343
- Martin JH (1991) Iron, Liebig's Law, and the Greenhouse. *Oceanography* 4:52-55
- McPhaden MJ (1999) Genesis and evolution of the 1997-98 El Niño. *Science* 283:950-954
- Nair A, Sathyendranath S, Platt T, Morales J, Stuart V, Forget M-H, Devred E, Bouman H (2008) Remote sensing of phytoplankton functional types. *Remote Sens Environ* 112:3366-3375
- Raitsos DE, Lavender SJ, Maravelias CD, Haralambous J, Richardson AJ, Reid PC (2008) Identifying four phytoplankton functional types from space: An ecological approach. *Limnol Oceanogr* 53(2):605-613
- Ras J, Claustre H, Uitz J (2008) Spatial variability of phytoplankton pigment distributions in the Subtropical South Pacific Ocean: a comparison between *in situ* and predicted data. *Biogeosciences* 5:353-369
- Raven JA (1998) Small is beautiful: The picophytoplankton. *Funct Ecol* 12:503-513
- Ryan JP, Polito PS, Strutton PG, Chavez FP (2002) Unusual large-scale phytoplankton blooms in the equatorial Pacific. *Prog Oceanogr* 55:263-285
- Sathyendranath S, Stuart V, Cota G, Maas H, Platt T (2001) Remote sensing of phytoplankton pigments: a comparison of empirical and theoretical approaches. *Int J Remote Sensing* 22:249-273
- Sathyendranath S, Watts L, Devred E, Platt T, Caverhill C, Maass H (2004) Discrimination of diatoms from other phytoplankton using ocean-colour data. *Mar Ecol Prog Ser* 272:59-68

- Scharf FS, Juanes F, Rountree RA (2000) Predator size - prey size relationships of marine fish predators: interspecific variation and effects of ontogeny and body size on trophic-niche breadth. *Mar Ecol Prog Ser* 208:229-248
- Strutton PG, Chavez FP (2000) Primary productivity in the equatorial Pacific during the 1997-1998 El Niño. *J Geophys Res* 105:26089-26101
- Takahashi T, Sutherland SC, Sweeney C, Poisson A, Metzl N, Tilbrook B, Bates N, Wanninkhof R, Feely RA, Sabine C, Olafsson J, Nojiri Y (2002) Global sea-air CO<sub>2</sub> flux based on climatological surface ocean pCO<sub>2</sub> and seasonal biological and temperature effects. *Deep-Sea Res II* 49:1601-1622
- Thomas WH (1979) Anomalous nutrient-chlorophyll interrelationships in the offshore eastern tropical Pacific Ocean. *J Mar Res* 37:327-335
- Toggweiler JR, Carson S (1995) What are upwelling systems contributing to the ocean's carbon and nutrient budgets? In: Summerhayes CP, Emeis KC, Angel MV, Smith RL, Zeitzschel B (eds) *Upwelling in the ocean. Modern processes and ancient records*. John Wiley & Sons, Chichester, UK, p 337-360
- Uitz J, Claustre H, Morel A, Hooker SB (2006) Vertical distribution of phytoplankton communities in open ocean: An assessment based on surface chlorophyll. *J Geophys Res* 111:CO8005, doi:8010.1029/2005JC003207
- Vidussi F, Claustre H, Manca BB, Luchetta A, Marty JC (2001) Phytoplankton pigment distribution in relation to upper thermocline circulation in the eastern Mediterranean Sea during winter. *J Geophys Res* 106(C9):19,939-919,956
- Walsh JJ (1976) Herbivory as a factor in patterns of nutrient utilization in sea. *Limnol Oceanogr* 21:1-13
- Werdell PJ, Bailey SW (2002) The SeaWiFS Bio-optical Archive and Storage System (SeaBASS): Current architecture and implementation. NASA Tech. Memo. 2002-211617. In: Fargion GS, McClain C (eds) *NASA Goddard Space Flight Center. Greenbelt, Maryland*, 45 pp

## Theme: Fisheries and Aquaculture

---



## Case Study 10

# Use of Night Satellite Imagery to Monitor the Squid Fishery in Peru

Carlos Paulino\*<sup>1</sup> and Luis Escudero <sup>1</sup>

---

## 10.1 Introduction

The giant squid (*Dosidicus gigas*) lives mainly in the oceanic environment, but also occurs in neritic (relatively shallow) environments, and makes horizontal and vertical migrations. It is a physiologically tolerant species, characterized by opportunistic consumption habits and is also considered an ecologically important species, acting as predator and prey of a large number of species (including their own species). The distribution of *Dosidicus gigas* is far reaching since it is a highly migratory species. In the eastern Pacific Ocean its geographic habitat is from California (37°N) to southern Chile (47°S) and from the coasts of North and South America to 125°W. The greatest concentrations are located in the Peruvian coastal oceanic region in the southern hemisphere, and the Gulf of California in the northern hemisphere (Nesis, 1983). In Peru, the fishing activity of the giant squid or "pota" is exerted mainly by industrial Japanese and Korean squid jigging vessels with a holding capacity of 300–1000 tonnes, which have been fishing off Peru since 1991 (Taipe, 2001).

The squid jigging vessels operate at night, using powerful lights (2000 watts) to attract the squid. The lights are set at a specific height and angle to allow for a shade zone next to the ship where the squid concentrate. The number of lights per ship varies between 120 and 200 depending on vessel capacity. Squid are attracted to the light, creating massive concentrations around the luminous source, and allowing for easy harvest.

These lights can be observed as bright-light areas on night-time OLS (Operational Linescan System) images of the Defense Meteorological Satellite Program (DMSP). Cho et al. (1999), Kiyofuji et al. (2001), Rodhouse et al. (2001) and Waluda et al. (2002) have examined night-time visible images to determine the spatial distribution of fishing vessels. Cho et al. (1999) and Kiyofuji et al. (2001) determined that the bright areas in the OLS images, created by 2-level slicing, were caused by light

---

<sup>1</sup>Remote Sensing Division, Instituto del Mar del Perú, Av. Argentina 2245 Callao, Peru.

\*Email address: [cpaulino@imarpe.gob.pe](mailto:cpaulino@imarpe.gob.pe)

produced by the fishing vessels. Rodhouse et al. (2001) reported the frequency of light occurrences in cloud-free imagery, and associated these lights with fishing vessels. Waluda et al. (2002) analyzed the relationship between the number of lit pixels in DMSP/OLS night-time visible images and the number of fishing vessels around the Falkland Islands' fishery for *Illex argentinus*. Kiyofuji et al. (2004) examined the relationship between the number of pixels in the DMSP/OLS imagery and the number of fishing vessels, and demonstrated that fishing vessel numbers can, in fact, be estimated from DMSP/OLS night-time visible images. Kiyofuji and Saitoh (2004) used night-time visible images to detect Japanese common squid fishing areas and potential migration routes in the Sea of Japan.

The industrial fishing of giant squid (*Dosidicus gigas*) has been monitored through the ARGOS satellite tracking system since 1998, and is directed primarily at licensed vessels that fish off the Peruvian coast. However, other vessels are known to be engaged in fishing operations within the Peruvian Exclusive Economic Zone (EEZ), which cannot be detected by the system. For this reason, IMARPE has been using an alternate system of night satellite imagery since July 2003, that permits observation of the areas where squid vessels are operating.

The increasing demand for fishing resources and the necessity to exploit these from an economical view point, have encouraged fishing countries such as Peru to implement technologically advanced satellite systems for surveillance and control of fishing vessels, to better manage the fishing resources. This case study describes an example of how we use night-time satellite imagery to detection the location of squid fleets inside and outside the EEZ with the objective of understanding the distribution, concentration and characteristics of squid fishing fleets.

## 10.2 Study Area

The study area is located off the coast of Peru, between 3–18°S and 70–85°W. This area is dominated by the Humboldt-Peru eastern boundary current system, which generates the cold nutrient-rich coastal upwelling that makes this region so productive.

## 10.3 Materials and Methods

### 10.3.1 DMSP-OLS imagery

DMSP/OLS data were provided by the NOAA National Geophysical Data Center (NGDC) in Boulder, Colorado, USA. The DMSP satellite carries six sensors including the OLS. The OLS sensor monitors global cloud coverage by day and night via two channels (visible-near-infrared (VNIR) and thermal-infrared (TIR)), and has a swath of 3000 km. The VNIR and TIR channels observe radiation from 0.5 to 0.9  $\mu\text{m}$ , and

from 10 to 13  $\mu\text{m}$ , respectively. The VNIR band signal is intensified at night using a photomultiplier tube (PMT) for the detection of moonlit clouds. The low-light sensing capability of OLS at night permits the measurement of radiance down to  $10^{-9} \text{ W cm}^{-2} \text{ sr}^{-1} \mu\text{m}^{-1}$  (Elvidge et al. 1997a). However, the OLS is sensitive to scattered sun light, which saturates the visible band data (referred to as "glare" in the literature, Elvidge et al. 1997b). The visible band of DMSP/OLS has a 6-bit quantization, producing digital numbers (DN) ranging from 0 to 63 (Elvidge et al. 1999). Visible band digital numbers are relative rather than absolute values, with units in  $\text{W m}^{-2}$ .

DMSP Visible and IR images can be downloaded free of charge (June 1992 to present) from <http://spidr.ngdc.noaa.gov/spidr>. The web site provides data from 9 DMSP satellites, both day and night. The format of these images is L0 level (.OIS files) which therefore require digital processing in ENVI, ERDAS or other software. For this case study we used the image of 2 October 2008 (20:49 local time) obtained from DMSP for the coverage area 0–20°S and 70–90°W, corresponding to the area where the squid fishery was operational. OLS information is pre-processed by the National Geophysical Data Center (NGDC) and obtained through an annual subscription, which includes the use of data from the F15, F16 and F18 satellites. The images are downloaded in compressed format. The file used in this case study is named F16201001060040.d.peru.OIS, and can be downloaded from the IOCCG website at: <http://www.ioccg.org/handbook/Paulino/>. The file naming conventions are as follows: F##YYYYMMDDTTTT.region.\*, where F## = satellite number, YYYY = year, MM = month, DD = Day, TTTT = UT time at start of ascending data, region = Peru.

The location of fishing fleets in Peruvian waters (latitude, longitude, name and time) was obtained using ARGOS satellite-tracked data. ARGOS receiver-transmitters on each vessel receive information from GPS (Global Positioning System) satellites and transmit 30 daily reports of the geographical position of each boat. This information is received, processed and distributed to various users of the system e.g. the Ministry of Production (PRODUCE), Captain and Ports Directorate of the Navy (DICAPI) and IMARPE (Sisesat).

### 10.3.2 GIS Analysis

The spatial and temporal variability of squid fleet was analyzed using GIS, through integration of daily fishing vessel data (derived from ARGOS) and data on the number of illuminated pixels observed off the coast of Peru (derived from DMSP-OLS). GIS can be used to generate daily, weekly and monthly thematic maps to determine the spatial-temporal dynamics of the squid fleets. Thematic maps can be used to compare the number of light pixels to the number of known vessels in the area, to determine if any unlicensed fleets are operating illegally inside the Peruvian EEZ.

For the thematic mapping, both images must be geo-referenced. For DMSP images, this is done using algorithms developed by the National Geophysical Data

Center (NGDC), Boulder, CO (Elvidge et al., 1999). ARGOS data are geo-referenced using the same projection and data as the DMSP images, so that the location of vessels (X,Y coordinates) can be compared with the satellite images. For this case study we will select one position for each boat, closest to the time of the satellite overpass.

## 10.4 Demonstration

The DMSP/OLS images were captured at night between 19:00 to 22:00 local time, corresponding to the time when the fleets start their fishing operations. These images have been used by researchers to understand the spatial and temporal variability of *Dosidicus gigas*. In this section will show how to process the images, and subsequently how to interpret them.

**Step 1:** Open the OIS image in Envi (File → open external file → DMSP - NOAA). The image has two bands (visible and thermal-infrared ): the visible band has digital numbers from 0 to 63, where 63 is the maximum digital number (DN) of white pixels that represent vessel lights. In this image we can also see the lights of the main cities in Peru. DMSP/OLS images have also been used to identify urban areas (Imhoff et al. 1997, Owen et al. 1998).

Depending of the visibility, we can use images captured by the F15, F16 or F18 satellites, each of which passes over the study area at a different time. Figure 10.1 shows examples of these images. The image from satellite F15 (left) has missing data. Reception time is 17:01 (local time), and since this satellite flies in a dusk orbit it is not very useful. The image captured by satellite F16 (center) was captured at 18:04 local time, and can be considered the secondary day/night satellite. In some cases there are missing data, as can be seen on the image. Finally, the image from the F18 satellite (right) was taken at 19: 47 local time. This is the primary day/night satellite for Peru, and the city lights are clearly visible in this image.



**Figure 10.1** DMSP/OLS images over the study area ( $0^{\circ}$ - $20^{\circ}$ S and  $70^{\circ}$ - $90^{\circ}$ W) from satellite F15 (17:01) (left), F16 (18:04) (center) and F18 (19:47) local time (right).

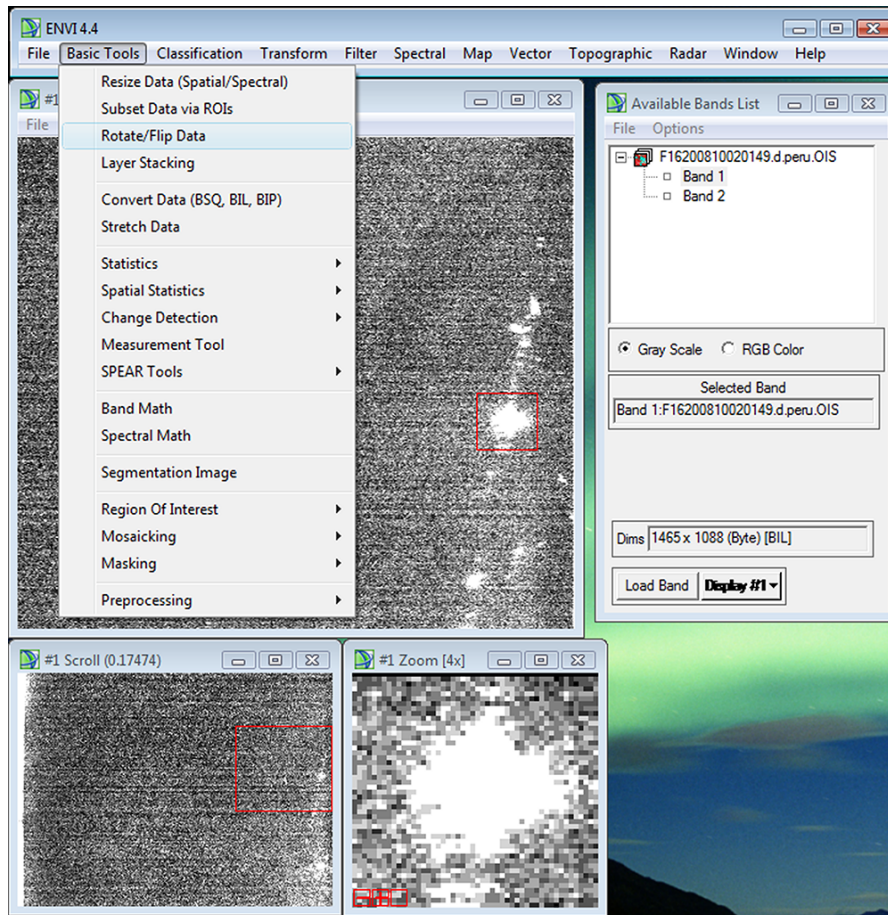


**Figure 10.2** Procedure for rotating the image using the basic tools menu, with 270° rotation.

**Step 2:** The image we have just opened is not geo-referenced so it is necessary to rotate the image. From the "Basic tools" menu, choose rotate/flip data. A new window will open (rotation input file). From here you can select the image (→ OK). In the rotation parameters window, choose angle 270 and click "yes" in transpose (see Figure 10.2). Insert an output filename. Next, load the rotated image into a new window. This step permits rotation of the image for better visualization (see Figure 10.3).

**Step 3:** To discriminate between light pixels and cloud pixels, we use the linear stretch function from the menu "Image → Enhance → Linear". The lights from the cities on land can now be seen, as well as some white pixels in the sea (see Figure 10.4). Cho et al. (1999) and Kiyofuji et al. (2001) determined that the bright areas in OLS images, created by 2-level slicing, were caused by the light produced by the fishing vessels. In some cases we found that pixels with a range of 18 to 30 DN could represent vessels (when compared with ARGOS data), but this does not imply

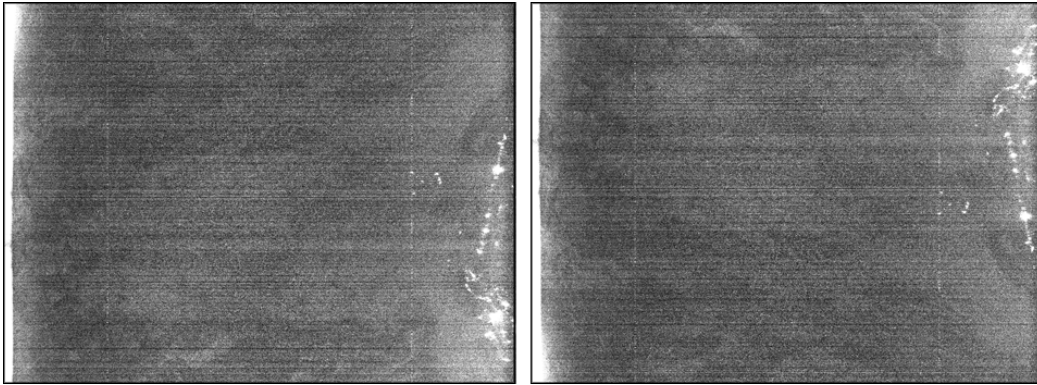


**Figure 10.3** View of the study area before and after rotation, showing coastal city lights on land and some white pixels over the sea, with digital numbers ranging from 0 to 63.

that they are necessarily catching squid; they could be searching for the best fishing grounds. In other images we can find clouds with DN value of 63 during full moon, one should be careful when interpreting these images.

**Step 4:** To discriminate even more pixels of light, we use enhanced interactive stretching to stretch the image data using histograms (from the display group menu bar, select Enhance → Interactive Stretching). An input and an output histogram appear in the "Interactive Contrast Stretching" dialog, showing the current input data and applied stretch, respectively. Two vertical dotted lines mark the current minimum and maximum values of the stretch. For this case, choose a DN range of 15 to 63, and apply. This step will improve the image and show only the pixels of light (Figure 10.5).

The ranges of DN values can be changed from 0 to 63 using interactive stretching. You can try adjusting different ranges of DN, which will make the pixels light or dark according to the range chosen. However, each pixel maintains its digital number value. To identify the composition of the digital values of the pixels, we can perform a classification of the DN values of one bright-light area using polygons. In this area, at least 6 digital value ranges can be found, and are shown in Figure 10.6: 63 (red), 61 (blue), 56 (yellow), 55 (cyan), 49 (green) and 46 (magenta). After this processing the image will be geo-referenced using geographic projection and WGS 84 data (World Geodetic System, a reference coordinate system used by the GPS) and exported as a tiff image for visualization in GIS software.

**Step 5:** We used ARGOS data to determine if the bright pixel areas correspond to vessels. For this example we use the file Calamar02102008.dbf (2 October 2008, available at <http://www.ioccg.org/handbook/Paulino/>), which contains lat/long information of licensed fishing fleets (Figure 10.7).

Location data for the fishing vessels can be obtained using the MacPesca software

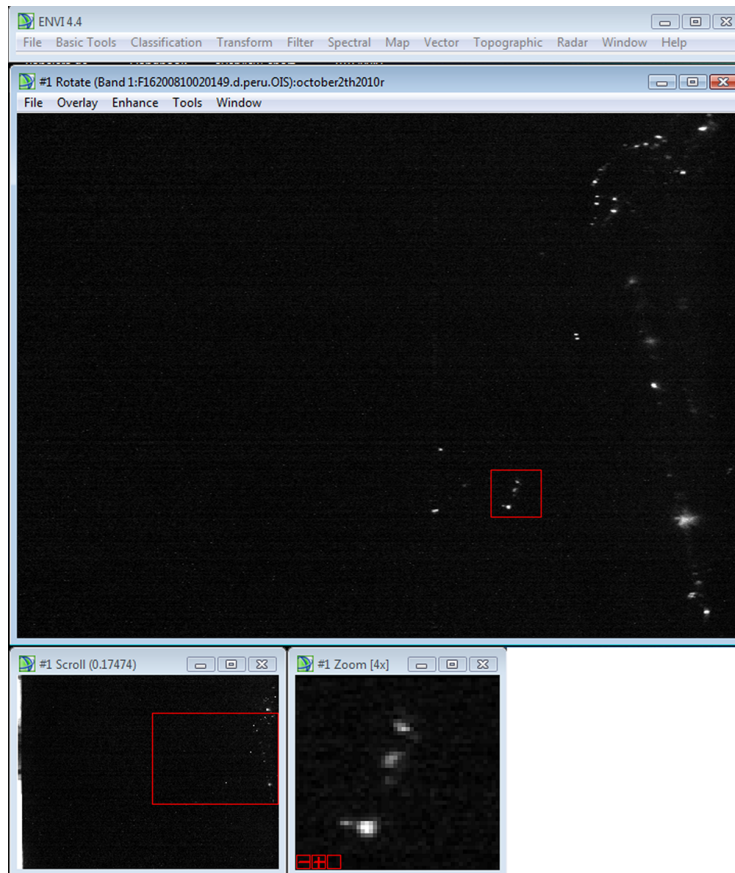


**Figure 10.4** This image shows bright-light areas as white pixels that could be city lights or vessel lights.

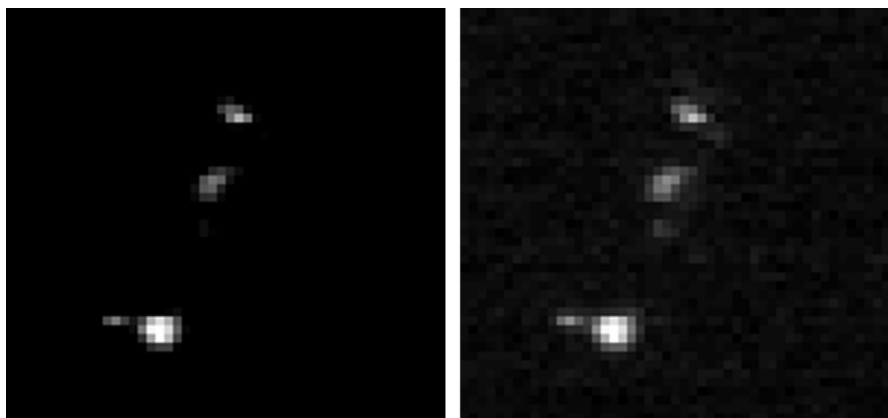


**Figure 10.5** Zoomed in view showing the use of interactive stretching. We changed the DN value default from 0 to 63 (left) to 15 to 63 (right). According to this image, three boats are operating outside of the Peruvian Exclusive Economic Zone.

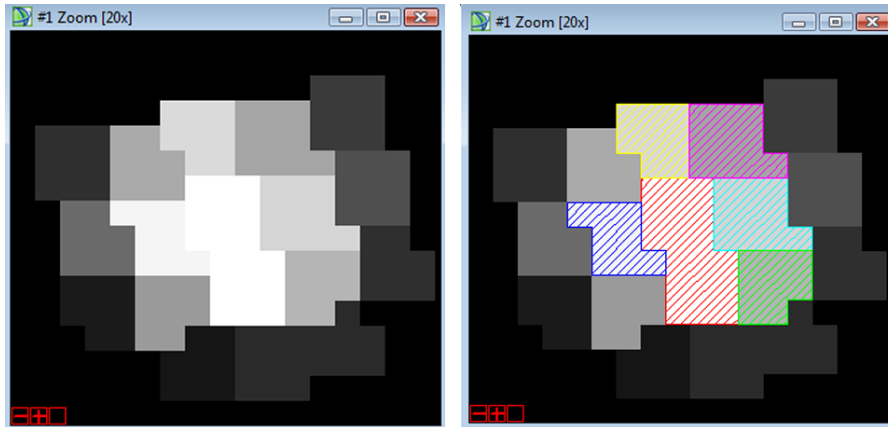


**Figure 10.6** Classification of the DN value of one bright-light area as polygons: 63 (red), 61 (blue), 56 (yellow), 55 (cyan), 49 (green) and 46 (magenta).

developed for MapInfo, a powerful mapping and geographic analysis application. Vector files such as coast line or 200 nautical mile limit can be used in MapInfo for a better visualization of the licensed fleet positions. Load the DMS image and ARGOS data in MapInfo to compare pixel areas and number of vessels. Remember that in order to validate the ARGOS data, the ARGOS dbf file must have one position (X/Y) per vessel, taken at the same time (or close to) the time of the satellite overpass.

## 10.5 Training and Questions

We will now examine and interpret the processed images to verify their use in the monitoring of the squid fishery. Looking at the images from the F15, F16 and F18 satellites (Figure 10.1), please answer the following questions:

- Q1:** How we can distinguish pixels from vessel lights from those associated with clouds?
- Q2:** If we have more than one image per day, which satellite image should we use?
- Q3:** Do the satellites pass over the exact same area every day?
- Q4:** What is the minimum value used to represent the position of one vessel?
- Q5:** Is noise the only problem with the images?
- Q6:** Is it possible to know how many vessels are in a light pixel area?
- Q7:** Is it possible to use this kind of imagery for detection of vessels that operate outside the 200 nautical mile limit?

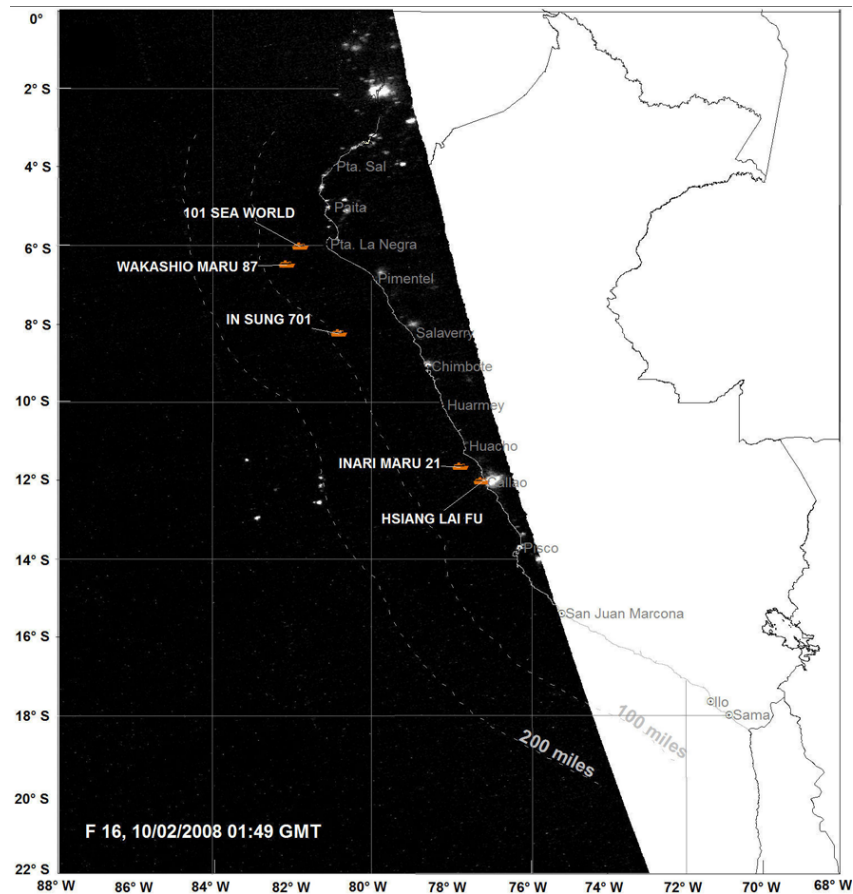


**Figure 10.7** Localization of fishing vessels from ARGOS data superimposed on a DMSP/OLS image using GIS software, to compare ARGOS data with white light pixels.

## 10.6 Answers

**A1:** After processing the images, we identified bright-light areas that represent vessel lights, which we adjust and classify according to DN values (Figures 10.3 and 10.4). Since we know that the digital number (DN) of saturated light pixels is 63, we can use this information to discriminate between vessel lights and clouds, applying the linear stretch function. Clouds have a DN range of 10–15 and occupy large areas, whereas fishing vessels have  $DN \geq 30$ .

**A2:** F16 is the primary satellite, but we recommend that F18 be used for over Peru, since it has better imagery over that region. Occasionally you may see images that are either completely black or white, as a result of missing data (Figure 10.1, F15 and F16 images). If there is a problem with one of the satellites you can always view the data from another one, for that night.

**A3:** On some nights you will get two images from each satellite and other nights you will get only one image. This is because each satellite does not fly over the exact same area every night, and depending on where the satellite is in its orbit, the number of images for each night may vary. In Figure 10.1, you can see the different overpass times of each satellite: F15(17:01), F16(18:04) and F18(19:47) local time.

**A4:** The DN that represents one vessel is  $\geq 30$ , but in some images we detected vessel lights with DN values between 18 and 30. This does not imply that they are catching squid, but it is possible that they are looking for the best fishing grounds.

**A5:** Noise is not the only problem with the images: a full moon can also affect the VIS image. When there is high lunar illumination ( $>50\%$ ), there may be reflectance off the clouds in the image. In this case, it is more difficult to distinguish between cloud reflection and fishing boats, but you can still identify pixels with a DN  $>15$  on the images. The thermal band can be used to identify clouds with greater accuracy.

**A6:** Kiyofuji et al. (2001) and Waluda (2004) investigated the relationship between the number of pixels (area) in the DMSP/OLS imagery and the numbers of fishing vessels, and demonstrated that fishing vessel numbers can be estimated from DMSP/OLS night-time visible images. For this research they used ARGOS data (the same kind of data that we used) for the time period 3 July to 31 December 1999.

**A7:** This case study demonstrates that light detection by satellite remote sensing can be used to observe spatial-temporal location of squid jigging vessels both inside and outside the Peruvian Exclusive Economic Zone.

## 10.7 References

- Cho K, Shimoda H, Sakata T (1999) Fishing fleets lights and sea surface temperature distribution observed by DMSP/OLS sensor. *Int J Remote Sens* 20:3-9
- Elvidge CD, Baugh KE, Hobson VR, Kihn EA, Kroehl HW, Davis ER, Cocero D (1997a) Satellite inventory of human settlements using nocturnal radiation emissions: a contribution for the global tool chest. *Glob Change Bio* 3:387-395
- Elvidge CD, Baugh KE, Kihn EA, Kroehl HW, Davis ER (1997b) Mapping city lights with night-time data from the DMSP operational linescan system. *Photogram Eng Remote Sens* 63:727-734
- Elvidge CD, Baugh K, Dietz JB, Bland T, Sutton PC, Kroehl HW (1999) Radiance calibration of DMSP-OLS low light imaging data of human settlements. *Rem Sens Environ* 68:77-88
- Imhoff ML, Lawrence WT, Elvidge CD, Paul T, Levine E, Privalsky MV, Brown V (1997) Using night-time DMSP/OLS images of city lights to estimate the impact of urban land use on soil resources in the United States. *Remote Sens Environ* 59:105-117
- Kiyofuji H, Kumagai K, Saitoh S, Arai Y, Sakai K (2004) Spatial relationships between Japanese common squid (*Todarodes pacificus*) fishing grounds and fishing ports: an analysis using remote sensing and geographical information systems. In: Nishida T, Kailola PJ, Hollingworth CE (eds) *GIS/Spatial Analyses in Fishery and Aquatic Sciences* (Vol. 2). Fishery-Aquatic GIS Research Group, Saitama, Japan. p 341-354
- Kiyofuji H, Saitoh S, Sakurai Y, Hokimoto T, Yoneta K (2001) Spatial and temporal analysis of fishing fleet distribution in the southern Japan Sea in October 1996 using DMSP/ OLS visible data. In: Nishida T, Kailola PJ, Hollingworth CH (eds). *Proceeding of the First International Symposium on GIS in Fisheries Sciences*. Fishery GIS Research Group, Saitama, Japan. p 178-185

- Kiyofuji H, Saitoh S-I (2004) Use of night-time visible images to detect Japanese common squid *Todarodes pacificus* fishing areas and potential migration routes in the Sea of Japan. *Mar Ecol Prog Ser* 276: 173-186
- Nesis KN (1983) *Dosidicus gigas*. In: Boyle PR (ed.), Cephalopod life cycles, Academic Press, p 215-231
- Owen TW, Gallo KP, Elvidge CD, Baugh KE (1998) Using DMSP-OLS light frequency data to categorize urban environments associated with US climate observing station. *Int J Remote Sens* 19:3451-345
- Taipe A, Yamashiro C, Mariategui L, Rojas P, Roque C (2001). Distribution and concentrations of jumbo flying squid (*Dosidicus gigas*) off the Peruvian coast between 1991 and 1999. *Fish Res* 54:21-32
- Rodhouse PG, Elvidge CD, Trathan PN (2001) Remote sensing of the global light-fishing fleet: an analysis of interactions with oceanography, other fisheries and predators. *Adv Mar Biol* 39:261-303
- Waluda CM, Trathan PN, Elvidge CD, Hobson VR, Rodhouse PG (2002) Throwing light on straddling stocks of *Illex argentinus*: assessing fishing intensity with satellite imagery. *Can J Fish Aquat Sci* 59:592-596
- Waluda, C., Yamashiro, C., Elvidge, C., Hobson, V., Rodhouse, P. (2004). Quantifying light-fishing for *Dosidicus gigas* in the eastern Pacific using satellite remote sensing. *Remote Sens Environ* 91:129-133

### 10.7.1 Further readings

- Cinzano P, Falchi F, Elvidge C, Baugh K (1999). Mapping the artificial sky brightness in Europe from DMSP satellite measurements: The situation of the night sky in Italy in the last quarter of century. *R Astron Soc* 9905340. <http://www.lightpollution.it/cinzano/download/9905340.pdf>
- Cinzano P, Falchi F, Elvidge C, Baugh K (2000) The artificial night sky brightness mapped from DMSP satellite Operational Linescan System measurements. *R Astron Soc* 318:641-657
- Fuller D, Fulk M (1999) Comparison of NOAA-AVHRR and DMSP-OLS for operational fire monitoring in Kalimantan, Indonesia. *Int J Remote Sens* 21:181-187
- Mariategui L, Tafur R, Moron O, Ayon P (1997) Distribución y captura del Calamar gigante (*Dosidicus gigas*) a bordo de buques calamareros en aguas del Pacífico centro oriental y en aguas nacionales adyacentes. *Inf Prog Inst Mar Perú* 63:3-36
- Yatsu A, Yamanaka R, Yamashiro C (1999) Tracking experiments of the jumbo flying squid (*Dosidicus gigas*) with an ultrasonic telemetry system in the eastern Pacific Ocean. *Bull Nat Res Ins. Far Seas Fish* 36:55-60



## Case Study 11

# Spring Algal Bloom and Haddock Larvae Survival on the Scotian Shelf (Northwest Atlantic)

César Fuentes-Yaco\*<sup>1</sup>, Trevor Platt<sup>2</sup>, Shubha Sathyendranath<sup>2</sup>,  
Marie-Hélène Forget<sup>3</sup> and Venetia Stuart<sup>1</sup>

---

## 11.1 Background Information

According to the Hjort-Cushing match-mismatch hypothesis (Hjort 1914; Cushing 1974; 1990), the survival rate of fish and invertebrate larvae is a function of the match between the timing of the hatching of the eggs and the timing of the spring phytoplankton bloom. Testing such a hypothesis has been possible only with the advent of remotely-sensed data, which provides information at the appropriate scales of time and space (Platt et al., 2007). These types of data offer the opportunity to characterize the spring bloom with respect to the timing of initiation, the amplitude of the bloom, the duration of the bloom, and the timing (phase) of the bloom (Figure 11.1). These properties can be calculated for all pixels in the region of interest, in such a way that all spatial structure is preserved. The statistical moments of all of these properties, and their variation between years, can also be calculated and the results used to analyze the effect of ecosystem fluctuations on exploited stocks. The case study presented here shows the relationship between the phytoplankton bloom characteristics computed from remotely-sensed images and haddock (*Melanogrammus aeglefinus*) larvae survival on the Canadian Scotian shelf (Platt et al., 2003).

To understand this example, we will demonstrate how to generate a time-series of satellite ocean-colour images from different sensors, and will also show how to compute a climatology (temporal average) as well as the anomalies (deviation from the normal). Finally, we exemplify the association of these results with independent time-series data (non-satellite), on the larvae survival normalized by the spawning stock. The study area is the "Canadian Atlantic Zone", on the eastern seaboard of

---

<sup>1</sup>Bedford Institute of Oceanography, PO Box 1006, Dartmouth, Nova Scotia, B2Y 4A2, Canada.

\*Email address: [fuentes-yacoc@mar.dfo-mpo.gc.ca](mailto:fuentes-yacoc@mar.dfo-mpo.gc.ca)

<sup>2</sup>Plymouth Marine Laboratory, Prospect Place, Plymouth, PL1 3DH, UK

<sup>3</sup>Dalhousie University, Department of Oceanography, Halifax, NS, B3H 4J1, Canada

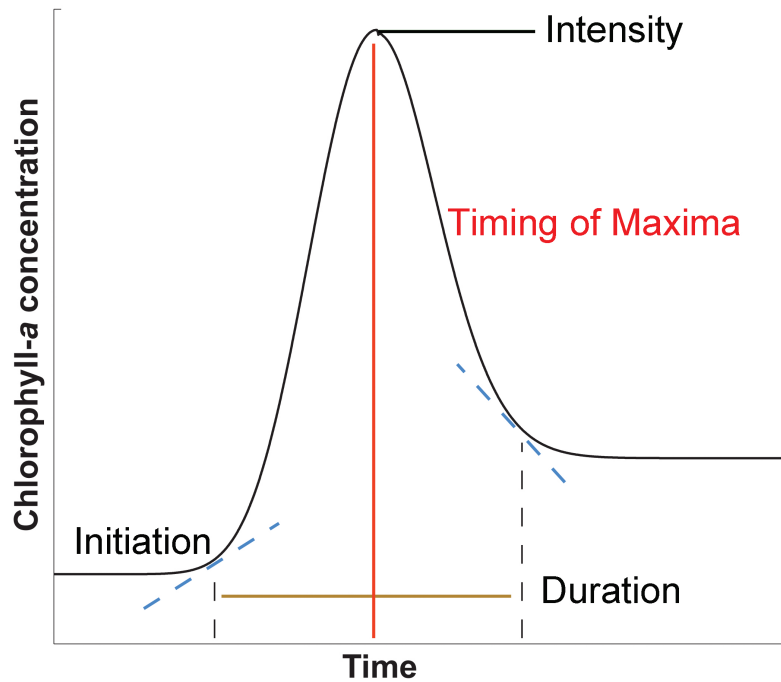


**Figure 11.1** Characteristics of the phytoplankton spring bloom: the maximum observed chlorophyll-*a* concentration (an index of phytoplankton biomass) referred to as the intensity; the weeks elapsed since beginning of February when the biomass first exceeded 20% of the maximum (bloom initiation); the weeks elapsed when the maximum intensity occurred (bloom timing); and the period during which the biomass remained above the 20% threshold (bloom duration).

Canada (Figure 11.2).

## 11.2 Materials and Methods

The ocean-colour images for the original work mentioned in this example (Platt et al., 2003) were captured and processed at the Bedford Institute of Oceanography. Currently, these images can be downloaded freely from the Internet at the sites given below.

Chlorophyll concentration was estimated from three different ocean-colour sensors: Coastal Zone Color Scanner (CZCS), POLarization and Directionality of the Earth's Reflectances (POLDER-1), and Sea-viewing Wide Field-of-view Sensor (SeaWiFS). Data from CZCS and SeaWiFS are available from NASA's Ocean Color website (<http://oceancolor.gsfc.nasa.gov/>). POLDER images are available from the French space agency CNES (<http://polder.cnes.fr/en/index.htm>), and the Japan Aerospace Exploration Agency (JAXA), (<ftp://ftp2.eorc.jaxa.jp/pub/ADEOS/OCTS/GAC3BM/Ver5/CHLO/daily/>).

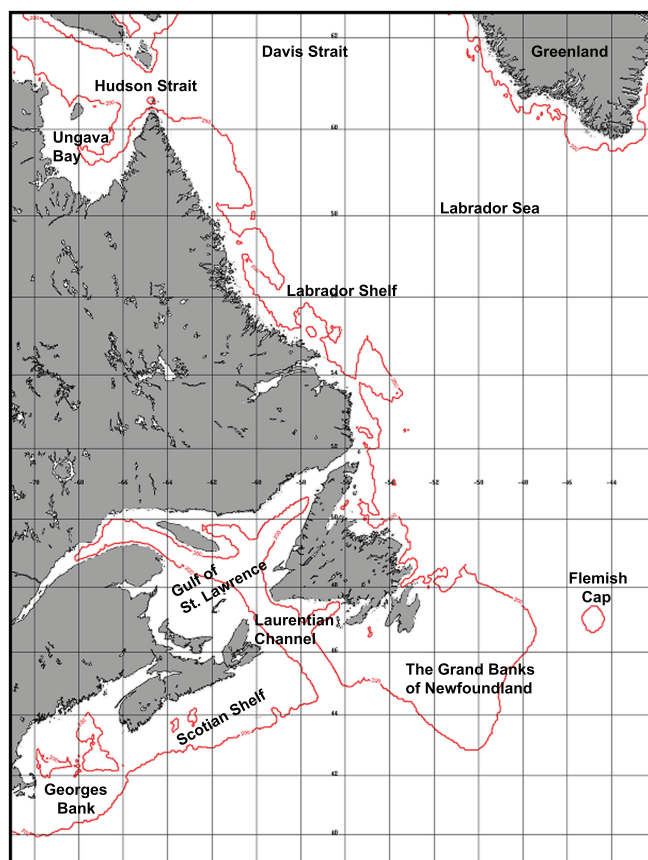


**Figure 11.2** The Canadian Atlantic Zone (39°N to 62.5°N and 42°W to 71°W). The 200 m isobath is also indicated.

Current CZCS Level-2 images on the NASA website are computed using the OC3 algorithm from O'Reilly et al. (2000), but tuned for bands at 443, 520, and 550 nm. This sensor provided data for the period between 1979 and 1981 of the example shown here. The current POLDER chlorophyll algorithm uses a bio-optical algorithm with three wavelengths (443, 490 and 565 nm), customized for POLDER data (Loisel et al., 2005). POLDER images for 1997 were used for this exercise. The OC4V4 algorithm is used for SeaWiFS for the interval from 1998 to 2001. Note that NASA has maintained the flow of SeaWiFS data until the present time (May 2010).

In all cases, the algorithms were applied to individual images after selection of cloud free pixels, and stratospheric and atmospheric corrections. Finally, the images were mapped to Mercator projections. The time-series for the study area was created by combining individual satellite passes to make weekly composite images with a nominal spatial resolution of 1 km per pixel. The temporal window used for the phytoplankton bloom characteristics is from February to September. Here we show only half-month composite images for the period mentioned (Figure 11.3).

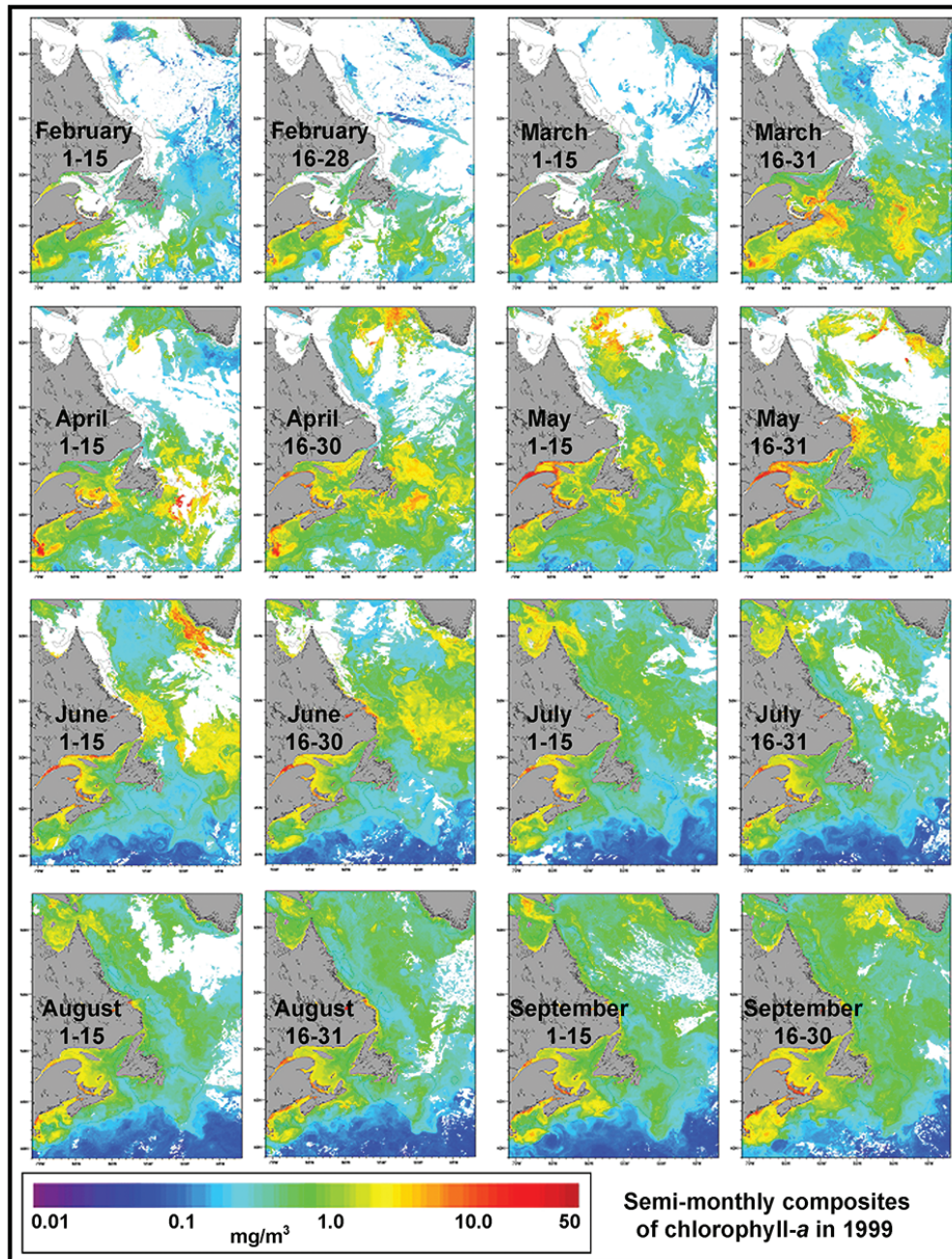


**Figure 11.3** Time-series of concentration of chlorophyll-*a* ( $\text{mg m}^{-3}$ ), for the Canadian Atlantic Zone created by combining satellite individual passes to make half-month composite images with a nominal spatial resolution of 1 km per pixel. The temporal window is delimited between February and September 1999.

## 11.3 Demonstration

### 11.3.1 Characterization of the phytoplankton bloom

The phytoplankton bloom can be characterized for each of the following ecosystem properties: maximum intensity, initiation, timing of maximum and duration of the bloom. To begin this process, load your 12 semi-monthly images shown in Figure 11.3, using your preferred software (SeaDAS, PCI, ENVI, etc.). For every pixel:

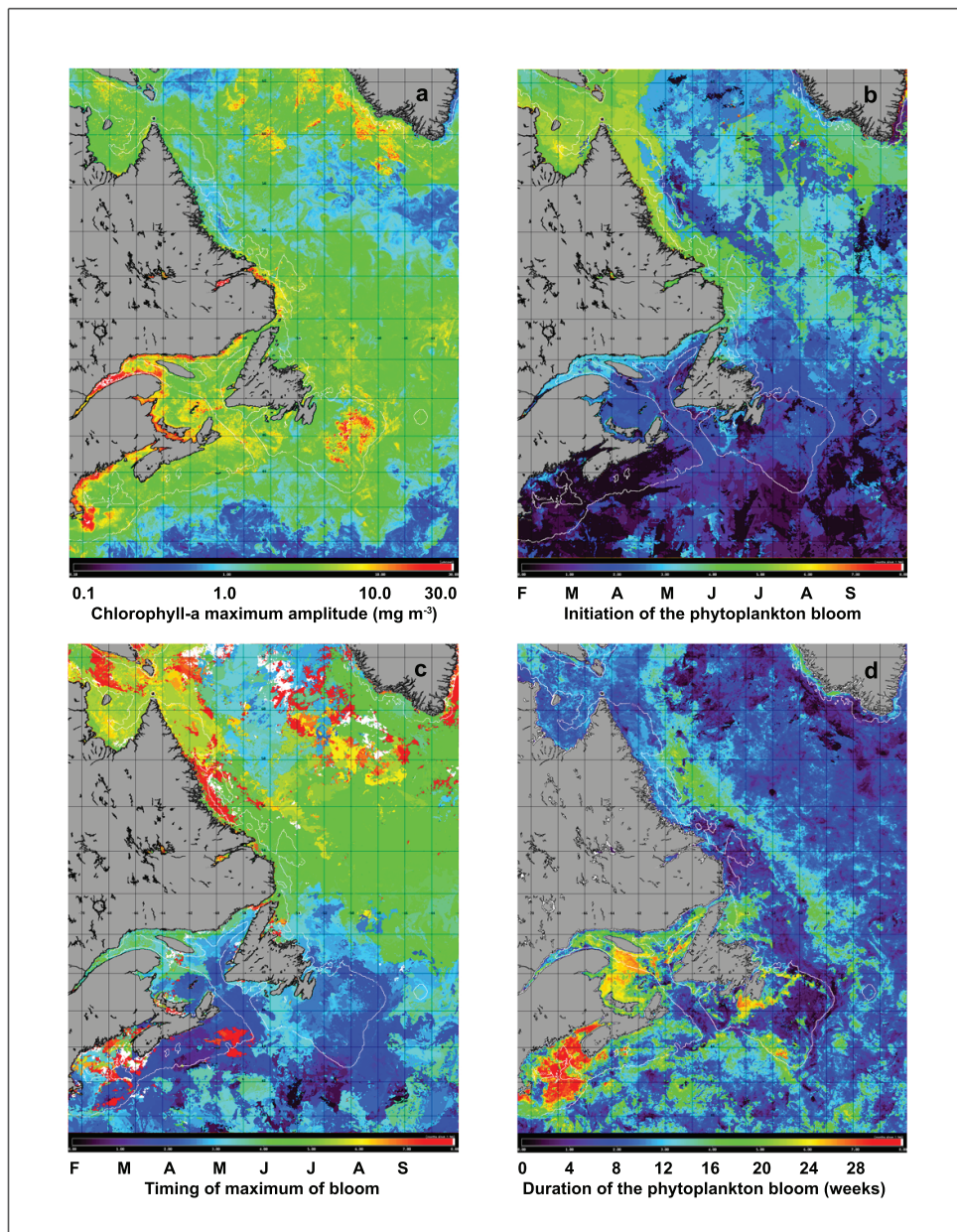
- a) Compute the maximum observed chlorophyll-*a* concentration (an index of phytoplankton biomass) referred to as the intensity.
- b) Compute the bloom initiation by counting the weeks elapsed since beginning of February when the biomass first exceeded 20% of the maximum.
- c) Compute the bloom timing, i.e. the weeks elapsed until the maximum intensity occurred.
- d) Compute the bloom duration, i.e. the period during which the biomass remained above the 20% threshold (bloom duration).

Figure 11.4 shows the spatial distribution of these indices in the study area, corresponding to the time-series between February and September 1999. The ecological indicators can be evaluated for all years in the time-series using data from all the satellite sensors, and the climatology (long-term average) can also be computed (Figure 11.5). The indices can be estimated for every pixel in the composite images, preserving all spatial structure in the fields.

The anomalies (deviations from the normal) for these ecological properties can be computed for particular years, i.e. the indices of the bloom can be calculated for individual years and compared with the climatological average (i.e. for every pixel, the difference between individual years minus the long-term mean value). In this way, it is possible to assess inter-annual variations in properties and also to evaluate whether, in a particular year, events are retarded or advanced compared with the mean. Anomalies for the timing of the maximum chlorophyll concentration can be seen for the years 1998 to 2001 in Figure 11.6. We used local anomalies, i.e. the climatology was calculated separately for each of the three sets of ocean-colour data: CZCS (1979-1981), and POLDER (1997) and SeaWiFS (1998-2001), and the anomalies in each set were calculated from the appropriate climatology.

### 11.3.2 Test of the match/mismatch hypothesis

The indices derived from the remotely-sensed time-series can be used to evaluate the effect of ecosystem fluctuation on exploited stocks (Platt et al., 2003). The operational test of the match/mismatch hypothesis is assessed under the null hypothesis that 'between-year' variance in recruitment is independent of fluctuations in the properties of the spring bloom. The time-series of the timing of the bloom was compared to an independent data series of haddock (*Melanogrammus aeglefinus*) recruitment, collected on the continental shelf off Nova Scotia. This is a 31-year time



**Figure 11.4** Spatial distribution of the ecological indices for phytoplankton blooms in the Northwest Atlantic for the year 1999: a) intensity, b) initiation, c) timing, and d) duration.

series (1970 – 2001) in which two years stand out as having produced exceptional year classes (Figure 11.7). For both years (1981 and 1999), remotely-sensed data of timing of maxima were available. The climatology of the timing of the chlorophyll-*a* maximum concentration from 1998 to 2001 is shown in Figure 11.5c.

For the study area described in Platt et al. (2003), the recruitment of haddock, normalized to biomass of the spawning stock, was highly correlated with the timing of the bloom. Early blooms were associated with better recruitment. The two exceptional year classes occurred in years with unusually early spring blooms. As a consequence, the null hypothesis was rejected. Anomalies of bloom timing accounted for 95% of the variance in normalized recruitment of haddock under a quadratic model (Figure 11.8).

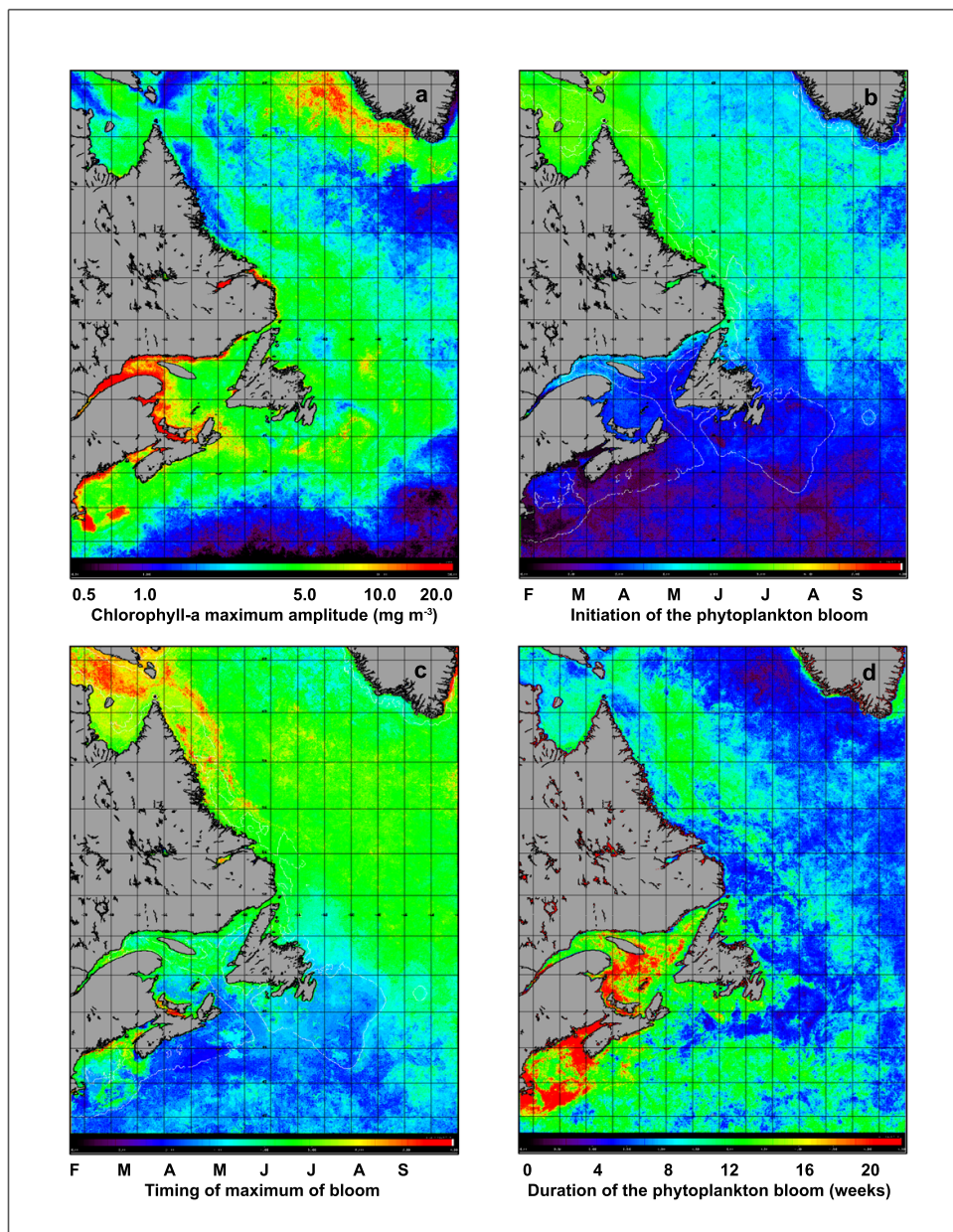
The results shown in this example argue for the importance of a trophic link between phytoplankton and fish stocks, especially the importance of fluctuations between years at the autotrophic level. The tentative explanation advanced for the result was that, for species with protracted spawning (such as haddock), an early spring bloom would confer enhanced survival on early larvae because the larvae will have adequate food supply.

## 11.4 Training

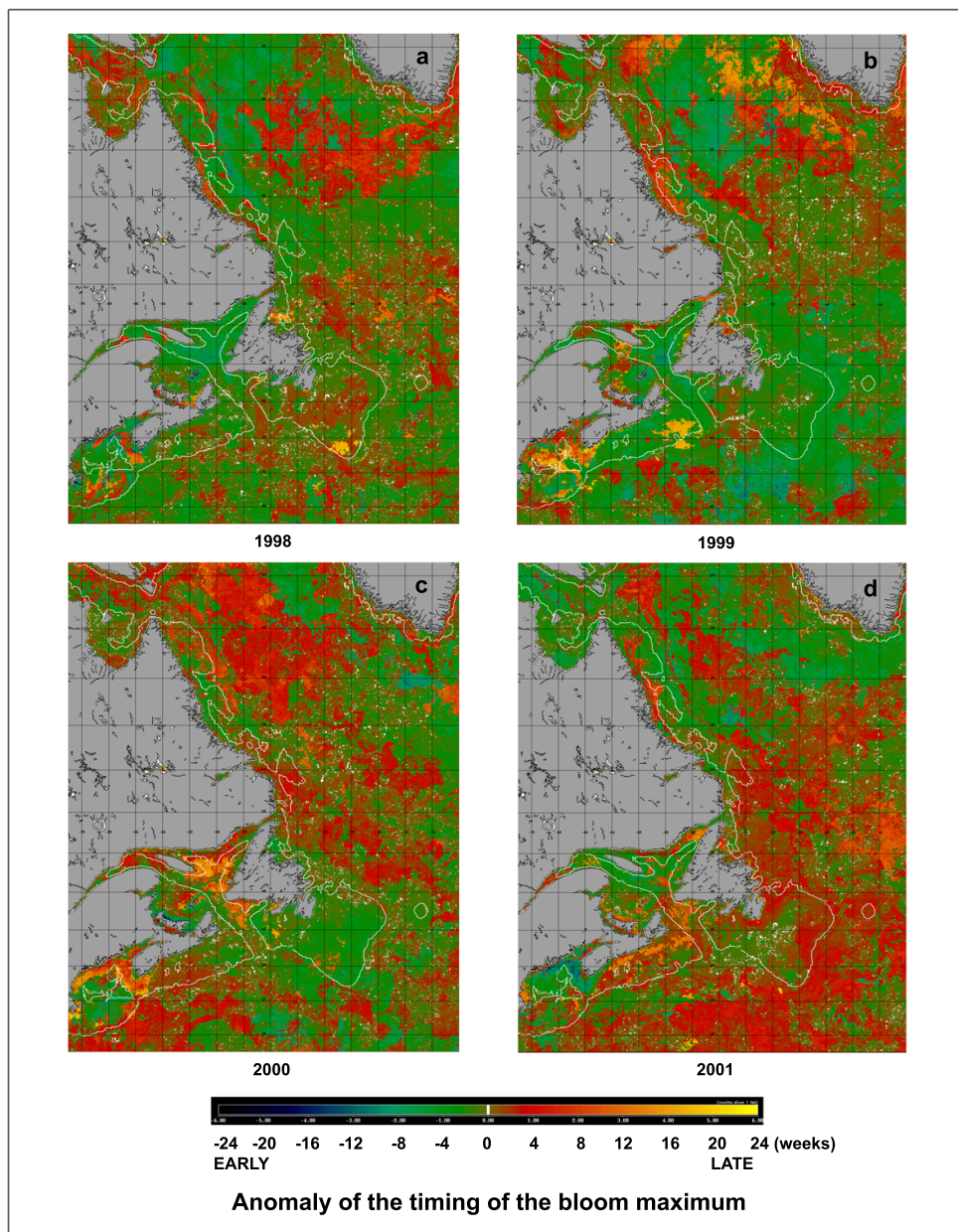
In this section you will visualize some examples before making your own time-series to compute the ecological indices.

Figure 11.3 represents a time-series of chlorophyll-*a* concentration between February and September 1999 in the northwestern Atlantic Canada region. Each composite image is averaged over a ~15 day period with a nominal spatial resolution of 1 km per pixel. This time-series is used to compute the ecological indices, described in detail in the text, and illustrated in Figure 11.1. Figure 11.4 shows the ecological indices derived from the phytoplankton bloom in the study area for 1999. The image 11.4a represents the maximum amplitude of chlorophyll concentration (intensity). The most frequent values fluctuate between 1.0 and 10 mg m<sup>-3</sup>, with areas of higher concentration in the Georges Banks and the Grand Banks of Newfoundland. The Gulf Stream can be identified in the southern part of the study area as the region with relatively low chlorophyll values. It is important to observe that in some coastal regions that are influenced by high river runoff or intense tides, the standard chlorophyll algorithms do not produce viable results as they are affected by the high concentration of detritus, sediments and yellow substances. These waters are referred to as "Case-2" waters and are characterized by an optical signature dominated by substances other than chlorophyll-*a* (e.g. sediments, yellow substances). The resulting estimates of pigment concentration are frequently overestimated in these waters. Figure 11.4b characterizes the onset of algal bloom, showing the process advancing from south to north. Note that in

some northern regions (Davis Strait and



**Figure 11.5** Climatology of ecological indicators for the period between 1998 and 2001: a) intensity, b) initiation, c) timing, and d) duration.



**Figure 11.6** Anomalies of the bloom timing (weeks elapsed when the maximum intensity occurred) for the years 1998 to 2001.

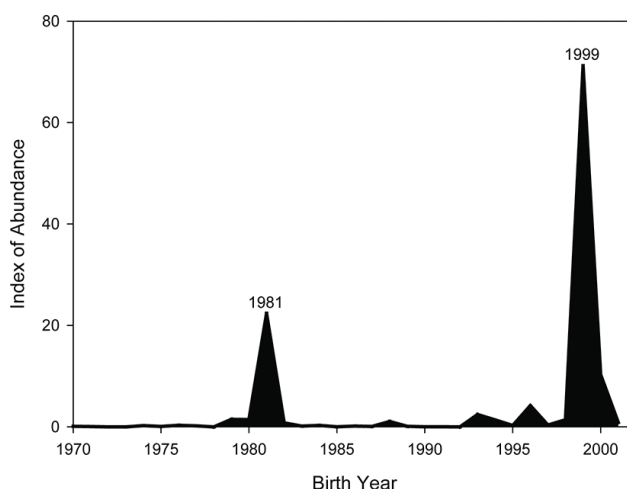


**Figure 11.7** Time-series of haddock (*Melanogrammus aeglefinus*) at age-0, sampled on the continental shelf off Nova Scotia between 1970 and 2001.

western Greenland) the bloom initiation is relatively early in the year, compared with the rest of the region. Typically, the bloom starts later on the continental shelf of Labrador because of winter-ice that delays the event. Figure 11.4c describes the time required to reach the maximum concentration of chlorophyll. The spatial patterns of the ecological index are related to those of the bloom initiation, but they have a time lag determined by local conditions. Figure 11.4d shows the phytoplankton bloom duration. In general, in the northern regions the duration of the bloom is shorter than in southern areas. However, some areas in the north also maintain significant concentrations of phytoplankton for several months.

Figure 11.5 shows the average (climatology) of ecological indices for the period between 1998 and 2001. Note that the averaging of several years of data moderates the outlier values that are seen in the one-year images (Figure 11.4). Figure 11.5a shows the maximum amplitude of chlorophyll concentration. High values (between 2.0 and 10 mg chlorophyll  $m^{-3}$ ) occur over the continental shelves and the lower values are in open sea areas. Figure 11.5b displays the onset of the algal bloom and shows a significant front north of Newfoundland. Note how the phytoplankton in the region to the south of this geographical division start to increase well before the northern zone. Figure 11.5c shows the timing of maximum bloom concentration and is closely associated with the initiation of the bloom. However, the front observed in the previous image is less obvious and in fact, some southern regions tend to reach the bloom maximum relatively late. Enlarge the coastal area of central Nova Scotia for a close analysis of the study area of Platt et al. (2003). These data represent weekly measurements averaged from February to September, between 1998 and 2001. Observe that the continental shelf's central region reached the highest concentration of chlorophyll earlier than the western areas. In this region the turbulence due to vertical mixing by tides (the most intense in the world)

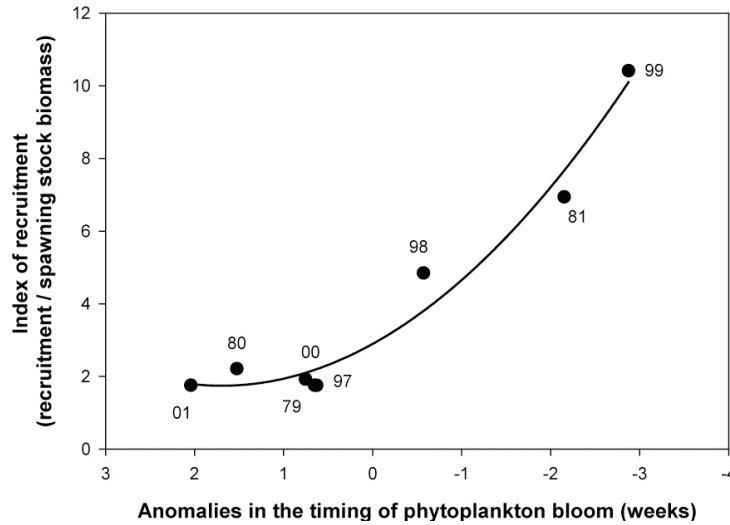


**Figure 11.8** Quadratic regression of the recruitment of haddock, normalized to biomass of the spawning stock, with the data of timing of the phytoplankton bloom. Anomalies of bloom timing accounted for 95% of the variance in recruitment of haddock.

prevents early stratification of the mixed layer, thus delaying the phytoplankton blooming. The image 11.5d characterizes the duration of the phytoplankton bloom, and clearly illustrates the shorter bloom duration in several parts of the northern study area compared with the southern areas. Note that the northwestern region also exhibits longer blooms, a critical fact for higher trophic strata.

The maps in Figure 11.6 correspond to the anomalies of the timing of maximum concentration of chlorophyll in the years 1998 to 2001. Green colours indicate the pixels where the chlorophyll maximum was reached sooner than the 5-year average, while red colours represent areas where the bloom peaked later than expected. This ecological metric is important for basic research and more directed purposes in several areas such as ecology, oceanography, fisheries, etc. In the present case-study, it is useful to understand that an early phytoplankton bloom can diminish the number of larvae that may suffer from starvation. However, larval stages of different species may not all benefit from an early bloom; some species such as the northern shrimp (*Pandalus borealis*) seem to benefit if the phytoplankton bloom is delayed until the surface waters warm (explore Further Readings).

## 11.5 Questions

**Q 1:** Why do we find such apparent high chlorophyll concentrations in the St. Lawrence River and in the southern Gulf of St. Lawrence in Figure 11.3?

**Q 2:** What approach was used to circumvent the bias introduced by the use of

different platforms to construct such a long time-series of ocean-colour data?

**Q 3:** In Figure 11.4a, why is the peak of chlorophyll concentration during the spring bloom higher over Georges Bank and Grand Banks, and what is the ecological significance.

**Q 4:** Is it always advantageous for fish larvae to have an early phytoplankton bloom?

## 11.6 Answers

**A 1:** The standard chlorophyll algorithms developed for Case-1 waters are affected by high concentrations of detritus, sediments and yellow substances which may dominate the optical signature in coastal Case-2 waters. Thus the chlorophyll concentration estimated using standard Case-1 water algorithms in these waters may be biased. More complex algorithms are required to discriminate the various components in coastal waters. For example, neural network analysis is used to retrieve concentrations of phytoplankton pigment (Algal Pigment Index II), suspended matter and yellow substances from MERIS data. For further information, see the MERIS Product Handbook (<http://envisat.esa.int/handbooks/meris/>) and the Algorithm Theoretical Basis Document 2.12 (ATBD) ([http://envisat.esa.int/instruments/meris/pdf/atbd\\_2\\_12.pdf](http://envisat.esa.int/instruments/meris/pdf/atbd_2_12.pdf)).

**A 2:** The climatologies were calculated separately for each of the three time-series of ocean-colour data (CZCS, POLDER and SeaWiFS). For each mission, the anomalies were calculated in relation to the appropriate climatology, resulting in a long-term time-series of local anomalies. Moreover, the use of the timing of the bloom, instead of actual pigment concentration at the peak of the bloom, is independent of the algorithm used by each mission to estimate chlorophyll concentration.

**A 3:** The elevated chlorophyll concentration in these regions is likely supported by the vigorous mixing of the relatively shallow waters by tidal currents. The spring bloom typically begins once the critical depth becomes shallower than the water depth. The high chlorophyll concentration in these two ecosystems supports a large marine community and results in two exceptionally productive environments, with extensive fisheries.

**A 4:** Not necessarily. It is true that some species require an abundant food supply for their early stages, but other species may not benefit from an early surplus of food. Their life cycle may require other ecological conditions, such as warmer surface water, to take full advantage of the seasonal event.

## 11.7 References

- Cushing DH (1974) The natural regulation of fish populations. In: Harden Jones FR (ed) *Sea Fisheries Research*, Elek Science, London pp 399-412
- Cushing DH (1990) Plankton production and year-class strength in fish populations: an update of the match/mismatch hypothesis. *Adv Mar Biol* 26: 249-294
- Hjort J (1914) Fluctuations in the great fisheries of northern Europe, viewed in the light of biological research. *Rapp P-V Reun CIESM* 20: 1-228
- Loisel H, Deschamps PY, Nicolas JM, Moulin C, Poteau A (2005) POLDER-2/Ocean Color ATBD Bio-Optical Algorithms. Algorithm Theoretical Basis Document, [http://smc.cnes.fr/POLDER/Algo/ATBD\\_algo\\_bio2.pdf](http://smc.cnes.fr/POLDER/Algo/ATBD_algo_bio2.pdf)
- O'Reilly JE, and 24 co-authors (2000) Ocean color chlorophyll-*a* algorithms for SeaWiFS, OC2 and OC4: Version 4. *SeaWiFS Postlaunch Technical Report Series*, 11(3): NASA/TM-2000-206892
- Platt T, Fuentes-Yaco C, Frank KT (2003) Spring algal bloom and larval fish survival. *Nature* 423: 398-399
- Platt T, Sathyendranath S, Fuentes-Yaco C (2007) Biological oceanography and fisheries management: perspective after 10 years. *ICES J Mar Sci* 64: 863-869

### 11.7.1 Further reading

- Fuentes-Yaco C, Koeller PA, Sathyendranath S, Platt T (2007) Shrimp (*Pandalus borealis*) growth and timing of the spring phytoplankton bloom on the Newfoundland-Labrador Shelf. *Fish Oceanogr* 16(2): 116-129
- Fuentes-Yaco C, Koeller P, Zhai, L, Platt T, Sathyendranath S, Covey, M, Prabhukonkar, S (2010) Condition factor of northern pink shrimp *Pandalus borealis* in the North West Atlantic. *ICES J Mar Sci*, In press
- IOCCG (2009) Remote Sensing in Fisheries and Aquaculture. Forget M-H, Stuart V, Platt T (eds.) Reports of the International Ocean-Colour Coordinating Group, No 8, IOCCG, Dartmouth, Canada.
- Koeller P, Fuentes-Yaco C, Platt T (2007) Decreasing shrimp sizes off Newfoundland and Labrador - environment or fishing? *Fish Oceanogr* 16(2): 105-115
- Koeller P, Fuentes-Yaco C, Platt T, Sathyendranath S, Richards A, Ouellet P, Orr D, Skúladóttir U, Wieland K, Savard L, Aschan M (2009) Basin-scale coherence in phenology of shrimps and phytoplankton in the North Atlantic Ocean. *Science* 324(5928): 791-793
- Koeller P, Friedland KD, Fuentes-Yaco C, Han G, Kulka DW, O'Reilly J, Platt T, Richards A, Taylor M (2009) Remote sensing applications in stock assessments. In: Forget M-H, Stuart V, Platt T (eds) *Remote Sensing in Fisheries and Aquaculture*, IOCCG, Rep No 8, pp 29-42

## Case Study 12

# Application of Multi-Sensor Satellite and Fishery Data, Statistical Models and Marine-GIS to Detect Habitat Preferences of Skipjack Tuna

**Robinson Mugo<sup>\*1,2</sup>, Sei-Ichi Saitoh<sup>1</sup> Akira Nihira<sup>3</sup> and Tadaaki Kuroyama<sup>3</sup>**

---

## 12.1 Introduction

Advances in satellite remote sensing of the oceans have expanded our knowledge of oceanographic phenomena at spatial and temporal scales previously inconceivable from ship and buoy platforms. Satellite remote sensing data used in oceanographic work is mainly from sea surface temperature (SST), ocean colour and ocean altimetry. Application of geographic information systems (GIS), remotely-sensed imagery and statistical models in fisheries oceanography (Valavanis et al., 2008) are also widening the scope of marine studies in time and space. GIS, widely developed for land-based applications, have grown to accommodate oceanographic work by incorporating functions that handle multiple dimensionality and dynamism of marine data (Wright and Goodchild, 1997). Analyses of remotely-sensed data and fisheries data under a GIS environment have facilitated elucidation of fundamental relationships between marine biota and their oceanic environment (Valavanis et al., 2008). Coupling of GIS applications and geo-statistical models thus provide a platform for integrating diverse forms of data to provide scientifically underpinned information for marine resource management. The objective of this case study is to illustrate how remotely-sensed information can be used to derive habitat indices for pelagic species such as skipjack tuna.

---

<sup>1</sup>Laboratory of Marine Environment and Resource Sensing, Graduate School of Fisheries Sciences, Hokkaido University, 3-1-1 Minato-cho, Hakodate, 041-8611, Hokkaido, Japan. \*Email address: [robin\\_mugo@salmon.fish.hokudai.ac.jp](mailto:robin_mugo@salmon.fish.hokudai.ac.jp)

<sup>2</sup>Kenya Marine & Fisheries Research Institute, P.O. Box 81651, Mombasa, Kenya

<sup>3</sup>Ibaraki Prefecture Fisheries Research Station, Japan

## 12.2 Background

Global tuna catches have increased steadily from a half million tonnes in 1950 to almost 4 million tonnes in 1999 (Miyake et al., 2004). The Pacific Ocean has the highest proportion of catches (65%) compared to about 15 and 20% for the Atlantic and Indian Oceans respectively (Miyake et al., 2004). Skipjack tuna is one of the species whose catches have risen consistently in the past decade (FAO, 2009), and in catch volumes, the species ranks third after anchovies and the Alaskan Pollock. The western Pacific produces substantial skipjack tuna catches. Skipjack tuna utilize the upper pelagic environment for their habitat; hence satellite data provide appropriate observations for their horizontal habitats. Skipjack tuna are known to associate with thermal fronts, warm water streamers and eddies in the western North Pacific (Tameishi and Shinomiya, 1989; Sugimoto and Tameishi, 1992), which are features that can be distinguished from satellite remotely-sensed SST, ocean colour or altimetry data. Studying skipjack tuna's habitat from remotely-sensed environmental data provides a scientific basis for understanding their response to externalities such as climate change and fishing pressure. Habitat models based on remotely-sensed data can facilitate fishery forecasting, effort control or design of dynamic marine protected areas.

Skipjack tuna in the western Pacific migrate as far as 44°N off Japan (Wild and Hampton, 1993; Langley et al., 2005). Migration patterns follow a north-south seasonal cycle where migration to higher latitudes occurs in the fall-summer season (Kawai and Sasaki, 1962; Matsumoto, 1975; Ogura, 2003). Migration is influenced by ocean currents and the fish move along prevailing currents utilizing them as foraging habitats (Uda and Ishino, 1958; Uda, 1973). The western most groups are comprised of one originating from the Philippine islands and a second group from the Marianna-Marshall islands (Figure 12.1). These groups migrate northwards along the Japanese coastal waters. A third group originates east of the Marshall Islands and moves in a northwesterly direction into Japanese offshore waters (Matsumoto, 1975). Part of this group could move farther downstream of the Kuroshio Current to the east of the Midway Island. In late summer and early autumn, the fish begin their southward migration.

## 12.3 Data and Methods

### 12.3.1 Study area

To enable one to appreciate the application of remotely-sensed imagery used in tuna ecology in the western North Pacific, a brief description of the key physical oceanographic features of this ecosystem is given here. The western North Pacific (Figure 12.1) is a productive ecosystem influenced mainly by the Kuroshio Current, Oyashio Current and the Tsugaru Warm Current (Talley et al., 1995). First, we

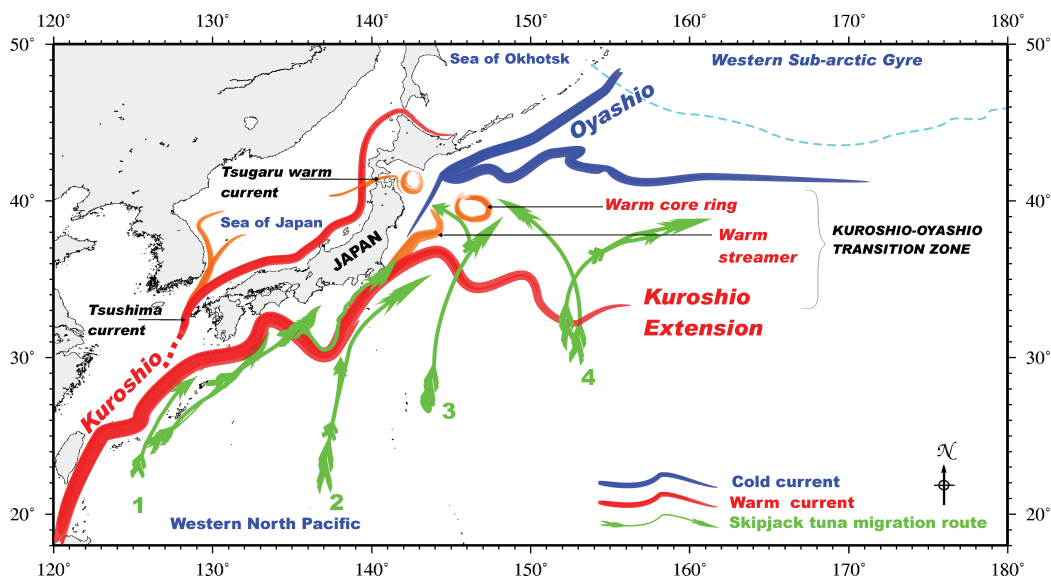


**Figure 12.1** Northern migration (mainly from spring) pattern of skipjack tuna (green lines) off the south and east coasts of Japan in the western North Pacific. The migration pattern is largely influenced by temperature and ocean currents. Modified from Nihira (1996).

will describe the two main currents in this ecosystem: the Kuroshio and Oyashio currents. The Oyashio Current (Figure 12.1), formed by waters from the Okhotsk Sea and the Subarctic Gyre (Yasuda, 2003), flows southward, transporting low-temperature, low-salinity and nutrient-rich waters to the North Pacific Subtropical Gyre (Sakurai, 2007). The current commonly meanders twice after leaving the coast of Hokkaido, generating the first and second intrusions (Kawai, 1972). The meanders are separated by a warm core ring (WCR) originating from the northward movement of the ring produced by the Kuroshio Current (Yasuda et al., 1992). The southern limit of subpolar waters is often referred to as the Oyashio Front (Talley et al., 1995). The Oyashio ecosystem is an important fishing ground for several subarctic species and subtropical migrants (Saitoh et al., 1986). The Kuroshio Current (Figure 12.1) originates from the subtropical gyre and is distinguished by low density, nutrient poor, warm and high salinity surface waters (Kawai, 1972; Talley et al., 1995). The Kuroshio Extension is an eastward-flowing inertial jet characterized by large-amplitude meanders and energetic pinched-off eddies, with high eddy kinetic energies (Qiu, 2002). Confluence of the two currents results in a mixed region, the Kuroshio-Oyashio Transition Zone (Yasuda, 2003). The behaviour of the Kuroshio Extension, warm streamers and WCRs in the Transition Zone is important to the fishing industry (Saitoh et al., 1986; Sugimoto and Tameishi, 1992). The Tsugaru Warm Current originates from the Tsushima Current and flows with warm and saline water from the Sea of Japan (Talley et al., 1995). The recognition of these dynamic oceanographic features by satellite sensors at varying time scales makes remote

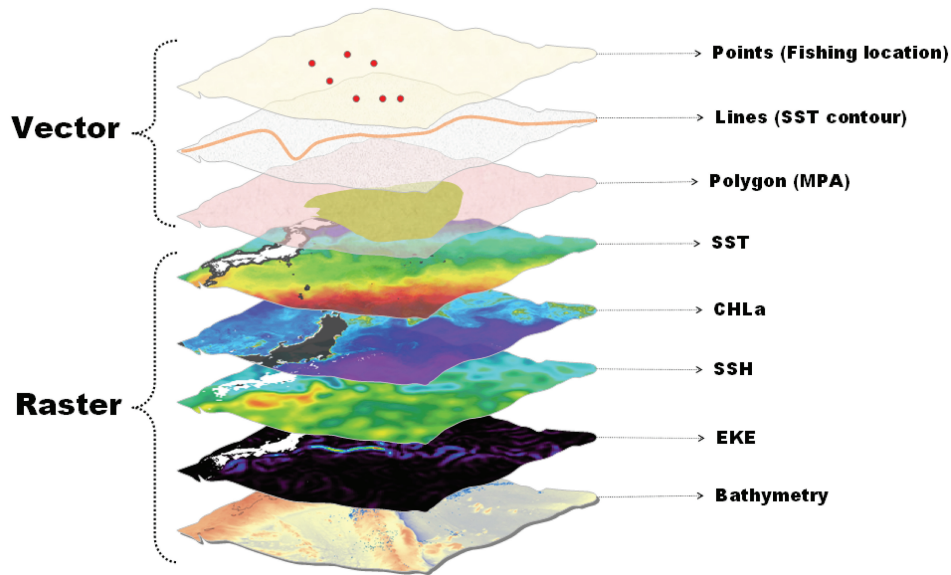


**Figure 12.2** A graphic representation of the core GIS data types, vector (point, line and polygon) and raster (imagery) data.

sensing an invaluable tool in ecological studies.

### 12.3.2 GIS data types

Geographic information system data types are largely classified into vector and raster data types (Figure 12.2). Vector data are data types that represent real world features as points (fishing location or buildings), lines (a contour or road), or polygons (a marine protected area or car park). Raster data represent real world features as grids, which store values that are used to interpret the real world feature (e.g. a SST image or bathymetry). Both data formats are useful in a GIS in different scenarios. It is important to point out the differences so as to make their usage in subsequent sections convenient. A schematic diagram illustrating how the different types of data are integrated in a GIS during analyses is shown in Figure 12.3.

### 12.3.3 Image processing and GIS software

There are several types of image processing and GIS software available that can be used to analyze remotely-sensed oceanographic data. Some are commercial while others can be downloaded freely from the internet. It is not possible to draw an exhaustive list of available software here, but ArcGIS, Erdas Imagine and Idrisi are some of the commercially-available software capable of working with remotely-sensed imagery. On the other hand, the generic mapping tools (GMT), SeaDAS and GRASS are freely available for download from the internet. For this case study, we

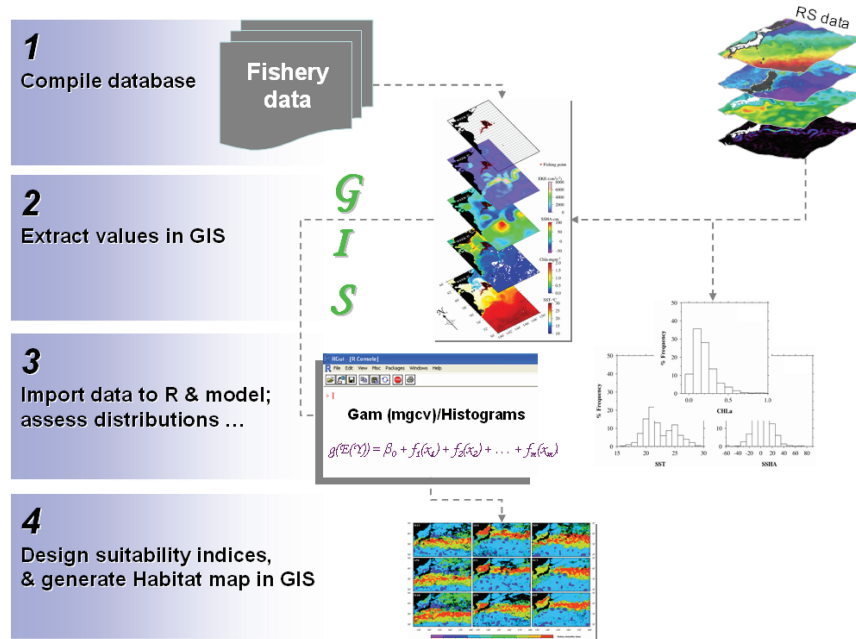


**Figure 12.3** A schematic flow of methods and tools used in the analyses.

will mainly use ArcGIS 9.2 and some of the associated add-in programs that can be ported to the program. As utilization of oceanographic remotely-sensed imagery continues to grow, various add-in software continue be designed that enable users to read the data directly into a GIS platform. That reduces the time used to process the data and convert them between different formats, thus granting ecologists more time to concentrate on their research. Two examples of such software are the Environment Data Connector (EDC) and the Marine Geospatial Ecology Tools (MGET) (Roberts et al., in press). The EDC can be downloaded at <http://www.asascience.com/software/arcgistools/edc.shtml> while the MGET is available at <http://code.env.duke.edu/projects/mget>. Both have accompanying instructions for installation. They are useful for downloading remotely-sensed oceanographic data directly into ArcGIS and are appropriate especially for users who may not be conversant with other methods of reading such datasets. Once correctly installed, they are fairly easy to use.

### 12.3.4 Fishery data

Fishery data are useful mainly for indicating occurrence and abundance of a species in a certain area. Here we use fishery data from skipjack tuna fishing vessels in the western North Pacific from March to November 2004. The data are comprised of latitude and longitude positions, and catch per unit effort (CPUE). By mapping these data on to remotely-sensed images at corresponding time scales, they can

reveal the conditions under which catches were made. They were also used to make a generalized additive model (Wood, 2006) from which ranges of habitat variables important for skipjack tuna habitat were derived. Further reading on GAMs and their applications in fisheries work using remotely-sensed data can be obtained from Wood (2006), Valavanis et al. (2008), and Mugo et al. (2008), among others.

### 12.3.5 Remotely-sensed environmental data

We will use four types of remotely-sensed environment data, sea surface temperature (SST), surface chlorophyll concentration (chl-*a*), sea surface height anomalies (SSHA) and eddy kinetic energy (EKE) derived from geostrophic velocities. Each of these variables can be important indicators of the habitat of pelagic species. There are different ways of analyzing satellite datasets, given their spatial and temporal resolutions. Considering the temporal scale, one way would be to use the individual satellite passes for a certain variable, which can differ from hours to days depending on the repeat cycle. Another way would be to work with temporally-averaged data, either daily, 3 days, 7 days, 8 days, monthly etc, depending on the objective of the work at hand. Data averaging is commonly used to minimize instances of missing data due to weather conditions (clouds or rain) or instrument malfunction. Here we consider weekly- and monthly-resolved environment data in order to have (1) a relatively high temporal resolution to observe fishing fleet distribution (weekly scale) and (2) good coverage especially for SST and chl-*a* data (monthly-averaged data).

Working with ArcGIS 9.2 (and above), a relatively convenient way of downloading satellite datasets would be to use the Environment Data Connector tool or the MGET. In principle, these tools connect to remote databases (using the internet) and download data according to user specified input. Here we will illustrate briefly the process of downloading and sampling raster (image) data using the EDC. It is assumed that the user has already installed the tool and can access it from ArcGIS. For a step by step process on how to download a chlorophyll image, refer to Figure 12.4, steps 1-3. Steps 4-6 can be used to resample the image from one resolution value to another, and extract geo-physical values from the image using a set of known latitude-longitude positions.

**Step 1:** Connect to online databases using EDC and select the type of satellite data set to download. For example, to download monthly chlorophyll-*a*, select "Satellite datasets", "Colour", and select an ocean-colour dataset that suits your work. A brief description about the dataset is also given as metadata.

**Step 2:** Select the spatial extent and temporal resolution for the selected dataset. Click "process" to download data. In this case, the western North Pacific (18-50°N; 125-180°E) is selected for September, 2004.

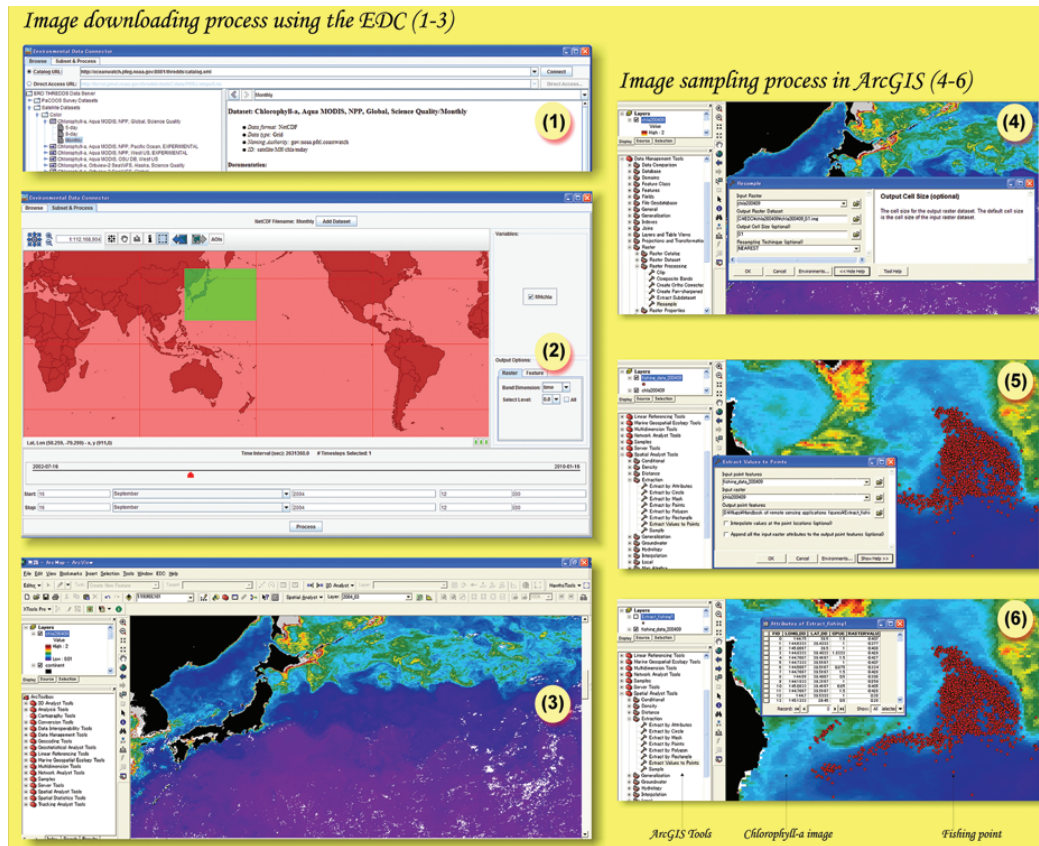


**Figure 12.4** The process of downloading satellite data into ArcGIS using the EDC (1-3) and subsequent re-sampling of the data and extraction of geo-physical values corresponding to fishing locations. The processes are illustrated using a chlorophyll-*a* image and can be replicated with other satellite datasets such as SST or SSHA.

**Step 3:** In the resulting raster image, BLACK represents land while WHITE is missing data.

**Step 4:** Use the ArcGIS ToolBox to resample the data to a desired resolution by selecting; "Data management tools", "Raster", "Raster processing" and "Resample". Complete the dialog box to finish the process.

**Step 5:** Overlay the chlorophyll-*a* image with fishing locations and sample (extract) the pixel values corresponding to the latitude-longitude positions. On the ArcGIS ToolBox, select "Spatial Analyst Tools", "Extraction", "Extract values to Points", complete the resulting dialogue box to sample the image.

**Step 6:** The results of the extraction process are a table showing the latitude-longitude positions of fishing locations and the corresponding chlorophyll-*a* values at those locations. These data can then be exported to Excel or any other software

	A	B	C	D	E	F	G	H	I
1	Longitude	Latitude	YEAR	MONTH	DAY	CPUE	SST	CHLA	SSHA
2	142.883	39.283	2004	9	1	0.500	19.936	0.306	-6.22
3	143.283	38.500	2004	9	1	0.500	20.617	0.388	-14.71
4	142.933	39.300	2004	9	1	3.667	20.027	0.279	-6.22
5	143.150	39.317	2004	9	1	1.833	19.956	0.284	-10.478
6	143.017	38.100	2004	9	1	0.500	22.125	0.266	9.151
7	143.167	38.433	2004	9	1	2.333	19.712	0.416	-14.711
8	143.233	38.367	2004	9	1	2.000	21.730	0.283	-14.711
9	143.133	38.450	2004	9	1	0.833	19.778	0.373	-14.711
10	143.283	38.433	2004	9	1	1.600	21.457	0.360	-14.711
11	143.133	38.467	2004	9	1	2.000	19.778	0.373	-14.711
12	143.133	38.467	2004	9	1	2.667	20.524	0.322	-14.711
13	143.450	39.100	2004	9	1	0.833	20.841	0.265	-14.711
14	143.450	38.867	2004	9	1	0.500	20.629	0.280	-10.478
15	143.067	39.133	2004	9	1	1.500	20.907	0.236	-12.500
16	143.533	39.283	2004	9	1	1.500	20.907	0.236	-12.500

**Figure 12.5** A sample fishery environment database showing the spatial information (longitude and latitude), the temporal information (year, month and day), fishery information (CPUE) and environmental information derived from remotely-sensed images (SST, chl-*a* and SSHA). Such a database is useful for modelling the habitat conditions of the species under study.

for further analysis.

Re-sampling the image resolution is an important step, especially in cases where the datasets in use have different spatial resolutions. Harmonizing the resolution before analyzing the data further ensures that the pixel values for all images have the same "dimensions". These steps assume that the user has some basic knowledge of using ArcGIS (ArcView), with at least the Spatial Analyst extension. To obtain data for other variables (SST and SSHA) repeat these steps for each respective image. For this exercise, we download weekly and monthly datasets for each parameter. Utilization of the MGET tool is not illustrated here but it is fairly straight forward. For example, we can use MGET to download weekly geostrophic current velocity images,  $1/3^\circ$  resolution ( $u$  and  $v$  components) as ArcGIS rasters from AVISO. The  $u$  and  $v$  weekly rasters are then used to calculate EKE with the Raster Calculator function in Spatial Analyst extension (ArcGIS 9.2) using Equation 1 (Robinson, 2004). Further, we can average the weekly EKE rasters into monthly data, using the Raster Calculator function in Spatial Analyst extension, by simply adding the rasters and dividing by the total number of rasters. The resulting raster can then be subjected to steps 4 - 6 in Figure 12.4.

$$\text{EKE} = \frac{1}{2}(u^2 + v^2) \quad (12.1)$$

Since we have used the same latitude and longitude positions to sample/extract values from four different monthly images, it is possible to combine the values extracted from each image into one final database as shown in Figure 12.5.

## 12.4 Demonstration Section

Thermal and ocean-colour fronts, meso-scale phenomena such as warm and cold core eddies, and ocean currents are key features that determine the distribution of pelagic fish. Since the advent of ocean satellite remote sensing, it is possible to monitor the development of these features at relatively large spatial scales and hence assess their effect on fish habitat. Information from such studies has had applications in operational fisheries oceanography and marine resource conservation.

To enhance our understanding of satellite image interpretation in relation to tuna ecology, we will first consider one set of four images (SST, chl-*a*, SSHA, EKE), each of which is overlaid with weekly-resolved fishing locations (Figure 12.6). All the images are of the same week (week 37). Figure 12.6a is a SST image, colour coded from blue to red. The red represents warm waters while blue shows cold waters or lower temperatures. The warm waters become progressively cooler as we move northwards, where they "meet" the southward flowing cold waters driven by the Oyashio Current. A northward flowing "stream" of warm waters (41°N, 146°E), 18-20°C (refer to the SST image colour bar) has made an "incursion" into the cold water region. Skipjack tuna fishing locations are also situated within this northward flowing stream of warm waters, indicating the temperature range within which the fish were found.

In Figure 12.6b, the same fishing locations as in Figure 12.6a are overlaid on a chlorophyll-*a* image. The blue areas of this image show low chlorophyll waters while the green to red colour represents relative high chlorophyll-*a* waters. It is interesting to note that the low chlorophyll or oligotrophic waters correspond to warm water areas while relatively eutrophic waters correspond to cold waters in the north. In this case, skipjack tuna fishing locations are aligned along the relatively oligotrophic waters but right at the "edge" of high chlorophyll waters. This "edge" appears to divide two water masses, a warm and oligotrophic water mass from a cold and eutrophic water mass, a phenomenon commonly referred to as a "front". Fronts have been shown to be one of the mechanisms that aggregate tuna.

Figure 12.6c illustrates fishing locations overlaid on a SSHA image. Sea surface height anomaly data are useful in showing meso-scale variability in the ocean. This involves the distribution of eddies and surface currents. In this image, areas with positive anomalies are shown as green to red, which are likely to indicate presence of warm core eddies. Dark blue to purple areas indicate areas with negative anomalies which represent cold core eddies. The distribution of fishing locations points to a pattern where the locations are associated predominantly with zero to positive anomalies and not much with the negative anomaly areas.

The EKE image (Fig. 12.6d) presents information on eddy kinetic energy which can tell us more about presence of strong eddies or fast flowing currents. For instance, the Kuroshio Current and Extension are clearly visible from this image. Such features also influence tuna migration and are thus important to consider

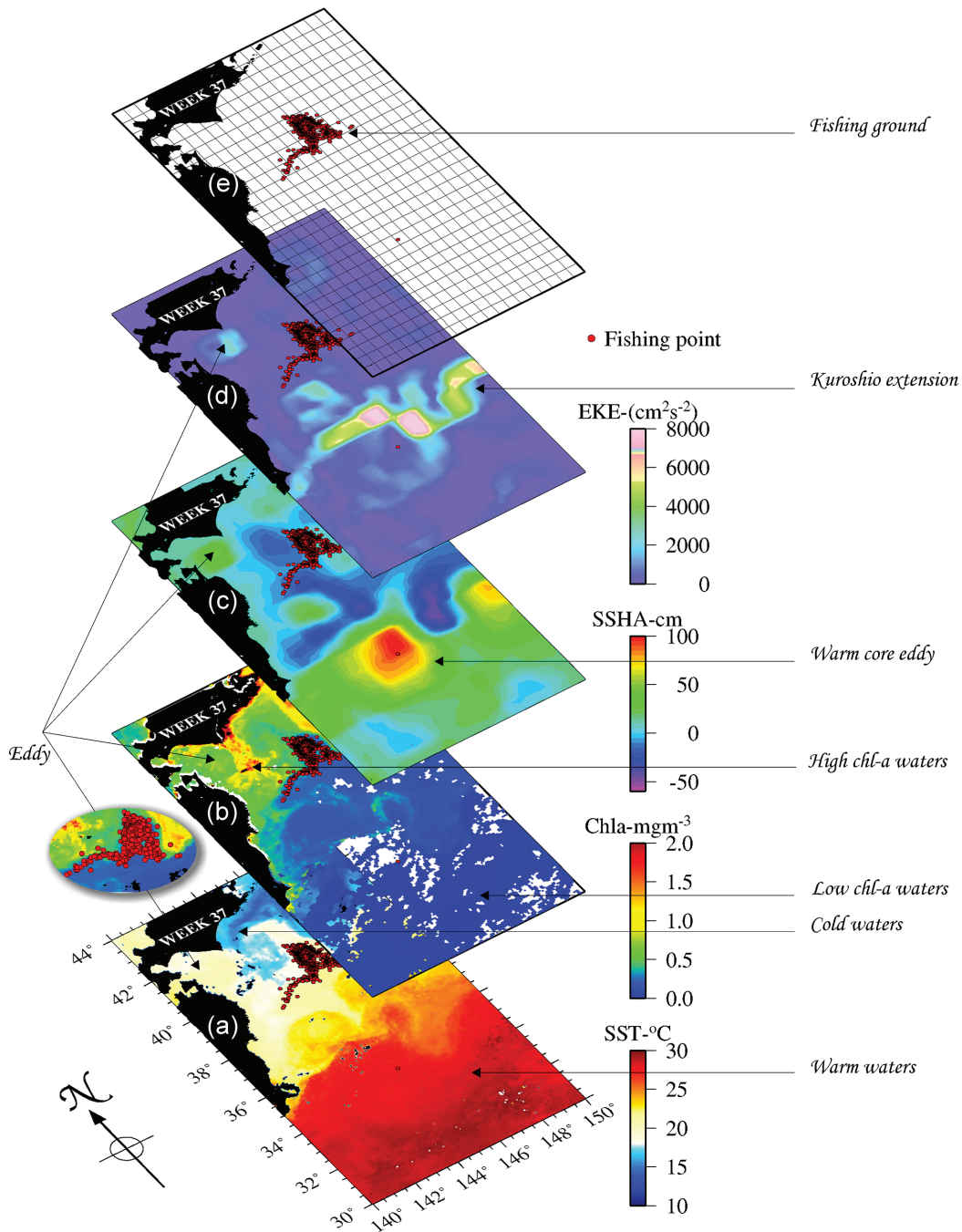
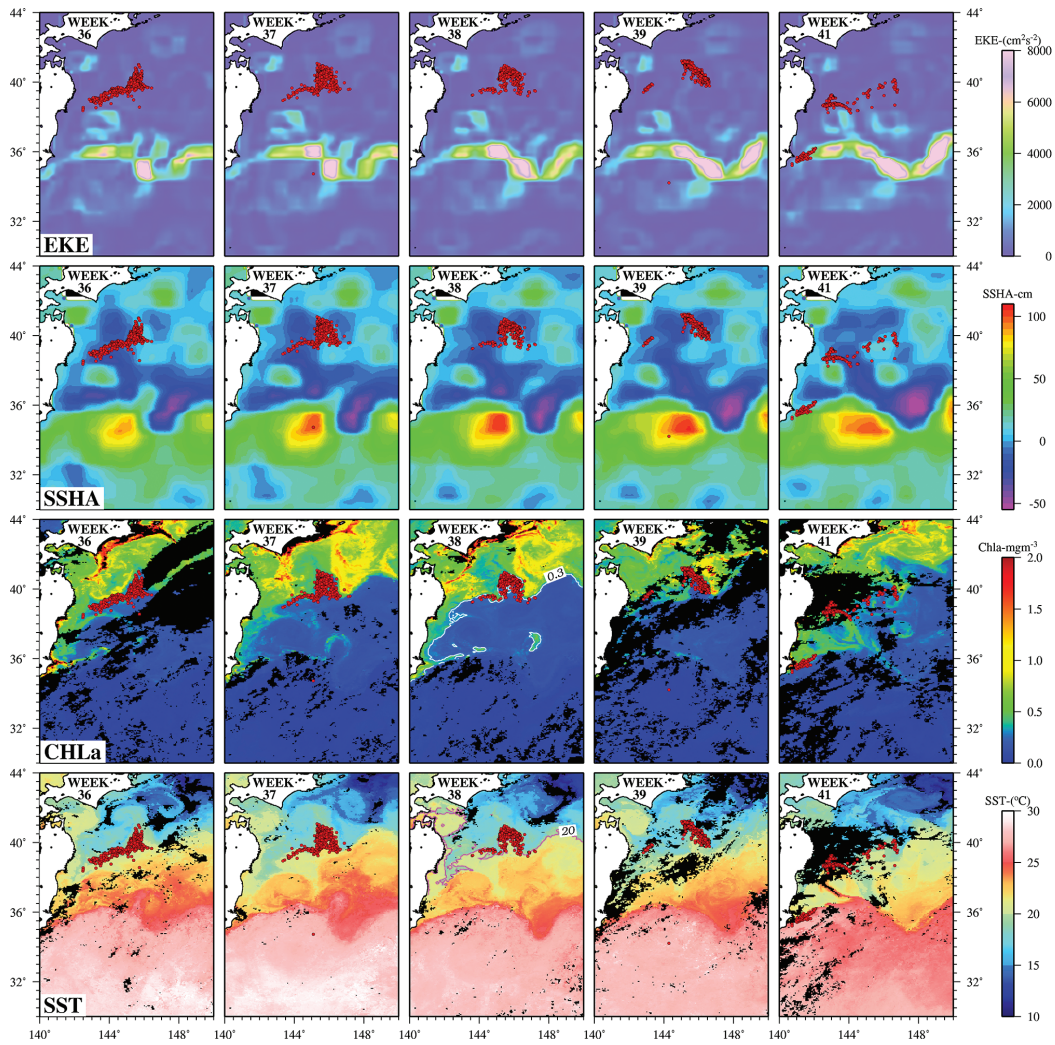


**Figure 12.6** Four images (SST, chl-a, SSHA and EKE), on the same time scale and overlaid with daily fishing locations for the same period.

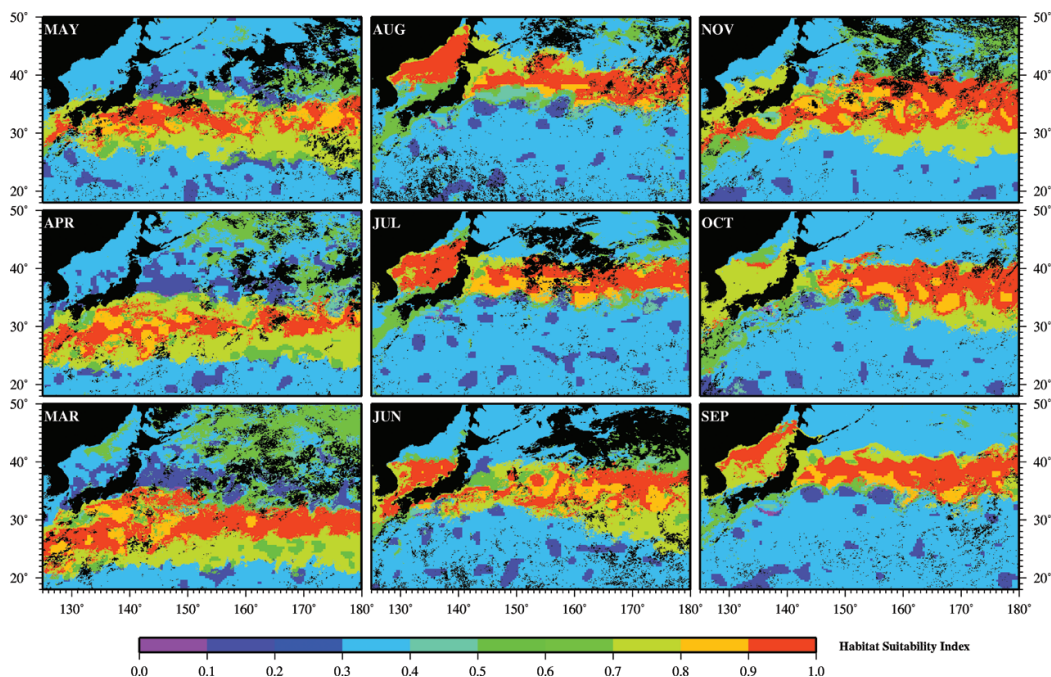
while looking at distribution of tuna resources relative to surface features. The relationship with the fishing locations during this week is not that apparent, but that information may be clearer with further analysis. A warm core eddy south of Hokkaido can be identified from this image and in the previous images as well.

Figure 12.7 illustrates a series of weekly images (SST, chl-*a*, SSHA and EKE) from week 36 to 41 with an exception of week 40, in September 2004. Daily fishing positions corresponding to the respective image time scale are superimposed on the images as red dots. All the images are colour coded to facilitate easy interpretation. Missing data are shown in black. The set of images we discussed above is shown in the second column. By applying the same concepts discussed above to the other images, it is possible to interpret them as well. In week 38, contours (vector data) have been added on the SST and chl-*a* images, showing the mean environmental conditions on the fishing grounds. Temperature and ocean-colour fronts (gradients) are observable on these images. The fishing positions show a spatial pattern consistent with oceanographic features observable from the SST, chl-*a* and some SSHA images. Notably, the fishing positions appear consistent with the 20°C SST isotherm, which appears to be a good proxy for the 0.3 mg m<sup>-3</sup> chl-*a* isopleth (e.g. week 38).

Having discussed the relationships between fishing locations and the four environmental factors derived from remotely-sensed images, let us draw some ecological interpretations with reference to skipjack tuna. Temperature as a habitat signature may explain part of the observed spatio-temporal variability in skipjack tuna fishing set distribution. SST is known to influence tuna migration (Sund et al., 1981). Considering the distribution of fishing locations overlaid on SST and chl-*a* images (both averaged on the same time scale), it is apparent that the fishing positions were aligned on the warm and oligotrophic side of the front. There are no fishing positions on the cold and eutrophic waters (mainly Oyashio waters). Relatively low chlorophyll waters, especially on the frontal edges of warm oligotrophic waters, have both physiological and trophic implications for skipjack tuna. It enables skipjack tuna to locate prey and forage on the periphery of highly productive frontal or upwelling zones, and also stay within tolerable temperatures (Ramos et al., 1996). Tunas are predominantly visual predators, feeding opportunistically and unselectively on micro-nekton and therefore highly turbid waters are unsuitable for them (Ramos et al., 1996; Kirby et al., 2000), while extremely oligotrophic waters would contain little food (Sund et al., 1981). A study in the western North Pacific on skipjack tuna ecology by Nihira (1996) showed that stomach contents of skipjack tunas caught near the front of a warm streamer were twice to five times heavier than those caught at the center of the warm streamer and thus concluded that the front was the most suitable feeding place. Fiedler and Bernard (1987) also found that skipjack tuna aggregated on the warm edge of waters near cold and productive water masses off southern California. Oceanic fronts are broadly understood to mark the boundary between two different water masses, manifested as regions of



**Figure 12.7** Spatial distribution of skipjack tuna fishing fleet in September 2004 overlaid on weekly averaged sea surface temperature (SST), sea surface chlorophyll (chl-*a*), sea surface height anomalies (SSHA) and eddy kinetic energy (EKE), off Japan in the western North Pacific. The fishing locations were in phase with the 0.3 mg m<sup>-3</sup> chlorophyll-*a* and 20°C SST contours.



**Figure 12.8** A habitat suitability map computed from monthly averaged SST, chl-*a*, SSHA and EKE whose habitat ranges for skipjack tuna were derived using a GAM. This demonstrates some of the products that can be derived from remotely-sensed oceanographic data. Land or areas with no data are shown in black.

strong horizontal gradients in temperature, salinity, chlorophyll and concentration of zooplankton and micronekton (Olson et al., 1994; Kirby et al., 2000).

The spatial relationship of fishing locations with SSHA images, though not as apparent as that of SST and chl-*a* images, points to the presence of warm and cold-core eddies near fishing locations. The fishing locations appear oriented on the periphery of warm core eddies. The EKE images also confirm the presence of eddies observed on SSHA images. The EKE images also clearly show the path of the Kuroshio Current. Aggregation of tuna along eddy edges has been attributed to nutrient injection or entrainment to the euphotic zone (Olson, 1991) and development of phytoplankton blooms which trigger secondary production (Bakun, 2006). This attracts nekton, with a net effect of aggregation of apex predators to forage on the lower trophic level organisms around the eddy edge (Ramos et al., 1996; Fonteneau et al., 2009).

The data sampled from the satellite images can be compiled into a database that describes the conditions where fishing is taking place, as is shown in Figure 12.5. Data from such a database can be used to generate models that provide more information on the habitat of the species in question. Different types of models can be applied depending on the objective of the work. In this case, we highlight the

application of a generalized additive model (GAM) (Wood, 2006), from which the ranges of environmental variables with a positive effect on CPUE were determined (results from GAMs are cited but not presented here). The terms derived from the GAM can be applied on monthly averaged SST, chl-*a*, SSHA and EKE images to derive a simple habitat index map shown in Figure 12.8. This can be done using tools in the Spatial Analyst extension of ArcGIS 9.2 (or higher). From this figure, it is possible to visualize the annual displacement of skipjack tuna habitat from the south to the north (March to August/September) and later southwards in October and November. Figures were done using GMT 4.4.0. Such results are important for assessing habitat distribution at a synoptic scale, which is vital for ecosystem based management.

## 12.5 Questions

**Q 1:** With reference to the SST images shown in Figure 12.7 (weeks 36 and 38-41), why do you think skipjack tuna fishing locations appear on the yellow to red parts of the image and not the blue parts? NOTE: the SST image is colour coded; the red shows warm waters while light to deep blue shows cold waters.

**Q 2:** With reference to the chl-*a* images shown in Figure 12.7 (weeks 36 and 38-41), and also in light of the discussion above, why do you think skipjack tuna fishing locations appear on the blue parts of the image and not the green to red areas? NOTE: the chl-*a* image is colour coded; the blue shows low chlorophyll waters which also correspond to warm waters while green to red shows relatively high chlorophyll waters which also correspond to cold water masses.

**Q 3:** What important information can we derive from altimetry data such as sea surface height anomalies? How is that information relevant to tuna ecology?

## 12.6 Answers

**A 1:** Skipjack tuna are warm water fish, and also aggressive feeders. Therefore SST can act as an index of their distribution especially when they have migrated towards higher latitudes where waters get progressively colder. They appear to track warm waters and avoid the cold waters below 17°C. They are also found on the oligotrophic side of fronts which are rich in food as a result of high primary and secondary production induced by upwelling.

**A 2:** Skipjack fishing locations appear not only in the low chlorophyll areas, but also in areas associated with steep colour gradients which indicate ocean-colour fronts. Such areas are productive zones that provide feeding opportunities for skipjack tuna. However, the tuna remain in relatively low chlorophyll waters where turbidity

is less, and visibility is good. This enhances their ability to locate food. Tunas are known to locate their food by sight. The relatively oligotrophic waters also happen to be regions with tolerable temperatures for the species.

**A 3:** Altimetry is a technology that measures height. Satellite altimetry measures the time taken by a radar pulse to travel from the satellite antenna to the surface and back to the satellite receiver. Combined with precise satellite location data, altimetry measurements yield sea-surface heights. Altimetry data are important at revealing meso-scale variability in the oceans. From these data, it is possible to track movement of eddies and strong currents in the oceans. Such features are important for exchange of heat and nutrients in the oceans, and thus can influence productivity of adjacent water masses and by extension the marine biota associated with them. Therefore, at times, movement of meso-scale features can affect the distribution of predators such as tuna. It follows that tracking such features through satellite remote sensing can provide information on ocean circulation and the associated biotic interactions. Further, altimetry data may provide a "glimpse", even though not as detailed, of oceanographic conditions where satellite surface temperature or surface chlorophyll data are missing due to cloud cover.

## 12.7 References

- Bakun A (2006) Fronts and eddies as key structures in the habitat of marine fish larvae: opportunity, adaptive response and competitive advantage. *Sci Mar* 70(S2): 105-12
- FAO (2009) The State of World Fisheries and Aquaculture 2008. FAO Fisheries and Aquaculture Department, Food and Agriculture Organization of the United Nations, Rome
- Fiedler PC, Bernard H (1987) Tuna aggregation and feeding near fronts observed in satellite imagery. *Cont Shelf Res* 7: 871-881
- Fonteneau A, Lucas V, Tewkai E, Demarcq H (2009) Mesoscale exploitation of a major tuna concentration in the Indian Ocean. *Aqua. Living Resour* 21: 109-121
- Kawai H (1972) Hydrography of the Kuroshio Extension. In: Kuroshio Its Physical Aspects, H Stommel and K Yoshida (ed) University of Tokyo Press, Tokyo
- Kawai H, Sasaki M (1962) On the hydrographic condition accelerating the skipjack northward movement across the Kuroshio Front (in Japanese, English abstract) *Bull Tohoku Reg Fis Res Lab* 20: 1-27
- Kirby DS, Fiksen O, Hart PJB (2000) A dynamic optimization model for the behaviour of tunas at ocean fronts. *Fish Oceanogr* 9: 4: 328-342
- Langley A, Hampton J, Ogura M (2005) Stock assessment of skipjack tuna in the western and central Pacific Ocean. WCPFC-SC1 SA WP-4. [http://www.spc.int/DigitalLibrary/Doc/FAME/Meetings/WCPFC/SC1/SC1\\_SA\\_WP\\_4.pdf](http://www.spc.int/DigitalLibrary/Doc/FAME/Meetings/WCPFC/SC1/SC1_SA_WP_4.pdf)
- Matsumoto WM (1975) Distribution, relative abundance and movement of skipjack tuna, *Katsuwonus pelamis*, in the Pacific Ocean based on Japanese tuna longline catches, 1964-67. NOAA Technical Report NMFS SSRF-695
- Miyake MP, Miyabe N, Nakano H (2004) Historical trends of tuna catches in the world. FAO Fisheries Technical Paper 467, FAO, Rome
- Nihira A (1996) Studies on the behavioral ecology and physiology of migratory fish schools of skipjack tuna (*Katsuwonus pelamis*) in the oceanic frontal area. *Bull Toh Natl Fish Res Inst* 58: 137-233
- Ogura M (2003) Swimming behavior of skipjack, *Katsuwonus pelamis*, observed by the data storage tag at the Northwestern Pacific, off northern Japan, in summer of 2001 and 2002. SCTB16 Working Paper. [http://www.spc.int/coastfish/Sections/reef/Library/Meetings/SCTB/16/SKJ\\_7.pdf](http://www.spc.int/coastfish/Sections/reef/Library/Meetings/SCTB/16/SKJ_7.pdf)
- Olson DB (1991) Rings in the Ocean. *Annu Rev Earth Planet Sci* 19: 283-311

- Olson DB, Hitchcock GL, Mariano AJ, Ashjian CJ, Peng G, Nero RW, Podesta GP (1994) Life on the edge: marine life and fronts. *Oceanography* 7(2): 52-60
- Qiu B (2002) The Kuroshio Extension system: Its large-scale variability and role in the midlatitude ocean-atmosphere interaction. *J Oceanogr* 58: 57-75
- Ramos AG, Santiago J, Sangra P, Canton M (1996) An application of satellite derived sea surface temperature data to the skipjack (*Katsuwonus pelamis* Linnaeus, 1758) and Albacore tuna (*Thunnus alalunga* Bonaterre, 1788) fisheries in the north-east Atlantic. *Int J Remote Sensing* 17: 749-759
- Roberts JJ, Best BD, Dunn DC, Trembl EA, Halpin PN (in press) Marine geospatial ecology tools: An integrated framework for ecological geoprocessing with ArcGIS Python, R, MATLAB, and C++. *Environ Modell Softw*. <http://mge1.env.duke.edu/tools>
- Robinson IS (2004) *Measuring oceans from space: the principles and methods of satellite oceanography*. Praxis Publishing, Chichester
- Saitoh S, Kosaka S, Iisaka J (1986) Satellite infrared observations of Kuroshio warm-core rings and their application to study of Pacific saury migration. *Deep Sea Res* 33: 1601-1615
- Sakurai Y (2007) An Overview of the Oyashio Ecosystem. *Deep Sea Res II* 54: 2526-2542
- Sugimoto T and Tameishi H (1992) Warm-core rings, streamers, and their role on the fishing ground formation around Japan. *Deep-Sea Res*, 39: S183-S201
- Sund PN, Blackburn M, William F (1981) Tunas and their environment in the Pacific Ocean: a review. *Oceanogr Mar Biol Ann Rev* 19: 443-512
- Talley LD, Nagata Y, Fujimura M, Kono T, Inagake D, Hirai M, Okuda K (1995) North Pacific intermediate water in the Kuroshio/Oyashio mixed water region *J PhysOceanogr* 25: 475-501
- Tameishi H, Shinomiya H (1989) Formation of southbound skipjack fishing grounds and its discriminant prediction off Tohoku sea area. *Nippon Suisan Gakkaishi* 55: 4 619-625
- Uda M (1973) Pulsative Fluctuation of oceanic fronts in association with the tuna fishing grounds and fisheries. *J Fac Mar Sci Technol* 7: 245-264
- Uda M, Ishino M (1958) Enrichment pattern resulting from eddy systems in relation to fishing grounds *J Tokyo Univ Fish* 44(1/2): 105-118
- Valavanis DV, Pierce GJ, Zuur AF, Palialexis A, Saveliev A, Katara I, Wang J (2008) Modelling of essential fish habitat based on remote sensing spatial analysis and GIS. *Hydrobiologia* 612: 5-20
- Wild A Hampton J (1993) A review of the biology and fisheries for skipjack tuna, *Katsuwonus pelamis*, in the Pacific Ocean. In: *Interactions of Pacific Tuna Fisheries*. Proceedings of the first FAO Expert Consultation on Interactions of Pacific Tuna Fisheries Nourmea, New Caledonia. Shomura RS, Majkowski J, Langi S (eds) FAO Fisheries Tech Paper 336(2) FAO, Rome. <http://www.fao.org/docrep/005/t1817e/T1817E01.htm#ch1>
- Wood SN (2006) *Generalized Additive Models: An Introduction with R*. Chapman & Hall, CRC Texts in Statistical Science, London
- Wright DJ, Goodchild MF (1997) Data from the deep: Implications for GIS community. *Int J Geogr Inf Sci* 11: 523-528
- Yasuda I (2003) Hydrographic structure and variability in the Kuroshio-Oyashio transition area. *J Oceanogr* 59: 389-402
- Yasuda I, Okuda K, Hirai M (1992) Evolution of a Kuroshio warm-core ring — variability of the hydrographic structure. *Deep-Sea Res* 39 (Suppl): S131-S161

### 12.7.1 Suggested Reading

- Mugo R, Saitoh S, Nihira A, Kuroyama T (2008) Exploiting the edge: evaluating predator-prey interactions between skipjack tuna, Pacific saury and squid using satellite remote sensing and GIS. In *Proceedings of the World Fisheries Congress (extended abstract)*. [http://www.terrapub.co.jp/proceedings/wfc/papers/1a\\_0005\\_234/exploiting\\_the\\_edge\\_evaluating\\_ppi\\_btn\\_skipjacktuna\\_saury\\_squid.pdf](http://www.terrapub.co.jp/proceedings/wfc/papers/1a_0005_234/exploiting_the_edge_evaluating_ppi_btn_skipjacktuna_saury_squid.pdf)

## **12.8 Glossary of Technical Terms**

Chl- <i>a</i>	Sea Surface Chlorophyll
CPUE	Catch Per Unit Effort
EDC	Environment Data Connector
EKE	Eddy Kinetic Energy
GAM	Generalized Additive Model
GIS	Geographic Information Systems
GMT	Generic Mapping Tools
MGET	Marine Geospatial Ecology Tools
SSHA	Sea Surface Height Anomalies
SST	Sea Surface Temperature
WCR	Warm Core Ring



## Case Study 13

# Monitoring Oysters Using Remote Sensing Data and Services: a Case Study of the Apalachicola River and Bay Watershed during Recent Droughts

Zhong Liu\*<sup>1</sup> and James Acker<sup>2</sup>

---

## 13.1 Background

### 13.1.1 Study Area: Apalachicola Bay and watershed

Apalachicola Bay is located on Florida's northwest coast, consisting of an estuary and lagoon (Figure 13.1a). The Apalachicola River watershed provides the largest inflow of fresh water to the estuary (Figure 13.1b). According to U.S. Geological Survey (USGS) data in 2002, the Apalachicola River, combined with other rivers, drains a watershed of over 20,000 sq. miles (~52,000 sq. km) at an approximate rate of 19,599 cubic feet per second (~550 kiloliters per second) of fresh water.

Apalachicola Bay is renowned for its oysters, supplying 90% of the oysters in the state of Florida. Major natural threats to the local oyster population are disease, predation and competition from other organisms. Researchers (e.g. Wilber, 1992) found that the balance of Bay water salinity is essential to oyster productivity. Increased salinity can invite marine (salt water) predators to enter the bay from the Gulf. Droughts in the watershed can thus cause less fresh water to flow into the bay and foster a rise in salinity. By contrast, low salinity due to a large fresh water discharge from the river can induce physiological stress to oysters, leading to oyster mortality.

Wilber (1992) compared oyster landings for Apalachicola Bay with historical Apalachicola River flows from 1960 - 1984 to determine how river flow and oyster production are related. Since oysters in Apalachicola Bay require 2 years of growth to reach a harvestable size, lag periods were incorporated into the analyses. Wilber (1992) found that low river flows were positively correlated with oyster catch per unit

---

<sup>1</sup>NASA Goddard Earth Sciences Data and Information Services Center; also UCEOSR, George Mason University, Fairfax, VA, USA. \*Email address: [Zhong.Liu@nasa.gov](mailto:Zhong.Liu@nasa.gov)

<sup>2</sup>NASA Goddard Earth Sciences Data and Information Services Center, Wyle IS LLC, Greenbelt, Maryland, USA

effort two years later. Wilber's analyses suggest that sustained high river flows were detrimental to the same year's harvestable oyster population. Although Wilber's analyses did not include salinity data, the results imply that a possible mechanism for this association is that lower minimum flows result in higher estuarine salinities, permitting predation by marine species on newly settled spat (juvenile oysters), and thus reducing harvestable oyster population sizes two years later (Wilber, 1992).

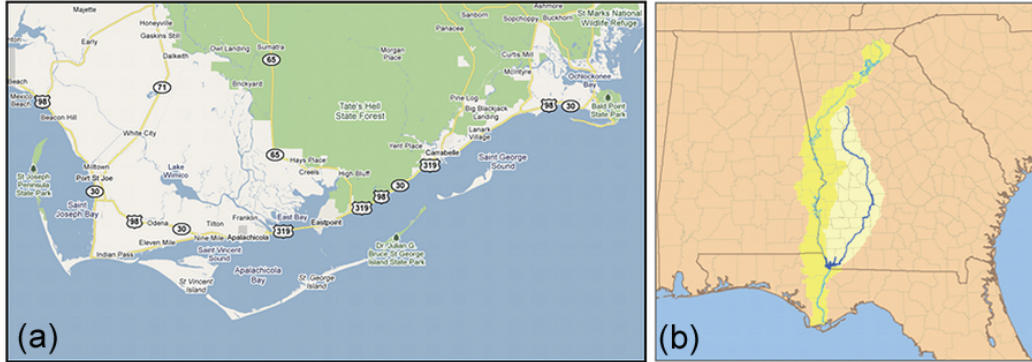


**Figure 13.1** (a) Apalachicola Bay on Florida's northwest coast, consisting of an estuary and lagoon; (b) the Apalachicola River watershed (created by "Pfly", based on USGS data, acquired from Wikimedia).

Several other studies have linked oyster growth to freshwater inflows and salinity. Wang et al. (2008) modelled oyster growth rate by coupling oyster population and hydrodynamic models for Apalachicola Bay. Their analyses and model simulations reveal that oyster growth rates were significantly related to salinity. Huang (2010) studied rainfall and river inflow effects on Apalachicola Bay with hydrodynamic modelling and eco-hydrological analysis.

During the period 2006 - 2008, historical drought conditions existed in the U.S. Southeast, resulting in severe water shortages. The water shortages were worsened by increasing population, increasing water consumption, and insufficient water conservation measures, which greatly reduced freshwater flow into Apalachicola Bay. Water control for the reservoir Lake Lanier, which provides water for metropolitan Atlanta, made the situation worse. The rising salinity in Apalachicola Bay nearly destroyed the \$134 million oyster industry, according to news reports.

### 13.1.2 Tropical Rainfall Measuring Mission (TRMM)

Drought conditions occur every year around the world. However, monitoring droughts can be a challenging task, especially in data-sparse regions. Satellite remote sensing technology (Maracchi et al., 2000; Liu et al., 2007) provides a unique way to supply precipitation monitoring data from space. In particular, the Tropical Rainfall Measuring Mission (TRMM) - a joint mission between NASA and the Japan Aerospace Exploration Agency (JAXA) - is designed to monitor and study tropical

and subtropical (40°S – 40°N) rainfall and latent heat (TRMM Special Issue, 2000). The TRMM satellite flies at an altitude of 402.5 km, and carries three rain-measuring instruments: the TRMM Microwave Imager (TMI), the Visible Infrared Scanner (VIRS), and the Precipitation Radar (PR). TRMM data products are archived and distributed by the Goddard Earth Sciences Data and Information Services Center (GES DISC).

### 13.1.3 Giovanni TOVAS (TRMM Online Visualization and Analysis System)

Accessing remote sensing products can be a challenging task for users in many developing countries and for non-experts (Liu et al. 2007). For example, many products require different software and computer platforms for processing and visualization, which could require a significant investment from the user side (Liu et al. 2007). To facilitate data access, GES DISC has developed the TRMM Online Visualization and Analysis System (TOVAS), as a part of the "Goddard Interactive Online Visualization ANd aNalysis Infrastructure" or "Giovanni" (Acker and Leptoukh, 2007; Liu et al. 2007; Berrick et al. 2009). With a Web browser and few mouse clicks, an individual can easily obtain global Earth science data visualizations and analyses.

The principle design goal for Giovanni was to provide a quick and simple interactive means for scientific data users to study various phenomena by trying various combinations of parameters measured by different instruments, arrive at a conclusion, and then generate graphs suitable for a report or publication. Alternatively, Giovanni can provide a means to ask relevant "what-if" questions and receive rapid results that would stimulate further investigations. These procedures can all be done without having to download and pre-process large amounts of data. A secondary design goal was for Giovanni to be easily configurable, extensible, and portable. GES DISC currently runs Giovanni on Linux, SGI, and Sun platforms. Another goal of Giovanni was to off-load as much of the data processing workload as possible onto the machines hosting the data, and thereby reduce data transfers to a minimum. Given the enormous amount of data at GES DISC in Hierarchical Data Format (HDF), it was a requirement that Giovanni support HDF, HDFEOS, as well as binary data.

Giovanni consists of HTML and CGI scripts written in Perl, Grid Analysis and Display System (GrADS <http://grads.iges.org/grads/>) scripts, and one or more GrADS Data Servers (GDS) running on remote machines that have GrADS readable data. In addition, an image map Java applet can be used to select a bounding box area to process.

GrADS was chosen for its widespread use in providing easy access, manipulation, and visualization of Earth science data. It supports a variety of data formats such as binary, GRIB, NetCDF, HDF, and HDFEOS. When combined with the Open-source Project for a Network Data Access Protocol (OPeNDAP), as in GDS, the result is a secure data server that provides subsetting and analysis across the network or even the Internet. The ability of GDS to subset data on the server drastically reduces

the amount of data that needs to be transferred across the network, and improves overall performance. GDS provides spatial or temporal subsetting of data while applying any of a number of analysis operations including basic math function, averages, smoothing, correlation, and regression. An equally important feature is the ability to run GrADS data transformations on the server.

This case study will demonstrate the use of remote sensing rainfall data products from TRMM (and other sources), combined with data analysis services, to monitor freshwater inflows and salinity that affect oysters in Apalachicola Bay. This study should enhance our ability to understand the dynamics of the Apalachicola Bay estuarine ecosystem, based on the relationships established in previous studies.

## 13.2 Materials and Methods

### 13.2.1 Tropical Rainfall Measuring Mission (TRMM) data products

TRMM standard products are available at three levels. Level 1 products are the VIRS calibrated radiances, the TMI brightness temperatures, and the PR return power and reflectivity measurements. Level 2 products are derived geophysical parameters (such as rain rate) at the same resolution and location as those of the Level 1 source data. Level 3 products are the time-averaged parameters mapped onto a uniform space-time grid. An evaluation of the sensor, algorithm performance and first major TRMM results appear in the Special Issue on the Tropical Rainfall Measuring Mission (see Section 13.6.1, *Further Reading*).

Observations from a single satellite usually suffer from limited spatial and temporal coverage. Multi-satellite data can provide wider spatial coverage and often more frequent measurements than a single satellite, making monitoring global environmental conditions a reality. Combined with other satellites (e.g. geostationary satellites and other microwave instruments), TRMM products can be greatly improved in terms of their spatial coverage and temporal resolution (Huffman et al. 2007), such as a 3-hourly TRMM multi-satellite precipitation analysis.

Because the TRMM satellite was launched in 1997, its data products can only provide limited historical records. To investigate longer periods, it is necessary to use other products, such as the Global Precipitation Climatology Project (GPCP) monthly precipitation product. GPCP provides a global merged rainfall analysis for research and applications. Data from over 6,000 rain gauge stations, satellite geostationary, and low-orbit infrared, passive microwave, and sounding observations have been merged to estimate monthly rainfall on a 2.5-degree global grid from 1979 to present (<http://www.gewex.org/gpcp.html>). In this case study, we will use:

- ❖ Monthly  $0.25^\circ \times 0.25^\circ$  merged TRMM and other sources estimates (3B43);
- ❖ the Monthly GPCP  $2.5^\circ \times 2.5^\circ$  merged product.

### 13.2.2 USGS streamflow data

To evaluate rainfall impact on fresh water discharge, we use streamflow measurements reported by the USGS (<http://waterdata.usgs.gov/nwis/rt>) for station 02359170 near Sumatra, FL, in the Apalachicola-Chattahoochee-Flint (ACF) River Basin (Lat 29°56'57", Lon 85°00'56" ). This station measures streamflow from a drainage area of approximately 19,200 mi<sup>2</sup> and provides records from September 1977 to the current year. The streamflow data can be downloaded from <http://waterdata.usgs.gov/nwis/uv?02359170>.

### 13.2.3 Giovanni TOVAS

Via the TOVAS Web interface, the user selects one or more precipitation data sets, the spatial area, the temporal extent, and the type of output. The selection criteria are passed to the CGI scripts for processing.

## 13.3 Demonstration

### 13.3.1 Drought Analysis

With TOVAS, users can investigate the spatial and temporal distribution of the precipitation in their area of interest as well as its climatology and anomalies. Examples are given as follows.

#### 13.3.1.1 Rainfall climatology

Before analyzing drought conditions, it is necessary to understand the rainfall climatology and inter-seasonal, annual variability in the Apalachicola River watershed. First, we will generate a latitude-longitude map and a time series plot, using a web browser to perform the following steps:

**STEP 1:** Visit, [http://gdata1.sci.gsfc.nasa.gov/daac-bin/G3/gui.cgi?instance\\_id=TRMM\\_Monthly](http://gdata1.sci.gsfc.nasa.gov/daac-bin/G3/gui.cgi?instance_id=TRMM_Monthly)

**STEP 2:** Select a region of interest. In this case, we selected a region that includes the Apalachicola river watershed (Figure 13.2a)

**STEP 3:** Select "Climatology" from Analysis Options and "Rain Rate" from the TRMM 3B43 V6 pull-down menu.

**STEP 4:** Select Jan (January) as Begin Date and Dec (December) as End Date in the Temporal selection menu.

**STEP 5:** Click "Generate Visualization". Figure 13.2b is the 12-month climatology (average rain rate) for the region (it may look slightly different based on the area

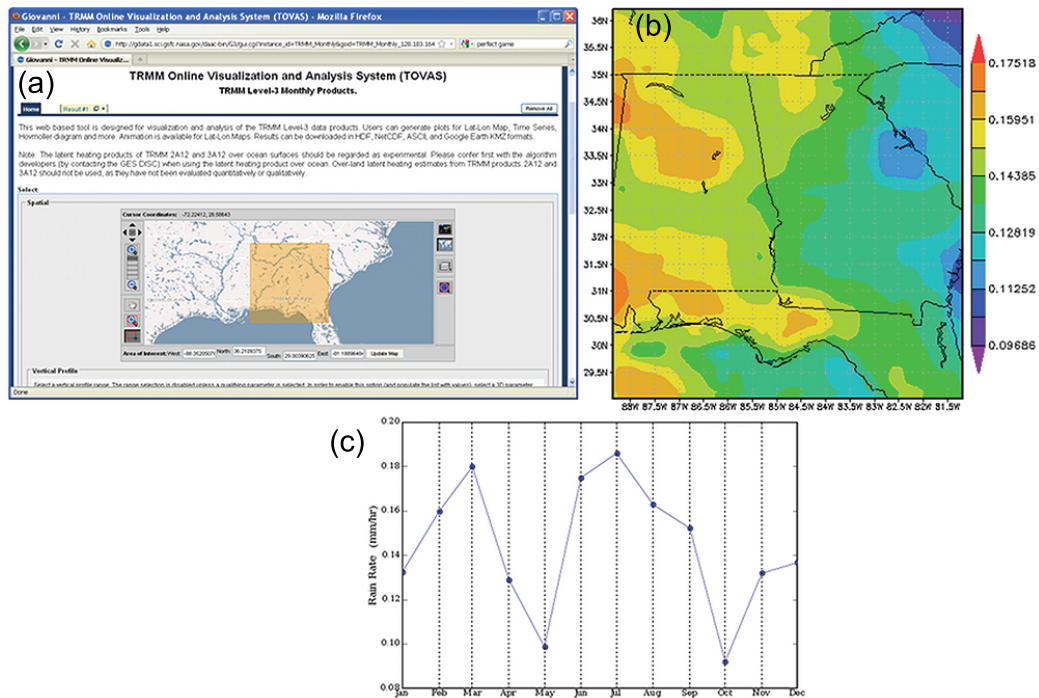


**Figure 13.2** (a) TOVAS website showing the area of interest including the Apalachicola watershed; (b) 12-month (Jan – Dec) climatology rain rate ( $\text{mm h}^{-1}$ ) for the region; (c) area-averaged time series rain rate climatology.

selected). To plot a time series, repeat the first 3 steps above, except type in the watershed region (Latitudes:  $30^{\circ} - 35^{\circ}\text{N}$ ; Longitudes:  $83^{\circ} - 86^{\circ}\text{W}$ ). Select "Time series" from the "Select Visualization" menu and click "Generate Visualization". The plot is shown in Figure 13.2c.

Repeat the above steps for different seasons (Dec-Feb, Mar-May, Jun-Aug, Sep-Nov) to obtain the climatology maps showing seasonal changes in rainfall spatial distribution (Figure 13.3). In winter (Dec – Feb) and spring (Mar – May), the highest rain intensity concentrates in the NE watershed and decreases toward the SE. In summer (Jun – Aug) and fall (Sep – Nov), the intensity gradient is reversed with highs in the southern part of the watershed (possibly related to tropical weather systems) along the coastal areas, and lows in the central and northern parts.

### 13.3.1.2 Obtaining time series and anomaly map in the watershed region

Using the latitudes and longitudes of the watershed, we next plot a 12-year time series of rainfall intensity. The steps are as follows:

**STEP 1:** Go to [http://gdata1.sci.gsfc.nasa.gov/daac-bin/G3/gui.cgi?instance\\_id=TRMM\\_Monthly](http://gdata1.sci.gsfc.nasa.gov/daac-bin/G3/gui.cgi?instance_id=TRMM_Monthly).

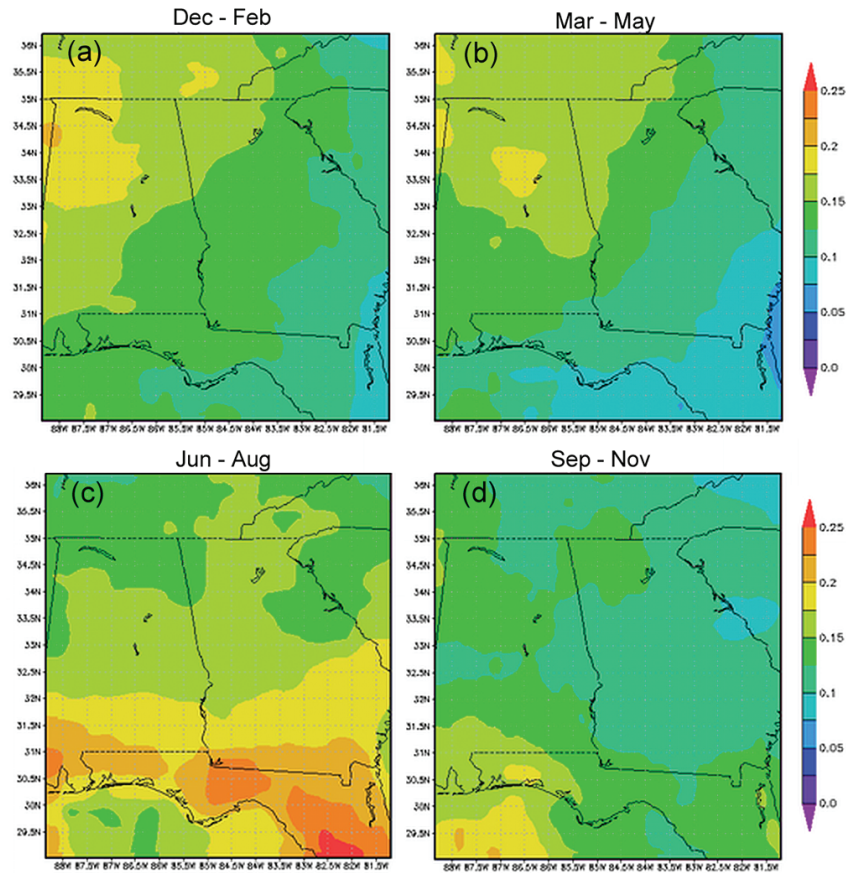


**Figure 13.3** Climatology maps showing seasonal changes in the spatial distribution of rainfall ( $\text{mm h}^{-1}$ ) for the Apalachicola watershed.

**STEP 2:** Select a region of interest. Type: Latitudes: 30 - 35° N; Longitudes: 83 - 86° W and click on "Update Map".

**STEP 3:** Select "Parameter" from Analysis Options and "Rain Rate" from the TRMM 3B43 V6 pull-down menu.

**STEP 4:** Select "Jan 1998" as Begin Date and "Feb 2010" as End Date in the Temporal selection menu.

**STEP 5:** Click "Generate Visualization". Figure 13.4a is the 12-year time series of the average rain rate for the selected region. Select "Anomaly" from the Analysis Options and repeat the above steps, which will obtain the anomaly time series plot (Figure 13.4b). To understand the spatial distribution of the anomaly, we next select two different periods: wetter years between 2003 and 2005 and drier years between 2005 and 2008, by repeating the above steps. Choose "Lat-Lon Map, time-averaged" from the Select Visualization menu to create the figures. The results are shown in Figure 13.5.

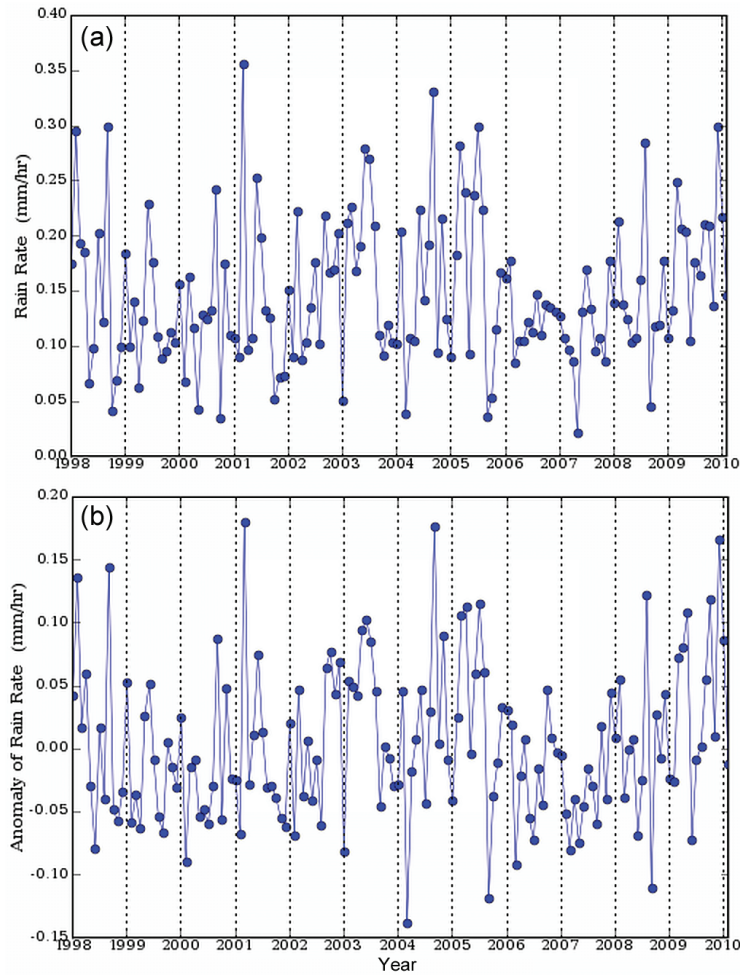


**Figure 13.4** (a) 12-year time series of average rain rate in the Apalachicola watershed; (b) anomaly time series plot for the same region and time frame.

### 13.3.1.3 Monitor droughts and floods

With TOVAS, users can monitor drought and flood development. Using the Monthly Rainfall (3B43) Anomaly Tool ([http://disc2.nascom.nasa.gov/Giovanni/tovas/rain.3B43\\_V6\\_anom.shtml](http://disc2.nascom.nasa.gov/Giovanni/tovas/rain.3B43_V6_anom.shtml)), users can generate the latest monthly rainfall, anomaly and normalized anomaly (normalized anomaly is defined as  $(\text{rainfall} - \text{climatology}) / \text{climatology}$ ). For example, Figure 13.6a shows the total rainfall in mm for February of 2010, Figure 13.6b shows the corresponding anomaly while Figure 13.6c shows the normalized anomaly in percentage. It can be seen that rainfall is highly non-uniform, with high rainfall being recorded in the Gulf of Mexico (Figure 13.6a). The Apalachicola watershed area also received more rainfall than the surrounding areas (about 20% more than normal).

TOVAS also provides near-real-time monitoring services (<http://disc2.nascom>).

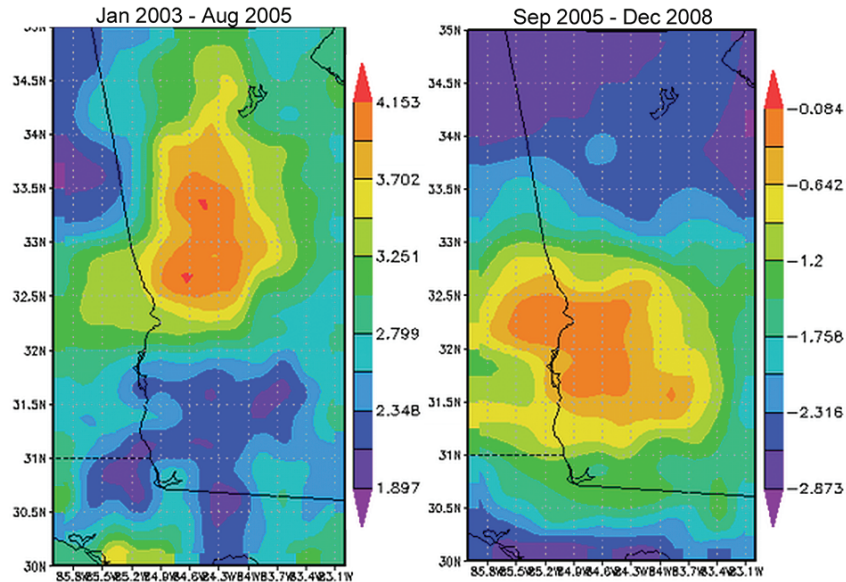


**Figure 13.5** Spatial distribution of the rain rate anomaly ( $\text{mm h}^{-1}$ ) in the Apalachicola watershed over wetter years (2003 – 2005) and drier years (2005 – 2008).

[nasa.gov/Giovanni/tovas/](http://nasa.gov/Giovanni/tovas/)) with only a few hours data latency. Users can examine rainfall conditions through TOVAS, which is very useful in monitoring floods. Using TOVAS, users can plot rainfall maps including accumulated rainfall and time series in the area and time period of interest.

#### 13.3.1.4 Further analysis

Users can conduct other analyses by using additional functions (e.g. Hovmöller diagrams, animations, exporting data in ASCII for customized analysis), or other rainfall products (e.g. 3-hourly, daily, 10-day). The following steps show how to download rainfall data in ASCII and import them in Microsoft Excel for further analysis.

**STEP 1:** Follow Section 13.3.1.2 and generate a time series for the period of interest.

**STEP 2:** Click "Download Data"

**STEP 3:** Click the ASCII thumbnail in "Download Files" to display the ASCII output data.

**STEP 4:** From your browser menu, click Edit and select "Select All". The data will be highlighted. Select "Copy" and paste them in a Microsoft Excel spreadsheet.

**STEP 5:** Highlight the data column and select "Data" and "Text to Columns". The action will split the pasted data into two columns.

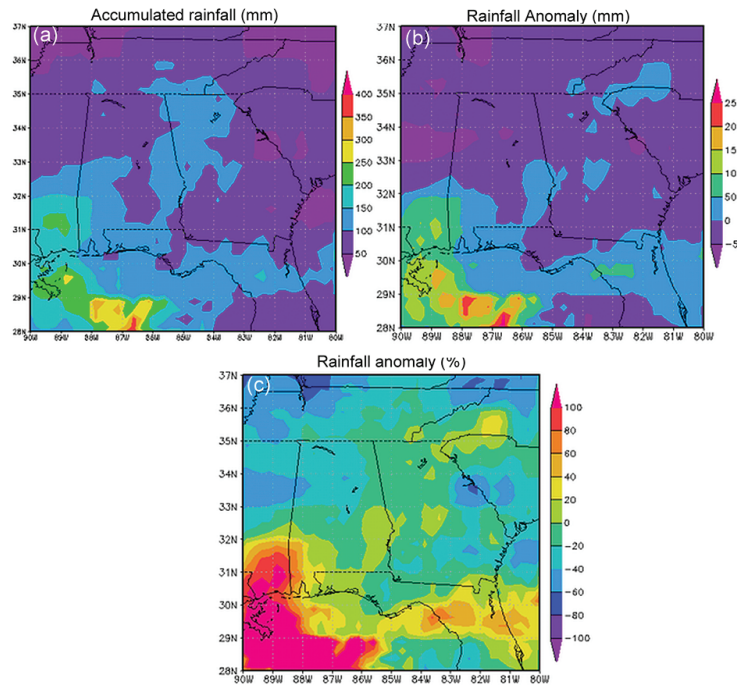


**Figure 13.6** (a) Total rainfall (mm) for February of 2010; (b) rainfall anomaly (mm) for February 2010; (c) normalized rainfall anomaly (%).

**STEP 6:** Plot the data and add a trend line (Figure 13.7). The files can be downloaded from: [http://disc.sci.gsfc.nasa.gov/giovanni/precipitation\\_case\\_study\\_files/](http://disc.sci.gsfc.nasa.gov/giovanni/precipitation_case_study_files/)

### 13.3.2 Impact Analysis

#### 13.3.2.1 USGS streamflow discharge

As mentioned in the Introduction, freshwater discharge has important impacts on Apalachicola Bay ecological systems. Users can obtain real-time and historical streamflow data for the Apalachicola Bay from the U.S. Geological Survey web site (<http://waterdata.usgs.gov/nwis/rt>). To demonstrate rainfall and its impact on streamflow, we use the monthly data. Below are the steps to obtain monthly streamflow time series:

**STEP 1:** Go to <http://waterdata.usgs.gov/nwis/uv?02359170>

**STEP 2:** Select Time-series: Monthly statistics from Available data for this site. Click "Go"

**STEP 3:** Select Parameter Code 00060. Select Tab-separated data. Select Display in browser. Click Submit.

**STEP 4:** In your web browser, click Edit, Select All and Copy, then paste into an Excel

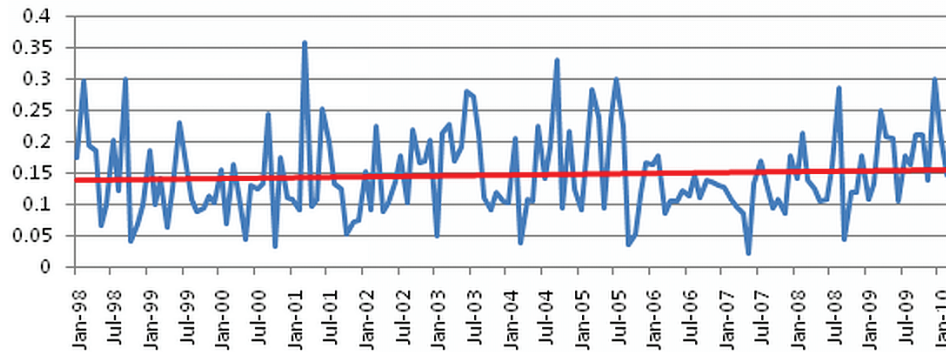


**Figure 13.7** Time-series of rain rate ( $\text{mm h}^{-1}$ ) plotted with MS Excel©, with a trendline added to the time-series data plot.

Spreadsheet. Since the GPCP rainfall product provides a longer period of monitoring, we demonstrate how to plot it against the USGS streamflow discharge data described above. The results are shown in Figure 13.8. In general, rainfall in the Apalachicola watershed region has a close tie to the streamflow discharge data measured near the bay at Sumatra, FL, although the discharge can be controlled by many factors including upstream water storage and withdrawals.

### 13.3.2.2 Salinity analysis

Salinity data downloaded from the National Data Buoy Center and imported into Microsoft Excel can be plotted along with the rainfall data for comparison. Figure 13.9a shows the time series of the rain rate averaged over the watershed region, and the salinity measured in the Apalachicola Bay. Note that when salinity rises, the rain rate is low and vice versa over the 30-month period. Similarly, we can plot the USGS streamflow discharge data along with the salinity data. Figure 13.9b shows that when streamflow discharge is high, salinity is low and vice versa. These two figures illustrate the impact of rainfall and streamflow discharge on salinity in Apalachicola Bay.

## 13.4 Training and Questions

**Q1:** Why are the data presented in mm/hr? How can I convert mm/hr in TRMM 3B43 to mm/month?

**Q2:** Describe the spatial distribution of rainfall in the watershed region. Is it uniform? When do the rainfall maxima in the study region occur for average conditions?

**Q3:** Is the spatial distribution of rainfall consistently the same for different seasons?

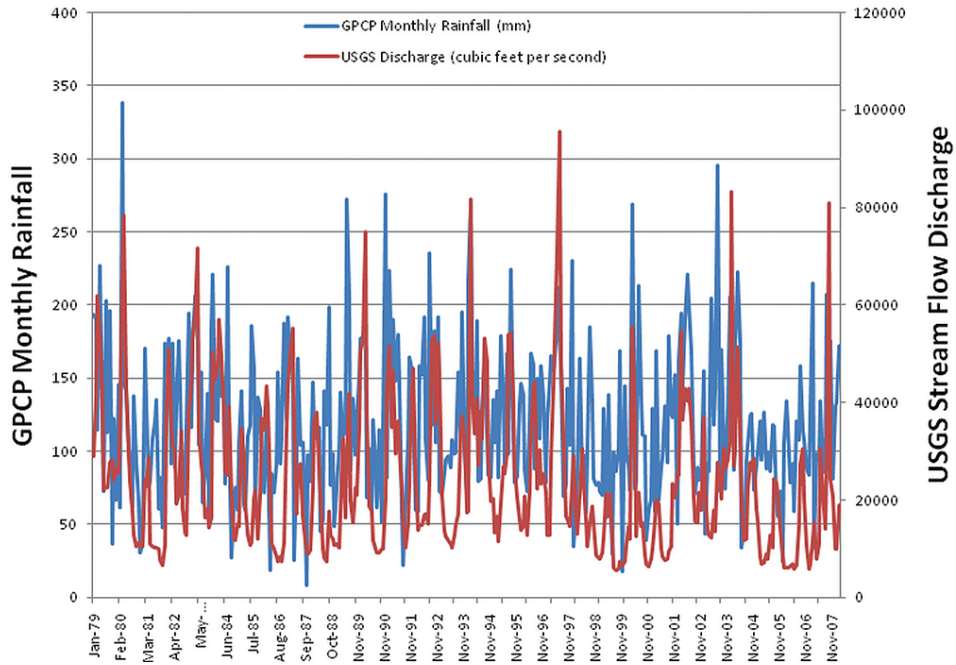


**Figure 13.8** The GPCP (Global Precipitation Climatology Project) monthly rainfall product (blue line) and the USGS streamflow discharge (red line) for Apalachicola Bay, from January 1979 to November 2007.

**Q4:** 4. In Figure 13.4a, attempt to identify months and periods with unusually high and unusually low rainfall. Then look at the anomaly time-series (Figure 13.4b). Are the periods you identified consistent with the rainfall anomalies? What were the main periods of below-average rainfall, according to Figure 13.4b?

**Q5:** 5. Is the spatial distribution of rainfall during dry years and wet years the same, or different? What meteorological phenomena might explain these observations?

**Q6:** Was rainfall in February 2010 in the watershed region above normal, approximately normal, or below normal, based on the climatological average? (Figure 13.6)

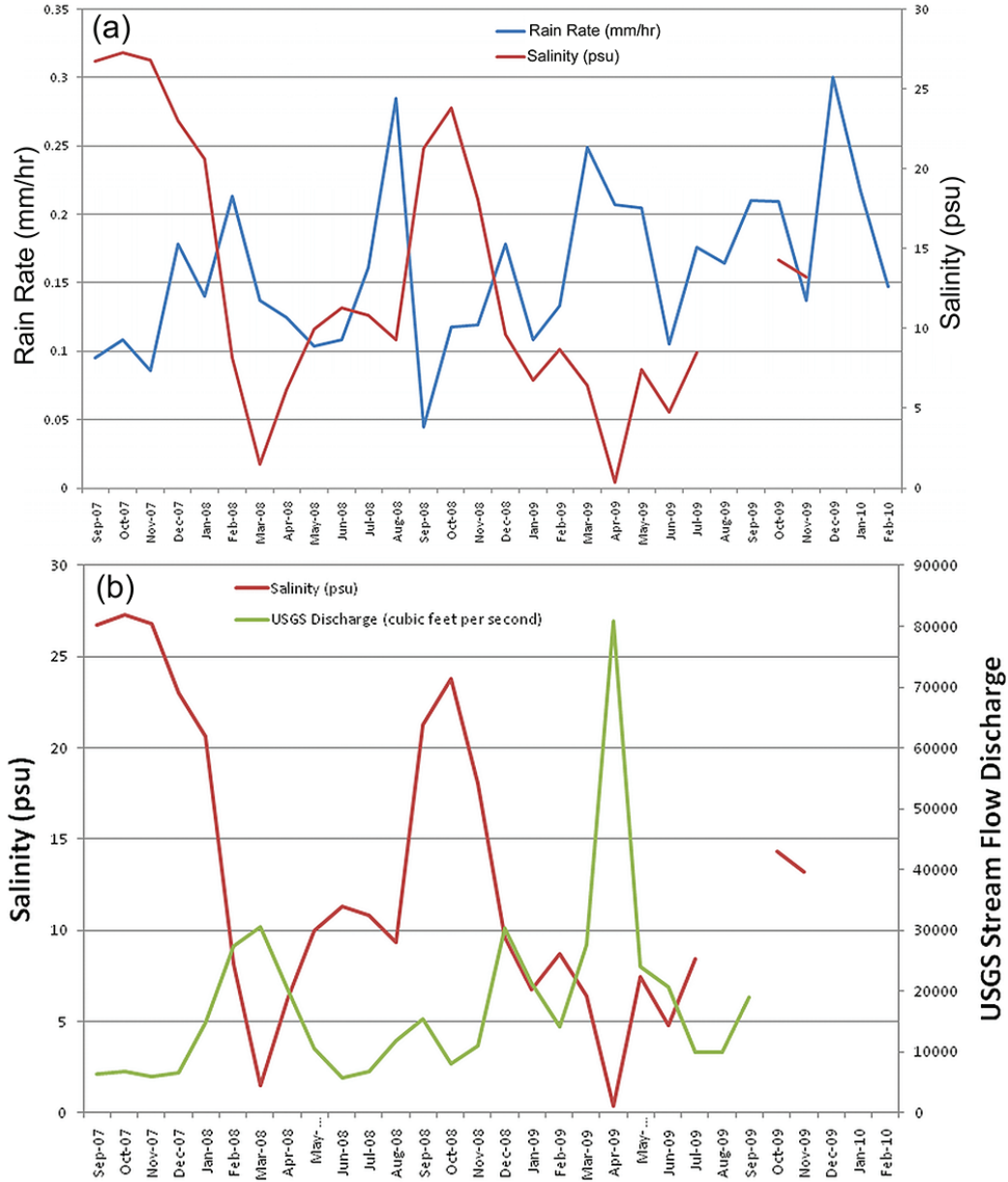


**Figure 13.9** (a) Time series of rainfall rate ( $\text{mm h}^{-1}$ ) averaged over the Apalachicola watershed region (blue line), and the salinity (psu) measured in the Apalachicola Bay (red line); (b) USGS streamflow discharge data (cubic feet per second, green line) along with the salinity data (red line).

**Q7:** 7. Based on Figure 13.8, is there a strong correlation, a weak correlation, or no correlation between the GPCP monthly rainfall values and the USGS streamflow discharge data? Does your conclusion surprise you?

**Q8:** Is there a positive correlation, a negative correlation, or no correlation between precipitation in the watershed and salinity in Apalachicola Bay as measured by the NOAA buoy (Figure 13.9a)?

**Q9:** Is there a positive, negative, or no correlation between streamflow in the watershed and salinity in Apalachicola Bay as measured by the NOAA buoy (Figure 13.9b)?

**Q10:** In light of the background information provided about the Apalachicola Bay oyster fishery, what recommendations could be made based on these observations regarding preservation of the fishery in relation to precipitation and streamflow in the watershed?

## 13.5 Answers

**A1:** Because the total number of days in each month are different, mm/hr is used for easy comparison. Since the 3B43 product is a monthly average, you could simply do the conversion by multiplying the hourly rain rate by the total number of hours in that month.

**A2:** From Figure 13.2b, it is seen that the spatial distribution of rainfall is not uniform in the watershed region. The rain intensity decreases from west to east with highs in the northern and southern ends of the region. The time series plot shows that there are two rain maxima, one in March and the other in July. May and November are the two months with minimum rainfall.

**A3:** 3. Figure 13.3 shows that seasonal changes in rainfall spatial distribution are different. In winter and spring, the highest rain intensity concentrates in the NE watershed and decreases toward the SE. In summer and fall, the intensity gradient is reversed with highs in the southern part of the watershed (possibly related to tropical weather systems) along the coastal areas, and lows in the central and northern parts.

**A4:** 4. From the time series of the past 12 years (Figure 13.4 a,b), it can be seen that the monthly rainfall intensity is highly variable. Between 1998 and 2003, the region experienced below normal rainfall intensity, and an above average rainfall intensity after that period. The region experienced another below average rainfall intensity from mid-2005 to -2008, but this dry spell has improved since 2009, with above-average rainfall. The time series also shows that the latest dry period (mid-2005 to

-2008) was the worst in this 12-year record. The region experienced more than 3 consecutive years of below-normal rainfall.

**A5:** Figure 13.5 shows that the spatial distributions of the anomaly between the wetter and drier than normal years are quite different. In the wetter years, more rain fell in the central and the northern parts of the region; in contrast, during the drier years, considerably less rain fell in the northern region. During dry years, one of the notable contributions to rainfall are storm systems in the Gulf of Mexico (either winter lows or tropical systems), which tend to bring more rain to the coast than inland.

**A6:** Rainfall in February 2010 was below normal, as demonstrated by both the rainfall anomaly, and normalized rainfall anomaly having negative values in the watershed region. The normalized rainfall anomaly indicates that rainfall in February 2010 was only slightly below normal.

**A7:** Figure 13.8 shows that during many periods of high precipitation, there is a strong correlation between high precipitation and high discharge. This is likely due to high discharge rates caused by a large contribution of runoff to streams in the watershed. However, during periods of average or low precipitation, the correlation is considerably weaker. This could be due to natural storage (i.e. replenishment of groundwater, filling of wetlands, increased soil moisture) as well as streamflow control by artificial impoundments, particularly reservoir lakes.

**A8:** There is a negative correlation between precipitation in the watershed and salinity in Apalachicola Bay. This indicates that high precipitation leads to reduced salinity in the Bay, and low precipitation leads to increased salinity in the Bay.

**A9:** There is an apparent negative correlation between streamflow (discharge) in the watershed and salinity in Apalachicola Bay. This indicates that elevated streamflow, which is related to increased precipitation, causes reduced salinity in the Bay, and that reduced streamflow (likely due to both drought and some degree of human control) causes increased salinity in the Bay.

**A10:** 10. Based on all of these observations, it appears that Apalachicola Bay should be guaranteed a minimum flow of freshwater to provide suitable survival conditions for the oyster industry. Obviously, the economic value of the oyster fishery must be balanced against other societal concerns, but it would likely take several years to recover from a significant degradation of the oyster fishery, under normal rainfall conditions.

## 13.6 References

Acker J G and Leptoukh G (2007). Online analysis enhances use of NASA earth science data. *Eos Trans Amer Geophys Union*, 88 (2), 14-17

- Berrick SW, Leptoukh G, Farley JD, and Rui H (2009) Giovanni: A Web service workflow-based data visualization and analysis system. *IEEE Trans Geosci Remote Sens*, 47 (1), 106-113
- Huang W (2010) Hydrodynamic modeling and ecohydrological analysis of river inflow effects on Apalachicola Bay, Florida, USA, *Estuarine, Coastal and Shelf Science*, Volume 86, Issue 3, 10 February 2010, Pages 526-534
- Huffman GJ, Adler RF, Bolvin DT, Gu G, Nelkin EJ, Bowman KP, Hong Y, Stocker EF, Wolff DB, (2007), The TRMM Multi-satellite Precipitation Analysis: Quasi-Global, Multi-Year, Combined-Sensor Precipitation Estimates at Fine Scale *J Hydrometeor*, 8(1), 38-55
- Liu Z, Rui H, Teng W, Chiu L, Leptoukh G, and Vicente G (2007), Online visualization and analysis: A new avenue to use satellite data for weather, climate and interdisciplinary research and applications. *Measuring Precipitation from Space - EURAINSAT and the future*, *Advances in Global Change Research*, 28, 549-558
- Wilber D (1992) Associations between freshwater inflows and oyster productivity in Apalachicola Bay, Florida. *Estuarine, Coastal and Shelf Science*, Volume 35, Issue 2, 179-190
- Wang H, Huang W, Harwell MA, Edmiston L, Johnson E, Hsieh P, Milla K, Christensen J, Stewart J and Liu X (2008), Modeling oyster growth rate by coupling oyster population and hydrodynamic models for Apalachicola Bay, Florida, USA , *Ecological Modelling*, Volume 211, Issues 1-2, 24 February 2008, Pages 77-89

### 13.6.1 Further Reading

Special Issue on the Tropical Rainfall Measuring Mission (TRMM) (2000) – a combined publication including:

- ❖ The December 2000 issue of the *Journal of Climate*
- ❖ Part 1 of the December 2000 *Journal of Applied Meteorology* (American Meteorological Society, Boston, MA)

## 13.7 Supplemental Information

### What are the other commonly-used TRMM data products?

The GES DISC also archives 3-hourly and daily rainfall products for analysis. Details are found in <http://disc2.nascom.nasa.gov/Giovanni/tovas/> or <http://mirador.gsfc.nasa.gov/cgi-bin/mirador/presentNavigation.pl?tree=project&project=TRMM>.

### Where can I find more information on the TRMM Data Set?

More information on the TRMM instruments and science can be found at the GES DISC TRMM Data Web site: <http://disc.sci.gsfc.nasa.gov/precipitation/>

### How current are the TRMM data?

The GES DISC receives, under normal circumstances, processed standard orbital/swath data products about 2-3 days after satellite data acquisition, depending on the level of processing required. In addition to this ongoing collection of data, archives of older data are maintained.

### **What is the GES DISC Search and Order Web Interface?**

The GES DISC data search and order interface is a simple point-and-click web interface that is based on a hierarchical organization of data, displayed as tables. At different levels of the hierarchy, the tables contain some or all of the following: a particular data product grouping such as data product name, year, or month in the first column on the left; followed by columns of short description, begin date, end date, number of items available in the archives, average item size, a preview feature (if a data product has browse images), and documentation ("readme"). The last column on the right allows one to "Select" an item. At certain levels of the hierarchy, you can also use orbital and parameter search features to customize your search. Specific help is provided at the top of each page of this system (<http://disc.sci.gsfc.nasa.gov/data/datapool/TRMM/index.html>).

### **Where can I find some documentation describing TRMM and TRMM data?**

Information about TRMM and TRMM data can be found in:

- ❖ TRMM related documentation, describing the science, the instruments, data processing, and data access.
- ❖ TRMM "ReadMe" and "Data Access" documents on the data products and direct data access.
- ❖ Precipitation Processing System/TRMM Science Data and Information System (PPS/TSDIS) documentation, providing the details of all the products.
- ❖ Tutorial for "Reading TRMM Data Products"

### **Where can I find information describing the TRMM algorithms?**

Information about algorithms used for the TRMM products can be found in the Algorithm Status Page, where the links to the products take you to brief descriptions of the status of the products and, for some products, key references.

### **How are the daily products computed from 3B42RT and Version 6 3B42 in TOVAS?**

These daily products are computed by averaging all the estimates available in the eight observation times of a given UTC day, namely 00, 03, ..., 21 UTC. Formally, this "day" covers the period from 2230 UTC of the previous day through 2230 UTC of the given day. Other "day" products can be computed interactively for 3B42RT and Version 6 3B42 by specifying similar 8-period runs of data. For example, a day that starts at 09 UTC can be approximated by taking data from 09 UTC of one day through 06 UTC of the next. At present, there is no capability in TOVAS for a more exact approximation of a "day" for these data sets.

### **What is the key documentation describing the 3B42RT and Version 6 3B42 products?**

The paper by Huffman et al. (2007) describing the 3B42RT (real-time) and Version 6 3B42 (research quality) products of the TRMM Multi-satellite Precipitation Analysis (TMPA) is accessible at [ftp://meso.gsfc.nasa.gov/agnes/huffman/papers/TMPA\\_jhm\\_07.pdf.gz](ftp://meso.gsfc.nasa.gov/agnes/huffman/papers/TMPA_jhm_07.pdf.gz) Technical documentation is also available for the research product and real-time product, as is a WHATSNEW file, which contains recent notices about issues with the RT product.

### **What is the difference between the real time and research products of the TRMM Multi-satellite Precipitation Analysis (TMPA)?**

Version 6 research products are the "real" TRMM products. They are produced monthly, and are available 2-3 weeks after the end of the month. The upgrade to Version 6 happened in Spring/Summer 2005. Reprocessing evaluations for the next version of the data (Version 7) are currently being performed. Version 7 will constitute a reprocessing of the entire record from January 2008 to the present time. Institutionally, TRMM has been joined by a successor project, Global Precipitation Measurement (GPM), which has a nominal launch date of 2013. In the GPM era, a combination-product successor to the TMPA is a high priority, so there is a strong likelihood for a long time series of a consistent data product (via episodic reprocessing).

The real-time (RT) products are experimental products posted due to the high demand for such information. RT products are not reprocessed (except for processing failures). A major upgrade occurred in February 2005, so the processing scheme since then has been relatively consistent. The latest upgrade in February 2010 attempted to make the RT relatively consistent with Version 6 research products. For continuity, however, the data files will also include a precipitation field that is "more or less" the old RT result. Whenever possible, users are urged to take advantage of the improved quality of the research products. Some operational applications, however, cannot wait for the research products, and the RT products are intended for those application users.

### **What are the caveats in using TRMM Multi-satellite Precipitation Analysis (TMPA) products?**

The following are some caveats in using TMPA:

- ❖ The key caveat is that all of the TMPA products are research products, not "operational" (i.e. no contingency plans or backup system in case of a network failure or a disk crash).
- ❖ The TMPA is a gridded product, which is different from the point rain gauge data that might be more familiar to users, but grid values are more appropriate for certain applications.
- ❖ Although the TMPA analysis scheme is consistent for the time period of a given version, the suite of input data varies. For example, there is less of the

(higher-quality) microwave data before 2001; the infrared data are on a coarser grid in 1998 - 1999; gauge sites report individually, and are therefore subject to availability issues, particularly in developing countries.

- ❖ Occurrence of precipitation over land tends to be underestimated because satellite schemes tend to miss light precipitation and precipitation that is enhanced by flow lifting over mountains.
- ❖ Occurrence and amount of precipitation in some, but not all, coastal areas tends to be underestimated. Conversely, arid coastal areas (oceans and lakes) sometimes show persistent artefacts. Both effects are due to issues in the input microwave estimates.
- ❖ The RT amounts tend to be biased high in warm-season convective weather due to biases in the input microwave estimates.
- ❖ The Version 6 data tend to be biased low in regions of complex terrain due to gauge-location biases toward lower elevations.



## Theme: Marine Ecosystem Characterization

---



## Case Study 14

# Biological Response Associated With a Coastal Upwelling Event

Hervé Demarcq<sup>\*1</sup>, Dominique Dagorne<sup>2</sup> and Jacobus J. Agenbag<sup>3</sup>

---

## 14.1 Introduction and Background

This case study deals with one of the most powerful coastal upwelling regions on Earth. Upwelling is a physical phenomenon that sustains very high levels of marine life and diversity. The area of interest is the southern part of the Benguela upwelling region, particularly the west coast of Southern Africa, from 28 to 34°S. The Lüderitz upwelling cell, situated a little further north (at 27.5°S), where the trade winds blow strongly all year round, is one of the largest upwelling cells in the world, making this area a quasi-physical barrier, even for some small pelagic fish populations. At this location, the wind speed is very high (always  $>5 \text{ m s}^{-1}$ ) and the high turbulence level, associated with a relatively low water clarity and a strong offshore component of the currents, makes this particular area relatively unfavorable for the survival of ichthyoplankton (eggs and fish larvae) compared with the rest of the system, where the upwelling is less intense.

NASA's MODIS (Moderate Resolution Imaging Spectroradiometer) sensor, on board the Terra and Aqua polar orbiting satellites, offers a unique opportunity to study physical and bio-chemical processes occurring near the sea surface, by providing simultaneous views of both sea surface temperature (SST) and ocean colour (most common product is chlorophyll-*a* concentration). We use simultaneous synoptic views of SST and surface chlorophyll-*a* concentration (SCC) to describe and interpret the main spatio-temporal processes that occur in this highly dynamic coastal area. More precisely, the goal of this case study is to use spatially explicit, instantaneous information from both variables to explore the enrichment mechanisms that occur in the euphotic layer (i.e. the layer of the sea surface illuminated by sun light where photosynthesis can take place), in terms of mesoscale activity

---

<sup>1</sup>Institut de Recherche pour le Développement, Avenue Jean Monnet, BP 171, 34203 Sète cedex, France. \*Email address: [demarcq@ird.fr](mailto:demarcq@ird.fr)

<sup>2</sup>Institut de Recherche pour le Développement, Centre de Bretagne - BP 70, 29280 - Plouzané, France

<sup>3</sup>Marine and Coastal Management, Department of Environmental Affairs and Tourism, Private Bag X2, Rogge Bay 8012, South Africa

and algal growth. The availability of both SST and SSC from the same satellite is of crucial importance to understanding the links between the physics and the biology, and therefore to estimate the dynamics of the next trophic level, composed of zooplankton and ichthyoplankton that are highly sensitive to the environmental forcing that contributes to their survival, and ultimately to the success of their recruitment. Consequently pelagic fish species have developed specific strategies that take advantage of the richness of this region while minimizing the impact of the high environmental variability.

## 14.2 Materials and Methods

### 14.2.1 Information about image data

SST and ocean-colour data was acquired by the MODIS sensor on board the Aqua platform (launched 4 May, 2002). MODIS detects emitted and reflected radiance in 36 channels spanning the visible to infrared (IR) spectrum. Further information about the instrument can be found on the NASA MODIS web site at <http://modis.gsfc.nasa.gov/about/specifications.php>. The standard MODIS Chlorophyll-*a* algorithm (OC3; O'Reilly et al., 2000) relies on reflectance ratios at channels at 443, 488 and 551 nm.

The SST data used in this case study originates from the infrared part of the spectrum, between 11 and 12  $\mu\text{m}$ . A second SST measurement (not used here) is also recorded at three wavelengths between 3.7 and 4.0  $\mu\text{m}$  in the near infrared part of the spectrum. The electromagnetic radiation emitted from the sea surface can be inverted (using Planck's law, see [http://en.wikipedia.org/wiki/Planck's\\_law](http://en.wikipedia.org/wiki/Planck's_law)) to deduce the surface temperature of the target. For remote sensing applications, the 11–12  $\mu\text{m}$  spectral window is used most frequently because of its relatively low sensibility to the Earth's atmosphere. The nominal image resolution of the data (at the satellite nadir) is 1 km and its effective radiometric resolution for SST is 0.1°C. The chlorophyll concentration is displayed using a chlorophyll scale with values ranging from 0.01 to 58 mg chl-*a* m<sup>-3</sup>. Both parameters are extracted from "Level 2" data i.e. in orbit form, including geolocation and atmospheric correction. Wind data from the SeaWinds scatterometer, on board the QuikSCAT satellite, was also used in this case study. QuikSCAT was launched in June 1999 after the unexpected failure of the NASA scatterometer (NSCAT) satellite. The SeaWinds instrument is a specialized microwave radar that measures both the speed and direction of winds at the sea surface, at a spatial resolution of 25 km. This mission ended operation on 21 November 2009 due to an antenna rotation failure. The wind data used in this study are "Level 3" i.e. gridded and spatially and temporally combined.

### 14.2.2 Description of physical processes

The coastal upwelling principle was determined by physicist W.K. Ekman (1905) who examined the frictional effects of wind moving over the ocean surface. The net effect is that the current flow induced by the wind friction is deviated to the right of the wind direction in the northern hemisphere, and to the left of the wind direction in the southern hemisphere (Figure 14.1a). At the surface, the current moves at an angle of about 45 degrees to the wind direction. The net transport of water through the entire wind-driven water column is approximately 90 degrees to the direction of the wind. This movement of water is called **Ekman transport** or **Ekman flow**. Figure 14.1b shows the simplified cross-shore section of the water flow.

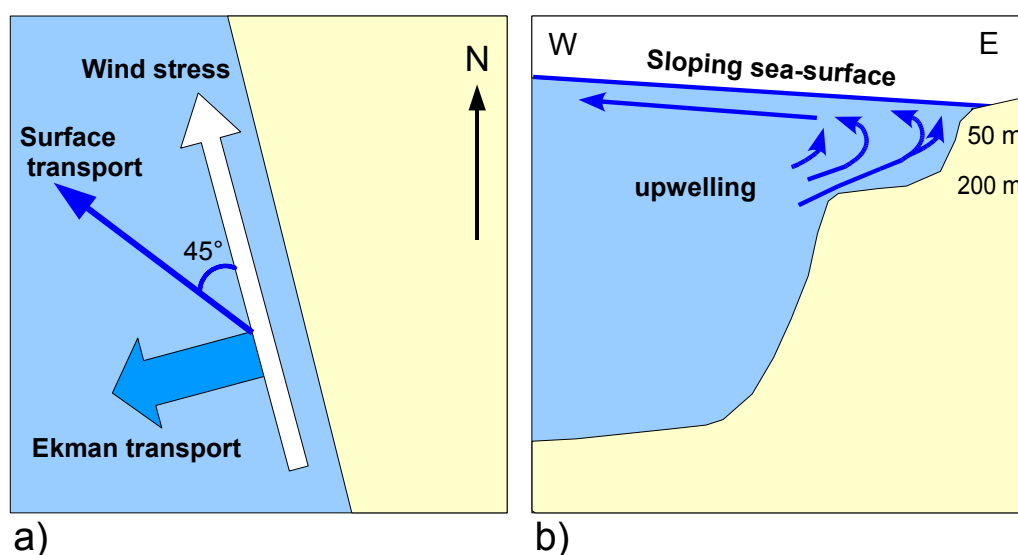


**Figure 14.1** Schematic illustration of wind-driven, coastal upwelling in the southern hemisphere due to Ekman transport (adapted from Ocean Circulation, by The Open University).

Winds and currents thus combine to bring cold water from below the seasonal thermocline (50-200 m) to the surface, especially near the coast where the upwelling flow is maximum. Because of the temperature difference between the coastal and offshore water masses, the surface temperature is a very good descriptor of coastal upwelling (Figure 14.2a), the dynamics of which can be studied from space. Furthermore, ocean-atmosphere interactions make these regions less cloudy than many other coastal regions. The presence of cold surface water decreases the evaporation, and therefore lowers the water vapor content of the atmosphere (one of the major absorbing components of the remote sensing reflectance signal, together with clouds and aerosols). Figure 14.2a shows that the coldest water (in white) is very close to the coast, a primary physical characteristic of a coastal upwelling region, and the most visible from space. Figure 14.2b shows the corresponding

concentration of chlorophyll-*a* (the main photosynthetic pigment of most unicellular algae). The comparison between the SST and SCC images shows that, at first glance, there is a strong spatial link between both parameters. The mechanism responsible for this relationship are the focus of this case study.

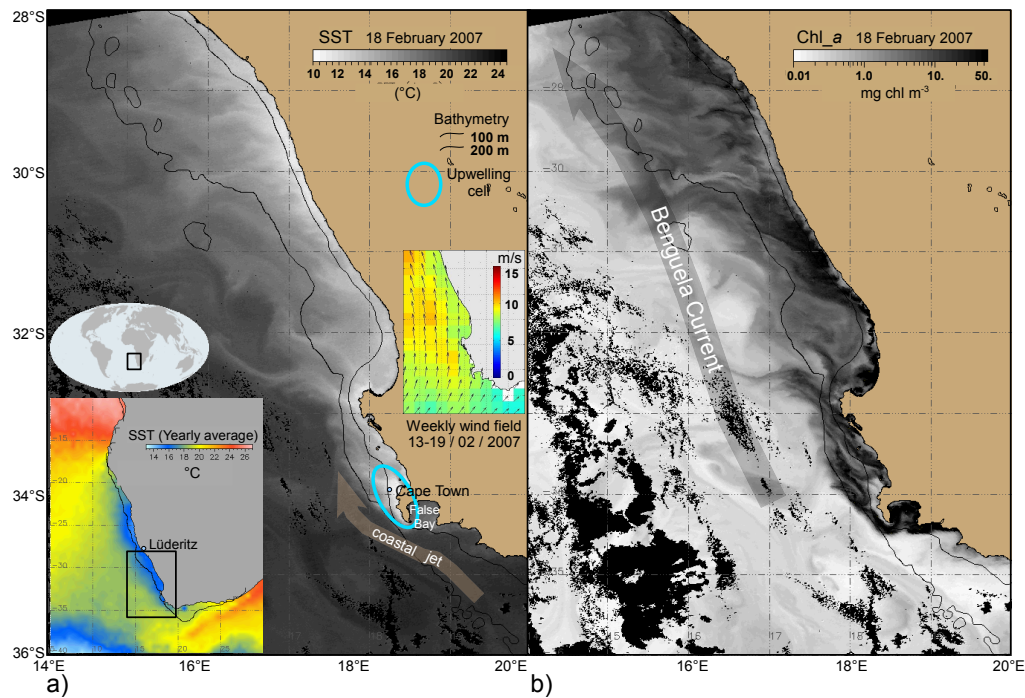


**Figure 14.2** Region of interest showing (a) SST ( $^{\circ}\text{C}$ ) and (b) chlorophyll-*a* concentration ( $\text{mg m}^{-3}$ ) computed from MODIS satellite data for the southern Benguela upwelling system, on 18 February 2007, during the upwelling season. The spatial resolution is 1 km. The left colour insert is the yearly average SST for the whole Benguela region, and the right insert is the average wind field during the week preceding the MODIS observation. The black patches in the offshore part of the chlorophyll image are due to lack of data because of the presence of clouds. MODIS data provided by NASA/GSFC.

Satellite images provide a synoptic view that allows a precise description of the spatial extent of the superficial upwelled waters. More precisely, the SST difference between the coastal and the offshore water allows a semi-quantification of the upwelling intensity based on the surface cooling. Such differences have been used to compute a SST-based coastal upwelling index (see Demarcq and Faure, 2000). The intensity of the coastal cooling is not homogeneous along the coast, but is reinforced in some locations where the vertical surface flux is stronger. These areas are called upwelling "cells". One in particular is clearly visible at the southern part of the region, between Cape Town and the Cape of Good Hope, the southwestern tip of the Cape Peninsula.

Fronts, eddies, plumes and filaments are the main signatures of mesoscale activity at the sea surface, and are primarily visible from satellite SST images because the water masses involved in frontogenesis (the formation or strengthening of a front) are generally of different temperatures. These features can also be observed through the "colour" of the sea, from maps of surface Chlorophyll-*a* concentration, the most widely used ocean colour product. In coastal upwelling areas, fronts and filaments are useful tracers of marine productivity and of the retention processes associated with the coastal circulation of water masses. Retention processes allow eggs and larvae of many pelagic species (or demersal and benthic species which have a pelagic early life stage) to be retained in favorable coastal areas, instead of being advected offshore.

Bakun's triade hypothesis (Bakun, 2006) provides a conceptual scheme for this mechanism. Bakun proposed that biological success is only possible in a marine environment if a satisfying balance is preserved between three fundamental physical processes: enrichment, concentration and retention. In coastal areas, enrichment processes are represented by the nutrient-rich, upwelled waters that enter the euphotic zone. The "concentration" term represents the vertical and horizontal advection of water masses that result in the concentration of biological matter, primarily phytoplankton. Last, but not least, the retention processes represents the ability of surface currents to keep the planktonic portion of the marine life (phytoplankton, zooplankton and ichthyoplankton) in particular areas where they will be more protected from predators and/or unfavorable environmental conditions. Marine species that have evolved in such a variable environment, have developed strategies that minimize the negative impacts while maximizing the favourable ones. For example, anchovies in the study region have developed a strategy to spawn in warmer waters (the extreme southern part of the system) which are physiologically more adequate for spawning. The eggs and larvae then drift away, pushed westward (but maintained close to the coast) by the coastal jet, where they are then passively transported to favorable retention areas where food is abundant. Naturally, over 90% of the released eggs are lost, but the survival of the species is preserved. Upwelled waters have high nutrient concentrations as a result of the sinking of organic matter (decaying phytoplankton blooms) from the sunlit surface layers into the deep ocean, where the cells are decomposed by bacteria. This process enriches the deep waters with nutrients (mainly nitrate, silicate and phosphate) which cannot be used at depth because the light levels are too low for photosynthesis.

Biologically, the newly upwelled water becomes progressively richer in chlorophyll and the maximum phytoplanktonic growth is reached when the uptake of nutrients becomes a limiting factor. The spatial heterogeneity of the surface currents, due to the complexity of the bathymetry combined with the heterogeneity of the wind field, creates mesoscale structures, visible on both the temperature and chlorophyll fields (Figure 14.2a,b). The intensity of these surface currents, as well as their induced retention effect on passive particles (or inversely their dispersal

effect) are of primary importance in fisheries biology because they can cause the ichthyoplankton to drift far away from the coast where the feeding conditions are much less favorable for their survival. Consequently, the recruitment of these species could be impacted strongly by the natural variability of these currents. For example, it has been shown from satellite imagery that the length of the "pathway" associated with the meanders of the coastal jet in the southern Cape (Figure 14.2a), where both SST and chlorophyll gradients are very strong, is positively related to larvae survival, and therefore to the recruitment of the anchovy populations (Van der Lingen, 2006).

**Note about colour palettes:** The main images in Figure 14.2 are displayed in gray scale, the most objective way to represent a spatial continuum of a two-dimensional field for a single geophysical parameter. The disadvantage of a colour scale is the risk of artificially "contrasting" some parts of the image because a colour scale is always a compromise between smooth colour changes and a continuous light gradient. In a gray scale image, the light gradient is perfect and the eye is not influenced by the brightness of some colours. This is the best way to evaluate the global gradient of the image values. On the other hand, the determination of the local values is not as precise as for a colour scale (which is better in this respect), but far less objective for gradient estimation. Figures 14.3 and 14.4 show these two images using a false colour palette.

### 14.3 Training and Questions

**Q1:** Considering the physical principle of coastal upwelling (see Figure 14.1), how could it be characterized from a thermal point of view? What is the thermal contrast with the offshore oceanic water?

**Q2:** What mesoscale structures are visible in the SST and Chlorophyll images, either related to coastal upwelling processes, or not?

**Q3:** What is the main relationship between SST and SCC in the study area? More particularly, how can you interpret the spatial information in terms of temporal history?

**Q4:** What are the main characteristics of the upwelling cells from the information available in the images, and what explanations can you give compared to the rest of the upwelling area?

**Q5:** What could be a suitable place for fish larvae to feed and survive in reasonably good conditions, with a low probability of being driven offshore where the predation pressure is higher? Look at the direction of the currents and topographic opportunities.

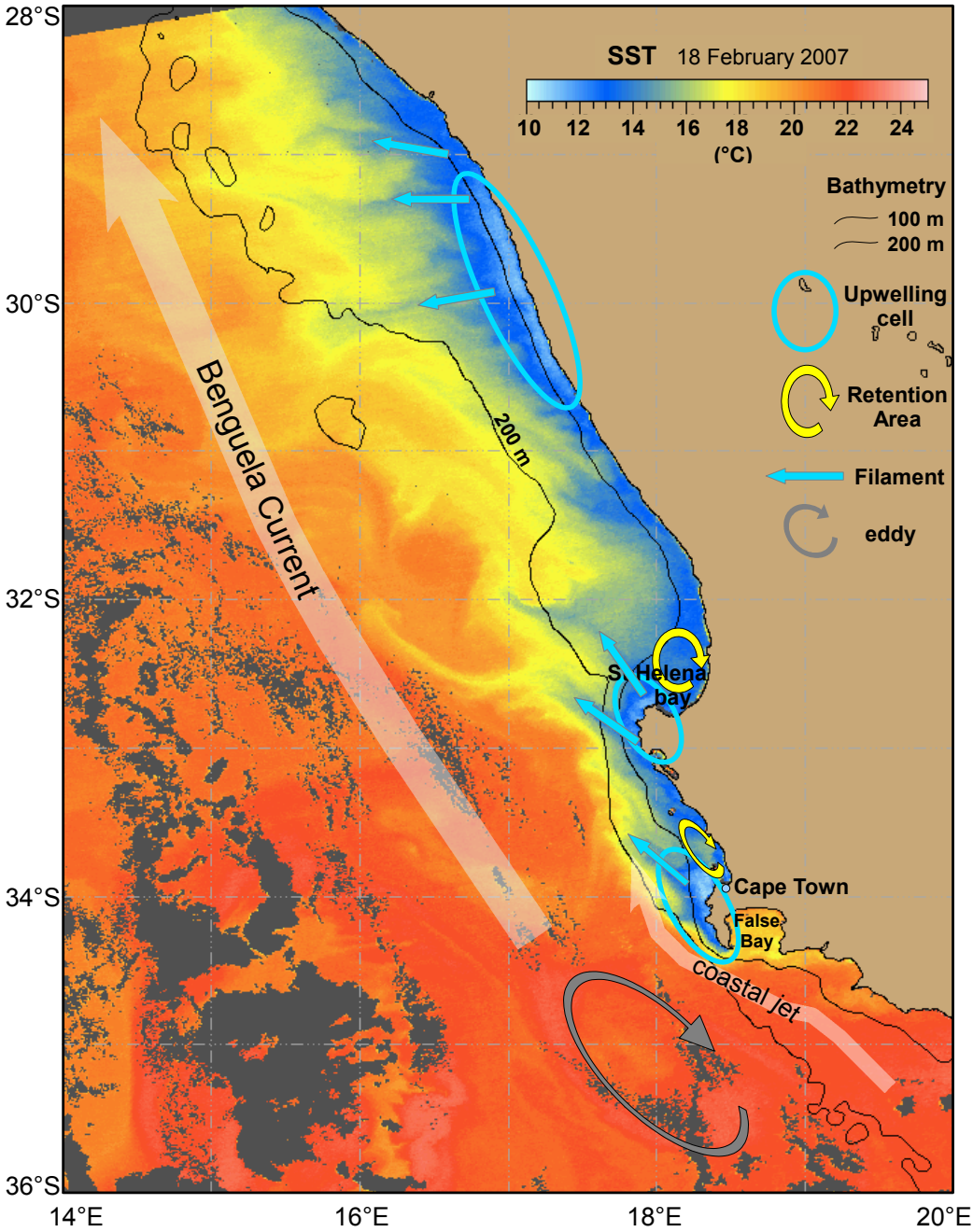


**Figure 14.3** Same as Figure 14.2a (SST) but using a colour palette. Upwelling cells, associated filaments and retention areas are superimposed. MODIS data provided by NASA/GSFC.

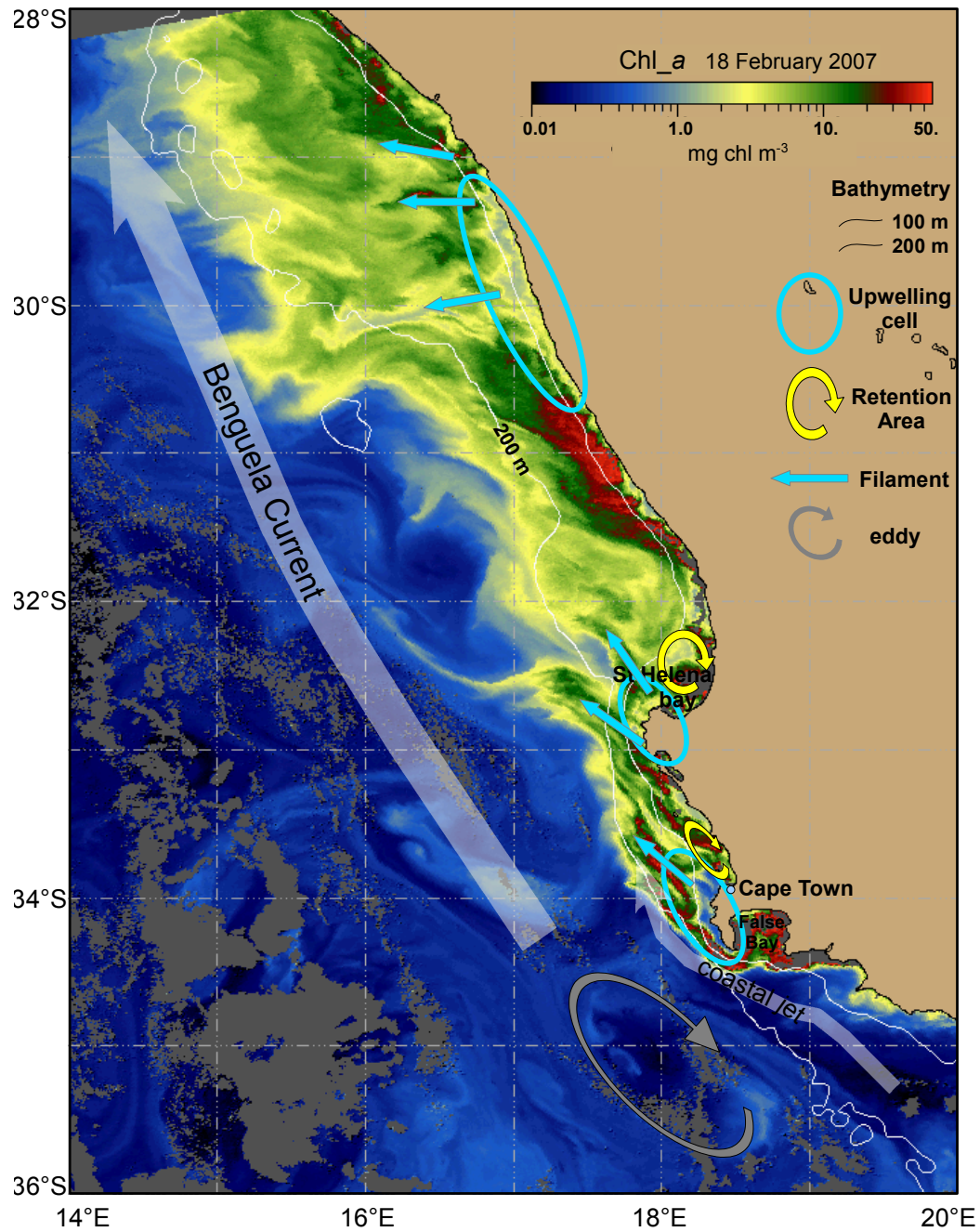


**Figure 14.4** Same as Figure 14.2b (Chl-*a*) but using a colour palette. Note the logarithmic scale that accounts for the irregular distribution of the chlorophyll values. MODIS data provided by NASA/GSFC.

## 14.4 Answers

**A1:** The SST field (Figure 14.3) provides a synoptic view of the near surface dynamics, where upwelled waters are much colder than the surrounding waters. The minimal

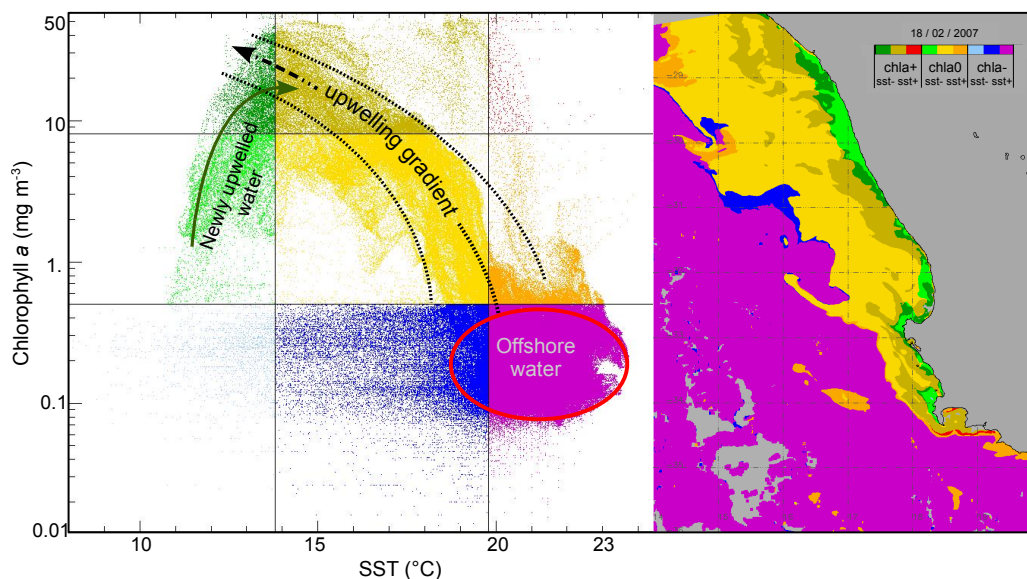


**Figure 14.5** Cluster plot of the SST and SCC values showing a general negative relationship between the two parameters, as well as the chlorophyll values of the newly-upwelled waters. MODIS data provided by NASA/GSFC.

temperature at the centre of the most active upwelling cell is close to  $10^{\circ}\text{C}$ , a temperature that is usually found at a depth of  $>100$  m (data not shown), suggesting that the origin of the upwelled water is close to the continental slope. Several distinct upwelling cells occur at specific locations where the wind component parallel to the coast is maximum, according the Ekman pumping theory. The SST difference between the cool upwelled water and the warm offshore water is close to  $10^{\circ}\text{C}$ . This temperature difference can also be used as a proxy to estimate the intensity of the coastal upwelling, or at least its thermal impact at the sea surface, complementing the Ekman upwelling index, a measurement of the upwelling intensity computed from Ekman theory. A closer look at the concomitant weekly wind field (insert in Figure 14.2) shows that the location of the three identified upwelling cells matches exactly with those coastal portions parallel to the wind direction, where the upwelling process is maximal, according the Ekman theory (Figure 14.1a).

**A2:** The location, intensity and shape of the thermal fronts associated with these coastal waters supplies a lot of information on the mesoscale circulation features and the influence of the coastline. Knowledge of the bathymetry (100 and 200m isobaths) is essential to study the effects of the continental shelf and to understand the forcing effects of the large scale circulation (the westward coastal jet in the southern part of the area). A long upwelling filament ( $\sim 200$  km), situated between  $32$  and  $33^{\circ}\text{S}$  is clearly visible on the SST image, as well as the chlorophyll image (Figures 14.3 and 14.4). Many other filaments are visible, all associated with the various upwelling cells identified. Outside the coastal upwelling area, a warm anticyclonic

eddy is clearly visible (grey arrow), partly generated by the frictional forces of the coastal jet current. Its central region, situated at 35°S and 18°E, is characterized by very low chlorophyll concentrations. This characteristic can be attributed to the deepening of the isotherms as a result of the surface convergent field associated with the "spinning up" of the eddy. An excellent description of eddies, as well as their importance as a temporary habitat for marine fish larvae, can be found in Bakun (2006).

**A3:** The surface chlorophyll field (Figure 14.4) provides an informative view of the biological response to surface enrichment resulting from coastal upwelling. At first glance, we observe a clear inverse relationship between SST and SCC, which is called the "upwelling gradient". Figure 14.5 summarizes what we can deduce from a careful observation of both the SST and SCC fields from Figures 14.3 and 14.4. The colours in Figure 14.5 represent 9 partitions of the relationship between the two variables, as well their spatial correspondence. The warm "offshore waters" are easily identified by temperatures  $>20^{\circ}\text{C}$  and low chlorophyll concentrations ( $< 0.5$  to  $0.6 \text{ mg m}^{-3}$ ). When moving towards the coast, the main category of water is that associated with the "upwelling gradient", where we can observe the progressive transformation of the recently-upwelled water (shown in green) as it reaches the euphotic layer. The chlorophyll concentration in this water mass increases progressively as photosynthesis takes place and the phytoplankton cells increase in number. The maximum chlorophyll values are extremely high (close to signal saturation). Chlorophyll concentration generally decreases as the water drifts offshore because of the "dilution" of the upwelled water. This upwelling gradient is maximum in the coastal area for high chlorophyll values  $> 10 \text{ mg m}^{-3}$  (dark green and brown-green colours) before nutrients start to become a limiting factor for algae growth. To fulfill the view of this ecological gradient we may imagine the role of the zooplanktonic grazers (mainly large copepod species) that feed actively on the large diatom cells commonly found in upwelling areas. Similarly, small pelagic fish such as anchovies feed on the copepods. This chain of events evolves both in time and space, along a cross-shore gradient of progressively more mature waters.

**A4:** A closer look at the centre of the upwelling cells (particularly those off the Cape coast, indicated by blue rings) shows very low values of SCC as opposed to the previously observed negative relationship between SCC and SST. This surprising result can be explained by the residence time of the water masses in the euphotic layer, which is too short (less than a few days) to allow for a significant multiplication of the algae (diatoms in our case). Effectively, the time for cell division to take place is about 5 days. Further offshore, where the residence time at the surface becomes higher, photosynthesis takes place, the cells multiply and the chlorophyll concentration increases. A typical time period for a chlorophyll increase from  $1 \text{ mg m}^{-3}$  to  $10\text{-}20 \text{ mg m}^{-3}$  in this area is 6-7 days (Brown and Hutchings, 1987).

**A5:** Any particle (e.g. phytoplankton cell, fish larvae) close to an upwelling cell has a high probability of being driven rapidly far offshore, especially if it is retained in an upwelling filament. In contrast, certain areas in this region make it possible for the same particles to be retained in a favorable environment for days or even weeks. The coastal complexity and the presence of capes induce such privileged areas. This is the case in St Helena Bay (indicated as a "retention area" in Figure 14.3) as well as the bay of Cape Town. Further south, False Bay provides a good retention area, combining relatively warm water associated with a strong enrichment, horizontally advected from coastal counter currents. This area is known for its high species diversity, including seals, white sharks, and even surfers!

## 14.5 References

### 14.5.1 Information for downloading data used in this case study

- ❖ MODIS data general access (ordering "Level 2" data): <http://oceancolor.gsfc.nasa.gov/cgi/browse.pl>
- ❖ Direct access to 1-km full orbit "Level 2" MODIS chlorophyll and SST data: <http://oceandata.sci.gsfc.nasa.gov/MODISA/L2/>
- ❖ SeaWinds data and "browse" images can be downloaded in various formats from [http://podaac.jpl.nasa.gov/DATA\\_CATALOG/quikscatinfo.html](http://podaac.jpl.nasa.gov/DATA_CATALOG/quikscatinfo.html)
- ❖ "Level 3" gridded data in HDF4 format, along with various decoding software in C, Fortran, IDL and MATLAB: [http://aspera.jpl.nasa.gov/download/pub/ocean\\_wind/quikscat/L3/](http://aspera.jpl.nasa.gov/download/pub/ocean_wind/quikscat/L3/)

### 14.5.2 Information for related data and documentation

- ❖ Aqua sensor: <http://aqua.nasa.gov/>
- ❖ MODIS ocean colour products: <http://picasso.oce.orst.edu/ORS00/MODIS/code/Table1Products.html> (see also [http://oceancolor.gsfc.nasa.gov/DOCS/MSL12/master\\_prodlst.html](http://oceancolor.gsfc.nasa.gov/DOCS/MSL12/master_prodlst.html) for more detailed information)
- ❖ EOS products: [http://eosps0.gsfc.nasa.gov/eos\\_homepage/for\\_scientists/index.php](http://eosps0.gsfc.nasa.gov/eos_homepage/for_scientists/index.php)
- ❖ The Earth Science Reference Handbook: (291 pages, 7.5 MB, PDF document) [http://eosps0.gsfc.nasa.gov/ftp\\_docs/2006ReferenceHandbook.pdf](http://eosps0.gsfc.nasa.gov/ftp_docs/2006ReferenceHandbook.pdf)
- ❖ SeaWinds products: [http://podaac.jpl.nasa.gov/DATA\\_CATALOG/quikscatinfo.html](http://podaac.jpl.nasa.gov/DATA_CATALOG/quikscatinfo.html)
- ❖ Ready to use data series: some of the data included in this case study was extracted from the AOS web site (<http://aos.mpl.ird.fr/>), a satellite image series finder, developed at IRD, Institut of Research for Development by the CRH (Centre de Recherches Halieutiques).

### 14.5.3 References and Suggested Reading

- Ekman WK (1905) On the influence of earth's rotation on ocean currents. *Arkiv för Matematik, Astonomi och Fysik* 2 (11): 1956
- Bakun A (1975) Daily and weekly upwelling indices, West coast of North America, NOAA Technical Reports, NMFS SSRF-693, 1967-73
- Bakun A (2006) Front and eddies as key structures in the habitat of marine fish larvae: opportunity, adaptative response and competitive advantage. *Scientia Marina*, 70S2: 105-122
- Brown PC, Hutchings L (1987) The development and decline of phytoplankton blooms in the southern Benguela upwelling system. 1. Drogue movements, hydrography and bloom development. In:

- Payne AIL, Gulland JA, Brink KH (Eds), The Benguela and Comparable Ecosystems, S Afr J Mar Sci 5:357-391
- Brown OB, Minnett PJ (1999) MODIS Infrared Sea Surface Temperature Algorithm Theoretical Basis Document, Ver 2.0 [http://modis.gsfc.nasa.gov/data/atbd/atbd\\_mod25.pdf](http://modis.gsfc.nasa.gov/data/atbd/atbd_mod25.pdf)
- Carder KL, Chen FR, Cannizzaro JP, Campbell JW, Mitchell BG (2004) Performance of the MODIS semi-analytical ocean color algorithm for chlorophyll-a. Adv Space Res 33:1152-9
- Demarcq H, Faure V (2000) Coastal upwelling and associated retention indices from satellite SST. Application to Octopus vulgaris recruitment. Oceanol Acta 23(4):391-408
- Demarcq H, Barlow R, Hutching L (2007) Application of a chlorophyll index derived from satellite data to investigate the variability of phytoplankton in the Benguela ecosystem. Afr J Mar Sci 29(2):271-282
- Lasker R, Pelaez J, Laurs RM (1981) The use of satellite infrared imagery for describing ocean processes in relation to spawning of the northern Anchovy (*Engraulis mordax*). Rem Sens Environ 11:439-453
- O'Reilly JE and 24 co-authors (2000) SeaWiFS Postlaunch Calibration and Validation Analyses, Part 3. NASA Tech Memo 206892, 11: NASA Goddard Space Flight Center, Greenbelt, Maryland
- Tang W, Liu WT, Stiles BW (2004) Evaluation of high-resolution ocean surface vector winds measured by QuikSCAT Scatterometer in coastal regions. IEEE 2(8):1762-1769
- Van der Lingen C, Fréon P, Hutchings L, Roy C, Bailey G, Bartholomae C et al. (2006) Forecasting shelf processes of relevance to marine resources in the BCLME. In: Rizzoli P, Woods J (Eds). The Benguela: Predicting a Large Marine Ecosystem. Elsevier Series
- Walton CC, Pichel WG, Sapper JF (1998) The development and operational application of nonlinear algorithms for the measurement of sea surface temperatures with the NOAA polar-orbiting environmental satellites. J Geophys Res 103(C12):27,999-28,012

## Case Study 15

# Comparison of *In Situ* and Remotely-Sensed Chl-*a* concentrations: A Statistical Examination of the Match-up Approach

E. Santamaría-del-Ángel\*<sup>1</sup>, R. Millán-Núñez<sup>1</sup>, A. González-Silvera<sup>1</sup> and R. Cajal-Medrano<sup>1</sup>

---

## 15.1 Background

With the launch of the Coastal Zone Color Scanner (CZCS) in November of 1978, a new era in oceanographic studies began. This was the first instrument dedicated to the measurement of ocean colour using satellite imaging, and its main purpose was to determine whether spectroradiometric observations could be used to identify and quantify suspended or dissolved matter in ocean waters (IOCCG, 2000; 2004; 2006). CZCS imagery encompassed large geographic areas and was collected over short periods of time, something that was not possible with previous measurement techniques (ships, buoys, airplanes). CZCS was a ‘proof-of-concept’ mission, to determine whether Chlorophyll-*a* concentration (Chl-*a*) could be estimated from space, based on spectrophotometric principles. Studies using CZCS data (Peláez and McGowan 1986; Yoder et al., 1987; Muller-Karger et al., 1991; Santamaría-del-Ángel et al. 1994a,b) showed that measurement of the colour of the ocean is a powerful tool for oceanographic studies, and that this method can yield information about the ocean surface at meso- to macro-scales. These studies provided justification to launch other sensors such as SeaWiFS (Sea-viewing Wide Field-of-view Sensor), MODIS-Aqua (MODerate resolution Imaging Spectroradiometer) and MERIS (MEdium Resolution Imaging Spectrometer).

Data extracted from ocean-colour images allows one to examine the temporal-spatial variability of the surface layer of the oceans. For example, Chl-*a* is an index of phytoplankton biomass, so a time series of Chl-*a* concentrations can be used in modelling studies that require phytoplankton biomass as an entry variable, such as primary productivity models (Platt et al. 1988; Barocio-León et al., 2007) or carbon

---

<sup>1</sup>Facultad de Ciencias Marinas, Universidad Autónoma de Baja California (FCM-UABC) Carretera Tijuana-Ensenada Km 106 C.P. 22860 Ensenada BC. Mexico. \* *Email address:* [santamaria@uabc.edu.mx](mailto:santamaria@uabc.edu.mx)

flux models (Camacho-Ibar et al., 2007). In addition, ocean-colour images can provide information about oceanographic surface structures at the meso-scale and allow for tracking of their space-time variations (Traganza et al. 1980; Santamaría-del-Ángel et al., 2002; González-Silvera et al., 2004, 2006; López-Calderón et al., 2008). Such technology may also be able to provide data for fishery studies (IOCCG, 2009; Dulvi et al., 2009).

One of the main challenges in using ocean-colour imagery is to determine the degree of correlation between the *in situ* measurements and the satellite-derived data. NASA uses the 'match-up' technique, which is based on a hypothetical linear relationship between satellite Chl-*a* concentrations ( $Chl_{a_s}$ ) and the *in situ* values obtained from water samples ( $Chl_{a_i}$ ). For most data, a 70% correlation (or 30% error) is considered a good fit (Gregg and Casey, 2004; Djavidnia et al., 2006). To understand the match-up approximation, and to consider the pros and the cons of this method, several statistical considerations must be taken into account: (a) the pattern of data variability, (b) the association indexes used to express the relationship between the *in situ* and satellite data, and (c) the number of data points considered when applying this approximation. It is also important to consider the data scales e.g., *in situ* measurements are generally based on ~1 liter of sea water, while remotely-sensed estimations are obtained from an area of ~1 km<sup>2</sup>. It is difficult to obtain an ideal match-up in space and time. Ideally, *in situ* measurements should be collected at the same time as the radiometric measurements required to validate ocean-colour algorithms.

The spatial distribution of phytoplankton on the ocean surface is not homogeneous; similarly, the vertical distribution in the water column is not homogeneous and generally exhibits a sub-surface maximum (Cullen and Eppley, 1981; Millán-Núñez et al., 1996). The distribution and size of the patches depends on a number of physical (light, turbulent mixing processes such as wind, surges), chemical (nutrients) and biological (algal type) factors. The  $Chl_{a_s}$  data provides information about the phytoplankton biomass in the first optical depth at a scale of ~1 km per pixel (Figure 15.1) while the  $Chl_{a_i}$  data are derived from discrete bottle samples near the ocean surface. Differences in sampling techniques are one of the factors contributing to the variability of the two datasets. Both approximations seek the concentration of Chl-*a*, but while the *in situ* samples are based on spectrophotometric, fluorometric, or HPLC determinations of ~1 liter of water, remote sensor measurements integrate data (through marine optics approximations) from a greater volume, yielding average values of Chl-*a* concentration (Fig. 15.1). Thus the *in situ* and remote sensor measurements evaluate processes on different space/time scales (Fig. 15.2). Satellite remote sensing allows the study of processes >10 km horizontal scale, encompassing several decades, while *in situ* measurements study processes over a much smaller time and space scales (cm to meters, minutes to days).

The 'match-up approximation', a graphical technique based on a theoretical straight line fitted to two variables with identical distribution patterns, can be used

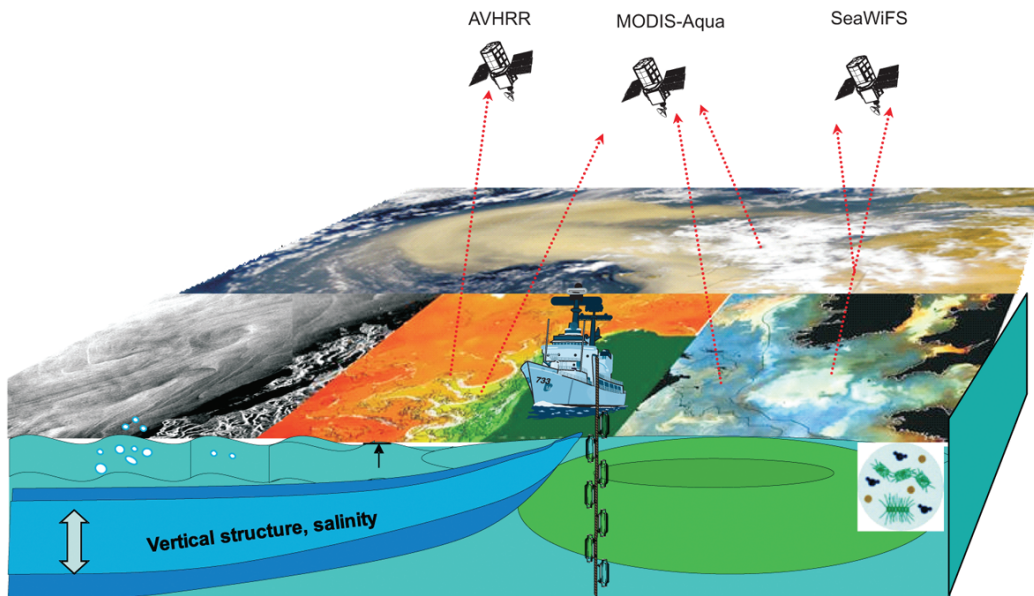


**Figure 15.1** Schematic representation of the *in situ* and satellite-based sampling methods.

to compare data. If one variable is plotted against itself, or two variables with different magnitudes are plotted, the resulting graph yields a straight line with a 45-degree slope. As the data distribution differs, the dispersion increases. To determine the statistical validity of the observed patterns, a statistical analysis can be applied to examine the level of linear association between variables. The most common linear association index is Pearson's correlation coefficient ( $r_p$ ), often simply just called 'correlation coefficient', denoted  $r$ . The mathematical expression is:

$$r_p = \frac{\text{Cov}_{A,B}}{SD_A \times SD_B} \quad (15.1)$$

where  $r_p$  = Pearson's correlation coefficient;  $\text{Cov}_{A,B}$  = Covariance of A and B;  $SD_A$  = standard deviation of A;  $SD_B$  = standard deviation of B. It is a measure of the correlation (linear dependence) between two variables A and B, giving a value between +1 and -1 inclusive (1 indicates a direct linear relationship, -1 indicates an inverse linear correlation, and zero indicates no linear relationship). It is expressed by the covariance of the two variables divided by the product of their standard deviations. A hypothesis test known as a 'correlation analysis' is carried out to determine if the coefficient is significant:

$$\begin{aligned} H_0 : r_p &= 0 \\ H_a : r_p &\neq 0 \end{aligned}$$

To accept or reject  $H_0$ , two values must be compared; the calculated value ( $r_{p_{\text{cal}}}$ ),

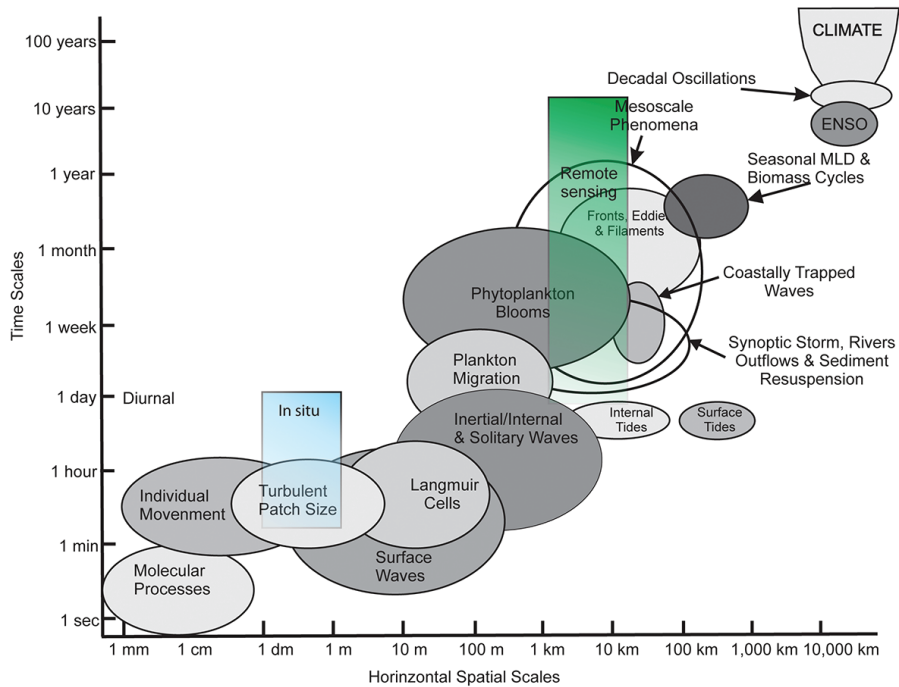


**Figure 15.2** Schematic representation of the temporal space scales that cover each type of sampling method.

derived from Equation 15.1, and the critical value ( $r_{P_{cr}}$ ) obtained from a table of critical values (found in any statistical textbook) based on the degree of freedom ( $df = n-1$ ) and the error  $\alpha$  (1-confidence level). Confidence levels are 90, 95 and 99% yielding errors of 10, 5 and 1, respectively.  $r_{P_{cr}}$  is the minimum significant value of  $r_P$ . If  $r_{P_{cal}} > r_{P_{cr}}$ ,  $H_0$  is rejected and is statistically significant. If  $r_{P_{cal}} < r_{P_{cr}}$ ,  $H_0$  cannot be rejected and  $r_P$  is not significant. Decision making becomes more robust with a greater number of data points, which is why the number of data points is critical. In general, only a small number of data points are obtained if one uses only the samples collected close the time of the satellite overpass, or on sunny days.

A significant value does not imply a cause-and-effect relationship. For example, a correlation coefficient of 0.975 between Chl-*a* and sea surface temperature (SST) does not imply an increase of Chl-*a* with an increase in temperature, but rather that SST can be used an indicator of temperature surge e.g. upwelled cool nutrient-rich water can cause an increase in the phytoplankton biomass in the euphotic zone. Furthermore, it should be noted that Chl-*a*<sub>s</sub> is expressed on a logarithmic scale while  $r_P$  is not, so a logarithmic transformation of the Chl-*a* data is required. To perform the match-up in a more direct manner, the use of Spearman's Non-Parametric Correlation Coefficient can be used (Equation 15.2):

$$r_S = \frac{\text{COV}_{RA,RB}}{SD_{RA} \times SD_{RB}} \quad (15.2)$$

where:  $r_S$  = Spearman's correlation coefficient;  $\text{COV}_{RA,RB}$  = covariance of the ranges of A and B;  $SD_{RA}$  and  $SD_{RB}$  = standard deviation of the ranges of A and B, respectively. The outcome for  $r_S$  is very similar to that of  $r_P$ , with a range of -1 to 1. The statistical significance of  $r_P$  can be determined through hypothesis testing similar to the tests described for  $r_S$  using a table of critical values of Spearman's coefficient. Case studies of two cruises are presented below as a practical demonstration:

1. **Case Study 1:** Only oceanographic stations sampled close to the time of the sensor overpass are considered, using data from the R/V IOFFE 2002 Ushuaia-Montevideo cruise (8-12 March, 2002).
2. **Case Study 2:** A combination of ten cruises in the CalCOFI (California Cooperative Oceanic Fisheries Investigations (<http://www.calcofi.org>) region is used from 2004 to 2006, sampled during daylight hours using both MODIS-Aqua and SeaWiFS data to help increase the number of observations.

SeaWiFS images with 1-km pixel resolution were used to make daily composites for both cruises. The concentration of Chl-*a* was calculated using the OC4-V4 algorithm (O'Reilly et al. 2000, Equations 15.3):

$$\text{Chla} = 10^{0.366 - 3.067R + 1.930R^2 + 0.649R^3 - 1.532R^4}, \quad (15.3)$$

where  $R = \log_{10} \left[ \frac{R_{rs443} > R_{rs490} > R_{rs510}}{R_{rs555}} \right]$ . The OC3M-V4 algorithm was used for the MODIS-Aqua images (O'Reilly et al. 2000, Equation 15.4):

$$\text{Chla} = 10^{0.283 - 2.753R + 1.457R^2 + 0.659R^3 - 1.403R^4}, \quad (15.4)$$

where  $R = \log_{10} \left[ \frac{R_{rs443} > R_{rs488}}{R_{rs551}} \right]$ .

## 15.2 Demonstration

### 15.2.1 Case Study 1

*In situ* data for this case study was collected during the R/V IOFFE Ushuaia-Montevideo cruise (8-12 March 2002) (Fig. 15.3), and was compared to SeaWiFS satellite data. Of the 337 oceanographic stations sampled during the cruise, only 14 fulfilled the requirements for match-up analysis i.e. samples collected between the hours of 10:00 and 14:00 (i.e. 2 hours before or after SeaWiFS overpass). In cases where the study area has high cloud coverage, all available satellite images are needed for analysis. Furthermore, some satellite images may not be centered directly over the sampling area, so some *in situ* sampling stations may not have adequate satellite data because of pixel degradation at the extreme edge of the sensor sweep (see Figure 15.4). In addition, clouds can prevent satellite data collection over a sampling

station. It is thus recommended that a  $3 \times 3$  pixel box centered over the station coordinates be used when extracting satellite data over a sampling station. There are several data extraction software packages available, including MatLab, WIM, ENVI and SEADAS.

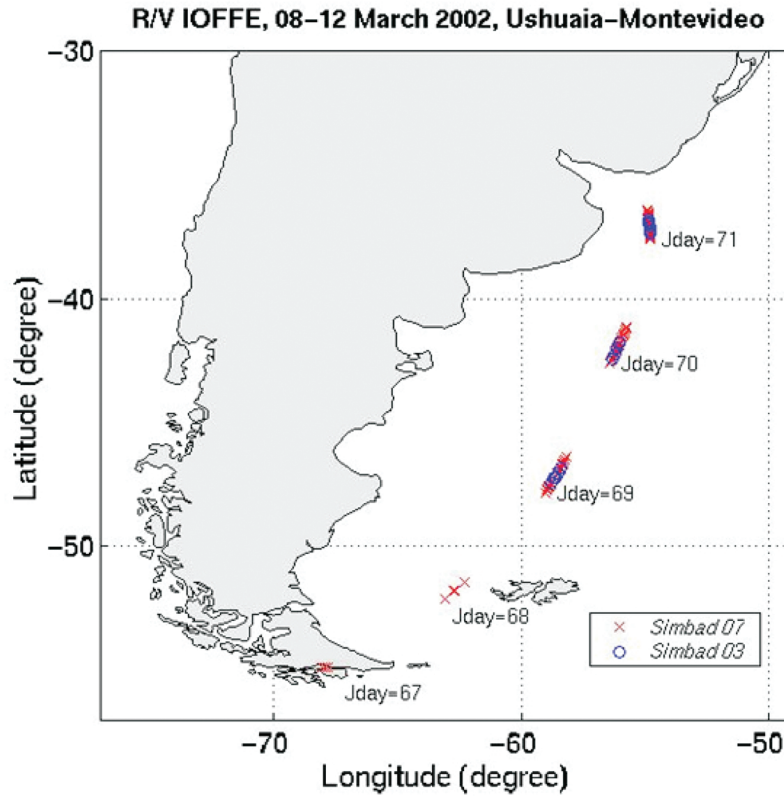


**Figure 15.3** Study area of the R/V IOFFE Ushuaia-Montevideo cruise (8-12 March 2002).

All files used in this case study can be downloaded from the IOCCG website at <http://www.ioccg.org/handbook/matchup/>. The Excel file 'case1data.xls' shows 14 stations with  $Chl a_i$  (determined by HPLC) and the averages of the  $3 \times 3$  box centered over the sampling station coordinates ( $Chl a_s$ ). Since  $Chl a_s$  represents integration over the first optical depth, samples within the first optical depth must be integrated for  $Chl a_i$ . The correlation between  $Chl a_s$  and  $Chl a_i$  is determined using  $r_p$ . Although 14 data points is a relatively small number,  $r_p = 0.852$  indicating that 85.2% of the total variability can be explained by one, or several, linear models. This value is statistically significant ( $\alpha = 5\%$ ,  $r_{p_{cr}} = 0.532$ ). Figure 15.5a shows that both *in situ* and satellite chlorophyll concentrations around  $0.3 \text{ mg m}^{-3}$  are remarkably similar. However, when  $Chl a_i > 0.6 \text{ mg m}^{-3}$ ,  $Chl a_s$  is underestimated.

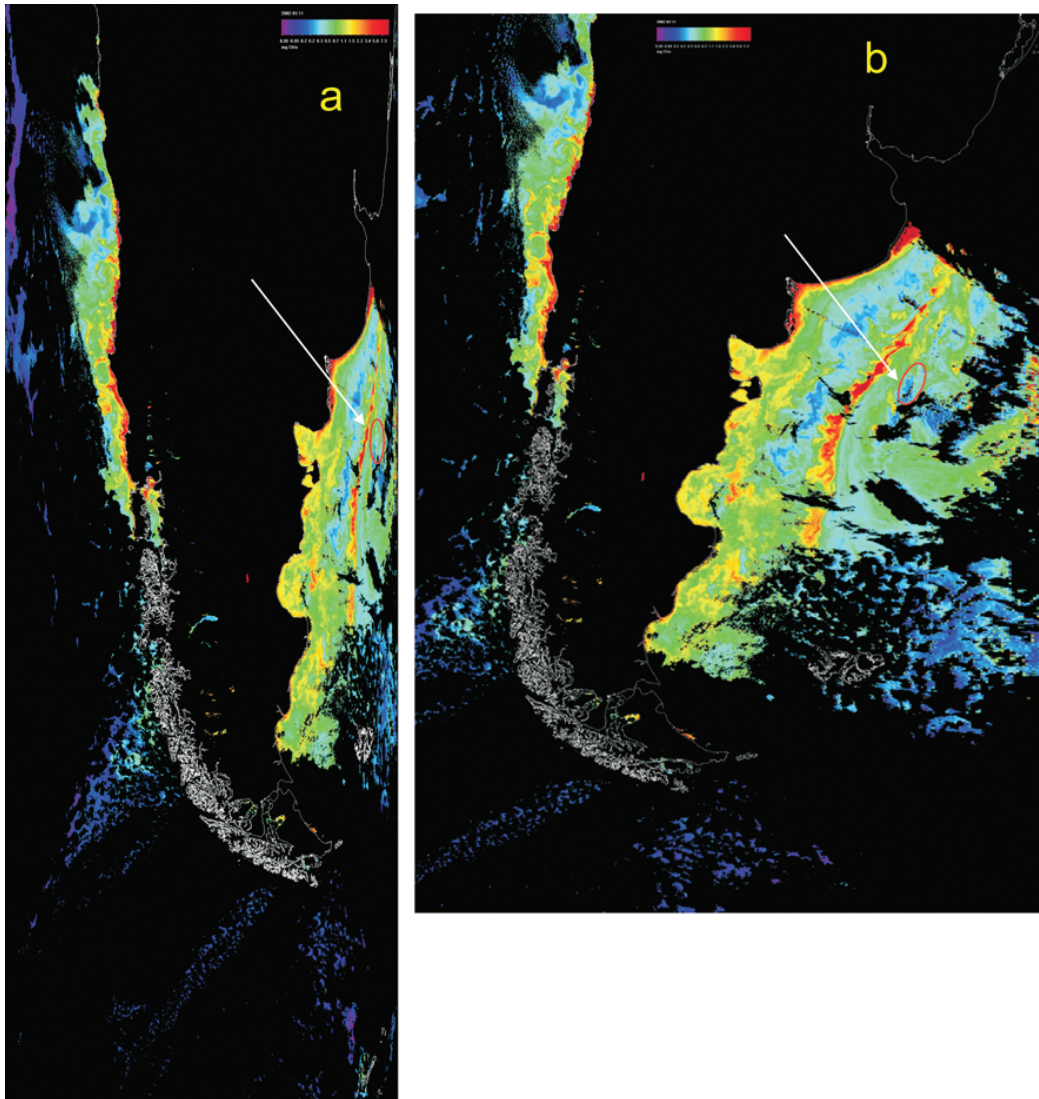


**Figure 15.4** Example of SeaWiFS chlorophyll image S2002070154515 processed to (a) Level 2, and (b) Level 3.

### 15.2.2 Case Study 2

This example will demonstrate how to increase the number of matchup data points in areas with high cloud coverage, using data from more than one satellite sensor. Data from 10 cruises in the CalCOFI region were used (2004 to 2006) in conjunction with MODIS-Aqua and SeaWiFS satellite imagery (Figure 15.6). Using data from two satellite sensors increases the possibility of matchup data over a given sampling station because of the different overpass times of the sensors, and changes in cloud cover patterns throughout the day. Figure 15.7 shows SeaWiFS and MODIS-Aqua images for 7 and 8 February 2006. A common area is defined by a yellow circle in

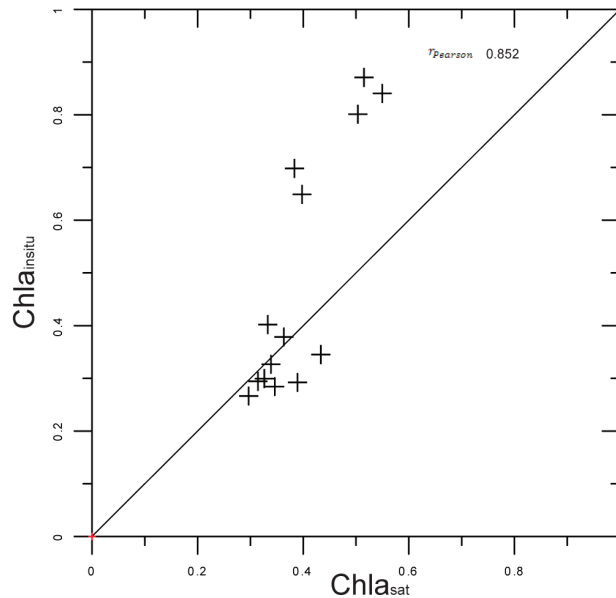


**Figure 15.5** Relationship between *in situ* chlorophyll measurements from the R/V IOFFE cruise, and satellite SeaWiFS-derived chlorophyll.

each image to highlight changes in cloud cover patterns. The database for this case study can be found in the Excel file ‘case2data.xls’ on the IOCCG website. There are five columns: station-cruise,  $Chla_s$  for MODIS-Aqua and SeaWiFS, the geometric mean of both, and  $Chla_i$ . The arithmetic mean ( $\bar{X}_a$ ) for each station is the sum of the data values divided by the total number of data points.

$$\bar{X}_a = \frac{\sum x}{n} \quad (15.5)$$

This mean uses all pixels, even those with no geophysical values, so the geometric mean ( $\bar{X}_g$ ) should be used to generate a value that is representative of the data:

$$\bar{X}_g = \frac{\sum x}{N_{in}} \quad (15.6)$$

i.e., the ratio of the sum of the valid data and the number of pixels that yielded these valid data points ( $N_{in}$ ). Using equations 15.1 and 15.2,  $r_p$  and  $r_s$  coefficients were calculated for the data as well as the base 10 log-transformed data (Table 15.1). Using only the MODIS-Aqua satellite data for the 10 cruises over almost 3 years would yield 128 match-up data points. If only SeaWiFS data were used, this number would increase to 142. Combining data from the two sensors and using the geometric mean, the number of data points increases to 172. Note that all the coefficients are statistically significant at  $\alpha = 5\%$ ; but only at concentrations  $< 1 \text{ mg Chla m}^{-3}$ .

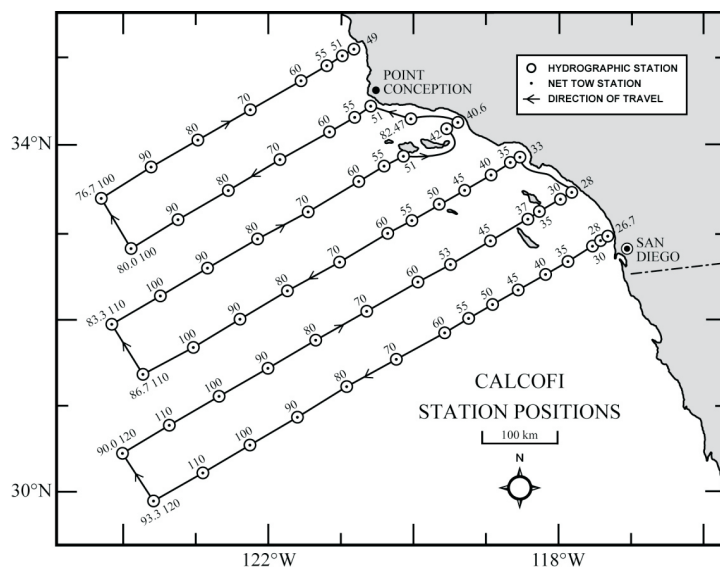
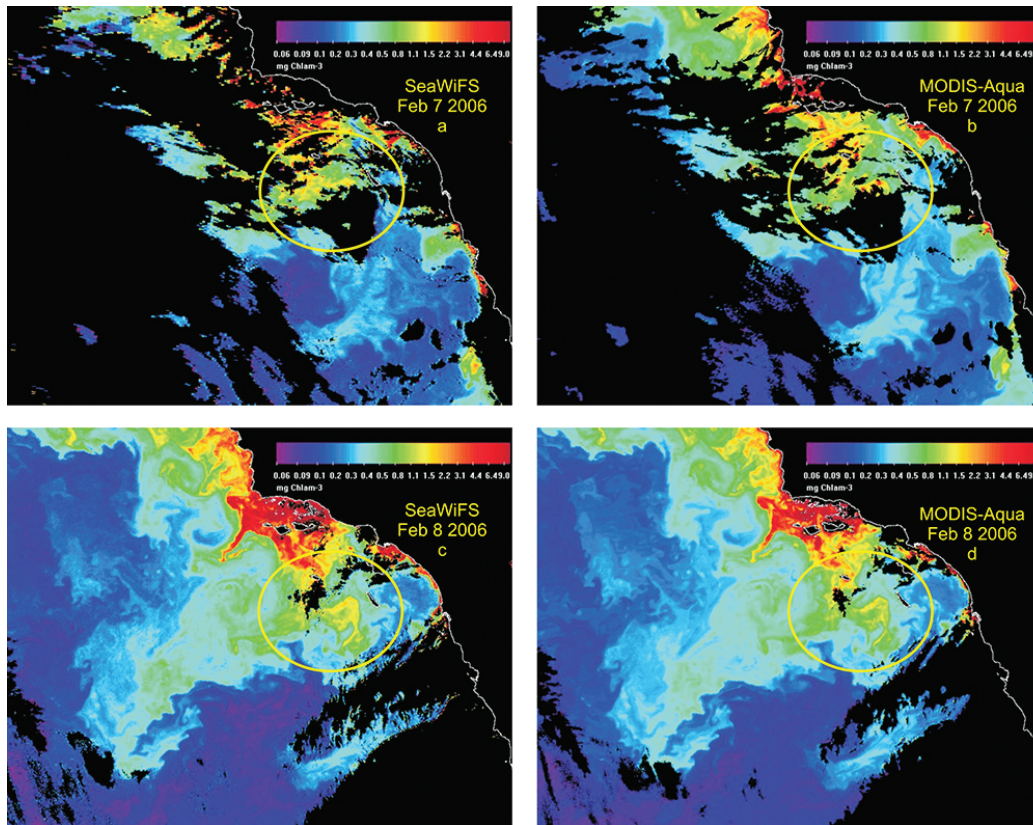


Figure 15.6 Location of the CALCOFI study area.

Table 15.1 Correlation between the *in situ* concentrations of chlorophyll-*a* and the concentrations derived from MODIS-Aqua, SeaWiFS and the combination of both sensors for CalCOFI cruises from 2004 to 2006.

	Data		Log <sub>10</sub> Data	
	$r_P$	$r_S$	$r_P$	$r_S$
MODIS-Aqua (n=128)	0.690	0.839	0.807	0.839
SeaWiFS (n=142)	0.588	0.859	0.802	0.859
Both (n=172)	0.664	0.882	0.834	0.882

Since  $r_P$  determines the degree of correlation expressed by the variability explained by linear relationship, while  $r_S$  determines the degree of correlation (including that explained by linear models), Spearman values will be greater than Pearson values, which is apparent in the non-transformed data.  $Chl_a_s$  is generally expressed on a logarithmic scale and it can be seen that  $r_P$  increases if the data is log-transformed, while  $r_S$  remains the same, suggesting that Spearman’s correlation coefficient is better for establishing the degree of correlation between  $Chl_a_i$  and  $Chl_a_s$ . Figure 15.8a shows that with non log-transformed data at low chlorophyll concentrations, there appears to be a high correlation between the satellite and  $Chl_a_i$  data, but at concentrations  $> 1 \text{ mg Chl a m}^{-3}$ , data dispersion increases considerably. This is less evident when expressing the same relationships on a logarithmic scale (Figure 15.8b). Note that expressing these relationships on a log scale only changes the visual representation, not the distribution pattern of the data points. Sampling can only provide a window of data into the global variability (Figure 15.8b gray



**Figure 15.7** Example images for the CalCOFI case study from 7–8 February 2006. a) SeaWiFS image from 7 February 2006, b) MODIS-Aqua image from 7 February 2006, c) SeaWiFS image from 8 February 2006, and d) MODIS-Aqua image from 8 February 2006. The yellow circle delineates an area to examine variability in cloud coverage.

squares), which is why linear relationships cannot explain all cases. For this reason, Spearman's correlation coefficient is a better indicator than Pearson's because it explores all types of relationships between two variables.

The CalCOFI region represents a system with a high space-time variability that is affected by climate fluctuations (Bograd et al., 2003). The increase in the water temperature and thermocline depth and the stratification of the water column are accompanied by changes in the populations of algae, invertebrates, zooplankton, fish and birds (Bograd et al., 2003). The CalCOFI database and the information derived from satellite imagery offers the potential to construct robust models that can explain the high variability of this area. This region is characterized by a strong oceanographic structure at the mesoscale, with the generation and evolution of meanders, eddies and filaments along the coast. The combination of data from several sources (including satellites and *in situ* measurements) in numerical models can be used to complement the descriptions of this variability at the mesoscale. Di

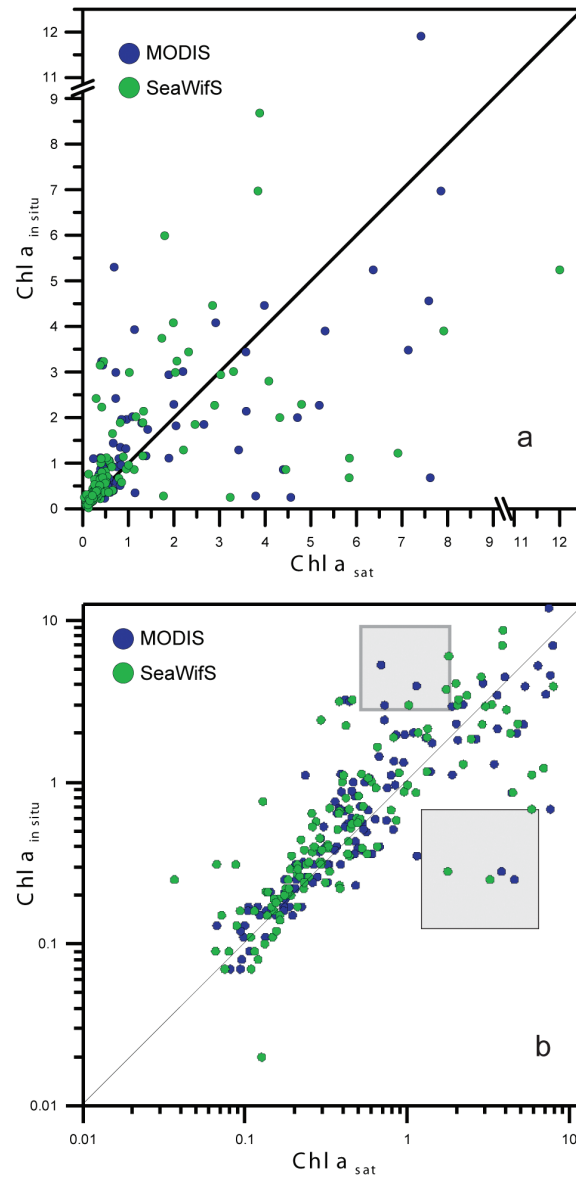


**Figure 15.8** Relationship between *in situ* chlorophyll data and SeaWiFS (green circles) and MODIS-Aqua (blue circles) chlorophyll data for the CALCOFI cruises from 2004 to 2006, plotted on a linear scale (a), and a logarithmic scale (b). The grey squares represent a hypothetical window when using data from one cruise only.

Lorenzo et al. (2004) used the CalCOFI database in combination with data derived from SeaWiFS to model the dynamic nature of the California Current system. They noted that the comparison of *in situ* Chl-a data with that derived from SeaWiFS was difficult due to the different sampling scales employed by each approximation. This case study proposes a better approximation to compare the *in situ* and satellite data,

allowing for the space-time resolution of both to be maximized.

### 15.3 Training

The files in the folder entitled "trainingfiles" (<http://www.ioccg.org/handbook/matchup/>) will be used in this section. First we will focus on data extraction from stations in the  $3 \times 3$  pixel boxes. The stations and images of the CalCOFI 0507 cruise (July 2005) will be used. Before starting, three points must be considered:

1. It is important for all images to have the same geographic projection to facilitate preparation of the script for data extraction (based on latitude, longitude and geophysical value data matrices). If the images do not have the same projection, the matrices will have different dimensions.
2. The text file '0507stations.txt' lists the details of the sampling stations in three columns: longitude, latitude (both in degrees and tenths of a degree) and station identification. The first row is used for column headers. Note that latitudes are positive in the northern hemisphere and negative in the southern hemisphere, and longitudes are positive in the eastern hemisphere and negative in the western hemisphere.
3. A text file must be generated with a list of addresses where the images are stored (see '0507imagery.txt').

We used the WIM (Windows Image Manager) software (<http://www.wimsoft.com>), specifically its WAM (WIM Automation Module) module called 'wam\_statist'. In the upper left hand corner, there is a window labeled "List of Images", where the file name '0507imagery.txt' is placed. In the upper right hand corner, there are two windows: the top one is labeled "Mask or Station File Name" where the name and address of the station file ('0507stations.txt') is placed. The name and address of the file where the data are stored ('0507wam\_statist\_result.csv') is placed in the bottom window. This type of file can be opened in Excel and yields 23 columns. Column A consists of the image names, columns B and C are the start and end years (if the images are composites). Columns D and E are the start and end days (if the images are weekly or monthly composites). This case study uses daily LAC images with B and C values of 2005 and D and E having the same value (until another image is analyzed). Column F identifies the station that is named in the third column of the station file ('0507stations.txt'). Column G indicates the number of pixels in the  $3 \times 3$  box that have data ( $G, N_{in}$ ) and column H indicates the number of pixels that do not have data ( $H, N_{out}$ ). The maximum value in each column is 9 and the minimum is 0, so that if column G has a value of 9, all the pixels in the  $3 \times 3$  box have data.

The basic geometric statistical parameters can be extracted from the data in column G, (based only on the valid pixels): minimum (I), maximum (J), mean (K), standard deviation (L), and median (M). When there are no data in the  $3 \times 3$  box due to cloud coverage, signal saturation, or other factors (i.e. column H has a value

of 9), the value in these columns is -99. Column N denotes the pixel centered in the geographical coordinates where the station was located. Columns P through W contain the values of the remaining pixels in the 3×3 box. These data allow comparisons to be made with other statistical parameters, e.g. the mode.

The next step is to generate a file where the extracted data can be combined with the *in situ* data. In this case, this file was generated by combining the data from CalCOFI cruise 0507 and the results of the extraction file '0507wam\_statist\_result.csv'. The resulting file ('0507match-up.xls') will be used in the second part of this section, where the focus will be on the calculation of Pearson's and Spearman's correlation coefficients to establish the degree of correlation between  $Chl_s$  and  $Chl_i$ . We will use data from MODIS-Aqua and SeaWiFS to increase the number of data points for the calculation of the two coefficients (using Equations 15.1 and 15.2), for both the log-transformed and raw data (Table 15.2).

**Table 15.2** Correlation between *in situ* chlorophyll-*a* and chlorophyll derived from MODIS-Aqua, SeaWiFS, and the combination of the two sensors, for the CalCOFI 0507 cruise.

	Data		Log <sub>10</sub> Data	
	$r_p$	$r_s$	$r_p$	$r_s$
MODIS-Aqua (n=5)	0.822	1.000	0.947	1.000
SeaWiFS (n=4)	0.933	1.000	0.881	1.000
Both (n=4)	0.873	0.964	0.946	0.964

Next, the statistical range must be calculated. This is done by labeling the smallest number in the data series 1, the next smallest 2 and so on, until the whole data series has been labelled. Table 15.3 shows three sets of data. Set A has no repeating values, so the range is calculated starting at 1 and ending in 10, since  $n = 10$ . Set B has repeating values (number 90 is repeated twice). The corresponding ranges would be 1 and 2, so a mean of the ranges is calculated and each would be assigned a value of  $1.5 (\frac{1+2}{2})$ . The next range to assign would be 3. Set C has a triple repeat of 124 and a double repeat of 128. In this case, 124 would have the corresponding ranges 4, 5, and 6, so a mean range of 5 is assigned to each, leaving the next range value as 7. For the 128 repeat, the corresponding ranges are 7 and 8 so a range value of 7.5 is assigned to each, leaving the next range value as 9.

Even with only a few data points (Table 15.2)  $Chl_s$  displays a high correlation with  $Chl_i$ . As noted previously,  $r_p$  coefficients are generally lower than  $r_s$  (= 100 in this study). Even when the  $r_p$  values are large, this does not imply a 1:1 relationship (Figure 15.9a). Rather, it implies that a high percentage of the variability can be explained by linear models. If the same graph is expressed on a log scale (Figure 15.9b), an apparent 1:1 linear relationship is observed. Note, the relationship of  $Chl_s$  to  $Chl_i$  is not the same as  $\log_{10}Chl_s$  to  $\log_{10}Chl_i$ .

**Table 15.3** Data demonstrating the calculation of ranges for one variable.

Set A	Rank A	Set B	Rank B	Set C	Rank C
133	6	129	6.0	128	7.5
137	8	132	8.0	124	5.0
99	3	90	1.5	110	3.0
138	9	136	9.0	131	9.0
92	2	90	1.5	98	2.0
89	1	93	3.0	84	1.0
130	4	114	4.0	147	10.0
132	5	129	6.0	124	5.0
141	10	150	10.0	128	7.5
135	7	129	6.0	124	5.0

If extrapolation of data (modelling one concentration based on the other) is desired in addition to generation of the linear model, tests on the significance of the intercept, the slope and the global significance of the model must be carried out. However, none of this is needed if only the degree of match-up is desired.  $r_p$  yields the degree of variability that can be explained by linear models. If one concentration is to be modeled based upon the other, the analysis can be based on empirical (linear) or mechanistic models. All the models have a determination coefficient ( $R^2$ ); i.e. the percentage of variability explained by a specific model. It is calculated as follows:

$$R^2 = \frac{SSM}{SST_o} \quad (15.7)$$

$$SSM = \sum_{i=1}^n (\hat{y}_i - \bar{y})^2 \quad (15.8)$$

$$SST_o = \sum_{i=1}^n (y_i - \bar{y})^2 \quad (15.9)$$

where  $SSM$  is the sum of the squared differences between the modelled data ( $\hat{y}_i$ ) and the mean of the observed data ( $\bar{y}$ ).  $SST_o$  is the sum of the squares between the observed data ( $y_i$ ) and the mean of the observed data ( $\bar{y}$ ) and defines of the total variability of the dependent variable.  $R^2$  is the ratio of the two sums of squares. When a linear model is used, it is assumed that  $R^2 = r_p^2$ , but this may not hold true for all data.

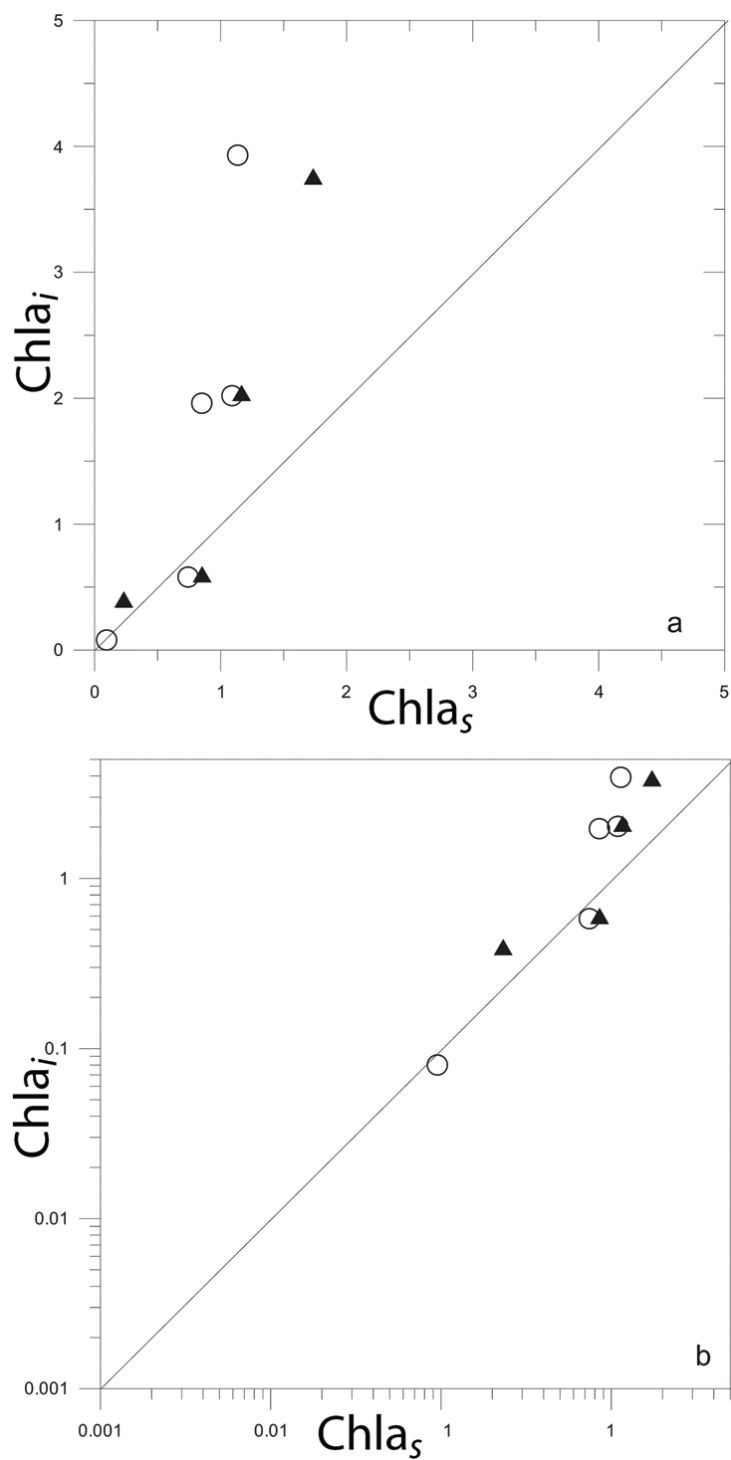


**Figure 15.9** Correlation between *in situ* chlorophyll and satellite-derived chlorophyll (triangles = SeaWiFS; circles = MODIS-Aqua) for the CALCOFI 0507 cruise, plotted on a linear (a) and (b) logarithmic scale.

## 15.4 Questions

1. Why is it important to have an *in situ* database for a defined grid, sampled over a long period of time?
2. Why is the CalCOFI area so important in this regard?
3. What is the weakness of the CalCOFI database, and how can that weakness be minimized?
4. What are the advantages and disadvantages of using satellite-derived data in this area?
5. Why is the relationship between *in situ* measurements and those derived from remote sensors important?
6. Are "normalized" data required to carry out match-up approximations? Do they have to be normalized with logarithms?
7. How should match-up study results be expressed?
8. What is the difference between  $R^2$  and  $r_p$ ?
9. Is Spearman's coefficient better than Pearson's?
10. How do you calculate the range for  $r_S$ ?
11. What is the geometric mean?
12. Is the geometric mean representative of the  $3 \times 3$  data extraction box?
13. Why is it important to have all the images at the same projection?

## 15.5 Answers

1. This sampling scheme allows variations over seasons, years, decades and longer time scales to be assessed in a more reliable manner and also allows the system to be modelled.
2. The CalCOFI area has a sampling record, for a defined grid, going back more than 60 years. A possible weakness of the CalCOFI database is that it only provides data four times a year, leaving nearly nine months with no monitoring in the area. The *in situ* observations of CalCOFI can be complemented with the use of ocean colour and SST images. Although these images only provide information about the surface of the ocean, they can provide a synopsis of changes in space and time.

3. Advantages include access to data on a daily time scale over a broad area, which allow the synoptic description of space-time variability and highlight oceanographic structures at the mesoscale. Currently, a long time series with a 1-km pixel size can be generated. Disadvantages of these data are that they only yield surface information and require cloudless days. Weekly or monthly data composites and long time series can be derived from remotely-sensed data.
4. The relationship between *in situ* measurements and those derived from remote sensors has three components: a) synoptic complementary data for space-time studies in windows where the *in situ* sampling does not yield any data; b) representation of indirect approximations, as well as those from remote sensors; and c) entry variables used to model the system.
5. No, if "normalized" means that the data fit a Gaussian distribution. Pearson's and Spearman's correlation coefficients do not require that the internal distribution of the variables fits a Gaussian curve.
6. The calculated value of the chosen coefficient must be presented as well as the significance given by the hypothesis tests, indicating the number of data points and the error,  $\alpha$ . A graph can be constructed with axes that have the same scale. A 45° straight line denoting the 1: 1 line should be included.
7.  $r_p$  is the degree of variability that can be explained by linear models (one or several), while  $R^2$  represents the variability explained by a given model. When a linear model is used, it is assumed that  $R^2 = r_p^2$ . However, this assumption may not be true in all cases. Furthermore,  $r_p$  calculated for variables AB is the same as that calculated for BA, but  $R^2$  is exclusive of a particular model.
8. Pearson's coefficient measures the degree of linear association, while Spearman's simply measures the degree of association. Spearman's coefficient is more robust if all that is sought is the degree of association.
9. Statistical ranges are defined as hierarchical indicators of a data set. A value of 1 is assigned to the smallest number in the series, the next smallest number is labeled with 2 and so on. The maximum range is equal to the number of data points. In the case of data points with the same values, the mean of the ranges assigned to the repeated number is calculated and assigned.
10. It is the sum of the valid data points divided by the number of pixels contributing to the valid data.
11. In general, the mean is considered representative of the data set but for satellite data sets, the geometric mean is more representative than the arithmetic mean.

12. It is important that all the images have the same geographic projection because it facilitates writing a data extraction program based on data matrices of latitude, longitude and geophysical values. If the images did not have the same projection, the matrices would have different dimensions, which would require another entry variable in the data extraction process.

## 15.6 References

- Barocio-León O, Millán-Núñez R, Santamaría-del-Ángel E, González-Silvera A (2007) Phytoplankton primary production in the euphotic zone of the California Current System from CZCS imagery and modeling. *Ciencias Marinas* 33(1): 59-72
- Bograd SJ, Checkley DA, Wooster WS (2003) CalCOFI: a half century of physical, chemical, and biological research in the California Current System. *Deep Sea Res II* 50 (14-16): 2349-2353
- Camacho-Ibar VF, Hernández-Ayón M, Santamaría-del-Ángel E, Dásele-Heuser LW, Zertuche-González JA (2007) Correlation of surges with carbon stocks in San Quintín Bay, a coastal lagoon in northwest Mexico. In: Hernández de la Torre B, Gaxiola Castro G (eds). *Carbon in Aquatic Ecosystems of Mexico*. Co-edited by the Department of Environmental and Natural Resources, National Ecology Institute NEI and the Center for Scientific Research and Higher Education of Ensenada CICESE, Mexico City pp 355-370
- Cox PM, Betts RA, Jones CD, Spall SA, Totterdell IJ (2000) Acceleration of global warming due to carbon-cycle feedbacks in a coupled climate model. *Nature* 408, 184-187
- Cullen, JJ, Eppley RW (1981) Chlorophyll maximum layers of the Southern California Bight and possible mechanisms of their formation and maintenance. *Oceanol Acta* 4: 23-32
- Djavidnia S, Mélin F, Hoepffner N (2006) Analysis of Multi-Sensor Global and Regional Ocean Colour Products. MERSEA - IP Marine Environment and Security for the European Area - Integrated Project Report on Deliverable D.2.3.5 European Commission - Joint Research Centre Ref: MERSEA-WP02-JRC-STR-0001-01A.pdf. 228 pp
- Dulvy N, Chassot E, Heymans J, Hyde K, Pauly D, Platt T, Sherman K (2009) Climate change, ecosystem variability and fisheries productivity. In: Forget M-H, Stuart V, Platt, T (eds), *Remote Sensing in Fisheries and Aquaculture*. IOCCG Report No. 8, IOCCG, Dartmouth, Canada pp 11-28
- Di Lorenzo E, Miller AJ, Neilson DJ, Cornuelle BD, Moisan JR (2004) Modelling observed California Current mesoscale eddies and the ecosystem response. *Int J Rem Sens* 25(7-8): 1307 - 1312
- Eber LE, Hewitt RP (1979) Conversion Algorithms for CALCOFI Station Grid. *CalCOFI Rep* XX: 135-137
- Friedlingstein, P, Cox PM, Betts RA, Bopp L, Von Bloh W, Brovkin V et al (2006) Climate-carbon cycle feedback analysis: results from the C4MIP model intercomparison. *J Climate* 19(14): 3337-3353
- Gregg WW, Casey NW (2004) Global and regional evaluation of the SeaWiFS chlorophyll data set. *Rem Sens Environ* 93: 463-479
- González-Silvera AG, Santamaría-del-Ángel E, Millán-Núñez R, Manzo-Monrroy H (2004) Satellite observations of mesoscale eddies in the Gulfs of Tehuantepec and Papagayo (Eastern Tropical Pacific). *Deep Sea Res II* 51: 587-600
- González-Silvera AG, Santamaría-del-Ángel E, Millán-Núñez R (2006) Spatial and temporal variability of the Brazil-Malvinas Confluence and the La Plata Plume as seen by SeaWiFS and AVHRR imagery. *J Geophys Res* 111: C06010, doi: 10.1029/2004JC002745
- Haidvogel DB, Wilkin JL, Young RE (1991) A semi-spectral primitive equation ocean circulation model using vertical sigma and orthogonal curvilinear horizontal coordinates. *J Comput Phys* 94: 151-185
- IOCCG (2000) *Remote Sensing of Ocean Colour in Coastal, and Other Optically-Complex, Waters*. Sathyendranath, S (ed), Reports of the International Ocean-Colour Coordinating Group, No. 3, IOCCG, Dartmouth, Canada
- IOCCG (2004) *Guide to the Creation and Use of Ocean-Colour, Level-3, Binned Data Products*. Antoine, D (ed), Reports of the International Ocean-Colour Coordinating Group, No. 4, IOCCG, Dartmouth,

Canada

- IOCCG (2006) Remote Sensing of Inherent Optical Properties: Fundamentals, Tests of Algorithms, and Applications. Lee, Z-P (ed), Reports of the International Ocean-Colour Coordinating Group, No. 5, IOCCG, Dartmouth, Canada
- IOCCG (2007) Ocean-Colour Data Merging. Gregg W (ed), Reports of the International Ocean-Colour Coordinating Group, No. 6, IOCCG, Dartmouth, Canada
- IOCCG (2009) Remote Sensing in Fisheries and Aquaculture. Forget M-H, Stuart V, Platt T (eds), Reports of the International Ocean-Colour Coordinating Group, No. 8, IOCCG, Dartmouth, Canada
- Lewis MR (1992) Satellite ocean colour observations of global biogeochemical cycles. In: Falkowski PG, Woodhead AD (eds). Primary Productivity and Biogeochemical Cycles in the Sea. Plenum Press NY pp 139-154
- Lopez-Calderon J, Martinez A, Gonzalez-Silvera A, Santamaria-del-Angel E, Millan-Nuñez R (2008) Mesoscale eddies and wind variability in the northern Gulf of California. *J Geophys Res* 113: C10001, doi:10.1029/2007JC004630
- Millán-Núñez R, Alvarez-Borrego S, Trees CC (1996) Relationship between deep chlorophyll and surface chlorophyll concentration in the California Current System. *CalCOFI Rep* 37: 241-250
- Müller-Karger FE, Walsh JJ, Evans RH, Meyers MB (1991) On the seasonal phytoplankton concentration and sea surface temperature cycles of the Gulf of Mexico as determined by satellites, *J Geophys Res* 96(C7):12,645-12,665
- O'Reilly JE, and 24 other authors (2000) Ocean colour chlorophyll-*a* algorithms for SeaWiFS, OC2, and OC4: version 4 In: Hooker SB, Firestone ER (eds) SeaWiFS Postlaunch Tech Rep Ser, Vol 11. SeaWiFS postlaunch calibration and validation analyses, Part 3. NASA, Goddard Space Flight Center, Greenbelt, MD, pp 9-23
- Pelaez J, McGowan JA (1986) Phytoplankton pigment patterns in the California Current as determined by satellite. *Limnol Oceanogr* 31(5): 927-950
- Platt T, Sathyendranath S, Caverhill CM, Lewis MR (1988) Oceanic primary production and available light: further algorithms for remote sensing. *Deep-Sea Res* 35: 855-879
- Santamaria-del-Ángel E, Alvarez-Borrego S, Müller-Karger FE (1994a) Gulf of California biogeographic regions based on coastal zone color scanner imagery. *J Geophys Res* 99(C4): 7411-7421
- Santamaria-del-Ángel E, Alvarez-Borrego S, Müller-Karger FE (1994b) The 1982-1984 El Niño in the Gulf of California as seen in coastal zone color scanner imagery. *J Geophys Res* 99(C4): 7423-7431
- Santamaria-del-Ángel E, Millán-Núñez R, González-Silvera AG, Müller-Karger FE (2002) The color signature of the Ensenada Front and its seasonal and interannual variability. *CalCOFI Rep* 43: 156-161
- Strub PT, Kosro PM, Huyer A, CTZ Collaborators (1991) The nature of the cold filaments in the California Current System. *J Geophys Res* 96(C8): 14,743-14,768
- Traganza ED, Nestor DA, McDonald AK (1980) Satellite observations of nutrients upwelling off the coast of California. *J Geophys Res* 85:4101-4106
- Yoder JA, McClain CR, Blanton JO, Oey LY (1987) Spatial Scales in CZCS-Chlorophyll Imagery of the Southeastern U. S. Continental Shelf *Limnol Oceanogr* 32(4): 929-941

### 15.6.1 Further reading

- Rebstock GA (2003) Long-term change and stability in the California Current System: lessons from CalCOFI and other long-term data sets *Deep Sea Res II* 50(14-16): 2583-2594